Conception rationnelle de nano-hybrides de carbone 1D pour l'application de nanocomposites diélectriques

Minhao Yang

université PARIS-SACLAY

NNT : 2018SACLC088

CentraleSupélec

Rational design of 1D carbon nano-hybrids for dielectric nanocomposites application

Thèse de doctorat de l'Université Paris-Saclay
préparée à CentraleSupélec

École doctorale n°579 Sciences mécaniques et énergétiques, matériaux et géosciences (SMEMAG)
Spécialité de doctorat: Science des Matériaux

Thèse présentée et soutenue à Gif-sur-Yvette, le 08 Nov. 2018, par

Minhao Yang

Composition du Jury :

Fabien MIOMANDRE Professeur, PPSM, École Normale Supérieure Paris-Saclay	Président, Examinateur
Valerie PRALONG Directeur de Recherche, CRISMAT, ENSICAEN	Rapporteur
Alain SYLVESTRE Professeur, G2ELAB, Université Grenoble Alpes	Rapporteur
Jinkai YUAN Chargé de Recherche, Centre de Recherche Paul Pascal	Examinateur
Jinbo BAI Directeur de Recherche, MSSMAT, CentraleSupélec	Directeur de thèse

Thèse de doctorat

Université Paris-Saclay
Espace Technologique / Immeuble Discovery
Route de l'Orme aux Merisiers RD 128 / 91190 Saint-Aubin, France

Acknowledgments

First of all, I would like to express my sincere gratitude to Prof. Jinbo Bai for his continuous support of my PhD study and research work, for his constant encouragement, guidance, patience, and immense knowledge, without which this work would not have been completed. I am also grateful to Dr. Delong He in particular for his guidance and support of my research work.

Besides my advisor, I would like to thank Prof. Zhi-Min Dang (Tsinghua University, China) for his recommendation during the PhD application process and precious guidance during PhD studies. Special gratitude is also extended to Prof. Dongrui Wang (University of Science and Technology Beijing, China) and Prof. Xianming Zhang (Zhejiang Sci-Tech University, China) for their helpful suggestions and continuous encouragement.

I would also like to thank Dr. Hang Zhao (Northwest University, China) and Dr. Jinkai Yuan (Centre de Recherche Paul Pascal, France) for their valuable suggestions and supports on the fabrication and measurement of samples.

I am also grateful to Dr. Zhongbin Pan (Ningbo University, China) and Dr. Jianwen Chen (Foshan University, China) for their assistance on the simulation of current density distribution. Additionally, I thank Dr. Paul Haghi-Ashtiani (CentraleSupélec, France) and Dr. Xinghua Li (Northwest University, China) for their help in the TEM characterization.

I am grateful to the engineers at MSSMAT, SPMS, and LGPM laboratories. Special gratitude is extended to Monsieur Nicolas Guiblin for his help in XRD characterizations, Madame Pascale Gemeiner for her help in Raman measurements, Monsieur Xavier Bril for his help in the measurement of D-E loops, Monsieur Thomas Reiss for his instruction of operating SEM, Madame Barbara Malinowska for her help in FT-IR measurement, Monsieur Gilbert Le Gal for fabricating the metallic moulds, and Monsieur Eric Perrin for repairing the controller of heating stage. I would also like to thank Mesdames Farida Djebarri and Sokona Konate for their assistance.

I also owe my sincere gratitude to my friends and fellows who gave me their help and time accompanying me during the past three years in France: Yang Wang, Yang Liu, Xiaofei Bai, Wangshu Chen, Salem Diana, Hanlu Zhang, Anne Zhang, Chaohe Hu, Yu Yang, Yi Hou, Jiemin Li, Mingsheng Zheng, Yajing Hou, Minglei Jing, and Jianbin Xue.

I would also like to thank Arkema Company who provides us with the PVDF (Kynar 761).

I wish to thank the China Scholarship Council (CSC) for funding my stay in France.

I dedicate this work to my beloved parents, who always supported and encouraged me, keeping me carrying on, no matter what kind of difficulties encountered.

Minhao Yang in Paris

20 August 2018

Université Paris-Saclay
Espace Technologique / Immeuble Discovery
Route de l'Orme aux Merisiers RD 128 / 91190 Saint-Aubin, France

Table of Contents

Acronyms and Symbols 1
Résumé en français 5
General Introduction 9
Chapter I 13
Electrical Energy Storage Technologies 13
1.1 Mechanical Energy Storage (MES) 14
1.1.1 Pumped Hydroelectric Energy Storage (PHES) 14
1.1.2 Compressed Air Energy Storage (CAES) 15
1.1.3 Flywheel Energy Storage (FES) 16
1.2 Thermal Energy Storage (TES) 17
1.2.1 Low Temperature TES 17
1.2.2 High Temperature TES 18
1.3 Chemical Energy Storage (CES) 19
1.4 Electrochemical Energy Storage (ECES) 20
1.4.1 Redox Flow Batteries (RFBs) 20
1.4.2 Lead-acid Batteries 21
1.4.3 Li-ion Batteries 21
1.4.4 Sodium Sulfur (Na-S) and Sodium-Metal Halide Batteries 23
1.4.5 Zinc Air (ZnAir) Battery 24
1.5 Electrical Energy Storage (EES) 25
1.5.1 Supercapacitor (Electrical Double-Layer Capacitor) 25
1.5.2 Conventional Capacitor 26
1.6 Concluding Remarks 32
Chapter II 35
Nanofillers for Dielectric Polymer Nanocomposites 35
2.1 Mechanism of Polarizations 35
2.2 Conductivity Effects of Nanofillers on Dielectric Properties of DPNs 37
2.2.1 CDPNs 37
2.2.2 DDPNs 49
2.3 Shape and Size Effects of Nanofillers on Dielectric Properties of DPNs 52
2.3.1 Shape Effects of Nanofillers on Dielectric Properties of DPNs 53
2.3.2 Size Effects of Nanofillers on Dielectric Properties of DPNs 55
2.4 Composition and Structure of Nanofillers on Dielectric Properties of DPNs 59
2.4.1 Core@Shell Structure for the CDPNs 60
2.4.2 Core@Shell Structure for the DDPNs 65
2.5 Orientation and Alignment of Nanofillers on Dielectric Properties of DPNs 74
2.6 Concluding Remarks 76
Chapter III 79
Ternary PVDF Nanocomposites with BNNSs and CNTs 79
3.1 Introduction 79

3.2 Experimental 80
3.3 Results and Discussions 81
3.4 Conclusions 87
Chapter IV 89
Core@Shell Structured CNTs@AC/PVDF Nanocomposites 89
4.1 Introduction 89
4.2 Experimental 92
4.2.1 Synthesis of Core-Shell Structured CNTs@AC Hybrids Fillers 92
4.2.2 Preparation of CNTs@AC/PVDF and P-CNTs/PVDF Nanocomposites 92
4.2.3 Characterizations 93
4.3 Results and Discussions 93
4.4 Conclusions 107
Chapter V 109
Core@Shell Structured BNNSs@Carbon PVDF Nanocomposites 109
5.1 Introduction 109
5.2 Experimental 111
5.2.1 Synthesis of BNNSs@C Hybrids Fillers 111
5.2.2 Preparation of BNNSs/PVDF and BNNSs@C/PVDF Nanocomposites 112
5.2.3 Characterizations 112
5.3 Results and Discussions 113
5.4 Conclusions 122
Chapter VI 123
Core@Shell Structured TiO_2@Carbon Nanowires PVDF Nanocomposites 123
6.1 Introduction 123
6.2 Experimental 125
6.2.1 Synthesis of TiO_2 NWs and TiO_2@C NW Hybrids 125
6.2.2 Preparation of TiO_2 NWs/PVDF and TiO_2@C NWs/PVDF Nanocomposites 126
6.2.3 Characterizations 127
6.3 Results and Discussions 127
6.4 Conclusions 147
Chapter VII 149
Core@Double-Shells TiO_2@Carbon@SiO_2 PVDF Nanocomposites 149
7.1 Introduction 149
7.2 Experimental 151
7.2.1 Synthesis of Core@Double-Shells Structured TiO_2@C@SiO_2 Nanowires 151
7.2.2 Preparation of TiO_2 NWs/PVDF, TiO_2@C NWs/PVDF and TiO_2@C@SiO_2 NWs/PVDF Nanocomposites 152
7.2.3 Characterizations 152
7.3 Results and Discussions 153
7.3.1 The Morphology and Composition of Core@Double-Shells Structured TiO_2@C@SiO_2 NWs with Variable Thickness of Carbon and SiO_2 Layers 153
7.3.2 The Influence of SiO_2 Layer Thickness on the Dielectric Performance of PVDF Nanocomposites 158
7.3.3 The Influence of Carbon Inner Shell Thickness on the Dielectric Performance of

PVDF Nanocomposites 163
7.3.4 Insights from the Computer Simulation 165
7.4 Conclusions 167
General Conclusions 169
Perspectives 173
References 175
Publications 193

Acronyms and Symbols

Acronyms

0D	0-Dimensional
1D	1-Dimensional
2D	2-Dimensional
3D	3-Dimensional
AC	Amorphous Carbon
Ag	Silver
Al	Aluminum
Ar	Argon
ATRP	Atom Transfer Radical Polymerization
BNNSs	Boron Nitride Nanosheets
BOPP	Biaxially Oriented Polypropylene
BT	Barium Titanate
C	Carbon
CAES	Compressed Air Energy Storage
CB	Carbon Black
CCTO	Calcium Copper Titanate
CDPNs	Conductive-Dielectric Polymer Nanocomposites
CES	Chemical Energy Storage
CNTs	Carbon Nanotubes
CTAB	Cetyltrimethylammonium Bromide
Cu	Copper
CVD	Chemical Vapor Deposition
DDPNs	Dielectric-Dielectric Polymer Nanocomposites
DMF	Dimethylformamide
DPNs	Dielectric Polymer Nanocomposites
DVB	Divinylbenzene
ECES	Electrochemical Energy Storage
EDLC	Electrical Double-Layer Capacitor
EDX	Energy Dispersive X-ray
EES	Electrical Energy Storage

Fe	Iron
FES	Flywheel Energy Storage
FT-IR	Fourier Transform Infrared Spectroscopy
GO	Graphene Oxide
HAADF	High-Angle Annular Dark-Field
HDPE	High Density Polyethylene
HR-TEM	High-Resolution Transmission Electron Microscope
IL	Ionic Liquid
Li	Lithium
MES	Mechanical Energy Storage
MMT	Montmorillonite
MWS	Maxwell-Wagner-Sillars
Ni	Nickel
ODA	4, 4'-Oxydianiline
PANI	Polyaniline
PA 6	Polyamide 6
Pb	Lead
PC	Polycarbonate
P-CNTs	Pristine Carbon Nanotubes
PDA	Polydopamine
PDMS	Polydimethylsiloxane
PE	Polyethylene
PET	Polyethylene Terephthalate
PHES	Pumped Hydroelectric Energy Storage
PI	Polyimide
PMMA	Polymethyl Methacrylate
PP	Polypropylene
PPFPA	Poly (pentaflurophenyl acrylates)
PPy	Polypyrrole
PS	Polystyrene
PSBs	Polysulphide/Bromine Flow Batteries
PSF	Polysulfone
PVA	Polyvinyl Alcohol
PVB	Polyvinyl Butyral

PVDF	Polyvinylidene Fluoride
PVP	Poly (vinyl pyrrolidone)
PZT	Lead Zirconate Titanate
RAFT	Reversible Addition-Fragmentation Chain Transfer
RFBs	Redox Flow Batteries
rGO	Reduced Graphene Oxide
S	Sulfur
SEM	Scanning Electron Microscope
SSA	Specific Surface Area
STAC	Stearyltrimethylammoniumchloride
TEM	Transmission Electron Microscope
TEOS	Tetraethyl Orthosilicate
TES	Thermal Energy Storage
TFP	Trifluorophenyl
TGA	Thermogravimetric Analysis
TPU	Thermoplastic Polyurethane
TrGO	Thermally Reduced Graphene Oxide
VRBS	Vanadium Redox Flow Batteries
WPU	Water-Borne Polyurethane
XRD	X-Ray Diffraction
ZBBS	Zinc/Bromine Flow Batteries

Symbols

A	Surface Area of Parallel Plate
C	Capacitance
d	Distance Between Two Parallel Plates
D	Electrical Displacement
E	Electrical Field
E_b	Electrical Breakdown Strength
f_{BNNSs}	Boron Nitride Nanosheets Concentration
f_c	Percolation Threshold
f_{CNT}	Carbon Nanotubes Concentration
f_{filler}	Experimental Filler Loading

P	Intensity of Electric Polarization
q	Dielectric Critical Exponent
s	Critical Exponent in the Insulating Region
t	Critical Exponent in the Conductive Region
$Tan\ (\delta)$	Dielectric Loss tangent
U_e	Energy Storage Density
vol. %	Volume Fraction
wt. %	Weight Fraction
ε_0	Vacuum Dielectric Constant
ε_r	Relative Dielectric Constant
σ_c	Conductivity
χ_e	Electrical Susceptibility
ω	Angular Frequency

Résumé en français

Les nanocomposites polymères diélectriques ayant une constante diélectrique élevée et une faible perte diélectrique ont reçu un large intérêt pour une large application dans le domaine du condensateur électrostatique, qui peut stocker et délivrer de l'énergie électrique très efficacement. Ces nanocomposites sont généralement composés d'une matrice polymères diélectriques et des nanocharges inorganiques ou organiques comme renforcement, dont les polymères diélectriques contribuent à fournir la bonne flexibilité et la haute résistance à la rupture électrique élevées, et les nanocharges devraient produire une constante diélectrique élevée.

De manière générale, les performances diélectriques des nanocomposites sont déterminées par le type et la nature des polymères et des nanocharges sélectionnées, ainsi que par l'effet de couplage interfacial entre la matrice et les nanocharges. Parmi ces facteurs, les propriétés physiques, les géométries et les structures des composants des nanocharges jouent un rôle.

Selon les conductivités des nanocharges, les nanocomposites polymères diélectriques peuvent être classés en deux catégories: les nanocomposites polymères diélectriques avec des nanocharges conductrices (CDPN) et les nanocomposites polymères diélectriques avec des nanocharges céramiques à constante diélectrique élevée (DDPN). Pour les CDPN, la constante diélectrique élevée est attribuée à l'effet de percolation, ce qui explique l'augmentation brutale de la constante diélectrique au voisinage du seuil de percolation. Pour les DDPN, la constante diélectrique élevée est directement attribuée à celle des nanocharges céramiques sélectionnées. Cependant, la perte diélectrique élevée accompagnée au voisinage du seuil de percolation pour les CDPN et la charge élevée de nanocharges en céramique entravent le développement de nanocomposites polymères diélectriques à haute performance. Cette thèse portera sur l'augmentation de la constante diélectrique et la suppression de la forte perte diélectrique des nanocomposites polymères diélectriques en optimisant rationnellement la structure des nanocharges sélectionnées.

Tout d'abord, les nanocomposites ternaires BNNS/CNTs/PVDF ont été fabriqués. L'incorporation de BNNS dans les nanocomposites binaires CNTs/PVDF a permis d'améliorer la dispersion des CNTs et d'optimiser le réseau conducteur, ce qui a contribué à l'amélioration de la constante diélectrique. La connexion directe entre CNTs pourrait être entravée en augmentant le contenu de BNNS.

Deuxièmement, des hybrides CNT@AC à structure cœur-coquille ont été préparés par la méthode CVD et ont ensuite été utilisés pour préparer des nanocomposites CNT/AC. La couche de carbone amorphe entrave le contact direct des CNTs, mais améliore également la dispersibilité des CNTs dans la matrice de PVDF. Le seuil de percolation augmente avec la prolongation du temps de dépôt du carbone. En plus, la perte diélectrique a subi une forte diminution après le processus de revêtement, ce qui a été attribué à la diminution du courant de fuite. Les résultats suggèrent que l'influence de la couche intermediaire en carbone amorphe sur la performance diélectrique finale après percolation était beaucoup plus évidente que celle avant percolation.

Troisièmement, les hybrides BNNSs@C avec des teneurs en carbone différentes ont été synthétisés par la méthode CVD. La fraction de carbone dans les hybrides BNNSs@C ainsi obtenus a été ajustée avec précision de 2.5 à 22.6 wt. % en faisant varier le temps de dépôt de carbone. Les nanocomposites BNNSs@C/PVDF ont été obtenus en incorporant les hybrides BNNSs@C dans la matrice de PVDF. Les nanocomposites BNNSs@C/PVDF obtenus ont présenté une excellente performance diélectrique qui ont pu être ajustées avec précision en ajustant la teneur en carbone. Les polarisations interfaciales améliorées des interfaces BNNS/C et C/PVDF ont doté les nanocomposites de performances diélectriques améliorées.

Quatrièmement, on a synthétisé des nanofils de TiO_2@C avec une enveloppe de carbone uniforme en combinant une réaction hydrothermale et la méthode CVD. L'épaisseur de la couche de carbone dans les nanofils de TiO_2@C obtenus pourrait être précisément ajustée de 4 nm à 40 nm en contrôlant le temps de dépôt du carbone. Les nanofils de TiO_2@C ont ensuite été introduits dans une matrice de PVDF pour

préparer des nanocomposites avec nanofils de TiO_2@C. De plus, les propriétés diélectriques des nanocomposites avec nanofils de TiO_2@C pourraient être ajustées avec précision en ajustant l'épaisseur de la coque en carbone. Les polarisations interfaciales améliorées des interfaces TiO_2/C et C/PVDF ont doté les nanocomposites d'excellentes performances diélectriques.

Enfin, des nanofils de TiO_2@C@SiO_2 structurés à double coques ont été synthétisés par une combinaison de réactions hydrothermales modifiées, de CVD et de réactions sol-gel. Les nanofils de TiO_2 étaient uniformément revêtus des coques en carbone et SiO_2. L'introduction de carbone comme enveloppe interne entre le noyau de TiO_2 et l'enveloppe externe de SiO_2 a induit deux types supplémentaires de polarisations interfaciales entre la couche intermédiaire de carbone et les couches d'oxyde adjacentes. Les nanocomposites de PVDF obtenus avec les nanofils de TiO_2@C@SiO_2 présentaient simultanément une constante diélectrique améliorée et des caractéristiques de perte diélectrique dimuniée. En outre, le noyau à double coque nanofils de TiO_2@C@SiO_2 structuré avec une coque en carbone et une épaisseur de coque SiO_2 variables a été obtenu en ajustant individuellement le temps CVD et la quantité de tétraéthyle orthosilicate ajoutée dans la synthèse sol-gel. La constante diélectrique des nanocomposites a été augmenté avec l'épaisseur de la couche interne de carbone et la perte diélectrique a été diminuée avec l'épaisseur de la couche externe de SiO_2. La relation entre la perte diélectrique et l'épaisseur de l'enveloppe extérieure en SiO_2 a été démontrée par les résultats de la simulation finie.

Mots clés : Nanocomposites polymères diélectriques; Constante diélectrique; Perte diélectrique; Nanofils; Coeur-coquille

General Introduction

Dielectric polymer nanocomposites with a high dielectric constant and low dielectric loss have received broad interest for use in the field of the electrostatic capacitor, which can uptake and delivery energy in a short period. Dielectric nanocomposites are usually composed of dielectric polymers as matrix and inorganic or organic nanofillers as the reinforcement. Dielectric polymers are supposed to provide the flexibility and high electrical breakdown strength, while the inorganic or organic nanofillers are expected to give a high dielectric constant. Generally, the improved dielectric performance of nanocomposites is decided by the type and nature of selected polymers and nanofillers as well as interfacial coupling effect between matrices and nanofillers. Among these factors, the physical properties, geometries, component structures of nanofillers play a critical role in deciding the dielectric performance of nanocomposites. According to the conductivities of nanofillers, the dielectric polymer nanocomposites can be classified into two types: conductive-dielectric polymer nanocomposites (CDPNs) with conductive nanofillers and dielectric-dielectric polymer nanocomposites (DDPNs) with high dielectric constant ceramic nanofillers. For the CDPNs part, the high dielectric constant is attributed to the percolation effect, which explains the abrupt increase in dielectric constant in the vicinity of the percolation threshold. As for the DDPNs system, the high dielectric constant is directly ascribed to the high dielectric constant of selected ceramic nanofillers. However, the accompanied high dielectric loss in the vicinity of the percolation threshold for CDPNs and high loading of ceramic nanofillers hinders the development of high performance dielectric polymer nanocomposites. This thesis will focus on increasing dielectric constant and suppressing dielectric loss of dielectric polymer nanocomposites by rationally optimizing the structure of selected nanofillers.

Firstly, ternary BNNSs/CNTs/PVDF nanocomposites were fabricated. The incorporation of BNNSs into the binary CNTs/PVDF nanocomposites improved the dispersion of CNTs and optimized the conductive network, which contributed to the enhanced dielectric constant. The direct connection between CNTs could be hindered

by increasing the content of BNNS.

Secondly, core-shell structured CNTs@AC hybrids were prepared by CVD method and they were subsequently used to prepare CNTs@AC/PVDF nanocomposites. The amorphous carbon layer not only hindered the direct contact of CNTs but also improved the dispersibility of CNTs in the PVDF matrix. The percolation threshold increased with the prolongation of carbon deposition time. More importantly, the dielectric loss underwent a sharp decrease after the coating process, which was attributed to the decrease in leakage current. The results suggested that the influence of AC interlayer on the final dielectric performance after percolation was much more obvious than that before percolation.

Thirdly, BNNSs@C hybrids with different carbon contents were synthesized by the CVD method. The carbon fraction in the as-obtained BNNSs@C hybrids could be accurately adjusted from 2.50 to 22.62 wt. % through controlling the carbon deposition time. The BNNSs@C/PVDF nanocomposites were obtained by incorporating the BNNSs@C hybrids into PVDF matrix. The as-obtained BNNSs@C/PVDF nanocomposites exhibited an excellent dielectric performance and the dielectric properties could be accurately tuned by adjusting the carbon content. The improved interfacial polarizations of BNNSs/C and C/PVDF interfaces endowed the nanocomposites with enhanced dielectric performance.

Fourthly, core-shell structured TiO_2@C NW hybrids with a uniform carbon shell were synthesized by a combination of a hydrothermal reaction and the CVD method. The carbon shell thickness in the obtained TiO_2@C NW hybrids could be precisely tuned from 4 nm to 40 nm by controlling the carbon deposition time. The TiO_2@C NW hybrids were subsequently filled into a PVDF matrix to prepare TiO_2@C NWs/PVDF nanocomposites and the resultant nanocomposites exhibited a percolative dielectric behavior. Moreover, the dielectric properties of the TiO_2@C NWs/PVDF nanocomposites could be accurately adjusted by tuning the carbon shell thickness. The enhanced interfacial polarizations of the TiO_2/C and C/PVDF interfaces endowed the nanocomposites with excellent dielectric performance.

Lastly, core@double-shells structured TiO_2@C@SiO_2 nanowires were synthesized by a combination of modified hydrothermal reaction, CVD, and sol-gel reaction. The TiO_2 NWs was uniformly coated with the carbon and SiO_2 shells. The introducing of carbon as an inner shell between the TiO_2 core and SiO_2 outer shell induced two additional types of interfacial polarizations between the carbon interlayer and adjacent oxide layers. The obtained PVDF nanocomposites with TiO_2@C@SiO_2 NWs exhibited simultaneously enhanced dielectric constant and suppressed dielectric loss characteristics. Besides, the core@double-shells structured TiO_2@C@SiO_2 NWs with variable carbon shell and SiO_2 shell thickness was achieved by individually adjusting the CVD time and the amount of tetraethyl orthosilicate added in the sol-gel synthesis. The dielectric constant and loss of nanocomposites increased with the increase of carbon inner shell thickness and decreased with the increasing of SiO_2 outer shell thickness. The relationship between the dielectric loss and SiO_2 outer shell thickness was further demonstrated by the finite simulation results.

Key Words: Dielectric Polymer Nanocomposites; Nanofillers; Dielectric Constant; Dielectric Loss; Nanowires; Core@Shell

Chapter I

Electrical Energy Storage Technologies

The current worldwide electricity generation capacity has grown significantly over the last decade. The gross production of electricity in 2016 is estimated to be about 25000 terawatt hours, of which fossil fuels (including coal, natural gas, and oil) contribute around 60 % of global electricity energy generation [1]. Although the percentage of fossil fuels has been decreasing gradually from 87 % in 1973 to 60 % in 2016, the reduction in fossil fuels share does not portray in actual terms a reduction in CO_2 emission [2]. On the contrary, the total amount of CO_2 emission from the fossil fuels increases from 16633 Mt in 1973 to 33432 Mt in 2016 [1, 2].

The CO_2 emission from fossil fuels has been widely considered as the main factor for threatening global environment due to its contribution to the global warming. Therefore, great efforts have been devoted to reducing the CO_2 emission. One of the most promising strategies is diminishing reliance on fossil fuels and the growing use of renewable energy sources [3]. However, most parts of renewable energy sources (including solar, wind, and wave energy) are inherently intermittent and non-controllable, which hinders the extensive utility of these renewable energy sources [1, 3]. To smooth out the intermittency of renewable energy production, electrical energy storage (EES) has been recognized as one of the most promising candidates to solve the critical issues of their applications in automobiles (transportation) and electrical grid (stationary) fields [4].

The EES technology refers to the process of converting electrical energy into a storable form that could be converted back to electrical energy when needed [3]. The EES technology owns multiple valuable functions to power network operation and load balancing, such as :(1) alleviating the inherent intermittent characteristic of renewable energy sources power generation; (2) contributing to meeting the peak electrical load demands; (3) improving the power quality and reliability; (4) reducing the electrical energy import during peak demand periods;energy import during peak

demand periods; (5) enabling the realization of a smart grid; (6) meeting the remote and vehicle load needs [3-5]. According to the storage form of EES, the EES could be easily categorized into the following forms.

1.1 Mechanical Energy Storage (MES)

1.1.1 Pumped Hydroelectric Energy Storage (PHES)

PHES is one of the most mature and widely implemented large-scale EES technologies. As shown schematically in Fig. 1-1, the PHES system is mainly composed of two water reservoirs located at different positions [2]. During the off-peak electricity demands, the water is pumped into the upper reservoir and the energy is stored in the form of hydraulic potential energy. During peak electricity demand hours, the water is released back into the lower reservoir to drive the operation of turbine units, which converts the potential energy to electricity. The amount of energy stored is proportional to the height difference between the two reservoirs and the volume of water stored. The rated power of PHES plants is determined by the water pressure and flow rate through the turbines.

PHES technology has been widely recognized as a mature technology with the characteristics of large volume, long storage period, and high efficiency. However, several disadvantages of PHES technology could not be neglected. The main drawback is that specific natural geological features are required for constructing the reservoirs and dams. Besides, the long time and high cost during the construction process and the corresponding environmental issues are the other three major constraints for implementing the PHES technology.

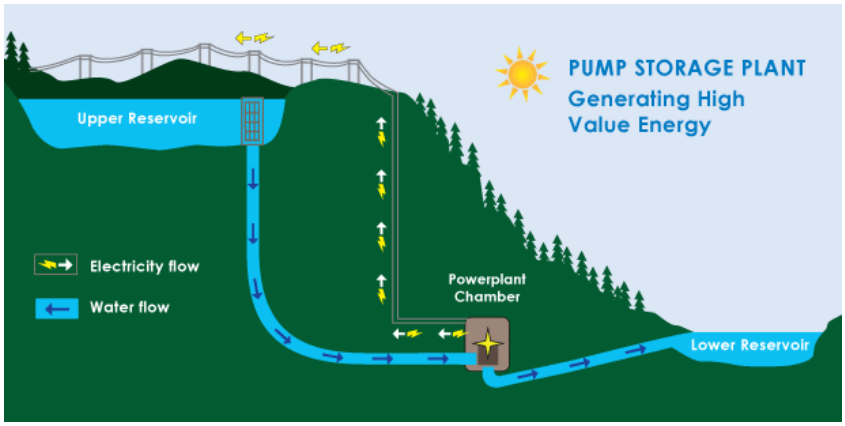

Fig. 1-1 *Schematic diagram of a PHES system [2].*

1.1.2 Compressed Air Energy Storage (CAES)

In addition to PHS, CAES is another type of commercially available EES technology capable of providing very large energy storage deliverability. The technology was first introduced in the 1970s as a load following and peaking power system. The process diagram of a CAES is shown in Fig. 1-2 [6]. During the periods of low power demand, the energy is stored by compressing the air into the storage container, which is either an underground cavern or over ground tanks. During the peak demand periods, the energy is released from the storage container and subsequently heated by a heating source. The expanded air drives the operation of the high-pressure turbine, which captures some energy from the compressed air. After that, the air is blended with fossil fuel and combusted with the exhaust expanded through a low-pressure turbine. The high-pressure turbine and low-pressure turbine are connected to a generator to output electricity.

The working principle of a CAES system allows the CAES unit switching quickly from the generation model to the compression one. Moreover, the CAES system can be easily designed from a small capacity to a large one. Compared with PHES system, the CAES system has less environmental effects. In addition, CAES system also owns the characteristics of the long storage period, low costs, and high efficiency. Similar to the PHES system, the main barrier to implement the CAES is seeking an appropriate geographical location. More importantly, the involved

combusting process of fossil fuels and the corresponding contaminating emission render the CAES less attractive [2, 3, 5].

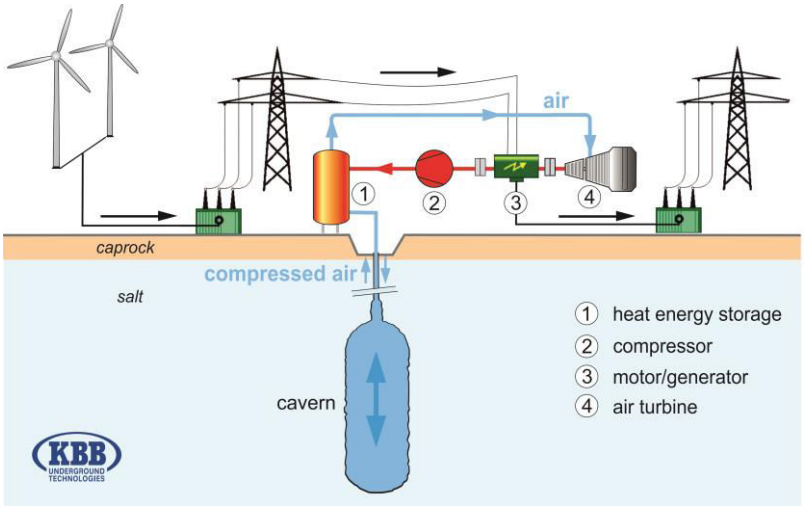

Fig. 1-2 *Schematic diagram of a CAES system [6].*

1.1.3 Flywheel Energy Storage (FES)

The FES system consists of a flywheel, a group of bearings, a reversible electrical motor/generator, a power electronic unit, and a vacuum chamber. A simplified structure of an FES facility is displayed in Fig. 1-3 [7]. As an energy storage device, FES was initially designed to deal with the short voltage disturbance problem, which is detrimental to the power quality. During the energy storage mode (charging process), the excessive electrical energy is used to accelerate the motor, which drives the rotor to rotate with the aid of a shaft. The rotation of the rotor produces an angular momentum and the electrical energy is stored in the form of kinetic energy. Therefore， the amount of stored energy is dependent on the rotating speed of flywheel and its inertia. During the discharging phase, the rotor decelerates and subsequently converts the kinetic energy into the electrical energy. In order to reduce the air resistance and corresponding energy loss, the FES system is normally installed in a high vacuum environment. The flywheels could be generally divided into two groups according to their rotational speed.

FES system has many favorable characteristics including high cycle efficiency, eco-friendly, wide operating temperature range, the ability to be operated in harsh

conditions and low costs for the maintenance. Therefore, flywheels are regarded as a perfect energy storage device. The main weakness of the FES system is that flywheels suffer from the idling losses when they are on standby, which leads to a high self-discharge.

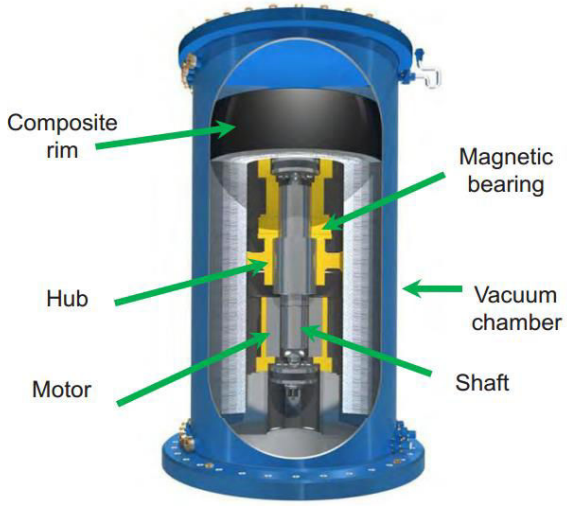

Fig. 1-3 *System description of a FES system [7].*

1.2 Thermal Energy Storage (TES)

TES includes a variety of technologies that store available heat energy using different approaches in insulated repositories The main working principle of TES system is converting the surplus electricity or other waste heat resources into the thermal energy and the stored thermal energy is transformed back into electricity during the peak demand periods. The choice of TES method depends on a variety of factors such as the storage temperature range, the specific application, and the storage media. According to the operating temperature, TES can be categorized into two groups: low-temperature TES and high-temperature TES.

1.2.1 Low Temperature TES

Low-temperature TES is generally considered as the TES system with the operating temperature below 200 °C and it is mainly composed of two types of technologies: aquiferous low-temperature TES and cryogenic energy storage. Water is

cooled or iced by a refrigerator during the off-peak period and stored for later use to meet the peak needs, which is more suitable for the peak shaving and industrial cooling loads. Cryogenic energy storage employs a cryogen (liquid nitrogen or liquid air) to achieve the electrical and thermal energy conversion. Cryogenic energy storage owns the advantages of high energy density, low capital cost, and long storage period. However, the low efficiency (40-50 %) restricts its further development.

1.2.2 High Temperature TES

The high-temperature TES consists of sensible heat storage, latent heat storage, and thermochemical heat storage systems. For the sensible heat storage system, the storage material does not undergo any form of phase change within the required temperature range. The concrete, cast ceramics, and molten salts are the representative storage materials. Their main drawback is the high freezing point, which could lead to the energy losses. The latent heat storage process is realized by the phase change materials, which stores or releases the energy by the phase changing. These materials exhibit a more excellent thermal energy storage performance than that of the non-phase changing counterpart due to their high latent heat during the phase change process. As shown in Fig. 1-4, the energy is stored by dissociating a chemical reactant into corresponding products, followed by separating the obtained products. During the discharging process, the stored products are mixed together and react to produce the initial reactant.

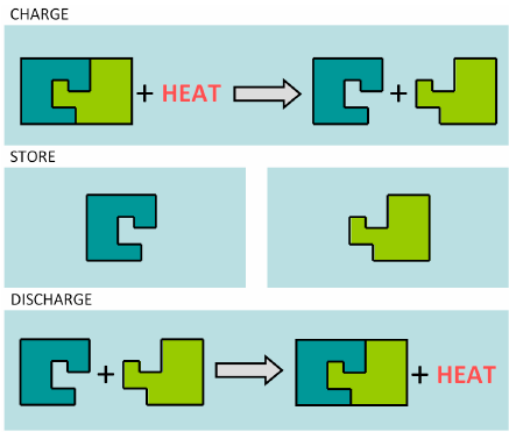

Fig. 1-4 *Schematic diagram of a thermochemical heat storage system [8].*

1.3 Chemical Energy Storage (CES)

Chemical energy storage concept involves all the technologies where electrical energy is used to produce chemical compounds and the obtained chemical products could be stored and used when needed for energy generation. Most of the chemical compounds have a higher energy density and this characteristic makes them an ideal energy storage medium. Several chemical compounds (including hydrogen, methanol, and hydrocarbons) have been widely used for the application of energy storage. Among them, synthesis of hydrogen is regarded as the shortest route to transfer the electricity into chemical compounds. Hydrogen is a storable, transportable, highly versatile, and clean energy carrier. The hydrogen can be stored either as compressed gas, liquefied gas, or metal hydrides. As presented in Fig. 1-5, the off-peak electricity is used to electrolyze water to produce hydrogen. During the discharging phase, the stored hydrogen is input into a fuel cell system to produce electricity and thermal energy. The process of electricity generation using the fuel cell produces less pollution and is more efficient than the fossil fuel combustion approach. The major drawback of using hydrogen for electricity storage is that disposal of exhaust fuel cells is relatively complicated due to the toxic metals component in the electrodes or catalysts.

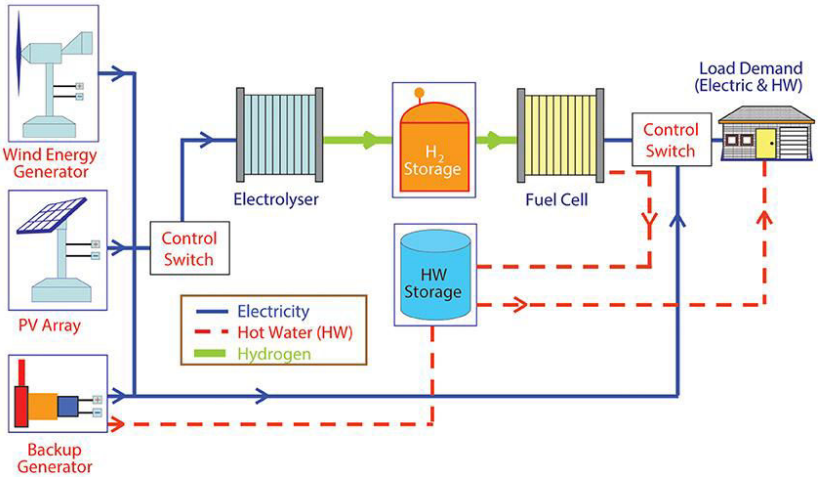

Fig. 1-5 *Schematic diagram of a hydrogen energy storage system [9].*

1.4 Electrochemical Energy Storage (ECES)

1.4.1 Redox Flow Batteries (RFBs)

An RFB energy storage system, as schematically shown in Fig. 1-6 is a type of rechargeable battery that stores the electricity in two soluble redox couples contained in external liquid electrolyte tanks. These electrolytes are pumped from the tanks to the cell stack which is composed of two compartments separated by an ion selective membrane. The membrane selectively allows the transport of non-reaction ions (e.g. H^+ and Na^+) to maintain neutrality and electrolyte balance. During the charging process, one type of pumped electrolyte is oxidized at the anode and another type of electrolyte is reduced at the cathode, thus the electrical energy is converted into the electrochemical energy. The above process is reversed during the discharging phase.

Unlike traditional batteries that store energy in electrode materials, the power and energy capacity of an RFB system can be designed separately. The power of the RFBs system is determined by the size of the electrodes and the number of stacked cells; whereas the storage capacity is determined by the concentration and volume of the electrolyte. More importantly, the stable and durable performance could be achieved by employing the RFBs system since it does not undergo the physical and chemical changes of the electrodes and the degradation of electrolytes during operation. Also, the suppressed self-discharge property is an inherent advantage of the RFBs system due to the electrolytes being stored in the separate sealed tanks In addition, the simplicity of the cell stacking structure allows for building large systems depending on the application. However, the need for pumps, sensors, reservoirs, power management and secondary containment makes them unsuitable for small-scale energy storage application. Flow batteries can be classified into the categories of redox flow batteries and hybrid flow batteries, depending on whether all electro-active components could be dissolved in the electrolyte. There are different types of RFBs systems as follows according to the anolyte and catholyte chemistries: all-vanadium redox flow batteries (VRBs), polysulphide/bromine flow batteries (PSBs),

zinc/bromine flow batteries (ZBBs), etc.

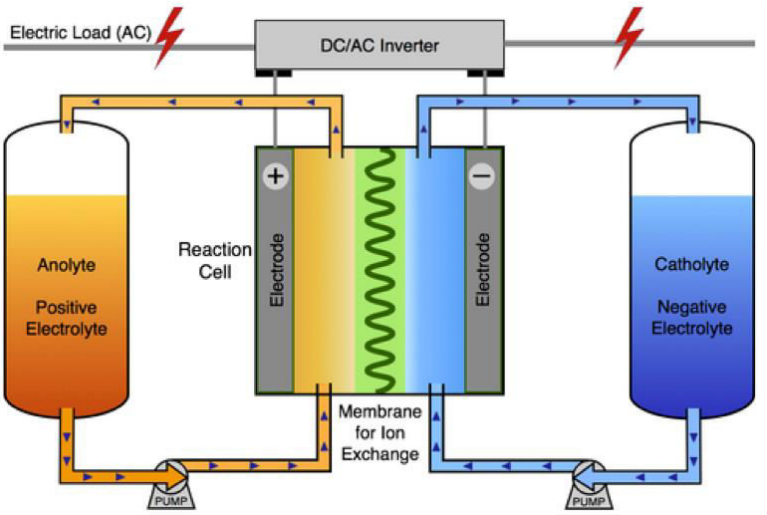

Fig. 1-6 *Schematic diagram of a redox flow battery system [10].*

1.4.2 Lead-acid Batteries

The lead-acid battery is the oldest and most widely used rechargeable battery for both household and commercial application. It is composed of a cathode electrode made of the lead oxide (PbO_2) and an anode electrode composed of metallic lead (Pb) with an electrolyte made of sulfuric acid (H_2SO_4). Lead-acid batteries have a low investment and maintenance cost, a high reliability, and a high efficiency. However, its application for energy management has been impeded by the short cycle life and low energy density due to the inherent high density of lead. Moreover, they perform poorly at low temperatures so a thermal management system is normally required, which increases the cost. Recently, traditional lead-acid batteries have evolved into versions where the lead-anode is partially or fully replaced by carbon. The carbon addition or replacement in the negative electrodes leads to improve performance and potentially reduced life-cycle cost over the traditional lead-acid batteries for stationary storage.

1.4.3 Li-ion Batteries

Li-ion batteries store electrical energy in electrodes made of Li-intercalation compounds. During the charging and discharging processes, Li-ions transfer across

the electrolyte between one host structure and the other, with concomitant oxidation and reduction processes occurring at the two electrodes. On the anode side, graphite is the material of choice for most lithium-ion candidate chemistries. While the electrolyte can be a liquid, a gel, or a solid polymer, the majority of electrolytes is normally composed of a non-aqueous organic liquid containing dissolved lithium salts. The representative operation process of the Li-ion battery is displayed in Fig. 1-7. Its favorable electrochemical performance in energy and power densities has made the Li-ion batteries a great success for mobile electronics. However, the lithiated-graphite anodic electrode normally operates at a potential close to that of metallic lithium, which is in favor of Li-dendrite growth and potential electrical shorting. The additional challenge is the high cost for the scaled-up applications.

Although the Li-ion batteries have demonstrated a high capacity and power behavior, the seeking for a higher energy density than what Li-ion batteries can achieve theoretically promotes the rapid development of two kinds of “beyond Li-ion batteries”. The Li-S and Li-air batteries have received widely attentions due to their high theoretical specific energies of 2600 Wh/kg and up to 12000 Wh/kg (based on the Li anode), respectively. However, the poor reversibility and slow reaction kinetics hinder the development of these technologies due to the poor stability of the electrode materials, irreversibility of the interfacial reactions, and unavoidable interactions with the electrolytes. Besides, the use of porous carbon to confine the sulfur in the cathode for Li-S battery and the use of porous carbon cathodes, special membranes, and packaging materials to make the Li-air battery work will significantly weaken the practical energy density that can be theoretically achieved.

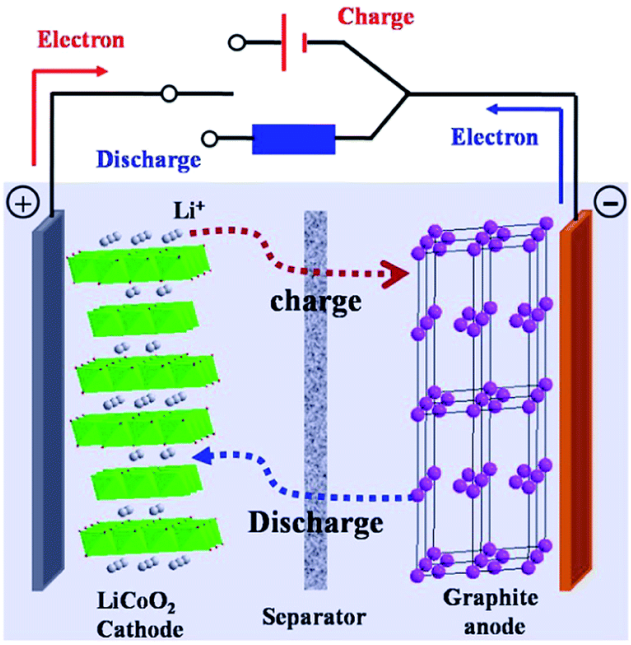

Fig. 1-7 *Schematic diagram of a representative Li-ion battery system [11].*

1.4.4 Sodium Sulfur (Na-S) and Sodium-Metal Halide Batteries

As shown in Fig. 1-8, Na-S battery is composed of the liquid (molten) sulfur at the positive electrode and liquid (molten) sodium at the negative electrode and these two electrodes are separated by a solid beta alumina ceramic electrolyte. The Na-S battery operates at temperatures of 270 °C to 350 °C so as to increase the ionic conductivity of beta alumina electrolyte and ensure that those two electrodes are molten. During the discharging process, sodium is oxidized at the interface of molten sodium negative electrode and alumina electrolyte. The resultant Na^+ migrates through the electrolyte to the molten sulfur positive electrode and reacts with the sulfur, forming Na_2S_5. During the charging process, the Na_2S_5 is oxidized and the released Na^+ moves from the sulfur electrode to a sodium electrode, which is followed by being reduced to form sodium. Na-S battery technology has been commercialized in electric utility distribution grid support, winder power integration and high-value grid services. The desirable features of the Na-S battery include high energy density, coulombic efficiency, cycling flexibility, and low maintenance requirements. The disadvantages of the Na-S battery are high operational temperature requirement, high capital cost, and harsh operating requirement due to the use of metallic sodium.

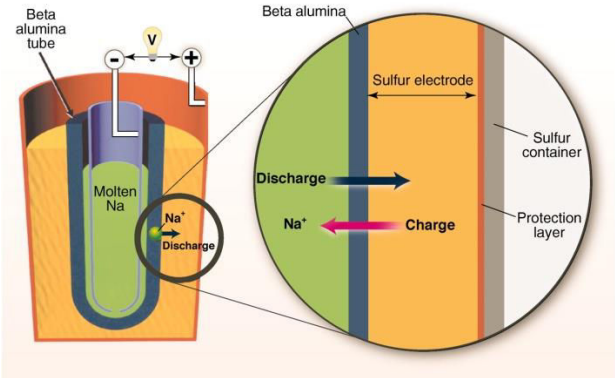

Fig. 1-8 *Schematic diagram of Na-S battey [4].*

The operational mechanism of Na-metal halide battery is similar to that of Na-S battery. Both of them are operated by the migration of Na^+ between the positive and negative (molten sodium electrode) electrodes and they employ the same beta alumina ceramic electrolyte with high ionic conductivity at high temperature. The positive electrode of Na-metal halide battery consists of the active metal chloride such as $NiCl_2$. During the discharging phase, metallic Na is oxidized and the resultant Na^+ ions migrate to the positive electrode to react with metal chloride, which leads to the formation of NaCl and the metal phase. Compared with Na-S battery, the Na-metal halide battery owns the characteristics of high cell voltage, tolerance to overcharge and discharge, and excellent anti-corrosion property.

1.4.5 Zinc Air (ZnAir) Battery

The zinc-air battery is one kind of metal-air batteries, which uses the metal as fuel and air as the oxidant. The anode in metal-air batteries is commonly available metals such as aluminum, magnesium, and lithium, which release electrons when they are oxidized. The cathode (air electrode) is often made of a porous carbon support or a metal mesh covered with proper catalysts. The electrolyte should own a high hydroxyl ion conductivity such as KOH. The electricity is produced when the air electrode is reduced with the aid of the catalyst, which leads to the formation of hydroxyl ions in the electrolyte. The major challenging of developing such technology is how to effectively avoid the influence of carbon dioxide from the air on the electrolyte and cathode as well as how to avoid the formation of the metal dendrite.

1.5 Electrical Energy Storage

1.5.1 Supercapacitor (Electrical Double-Layer Capacitor)

Supercapacitors, also known as electrochemical capacitors, store energy by utilizing either reversible ions absorption at the electrode-electrolyte interface (electrical double-layer capacitors (EDLC)) or redox reaction at the vicinity of the electrode surface (pseudo-capacitors), depending on the electrode materials employed [12]. The electrodes of the former capacitor are normally made of porous carbon or other porous materials with a high specific surface area (SSA) as the conductor with aqueous or non-aqueous electrolyte [13, 14]. The electrodes of the latter one are often composed of transition metal oxides/hydroxides or conductive polymers, where undergoes the faradaic charge transfer reactions or reversible oxide/reduce reactions [15]. Although the pseudo-capacitive electrode materials own a high theoretical specific capacitance and reversible and fast redox reaction, the application of their single component is limited due to their poor conductivity and framework swelling during charging and discharging process [16]. These inherent physical shortcomings will lead to a low power density and inferior cycling performance. Intrinsically, the pseudo-capacitors store the energy by converting the electricity into electrochemical energy, which is similar to those aforementioned batteries.

As shown in Figure 1-9, during the charging process, the positive electrode attracts the anions of electrolytes, whereas cations are accumulated in the vicinity of the negative electrode. Charges separation occurs at the electrode-electrolyte interface, resulting in a double layer capacitance. The obtained capacitance is usually proportional to the effective SSA of electrode materials. Therefore, in order to obtain a high capacitance, the electrode materials should have a high SSA value. Furthermore, the pores distributions should also be optimized to ensure the availability of electrolyte ions. Besides, the electrode materials with a high conductivity are in favor of high power performance and a high mechanical and thermal stability is beneficial to a long cycling life. Although compared with the

batteries, the EDLC owns a high charging and discharging rate, long cycling life, and high cycle efficiency, the self-discharge rate is high. Thus EDLC is suitable for short-term storage application but not for the large-scale and long-term requirements.

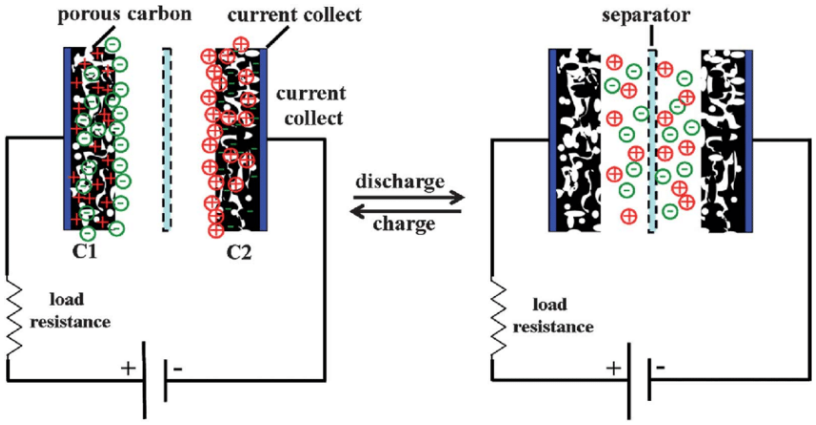

Fig. 1-9 *Schematic diagram of the charging and discharging process for an electrical double layer capacitor [17].*

1.5.2 Conventional Capacitor

A conventional capacitor is normally composed of two conductive electrodes separated by a dielectric layer [18-22]. When an external voltage is applied to the dielectric layer, the accumulated charges on the surfaces of the electrodes will induce the formation of electrical polarization inside of the dielectric layer (Fig. 1-10). Compared with the batteries and other electrochemical EES devices, the most distinguished feature of the conventional capacitor is that the energy uptake and delivery processes can be achieved in a very short period (nanoseconds to milliseconds), which endows it with a high power characteristic. Besides, the excellent cycling life and high uptake and delivery efficiency make it as a prominent candidate for the EES device with high power quality requirements, such as high voltage power correction, kinetic energy weapons launching, high power microwave transmitter, and electromagnetic armors. However, these potential applications are severely hindered by the low energy density of capacitors with currently commercialized dielectrics.

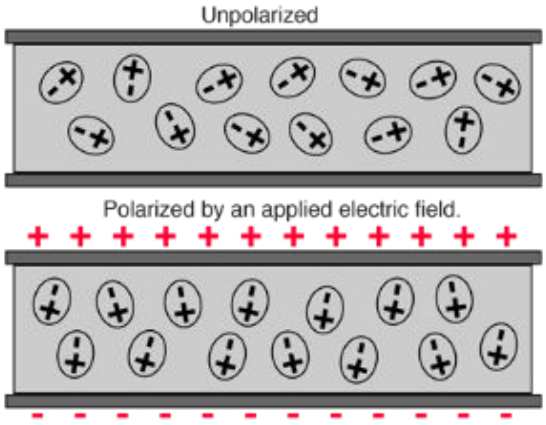

Fig. 1-10 *Graphical representation of a standard capacitor with a dielectric layer.*

Generally, the energy storage density (U_e) is described as,

$$U_e = \int EdD \tag{1-1}$$

where E is the electrical field and D is the electrical displacement. The D is defined as,

$$\mathrm{D} = \varepsilon_0 E + P \tag{1-2}$$

where ε_0 is the vacuum dielectric constant (8.85×10^{-12} F/m) and P is the intensity of electric polarization. For a linear dielectric, the P is denoted as,

$$\mathrm{P} = \varepsilon_0 \chi_e E \tag{1-3}$$

where χ_e is the electrical susceptibility. Therefore, for a linear dielectric, the equation 1-2 can be expressed as,

$$\mathrm{D} = \varepsilon_0 E + \varepsilon_0 \chi_e E = \varepsilon_0 (1 + \chi_e) E = \varepsilon_0 \varepsilon_r E \tag{1-4}$$

where $\varepsilon_r = 1 + \chi_e$ and ε_r is the relative dielectric constant of the dielectric. Thus the equation 1-1 can be illustrated as,

$$U_e = \frac{1}{2} \varepsilon_0 \varepsilon_r E^2 \tag{1-5}$$

However, for the non-linear dielectric, the U_e can be obtained merely by integrating the shaded area from the D-E loops (Fig. 1-11b and c).

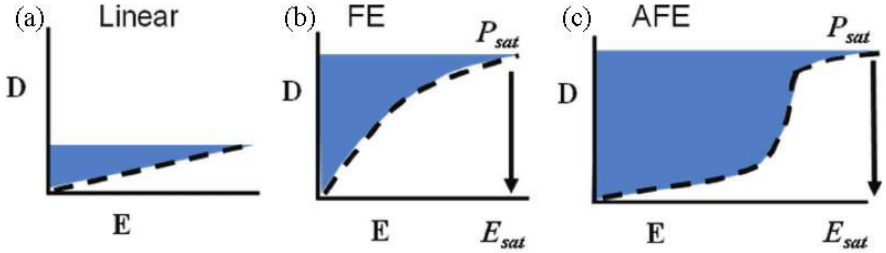

Fig. 1-11 *Schematic showing the D-E loops of linear, ferroelectric (FE), anti-*

ferroelectric (AFE) dielectrics [23].

For a linear dielectric, the ε_r does not change with the applied E. Therefore, as illustrated in equation 1-5, the U_e is mainly dominated by the applied E. Thus choosing an appropriated dielectric with a high εr and electrical breakdown strength (E_b) is critical for reaching a high U_e.

The traditional inorganic ceramic dielectrics possess a large ε_r, high stiffness, and excellent thermal stability. However, their inferior E_b, high density, and brittleness impede the application of these high-ε_r ceramics in portable and flexible electrostatic capacitors with a higher U_e. Compared with the conventional inorganic ceramics, organic polymer dielectric materials own the advantages of high electrical breakdown strength, easy processing, and mechanical flexibility. Nevertheless, the practical applications of the high-performance electrostatic capacitor are hindered by their intrinsic low dielectric constant values (ca. ε_r<10). For example, the biaxially oriented polypropylene (BOPP) owns a high E_b (ca. 640 KV/mm), but the maximized U_e is only 1.2 J/cm^3, which is attributed to the low ε_r of the BOPP films (ca. 2.2).

The composite approach offers a promising strategy to combine the merits of these two components by incorporating fillers into the polymer matrix. Previous studies about dielectric composites concentrated mainly on the microsized fillers incorporated systems, yet subsequent investigations show that the microsized filled ones have impairment in the dielectric properties from a long-serving time view due to the surface defects and stress cracking. Besides, the thickness of composite films is also often limited by the size of the microfillers. Thus replacing the microfillers with the nanofillers is the only method to overcome the aforementioned issues. The fillers with a nanoscale dimension can decrease the fillers loading and introduce a large number of interfaces between matrices and fillers, which would promote the exchange coupling effect through a dipolar interface layer, affording higher polarization levels, dielectric response, and breakdown strength. All these features offer a new opportunity for the design of advanced dielectric polymer nanocomposites with a high dielectric constant, low loss, and high energy storage density. The improved dielectric

and energy storage properties of nanocomposites normally depend on the type and nature of selected polymers and fillers as well as interfacial coupling effect between matrices and nanofillers, which would be briefly discussed as follows.

1) Effect of Polymer Matrix

A large amount of polymers have been employed according to their different properties, including fluorinated polymers, polyethylene (PE), polypropylene (PP), polystyrene (PS), epoxy, polyimides (PI), poly(methyl methacrylate) (PMMA), polyethylene terephthalate (PET), polycarbonate (PC), polydimethylsiloxane (PDMS), etc., to prepare dielectric polymer nanocomposites. Polymers can be divided into polar and nonpolar polymers based on their mean dipole moments. The polar polymers exhibit a higher dielectric constant when compared with that of non-polymers. The main obstacle to commercialize nonpolar polymers, such as PE, PP, and PS, in film capacitor field is their inherent low dielectric constant. For the polar polymers, poly(vinylidene fluoride) (PVDF) and its polymers are one type of the most frequently used polar polymer matrices for high-energy capacitors due to their high dielectric constant (ca. >10) and easy of modifying polymer molecular segments. Certain copolymers of PVDF, including poly(vinylidene fluoride-trifluoroethylene) (P(VDF-TrFE)), poly(vinylidene fluoride-hexafluoropropylene) (P(VDF-HFP)), poly(vinylidene fluoride-chloride trifluoride ethylene) (P(VDF-CTFE)), and poly(vinylidene fluoride-trifluoroethylene-chlorofluoroethylene) (P(VDF-TrFE-CFE)), have been widely used to optimize the dielectric properties of nanocomposites. Furthermore, the crystalline structure of the selected polymers also plays an important role in determining the dielectric performance of nanocomposites. For example, PVDF polymer owns five different types of crystalline structure, namely, α, β, γ, δ, and ε phases, according to different chain confirmations. Among these five types of crystalline structure, α phase is a nonpolar phase where the dipole moments cancel out each other due to a symmetrical structure. While others phases, especially β phase, exhibit a high polarizability due to the presence of net dipole moments. Thus their

corresponding PVDF polymers have a high dielectric constant as compared to the one with the α phase. Out of various types of PVDF mentioned above, only those PVDF polymers with a β phase have ferroelectric property in nature with thermodynamically stable spontaneous polarization. The PVDF polymer with an α phase can be obtained by cooling the melt at a normal rate and the one with a β phase can be produced from stretching the α one to induce the alignment of polymer chains to all-trans confirmation, melt crystallization under a high cooling rate, and adding the nucleating agents. Thus different polymers exhibit different properties; thereby, selection of a suitable polymer and an appropriate processing technology play a critical role in deciding the final energy storage property of the resultant dielectric polymer nanocomposites.

2) Effect of Nanofillers

Apart from polymers, the appropriate selection of nanofillers with a different physical property, geometries, and component structure also helps to improve the dielectric and energy storage properties of the polymer nanocomposites. According to the electrical conductivity of the incorporated nanofillers, the employed nanofillers in the dielectric nanocomposites could be divided into two categories: nonconductive and conductive nanofillers. Nonconductive fillers include the ceramic nanofillers with a high dielectric constant like barium titanate ($BaTiO_3$, BT), titanium dioxide (TiO_2), calcium copper titanate ($CaCu_3Ti_4O_{12}$, CCTO), lead zirconate titanate ($Pb(Zr, Ti)O_3$, PZT), etc. The other type of nanofillers with a conductive feature includes metallic nanofillers (Ag, Cu, etc), carbon family nanofillers (carbon black (CB), carbon nanotubes (CNTs), graphene, etc), and conductive polymers (polyaniline (PANI), polypyrrole (PPy), etc). The high dielectric constant achieved by using the conductive nanofillers could be explained by the percolation effect that the dielectric constant increases abruptly as the concentration of nanofillers approaches the percolation threshold. Besides, the shapes and sizes of the nanofillers also play an important role in determining the dielectric and energy storage properties. Different shapes of

nanofillers including spheres, tubes, wires, fibers, flowers, and sheets have been used in dielectric polymer nanocomposites. Nanofillers with different shapes could provide different interfacial polarizations and hence different dielectric and energy storage properties. Furthermore, for a specified shape, the size and size distribution of nanofillers is decisive in deciding the dielectric properties. In addition, different components could be constructed together to produce a novel hybrid with a unique heterostructure. Therefore, different heterostructure would also produce the different influence on the dielectric and energy storage properties. The physical properties and chemical composition of nanofillers are very important to affect the dielectric and energy storage properties of nanocomposites and also how to rational design the nanofillers is the main work of this PhD thesis. Therefore, in order to clarify the emerging issues and provide a comprehensive understanding view of this topic, we will review the recent progress in designing the nanofillers for the application of dielectric nanocomposites in chapter II.

3) Interfacial Coupling Effect

When nanofillers are incorporated into polymer matrices, a large number of interfacial areas would be introduced between the fillers and matrices, thus offering more active sites to intensity their interactions. Although these reinforced interactions may provide additional local polarization and charge separation at the interfacial areas, the intensive coalescence at the filler-matrices interface may generate the nonhomogeneous distribution of nanofillers due to their high surface energy, thus weakening the dielectric breakdown strength property of nanocomposites. Besides, the giant contract of electrical properties between nanofillers and polymer matrices makes it difficult for the charge carrier to freely cross the interfacial areas, thus leading to the accumulation of interfacial charges. Subsequently, these accumulated charges will intensify the conductivity of the interfacial region and a high-speed pathway will be formed. As a result, the leakage current is easy to be formed, thus decreasing the breakdown strength of nanocomposites. Besides, the local electric field

surrounding the nanofillers is several times larger than the applied electrical field, which would lead to the electrical failure of nanocomposites. Therefore, appropriate surface modification of the nanofillers is useful to improve the dielectric and energy storage properties of dielectric nanocomposites. The reported modification method could be classified into two types: organic modification and inorganic modification. For the organic modification part, it provides some chemical or physical interactions between the nanofillers and polymer matrices by grafting or adsorbing some small-molecule ligands or polymer chains into the surface of nanofillers. Thereby, the compatibility between the nanofillers and host polymer matrices would be consequently improved, thus ameliorating the dispersion of nanofillers in the matrices and eliminating the aggregations of nanofillers. As a result, the local electrical distortion would be weakened and the number of microstructural defects at the interface would be decreased. The other kind of method is employed by constructing an inorganic interfacial buffer layer with a medium dielectric constant between the filler and matrix into the surface of selected nanofillers. The obtained core@shell structure favors the alleviation of giant dielectric constant contracts between nanofillers and matrices, thus mitigating the local electrical field distortion. Therefore, the suitable selection of a modification method to improve the interfacial coupling interactions is a key factor in determining the dielectric and energy storage properties of dielectric nanocomposites.

1.6 Concluding Remarks

The growing demands for renewable and sustainable energy resources have sparked enormous research interests in the field of EES for their applications in portable electronic devices and hybrid electric vehicles. This chapter provides an overview of the operation principles, technical and economical features, and current and research and development of the important EES technologies. Among these EES technologies, the dielectric capacitor possesses an intrinsic high power density because of their fast energy uptake and delivery ability (Fig. 1-12) and thus is

considered as a prominent candidate for the generation of high-performance power electronics used in hybrid electric vehicles, portable electronic devices, and electrical weapon systems. The nanocomposites approach provides a promising avenue to overcome those aforementioned issues of the conventional ceramic or all-organic based dielectric by incorporating the nanofillers into the polymer matrices. More importantly, the physical property, geometries, component structure of the nanofillers plays and critical role in deciding the dielectric and energy storage properties of nanocomposites. Therefore, in order to clarify the principle for selecting an appropriate nanofillers and give a comprehensive understanding view to the design of nanofillers, we will review the recent progress in how to rationally design the nanofillers for the application of dielectric nanocomposites in chapter II.

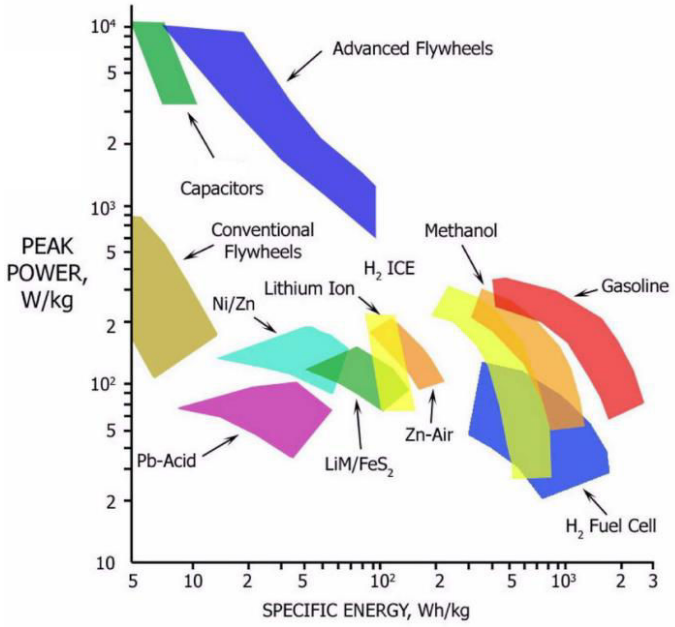

Fig. 1-12 *Ragone plot for comparing the EES technologies and their power density versus energy density characteristics [24].*

Chapter II

Nanofillers for Dielectric Polymer Nanocomposites

2.1 Mechanism of Polarizations

In order to clearly explain the influence of nanofillers on the dielectric properties of dielectric polymer nanocomposites, a detailed discussion about different types of polarizations will be first introduced. Generally, the dielectric property of a dielectric material is defined as the polarization behavior in response to an applied electrical field. The polarization of a dielectric material depends on the frequency of the applied electrical field. Therefore, the complex relative dielectric constant (ε_r) is a frequency dependent complex quantity and is described as follows.

$$\varepsilon_r(\omega) = \varepsilon_r'(\omega) + i\varepsilon_r''(\omega) \tag{2-1}$$

where ω is angular frequency, ε_r' represents the real part of dielectric constant, and ε_r'' denotes the imaginary part. The real part represents the contribution of polarization to the energy storage in the dielectrics and is often referred to as the relative dielectric constant of dielectrics. The imaginary part is usually regarded as the energy dissipative effect in the dielectrics. Generally, the energy dissipative effect is denoted as follows.

$$\tan\delta(\omega) = \frac{\varepsilon_r''(\omega)}{\varepsilon_r'(\omega)} \tag{2-2}$$

where *tan δ(ω)* is defined as the loss factor and is usually called as the dielectric loss.

Generally, the electrical polarizations could be divided into four types: electronic, ionic, dipolar (orientational), and interfacial (space charge) polarizations as displayed in Fig. 2-1, where the upper curve represents the frequency dependent behavior of dielectric constant and the lower one is the dielectric loss part.

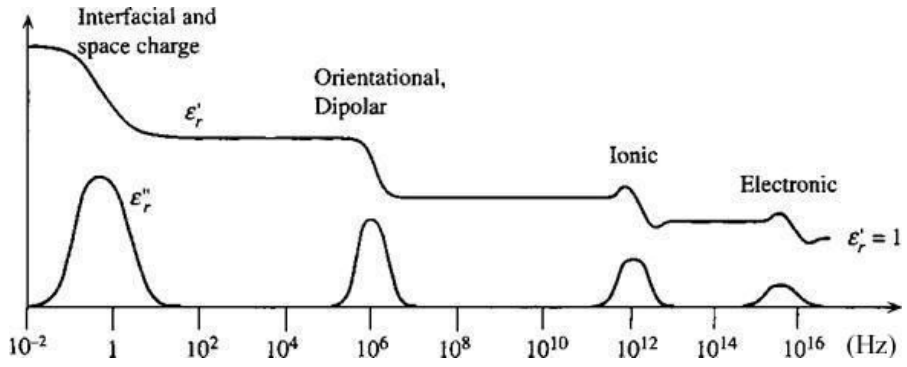

Fig. 2-1 *Schematic showing the four types of polarization and the frequency dependent behaviors of dielectric constant and loss [25].*

The electronic polarization occurs when the applied electrical field distorts the negative electrons cloud around the positive atomic nuclei in the opposite direction of the applied electrical field. The ionic polarization comes from the relative displacements between the positive and negative ions when an electrical field is applied to the dielectrics. For the organic polymers, the electronic polarization could be enhanced by designing the polymer chains with more delocalized electrons and the ionic polarization could be improved by replacing the carbon atom with some heteroatoms. These two kinds of polarization occur at a high frequency range and they could be negligible at the low measurement frequency range (10^{-2}-10^7 Hz). The dipolar polarization is an inherent polarization to the molecules with permanent dipole moments. The permanent dipole moments try to rotate to align with the applied electrical field. For organic polymers, increasing the mobility of polar polymer chains is a critical principle to enhance the dipolar polarization. The interfacial polarization occurs when the free charges or injected charges are accumulated at the interface between the heterogeneous components or between heterogeneous regions within a material. For a single component, the interfacial polarization may occur at the interface between the crystal and amorphous regions or the polycrystalline regions with different crystal states. For the heterogeneous components, like dielectric polymer nanocomposites, the interfacial polarization could also occur at the interface between the nanofillers and polymer matrices due to their different electrical conductivities. The interfacial polarization is a main polarization for the polymer

nanocomposites and thus understanding the interfacial polarization of different nanofillers filled nanocomposites is critical to design and produce high performance dielectric nanocomposites.

2.2 Conductivity Effects of Nanofillers on Dielectric Properties of DPNs

According to the conductivity of the incorporated nanofillers, the DPN could be divided into two types of nanocomposites. One type of nanocomposites is obtained by incorporating the conductive nanofillers into polymer matrices, often called as conductive-dielectric polymer nanocomposites (CDPNs). The other type of nanocomposites, also called as dielectric-dielectric polymer nanocomposites (DDPNs), is prepared by employing the nanofillers with a high dielectric constant.

2.2.1 CDPNs

The use of conducting fillers for CDPNs is motivated by the fact that they not only increase conductivity but also induce Maxwell-Wagner polarization. As a result, the induced polarization leads to a high dielectric constant in CDPNs. Generally, the electrical conductivity of percolative polymer nanocomposites shows a non-linear increase when the experimental filler loading is above the percolation threshold. At a low filler loading, the conductive fillers are separated from each other and the electrical behavior of CDPNs is dominated by the polymer matrices. However, with increasing the filler loading, some local particles clusters are formed and these adjacent clusters are connected to form a conductive network, thus resulting in a sudden increase of electrical conductivity. The percolation threshold represents a critical filler loading at which conducting paths come into contact with each other and it could be estimated by the power laws, which describes the relationship of conductivity (or dielectric permittivity) and experimental filler loading of CDPNs near the insulator-metal transition [26, 27].

For electrical conductivity,

$$\sigma_c \propto \left(f_{fillers} - f_c\right)^t \text{ for } f_{fillers} > f_c \quad (2\text{-}3)$$

$$\sigma_c \propto \left(f_c - f_{filler}\right)^{-s} \text{ for } f_{fillers} < f_c \quad (2\text{-}4)$$

For dielectric constant,

$$\varepsilon_r \propto \left(f_c - f_{filler}\right)^{-q} \text{ for } f_{fillers} < f_c \quad (2\text{-}5)$$

where σ_c is the conductivity, f_{filler} is the experimental fillers loading, f_c is the percolation threshold, t is the critical exponent in the conductive region, s is the critical exponent in the insulating region, and q is the dielectric critical exponent. The universality of percolation theory suggests that the dielectric constant exhibits the same power-law dependence on the filler loading as the conductivity below f_c. The critical dielectric constant behavior of CDPNs near percolation could be explained by the microcapacitor model. Namely, two neighboring conductive fillers and the polymer in between are treated as a local capacitor with the two fillers as two electrodes and the thin polymer layer as the dielectric, and the number of local microcapacitor expands with increasing the filler loading until forming a microcapacitor network. The sudden increase in capacitance contributed by these microcapacitors is attributed to the significant increase in the intensity of local electrical field as the filler loading approaches the percolation threshold. The enhanced local electrical field promotes the migration and accumulation of the charge carriers at the interface of nanofillers and polymer matrices due to their different relaxation time. This kind of interfacial polarization, also known as the Maxwell-Wagner effect, plays a key role in the high dielectric constant of CDPNs at low frequency range. In general, the conductive fillers employed in CDPNs could be divided into three types: conductive metal nanofillers, conductive low dimensional carbon family nanomaterials, and conductive polymers.

1) Conductive Metal Nanofillers

The metal particles have been widely incorporated into polymer matrices to fabricate CDPNs with a high dielectric constant at a low metal fillers loading. Dang et

al. incorporated the nickel (Ni) particles with an average diameter of about 5 μm into the PVDF matrices to fabricate Ni-PVDF composites [28]. The resultant composites exhibited a high dielectric constant about 400. However, a high percolation value (17 vol. %) was obtained due to the using of microsized Ni particles. The microsized aluminum (Al), iron (Fe), tungsten (W), and zinc (Zn) particles are also used to prepare the percolative composites [29]. The silver (Ag) particles with a diameter of 0.5 μm were filled into polyimide matrices and the resultant composites showed excellent dielectric properties [30]. Nevertheless, the benefits of high dielectric constant in these microsized fillers filled composites were counteracted by the high dielectric loss. In addition, the abrupt variation of dielectric constant near percolation value also made it difficult to employ those microsized fillers incorporated composites in the practical applications. Moreover, for practical dielectric capacitor application, the thickness of dielectric composites should be below 100 μm. Therefore, to make the metal particles incorporated composites practically useful, the size of metal particles should be taken into consideration. The nanosized particles could provide a large interfacial area in the composites and the increased interfacial areas are helping to promote the interfacial exchange coupling effect and consequently lead to the enhanced polarizability. The Ag particles with a diameter of 40 nm were synthesized by Qi et al. and these Ag nanoparticles were subsequently incorporated into epoxy to fabricate nanocomposites. The Ag-epoxy nanocomposites had a high dielectric constant (>300) and a low dielectric loss (<0.05) [31]. The diameter of Ag nanoparticles was further decreased to 10 nm by Liang et al. and the obtained Ag-epoxy exhibited the excellent dielectric and electrical breakdown strength performance [32]. Apart from the spherical metal nanoparticles, the metal nanowires with a high aspect ratio were also employed to improve the dielectric performance of metal nanofillers filled CDPNs. Silva et al. reported that the PVDF nanocomposites with copper (Cu) nanowires exhibited a high dielectric constant, low dielectric loss, and low percolation value[33]. The high dielectric constant was attributed to the high intrinsic conductivity of the fresh core in Cu nanowires and the

low dielectric loss was ascribed to the presence of an oxide layer on the surface of these nanowires, which hindered the direct contact of Cu nanowires. The high aspect ratio of Cu nanowires made it easier to construct the microcapacitor network at a low filler loading. It is also found that the employing of silver nanowires (Ag NWs) in the thermoplastic polyurethane (TPU) could endow the nanocomposites with a high dielectric constant, 9 times higher than that of TPU at 10^3 Hz, at a low filler loading (1.5 vol. %) [34]. Although the user of conductive metal nanofillers for CDPNs has been demonstrated as an effective way to improve the dielectric performance of CDPNs, the high density of metal nanofillers and the sensitivity to the moisture and oxygen make it difficult to be employed in the practical applications.

2) Conductive Low Dimensional Carbon Family Nanomaterials

Low dimensional carbon nanomaterials, including nanosized carbon black, carbon nanotubes, and graphenes, have aroused wide attention in the dielectric nanocomposites field due to their high specific surface areas, high electrical conductivities, low densities, and excellent thermal conduction and mechanical properties [35-44]. For the part of carbon blacks (CBs), its high electrical conductivity and low production cost make it as a kind of popular conductive fillers for the dielectric polymer composites in the past decades [45-50]. Nevertheless, the aggregation of CBs in polymer matrices is a bottleneck for the development of CBs filled dielectric nanocomposites. Especially for the nanosized CBs, its high specific surface areas and polar functional groups on the surface usually favor the formation of aggregates in the polymer matrices. Therefore, great efforts have been made to the surface modification of CBs, such as grafting crosslinking [51], plasma sputtering [52], and emulsion polymerization [53], for improving the dispersal behavior of CBs in polymer matrices.

In recent years, one-dimensional (1D) CNTs and two dimensional (2D) graphene nanosheets with a large aspect ratio have become the prominent candidates for the development of CDPNs. For the part of CNTs, it was firstly discovered by Sumio

Iijima in 1991 [54], and after that, great attentions have been focused on the mechanical, thermal, optical, and electrical applications of CNTs. For the application of CNTs in the CDPNs filed, it was firstly reported by Dang et al. [55]. Dang and his co-workers incorporated the CNTs into PVDF matrices to fabricate CNTs/PVDF nanocomposites and the obtained nanocomposites exhibited a percolative behavior where the dielectric constant increased abruptly in the vicinity of a critical filler loading. A high dielectric constant about 300 was obtained at a low filler loading (2.0 vol. %) and the percolation value is merely 1.61 vol. % [55]. However, the obtained high dielectric constant is always dependent on the experimental conditions due to the weak interaction between CNTs and polymer matrices and poor dispersibility of CNTs in matrices. In addition, a low percolation threshold of CDPNs is desirable for the flexibility application. Thus, a homogeneous dispersion of CNTs in polymer matrices is necessary to achieve the flexibility. Numerous efforts have been made to improve the dispersibility of CNTs in polymer matrices by improving the processing method and modifying the surface of CNTs.

It is well known that the carbon family nanomaterials have a strong ability to absorber the microwaves. For this reason, the microwave welding and curing method have been widely utilized to improve the dispersibility of CNTs in polymer matrices. Wang et al. reported that the CNTs based polymer nanocomposites could be fabricated by the method of microwave welding [56]. The intense heat, released from CNTs under the stimulus of microwave irradiation, was used to locally melt the adjacent thermoplastic polymer matrices. The CNTs and polymer matrices were subsequently interacted to form CNTs filled polymer nanocomposites. Rangari et al. proposed a kind of curing method to fabricate CNTs fille epoxy nanocomposites [57]. The curing time of epoxy could be reduced to a few minutes without comprising its mechanical and thermal properties. The dielectric properties of CNTs filled epoxy nanocomposites from microwave curing was reported by Chang et al. and they found that its dielectric constant (10^2 Hz) was about 2.5 times higher than that of thermally cured epoxy nanocomposites at the same filler loading (0.04 vol. %). Meanwhile, a

much lower dielectric loss was also obtained [58]. There are mainly two kinds of blending method for the fabrication of polymer nanocomposites: melt blending and solution blending. The former one (melt blending) is usually achieved by using two screws extruder equipment. The strong shear force, produced from two screws extrude, can break down the aggregates of CNTs. As a result, the dispersibility of CNTs is improved. However, the changes in processing conditions would have the significant influence on the dispersion performance of CNTs in polymer nanocomposites, thus leading to a totally different dielectric performance of nanocomposites. Prolonging the blending time or increasing the rotating speed of screws could efficiently decrease the percolation threshold. Besides, increasing the blending temperature is also useful for improving the dispersion of CNTs in polymer matrices. For example, Krause et al. reported that the dispersion of CNTs in polyamide 6 (PA6) could be improved by increasing the mixing time and increasing the mixing temperature [59]. Yuan et al. reported that the molecular level interaction between CNTs and PVDF was obtained by melt incorporating the CNTs into PVDF matrices [60]. The donor-acceptor complexes between the delocalized π-electron clouds of CNTs and strongly electrophilic F groups of PVDF chains favor the molecular level interaction (Fig. 2-2). The resultant nanocomposite exhibited an ultrahigh constant of 3800, which was approximately 380 times higher than that of pure PVDF while maintaining relatively low conductivity about 6.3×10^{-5} S m^{-1}. However, it should be noted that the breakage of CNTs during melt mixing at a higher rotating speed of screws was more pronounced, which results in a decrease of the aspect ratio of CNTs. Moreover, the viscosity of nanocomposites melts usually increases with increasing the amount of filler loading. Especially for the case with a high filler loading, the high viscosity makes it difficult to process the nanocomposites. The solution mixing approach is employed by blending the fillers and polymer matrices in a solvent, consequently decreasing the viscosity of the mixture. Therefore, the solution mixing method is an effective blending way for the high viscosity mixture. However, in most cases, a large amount of solvent is needed in order to

obtain a good dispersion state of fillers. Especially for the non-water-soluble polymers, the toxic organic solvents, such as toluene, chloroform, and dimethylformamide (DMF), are usually involved in the mixing procedures. Besides, the high gasification temperatures of these organic solvents make it difficult to remove these solvents totally from the pre-mixture of composites. Solution mixing approach has been widely used for dispersing CNTs in polymer matrices [61-64]. Dang et al. prepared a kind of functionalized CNTs filled PVDF nanocomposites with the aid of solution mixing method. A maximum dielectric value about 5000 is obtained, which is 500 times higher than that of PVDF pure matrices [61].

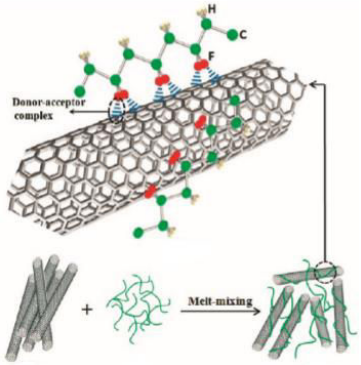

Fig. 2-2 *Schematic image of donor-acceptor complexes between individual CNT and PVDF chains [60].*

Apart from selecting an appropriate mixing method for the preparation of CNTs filled nanocomposites, optimizing the surface structure of CNTs is also necessary in order to enhance the coupling effect of CNTs and polymer matrices. In general, the surface modification of CNTs can be classified into two categories: physical modification and chemical modification. The physical modification approach is implemented by non-covalently wrapping or absorbing some mediating molecules on the surface of CNTs. The non-covalent surface modifications are mainly based on some weak interactions, such as van der Waals, π-π stacking, and hydrophobic interactions. For instance, the deposition of a thin amorphous carbon layer on the surface of pristine CNTs was considered as an effective strategy to weakening the dielectric loss of CNTs filled nanocomposites [65, 66]. Guo et al. prepared amorphous carbon layer coated CNTs hybrids by degrading the glucose powder in the

hydrothermal reaction (Fig. 2-3) and it was found that the dielectric loss of nanocomposites was largely suppressed [65]. The amorphous carbon barrier layer prevented the adjacent CNTs from being contacted with each other, thereby making it difficult to form the conductive network. As a result, the dielectric loss of nanocomposites would be decreased at the same fillers loading. The chemical modification is employed via covalent bonding of some functional groups. Covalent surface modifications feature functional groups that are attached to the surface of CNTs by covalent bonds. These functional groups include the carboxyl, hydroxyl, trifluorophenyl (TFP), and specific polymer chains. For example, Dang et al. reported that the TFP-functionalized CNTs could endow the corresponding PVDF nanocomposites with a giant dielectric constant about 5000. The strongly electrophilic F atoms on the surface of TFP-CNTs hybrids not only improved the dispersion of CNTs in PVDF matrices but also reinforced the Maxwell-Wagner effect. As shown in Fig. 2-4, Huang et al. synthesized the poly(methyl methacrylate) (PMMA) encapsulated CNTs (CNTs@PMMA) hybrids with tunable PMMA thickness via surface-initiated atom transfer radical polymerization [36]. They found that the dispersion of CNTs in PVDF was significantly improved and a higher percolation threshold was observed in CNTs@PMMA filled PMMA nanocomposites compared with that of pristine CNTs filled nanocomposites. Besides, the thick PMMA shell resulted in a higher percolation value. Although the surface engineering of CNTs has achieved great success, no matter the physical or chemical modification would weaken the intrinsic electrical properties of CNTs. Therefore, the surface characteristics and intrinsic properties of CNTs should be rationally balanced according to the specific requirements.

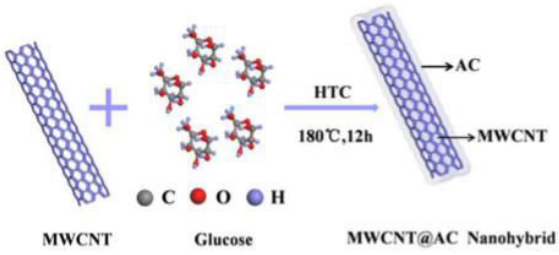

Fig. 2-3 *Schematic diagram showing the fabrication process of amorphous carbon*

layer coated CNTs hybrids [65].

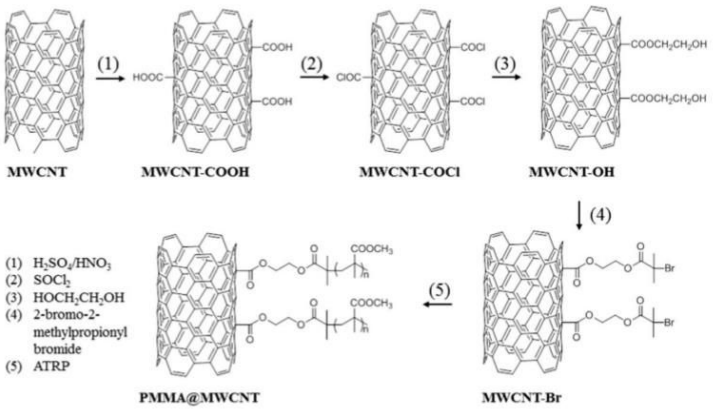

Fig. 2-4 *Schematic diagram illustrating the preparation process of CNTs@PMMA hybrids [36].*

Since the first discovery of graphene in 2004 by the group of Geim and Novoselov, graphene has been one of the most exciting research topics owing to its unique 2D structure and fascinating properties such as specific surface areas, excellent mechanical strength, extremely high thermal conductivity, and giant electron mobility. Compared with 1D structure of CNTs, the unique 2D structure of graphene nanosheets exhibits a high aspect ratio in-plane direction, which is useful for the formation of microcapacitors in the polymer matrices. Plenty of methods have been employed for preparing graphenes, among which the mechanical exfoliation, chemical vapor deposition (CVD) growth, and graphite-intercalation chemistry are three kinds of most preferred methods. The mechanical exfoliation method is usually implemented through mechanical milling or peeling off. The CVD growth method is involved in the decomposition of carbon source on the surface of the catalytic substrate in a high temperature. However, the low productivity of mechanical exfoliation and the complicated transfer process of graphene layers impede the large-scale production and application of graphenes. The key component of graphite-intercalation chemistry approach is inserting certain chemicals into the gap between the adjacent natural graphite layers and subsequently, some low molecular substances will be gasified and released from these gaps due to the violent reaction between the chemicals and graphite. The neighboring graphene layers are thereby separated by the

high energy produced from gas expansion. The graphite-intercalation chemistry method makes it possible to produce graphenes in a large scale. Nevertheless, the numerous defects on the surface and edge of graphene, resulted from the intense chemical reaction, is one of the drawbacks of this method. Among various intercalation chemistry methods, the Hummers method is the most widely used method for the preparation of graphenes [67]. As shown in Fig. 2-5, the strong oxidized acids are usually involved in the Hummers method to produce graphene oxide (GO) nanosheets [67]. The reduced graphene oxide (rGO) nanosheets are subsequently obtained by reducing the oxygen-containing groups on the surface of GO.

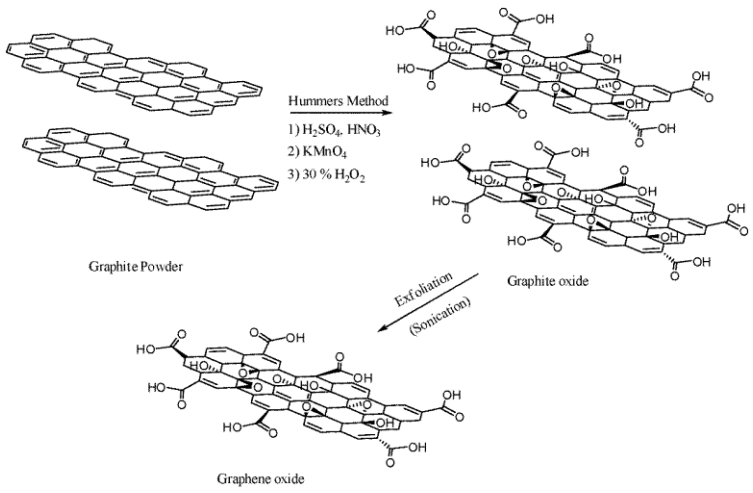

Fig. 2-5 *Schematic diagram showing the Hummers method for the preparation of GO nanosheets [67].*

Similar to the CNTs, the huge surface free energy and strong π-π stacking force of graphene layers make it difficult to separate these graphene layers and such a stacking behavior is harmful to the homogeneous dispersion of graphene layers in the polymer matrices, which is extremely critical to the final dielectric performance of CDPNs. Many efforts have been made to improve the dispersion of graphene nanosheets in the polymer matrices and enhance the interfacial coupling of graphenes nanosheets and polymer matrices. As discussed in the CNTs filled nanocomposites part, the methods used for improving the dispersibility of graphene nanosheets could be divided into two types: optimizing the processing method and modifying the

surface characteristic of graphene nanosheets. Apart from the traditional melt blending and solution blending methods as aforementioned in CNTs part, the in-situ polymerization provides a new sight for preparing the low dimensional carbon family nanomaterials filled dielectric nanocomposites. For instance, Wang et al. proposed an effective approach using in-situ polymerization, to fabricate GO nanosheets filled polyimide (PI) nanocomposites with outstanding dielectric and mechanical properties [68]. The GO nanosheets were employed to fabricate nanocomposites owing to various oxygen-containing functional groups, which provides abundant active sites for grafting the polymer chains on the surface and edge parts of graphene nanosheets. In this work, the 4, 4'-oxydianiline (ODA) was firstly bonded with the active sites of GO nanosheets to prepare NH_2-functionalized GO nanosheets. Then the functionalized GO nanosheets were added into the precursor solution of PI, and after that, the in-situ polymerization occurred not only on the surface of GO nanosheets but also in the polymer bulk. As shown in the scanning electron microscope (SEM) images of Fig. 2-6, the dispersion of GO nanosheets in PI matrices was significantly improved, which is responsible for the excellent dielectric and mechanical properties.

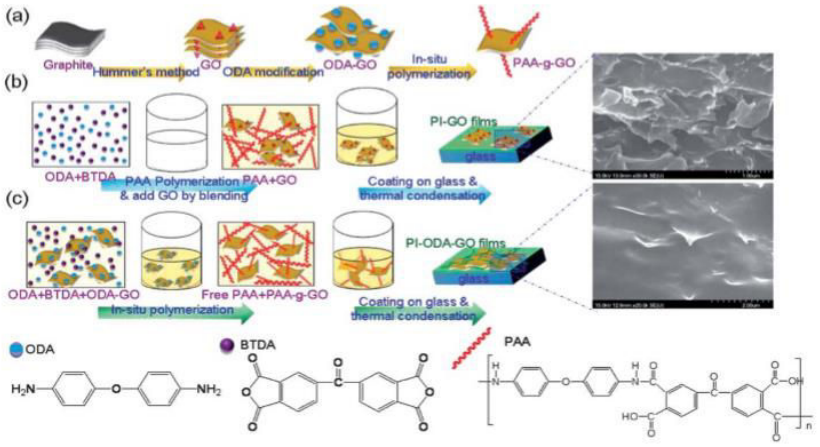

Fig. 2-6 *Schematic diagram showing the procedure for the preparation of (a) ODA-GO, (b) PI-GO films and (c) PI-ODA-GO films [68].*

As for the appropriate surface modification of graphene nanosheets, the methods used could also be classified into two parts: physical and chemical modification. For instance, Hsiao et al. hindered the re-stacking and aggregation of rGO nanosheets by

absorbing the cationic surfactant (stearyltrimethylammoniumchloride, STAC) on the surface of rGO nanosheets [69]. The non-functionalized rGO nanosheets in the suspension precipitated fast than the STAC absorbed rGO nanosheets (Fig. 2-7). Thereby, the obtained STAC absorbed rGO/water-borne polyurethane (WPU) nanocomposites exhibited a low electrical conductivity percolation threshold and an outstanding enhanced electrical conductivity of approximately 5.1 S/m. Wang et al. prepared the poly(vinyl alcohol)-modified rGO (rGO-PVA) hybrids by chemically bonding the carboxyl groups of GO with the hydroxyl groups of PVA chains [70]. The PVA functionalization of graphene surface can not only prevent the agglomeration of original rGO but also enhance the interaction between PVDF and rGO-PVA through the strong hydrogen bonds. Compared with the pristine rGO/PVDF nanocomposites, higher dielectric constant together with lower loss were achieved in rGO-PVA/PVDF nanocomposites.

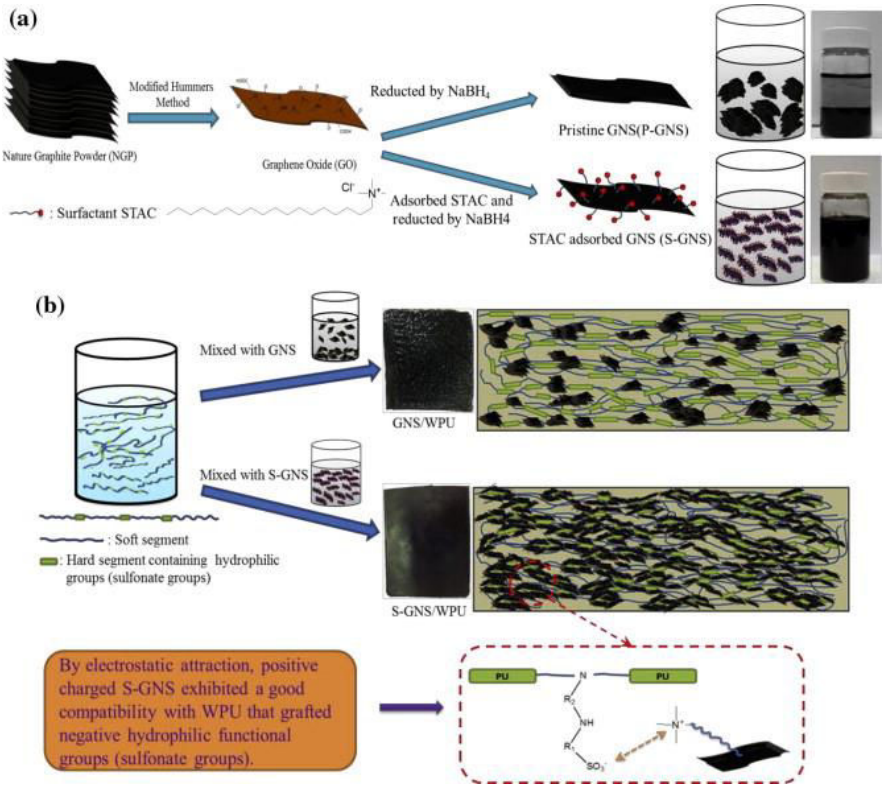

Fig. 2-7 *Schemes of the procedure for preparation of (a) pristine rGO and STAC absorbed rGO (b) pristine rGO/WPU and STAC-rGO/WPU composites [69].*

In general, the ideal uniform dispersion of low dimensional carbon family nanomaterials, especially for the 1D CNTs and 2D graphene nanosheets, and the

interfacial coupling effects between nanofillers and polymer matrices are two critical factors for the ultimate dielectric performance of CDPNs.

3) Conductive Polymers

Incorporating the conductive polymers into host polymer matrices is another strategy to prepare the CDPNs. The PANI and PPy are two kinds of most frequently used conductive polymer fillers for the dielectric application. The all-organic percolative nanocomposites give the nanocomposites with excellent flexibility and ease processing characteristics. For example, Yuan et al. reported that the PANI filled PVDF nanocomposites exhibited a high dielectric constant about 385 and an energy storage density value about 6.1 J cm^{-3}, which was three times higher than that of neat PVDF [71]. Zhang et al. fabricated the PPy nanoclips filled P(VDF-TrFE) nanocomposites [72] and the obtained nanocomposites showed a very low percolation threshold (< 8 wt.%) and exhibited a high dielectric constant.

2.2.2 DDPNs

The dielectric constant could also be enhanced by incorporating the ceramic fillers with a high dielectric constant into the polymer matrices. Ceramic particles with a high dielectric constant, such as $BaTiO_3$, TiO_2, $CaCu_3Ti_4O_{12}$, and $Pb(Zr, Ti)O_3$, are usually chosen as the nanofillers to prepare the DDPNs. In addition, an increase in the amount of fillers loading increases the interfacial areas between the ceramic fillers and polymer matrices. Therefore, the effect of interfacial polarization on the dielectric constant and loss can be significant. However, in order to obtain a high dielectric constant, a high fillers loading is usually needed. The increase in porosity and viscosity of DDPNs, resulted from the high fillers loading, would make it difficult to process the DDPNs.

In order to improve the dielectric constant of DDPNs for a given ceramic fillers loading, three main methods have been employed. One is to optimize the fabrication process of DDPNs so as to improve the dispersion of ceramic fillers and minimize the

pores in DDPNs. For example, Dang et al. reported that the dielectric constant of $BaTiO_3$ filled PI nanocomposites could be improved by the in-situ polymerization method associated with the degassing process. The in-situ polymerization strategy improved the dispersion of $BaTiO_3$ in PI matrices and the degassing process reduced the number of pores in the final nanocomposites [73]. Another one is to appropriately modify the surface of ceramic nanofillers. Similar to the CDPNs, the interfacial coupling between the ceramic fillers and polymer matrices play an important role in determining the dielectric performance of DDPNs. To improve the interaction between fillers and polymer matrices, the appropriate surface modifications of ceramic nanofillers are often needed. The small-molecule ligands are frequently used to tailor the surface of ceramic nanofillers to improve compatibility between the nanofillers and host polymers, consequently improving the dielectric performance of DDPNs. By using this method, the improvement of nanofillers dispersion and the elimination of nanofillers aggregation could be achieved, thus minimizing the local electrical field distortion and avoiding the formation of microstructural defects at the interfacial areas. Kim and co-workers reported that the use of $BaTiO_3$ nanoparticles with phosphonic acid ligands led to well dispersed $BaTiO_3$ nanocomposites with a high dielectric constant [74]. Zhou et al. prepared surface hydroxylated $BaTiO_3$ nanoparticles in the aqueous solution of a hydrogen peroxide (H_2O_2) [75]. The surface modified $BaTiO_3$ nanoparticles filled PVDF nanocomposites showed lower loss tangent and higher dielectric strength due to the formation of a hydrogen bond between nanoparticles and PVDF host polymer (Fig. 2-8). Gao and co-workers modified the surface of $BaTiO_3$ nanoparticles by the H_2O_2 and titanate coupling agent treatment [76]. The long chain segments of titanate coupling agent provided high molecular chains mobility and disordered structures to the shells, thus leading a loose shell and compact due to the chain entanglement with the PVDF matrices (Fig. 2-9). Besides, the hydrogen bonds between the hydroxyl groups on the surface of $BaTiO_3$ nanoparticles and the fluorine atoms of the PVDF intensified the interfacial interaction. The dielectric performance of PVDF nanocomposites with surface treated

$BaTiO_3$ nanoparticles was largely improved. Niu et al. utilized a series of carboxylic acids to modify the surface of $BaTiO_3$ nanoparticles [77]. The results showed that the modifiers could significantly improve the compatibility between the fillers and matrices. The last one is to develop novel ceramic nanofillers by doping the metal oxides to form a boundary layer structure. For the metal oxides with the ferroelectric characteristics, the dielectric constant usually exhibits a peak value in the vicinity of Curie point, where the transition of the ferroelectric substance from the ferroelectric state to non-ferroelectric state occurs. Some specific chemical additives or so-called shifters have been applied to $BaTiO_3$ or other ferroelectric ceramic nanofillers to move the Curie peak to the room temperature to improve the dielectric constant, and to smooth the Curie peak to obtain a lower temperature coefficient of dielectric constant. For instance, Kuo et al. synthesized the multi-doped $BaTiO_3$ ceramic nanofillers and the obtained hybrids exhibited a high dielectric constant about 25000, which is 10 times that of that of the undoped $BaTiO_3$ ceramic nanofillers [78]. As a result, the doped nanofillers filled epoxy nanocomposites showed a higher dielectric constant than that of undoped nanofillers filled nanocomposites at the same fillers loading.

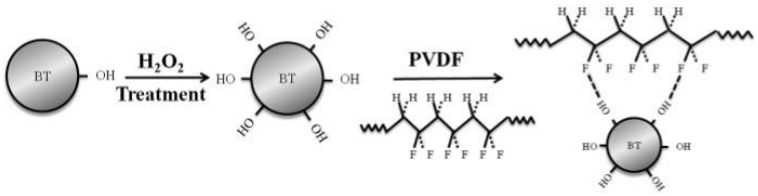

Fig. 2-8 *Schematic diagrams of the hydroxylation of $BaTiO_3$ nanoparticles and the formation of hydrogen bond in surface hydroxylated $BaTiO_3$ nanoparticles filled PVDF nanocomposites [75].*

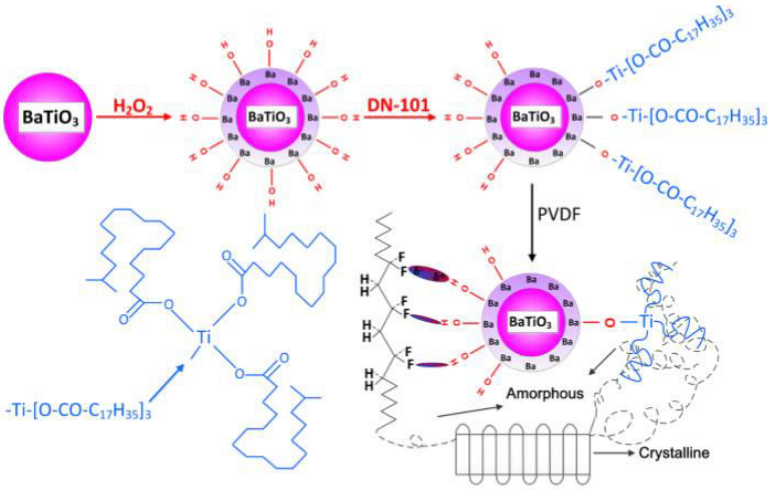

Fig. 2-9 *Diagrams of the modification of $BaTiO_3$ nanoparticles and interaction in PVDF nanocomposites with surface treated $BaTiO_3$ nanoparticles [76].*

Although the modifications of ceramic nanoparticles with small molecular ligands have been intensively used to improve the dielectric performance of DDPNs However, these methods still have some limitations in realizing the full potential of DDPNs with a high dielectric constant because the modifiers themselves usually do not play a vital role in the property enhancement of the nanocomposites. Therefore, the rational design of the surface structure of ceramic nanofillers is necessary to enhance the dielectric property of DDPNs.

2.3 Shape and Size Effects of Nanofillers on Dielectric Properties of DPNs

Different types of nanofillers including spherical, wires, tubes, fibers, and plates have been used in the DPNs with a high dielectric constant. For both the CDPNs and DDPNs, the shape of nanofillers is decisive in determining the dielectric properties of final DPNs. Nanofillers with different shapes have different surface areas resulting in different interfacial coupling areas in the DPNs, which leads to the different interfacial polarization and hence different dielectric properties. More importantly, different shapes of nanofillers can lead to the different types of connectivity in DPNs. Apart from the shape, the size of nanofillers for a specific shape also plays an important role in determining the dielectric properties of DPNs. Understanding the

size and size distribution of nanofillers helps to understand the dielectric properties of DPNs. The physical and chemical properties of nanofillers depend much on the size, which leads to the formation of size-dependent behavior for the dielectric constant of DPNs.

2.3.1 Shape Effects of Nanofillers on Dielectric Properties of DPNs

1) Shape Effects of Nanofillers on Dielectric Properties of CDPNs

For the CDPNs, the more the shape of nanofillers deviates from the spherical particles, the lower is the percolation threshold. Compared with the spherical nanofillers, the higher aspect ratios of 1D and 2D nanofillers make the electrical conducting network easy to be formed at a small nanofillers loading, thus resulting in a lower percolation threshold. For example, Huang et al. reported that the percolative behavior of PVDF nanocomposites with silver (Ag) nanoparticles (100 nm) didn't occur even when the loading of Ag nanoparticles was 20 vol. % [79]. However, the percolation threshold of PVDF nanocomposites with copper nanowires, obtained from the Silva and co-workers, was merely 0.27 vol. % [33]. Audoit et al. reported that the percolation threshold of Ag nanoplates filled PVDF nanocomposites was only 5.9 vol. % [80]. For the carbon family nanomaterials, the 1D structural CNTs and 2D structural graphene nanosheets could also give the nanocomposites a lower percolation threshold than that of carbon black filled one. Ma et al. reported that the percolation threshold of CNTs filled epoxy nanocomposites (0.3 wt. %) was lower than that of spherical carbon black filled one (0.6 wt. %) [81]. Wang and co-workers reported that the percolation threshold of graphene nanosheets filled high density polyethylene (HDPE) was only 6 wt. %, which was extremely lower than that of spherical carbon black filled one (22 wt. %) [82]. All these results suggest that the shape of nanofillers has a critical effect on the dielectric and electrical performance of CDPNs. Nanofillers with the 1D and 2D structures favor the formation of the conductive network in the percolative CDPNs, thus resulting in a lower percolation threshold.

2) Shape Effects of Nanofillers on Dielectric Properties of DDPNs

The shape of ceramic nanofillers also plays a vital role in determining the dielectric performance of DDPNs. A high ceramic nanoparticles loading (> 50 wt. %) is usually needed to obtain a considerable dielectric constant of DDPNs. However, the high loading of ceramic nanofillers would deteriorate the mechanical and electrical breakdown properties of DDPNs. Trade-offs between dielectric constant and breakdown strength have recently made by using ceramic nanofillers with a large aspect ratio instead of spherical nanofillers. As shown in Fig. 2-10, Song et al. reported that the epoxy nanocomposites with filled with $BaTiO_3$ nanofibers exhibited greater dielectric constant than that of nanocomposites with $BaTiO_3$ nanoparticles [83]. Tang et al. also demonstrated that the 1D structural $BaTiO_3$ nanowires could enhance the dielectric property of nanocomposites more efficiently than the $BaTiO_3$ nanoparticles [84]. As displayed in Fig. 2-11, the dielectric constant reached up to 70 at 17.5 vol. % of $BaTiO_3$ nanowires, while the dielectric constant is only around 52 at 30 vol. % of nanoparticles. Zhu et al. synthesized 2D TiO_2 nanosheets by the hydrothermal reaction [85] and found that the nanocomposite with 5 wt. % 2D nanofiller possesses the highest dielectric constant and lowest dielectric loss in relation to the nanocomposites with spherical and 2D nanofillers (Fig. 2-12).

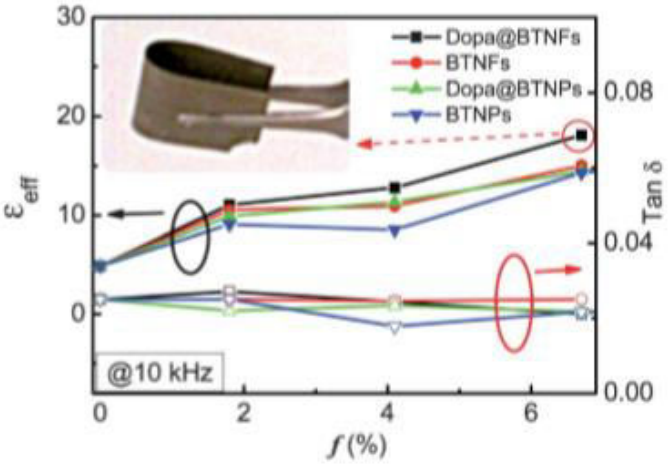

Fig. 2-10 *Variation of dielectric constant and loss with the volume fraction of $BaTiO_3$ nanofillers for epoxy nanocomposites [83].*

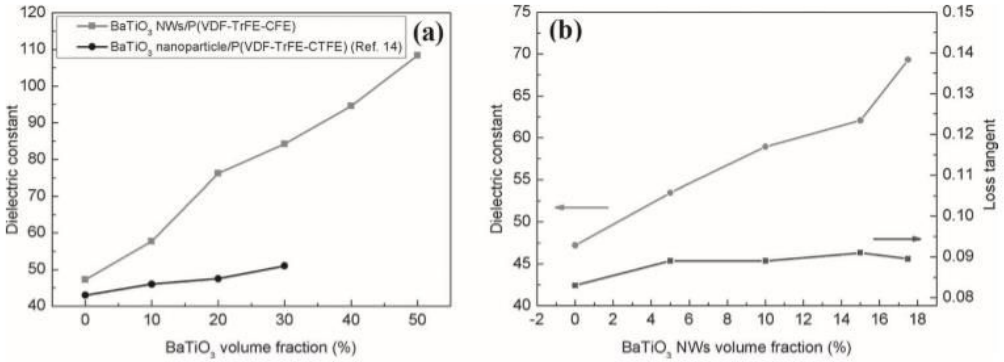

Fig. 2-11 *Dielectric properties of nanocomposites: (a) comparison of measured dielectric constant (at 10^3 Hz) of $BaTiO_3$ nanowires nanocomposites as a function of $BaTiO_3$ nanowires and nanoparticles volume fractions [86]; (b) dielectric constant and loss (at 10^3 Hz) of $BaTiO_3$ nanowires nanocomposites [84].*

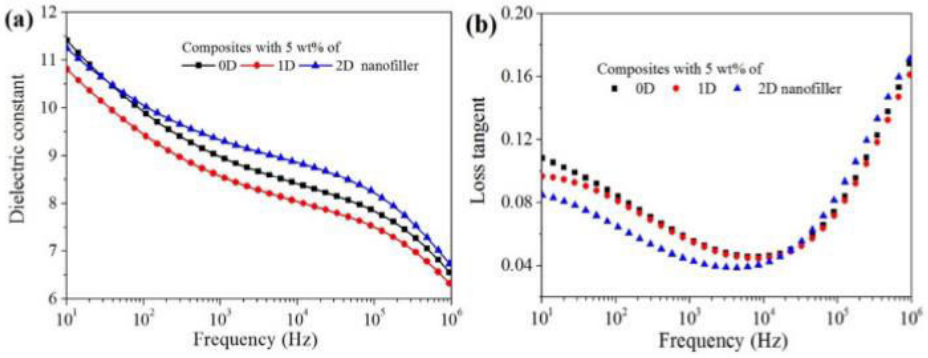

Fig. 2-12 *Frequency dependence of (a) dielectric constant, (b) dielectric loss of the nanocomposites with 0D, 1D, and 2D nanofillers [85].*

Compared with spherical ceramic nanofillers, the 1D structural ceramic nanofillers could enhance the dielectric constant of DDPNs more efficiently at the same nanofillers loading and the 2D structural ceramic nanofillers could effectively suppress the leakage current in the direction of perpendicular to the 2D plates, thus leading to a lower dielectric loss and higher electrical breakdown strength. Therefore, the shape of ceramic nanofillers is decisive in the final dielectric performance of DDPNs.

2.3.2 Size Effects of Nanofillers on Dielectric Properties of DPNs

1) Size Effects of Nanofillers on Dielectric Properties of CDPNs

For the CDPNs, the size or aspect ratio of conductive nanofillers is an important dominant factor for the final dielectric performance of CDPNs. For the spherical metal nanoparticles filled nanocomposites, Xue et al. reported that the percolation threshold theoretically decreased with increasing the metal nanoparticle axial ratio and decreasing the metal nanoparticle size (Fig. 2-13). Using the metal nanoparticles with larger axial ratio and smaller size helped to reduce the minimum metal nanoparticles loading required to reach a certain conductivity value [87].

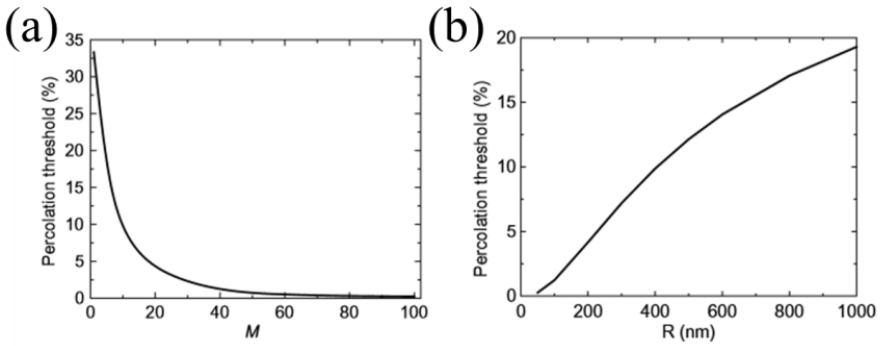

Fig. 2-13 *(a) The relation between the percolation threshold and the metal nanoparticles axial ratio; (b) The relation between the percolation threshold and the metal nanoparticles size [87].*

For the 1D and 2D structural nanofillers, the higher aspect ratio favors the formation of the conductive network at a small nanofillers loading. Li et al. reported that there was a critical value of aspect ratio, above which the aspect ratio and dispersion of CNTs became crucial while allowing the percolation threshold to vary several orders of magnitude. The entanglement and aggregation of CNTs were easy to be formed for the CNTs with a higher aspect ratio. Thereby, the dispersion of CNTs was another important factor in determining the percolation threshold for the CNTs with higher aspect ratio. In contrast, below this value, the percolation threshold decreased rapidly with increasing the aspect ratio [27]. As displayed in Fig. 2-14, Li et al. reported that the percolation threshold of 2D structural graphene nanosheets filled nanocomposites decreased with increasing the diameter of nanosheets and decreasing the thickness of nanosheets [88].

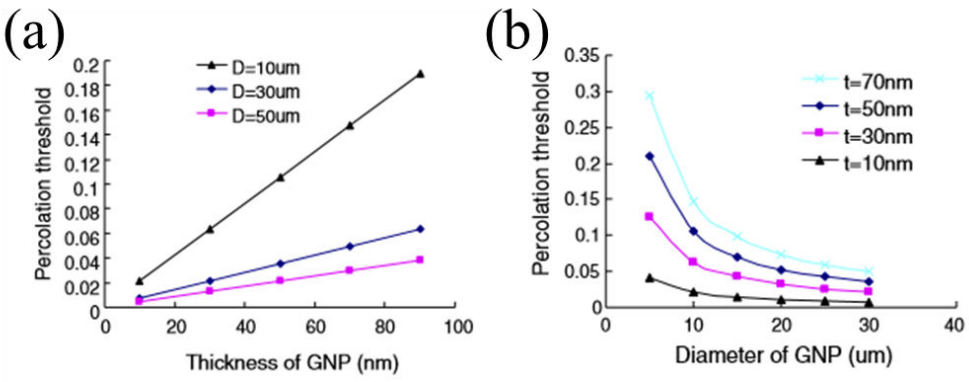

Fig. 2-14 *(a) Effect of the thickness of platelet on percolation threshold; (b) Effect of the diameter of platelets on percolation threshold [88].*

The size or aspect ratio of conductive nanofillers is critical to the final dielectric performance of CDPNs. However, before considering the correlation between the size or aspect ratio and percolation threshold, the influences of dispersion, entanglement, aggregation of nanofillers in CDPNs should be eliminated in order to obtain an accurate relationship between the percolation threshold and size or aspect ratio of nanofillers.

2) Size Effects of Nanofillers on Dielectric Properties of DDPNs

The size or aspect ratio of ceramic nanofillers is found to affect the dielectric performance of DDPNs greatly. Kobayashi et al. reported that the dielectric constant and loss of PVDF nanocomposites with different sized $BaTiO_3$ nanoparticles increased with increasing the crystal size of $BaTiO_3$ nanoparticles [89]. However, a different result was obtained by Mendes and co-workers [90]. They reported that the dielectric constant of PVDF nanocomposites increased significantly with decreasing the size of $BaTiO_3$ nanoparticles. According to their conclusion, the size-dependent behavior of PVDF nanocomposites filled with different sized $BaTiO_3$ nanoparticles was attributed to the space charge effects at the interface between $BaTiO_3$ nanofillers and PVDF matrices. It can be seen that the size-dependent behavior of dielectric constant of nanocomposites is not clear. In some cases, the dielectric constant decreases with increasing the size of nanofillers and in other cases it follows an opposite trend. One possible reason is that the different size range of nanofillers is

used in that literature. Another potential reason is that the morphology and size of nanofillers may be changed after the blending procedure due to the formation of some aggregates in the polymer matrices. The size of these aggregates is not exactly the same as the sized used before measurement.

For the 1D structural ceramic nanofillers, numerous theoretical and experimental results about the relationship between dielectric constant and aspect ratio of nanofillers have been reported. Andrews and his co-workers studied the influence of aspect ratio of nanofillers on the electro-elastic properties of corresponding nanocomposites [91]. As indicated in their models, the electromechanical coupling increased with increasing the aspect ratio of inclusion. Tang et al. synthesized $BaTiO_3$ nanowires with different aspect ratios by adjusting the temperature of the hydrothermal reaction and fabricated the corresponding PVDF nanocomposites to investigate the relationship between dielectric constant and aspect ratio of these $BaTiO_3$ nanowires [92]. As shown in Fig. 2-15, it was found that the dielectric constant of nanocomposites increased with the aspect ratio of the nanowires at the same nanofillers loading. For example, the nanocomposites with 30 vol. % $BaTiO_3$ nanowires at an aspect ratio of 45.8 reached a dielectric constant of 44.3, which was 30.7 % higher than samples with an aspect ratio of 9.3. Tang et al. also synthesized the PZT nanowires (higher aspect ratio) and nanorods (lower aspect ratio) [93]. As shown in Fig. 2-16, they found that the dielectric constant of nanocomposites containing nanowires was higher than those with nanorods at the same inclusion volume fraction.

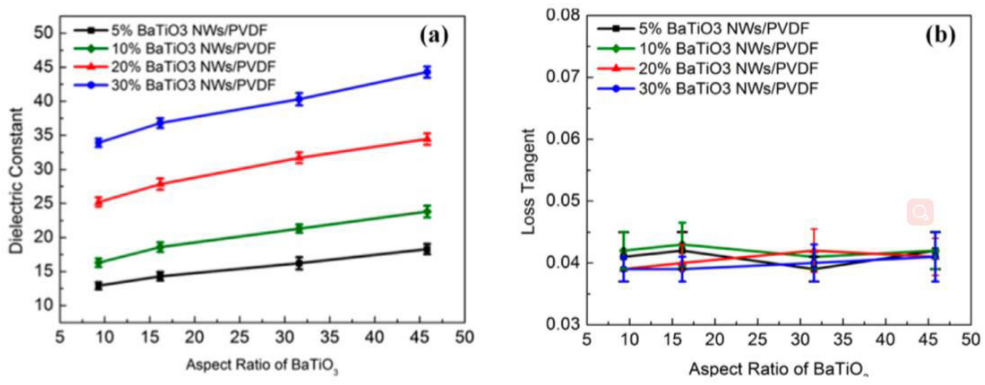

Fig. 2-15 *(a) Dielectric constant and (b) loss tangent of the nanocomposites measured*

at 10^3 Hz as a function of aspect ratio and volume fraction of $BaTiO_3$ NWs [92].

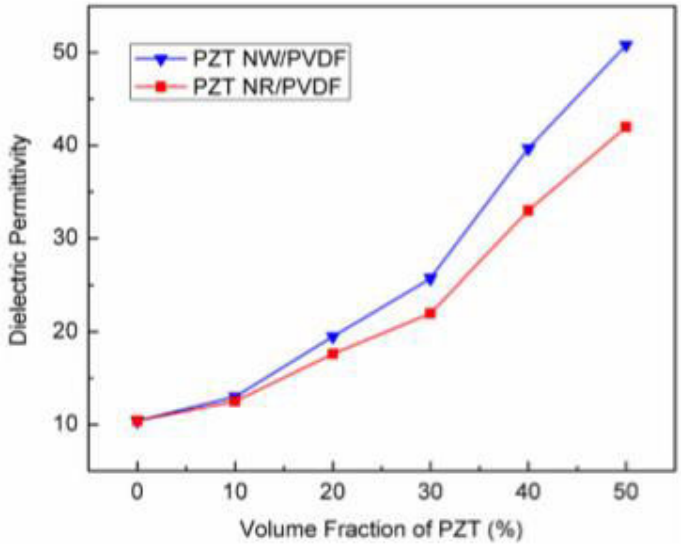

Fig. 2-16 *Comparison of measured dielectric constant at 10^3 Hz of nanocomposites as a function of PZT nanowires and nanorods volume fractions [93].*

Therefore, selecting the appropriate shape and size of nanofillers are extremely important to achieve a considerable dielectric constant of DPNs. The 1D and 2D structural nanofillers filled DPNs exhibit excellent dielectric performance than that of spherical nanofillers filled one. More importantly, the dielectric performance can be further optimized by regulating the aspect ratios of 1D and 2D nanofillers.

2.4 Composition and Structure of Nanofillers on Dielectric Properties of DPNs

There are some limitations of using nanofillers with the single component in the field of DPNs. The high dielectric loss is always accompanied with the high dielectric constant in the vicinity of the percolation threshold for the percolative CDPNs. As for the DDPNs, a high fillers loading is usually needed to reach a considerable dielectric constant. As a result, the flexibility, processability, and high voltage resistant property of DDPNs would be greatly weakened. Therefore, integrating two or more components to form a novel hybrid structure is necessary to overcome the aforementioned issues by taking full advantage of each component. Developing the

core@shell structure is a promising strategy to integrate two or more components [94-97]. In recent years, significant efforts have been made to develop the core@shell structured nanofillers. Generally, the core@shell structure could be divided into the following two groups according to their targeted nanocomposites.

2.4.1 Core@Shell Structure for the CDPNs

It is well known that the main drawback of percolative CDPNs is the unavoidable high dielectric loss in the vicinity of the percolation threshold. For this reason, great attentions have been focused on this issue to avoid the direct contact of adjacent conductive nanofillers.

For the metal nanofillers, Xu et al. synthesized an amorphous aluminum oxide (Al_2O_3) layer on the surface of aluminum (Al) core by self-passivating Al [98]. It was found that this unique core@shell structure endowed the nanocomposites with an extremely low loss of 0.02 at a filler loading as high as 50 wt. %. Shen and co-workers introduced an insulating interlayer of carbonaceous shell on the surface of Ag nanoparticles to reduce the tunnel current between the neighboring Ag cores, endowing the nanocomposites with stable and high dielectric constant and low dielectric loss [99]. As shown in Fig. 2-17, the dielectric constant, conductivity, and dielectric loss were greatly reduced at the same nanofillers loading and the percolation behavior was delayed. Silva also reported that the PVDF nanocomposites filled with copper nanowires exhibited a low dielectric loss and the low loss was ascribed to the presence of an oxide layer on the surface of these nanowires [33]. Zhang et al. prepared zinc oxide (ZnO) shell on the surface zinc (Zn) core by the heat treatment of raw Zn nanoparticles under air [100]. It was found that the duplex interfacial polarizations induced by the metal-semiconductor interface and semiconductor-insulator interface enhanced the dielectric constant and the presence of ZnO semiconductor shell suppressed the dielectric loss.

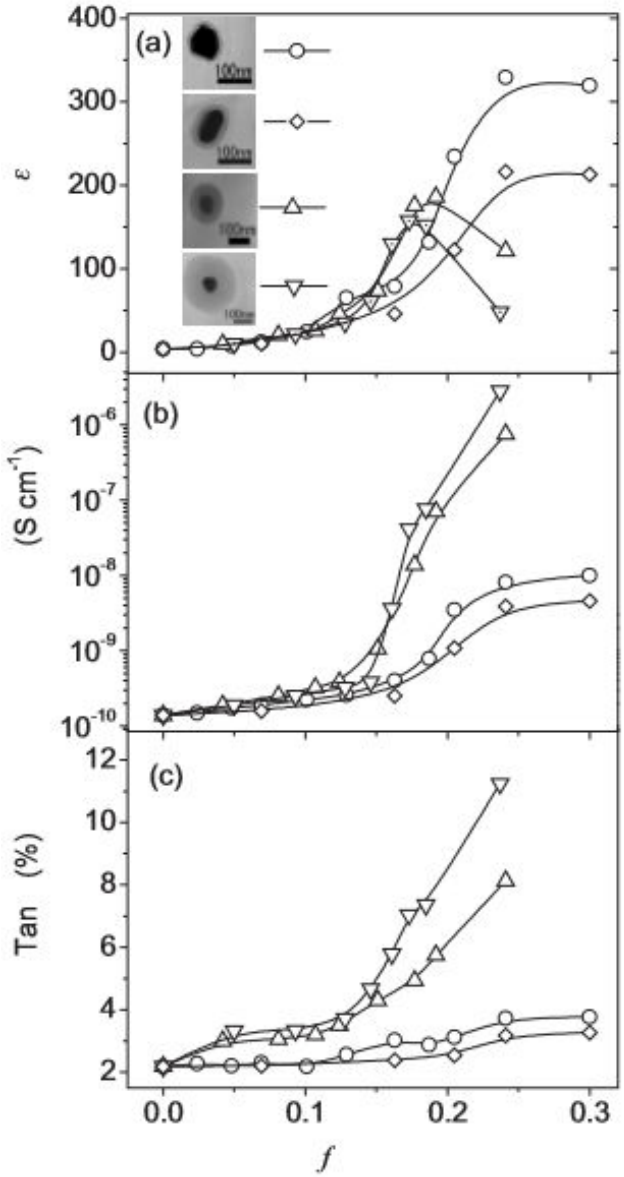

Fig. 2-17 *Variations of (a) dielectric constant, (b) conductivity, and (c) dielectric loss, with the volume fraction of the Ag@C nanoparticles at 10^3 Hz. The microscopy images in (a) indicate the representation of the symbols [99].*

Similarly, the core@shell structure has been widely applied to the carbon family nanomaterials. Liu et al. synthesized the polysulfone (PSF) coated CNTs nanofibers by a simple electrospinning method and fabricated the nanocomposites by a hot pressing technology as shown in Fig. 2-18 [101]. The nanocomposites exhibited high dielectric constant and low dielectric loss. The low dielectric originated from the PSF coating, which prevented the CNTs from being contacted. Guo et al. prepared the amorphous carbon (AC) shell on the surface of CNTs by degrading the glucose during

hydrothermal reaction [65]. Compared with the pristine CNTs filled PVDF nanocomposites, the core@shell structured CNTs@AC hybrids filled nanocomposites exhibited a much lower dielectric loss (Fig. 2-19). The uniform amorphous carbon shell provided an insulating layer between adjacent CNTs, which not only prevented the direct contact of CNTs but also improved the dispersibility of CNTs.

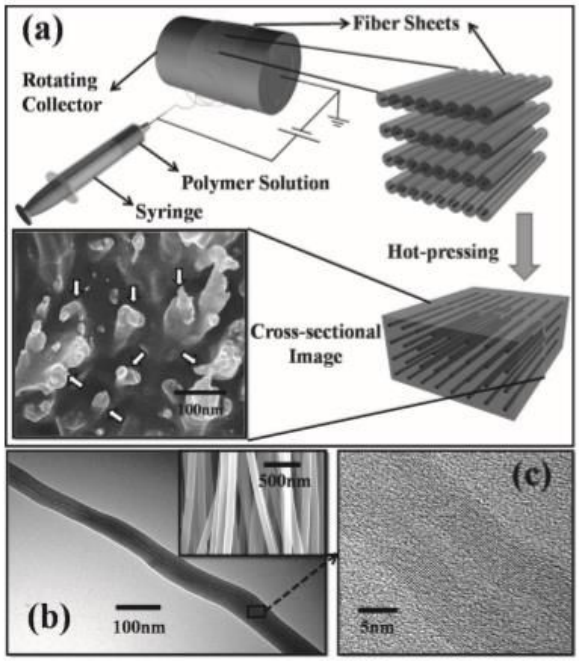

Fig. 2-18 *(a) Schematic illustration for preparation of CNTs/PSF nanocomposites. The scanning electron microscopy (SEM) image in the inset shows the cross-sectional image of the nanocomposites perpendicular to the fiber direction; CNTs are indicated by arrows. (b) Transmission electron microscopy (TEM) images for CNTs/PSF core@shell nanostructure nanocomposites nanofibers. The SEM image in the inset shows the CNTs/PSF nanofibrous sheet prepared by electrospinning. (c) High-resolution TEM (HR-TEM) image of a CNT [101].*

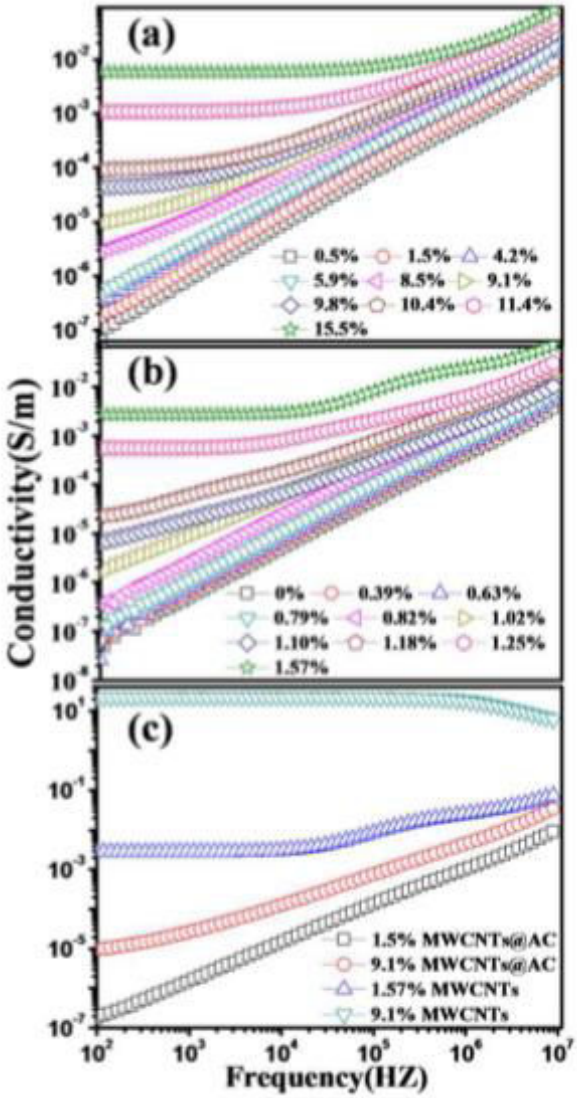

Fig. 2-19 *Frequency dependence of the conductivity of (a) CNTs@AC/PVDF nanocomposites and (b) Pristine CNTs/PVDF nanocomposites at different fillers volume contents. (c) Conductivity comparison between CNTs@AC/PVDF nanocomposites and pristine CNTs/PVDF nanocomposites [65].*

Wang et al. synthesized the poly(vinyl alcohol) coated rGO hybrids using solution-cast method [70]. The results demonstrated that the percolation threshold of PVDF nanocomposites was increased from 0.61 vol. % to 2.24 vol. % after the rGO nanosheets were wrapped with a PVA insulating layer. As shown in Fig. 2-20, Xu and co-workers fabricated a novel type of graphene nanosheets hybrids using a two-step process. including the decoration of an epoxy functionalized ionic liquid (IL) on the surface of thermally reduced graphene oxide (TrGO) through π-π interaction,

followed by the in-situ polymerization of IL [102]. The percolation threshold was increased from 0.41 vol. % to 0.63 vol. % after the coating process. When the loading of nanofillers approached the percolation threshold, the dielectric loss at 10^2 Hz was about 0.57 times that of unmodified graphene nanosheets filled cyanate ester nanocomposites. Yang et al. prepared the polydopamine-coated rGO (PDA-rGO) and fluoro-polymer functionalized rGO (PF-PDA-rGO) [103]. Among the P(VDF-HFP) nanocomposites with rGO, PDA-rGO, and PF-PDA-rGO, the PF-PDA-RGO hybrids filled nanocomposites exhibited the optimum performance with high dielectric constant and low dielectric loss. Li et al. reported that the dielectric loss of PVDF nanocomposites was suppressed to 0.337 after coating the graphene nanosheets with the PDA layer [104]. Li and co-workers also prepared the similar hybrids by coating the rGO with the poly(vinyl pyrrolidone) (PVP) layer [105]. It was found that the PVP layer played an important role in suppressing the dielectric loss of corresponding PVDF nanocomposites.

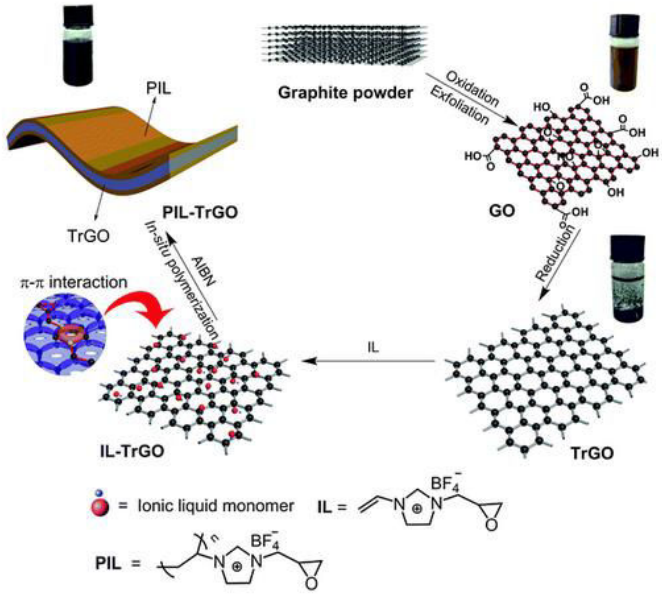

Fig. 2-20 *Schematic illustration for the preparation of PIL–TrGO hybrids [102].*

The conductive PANI polymer was also encapsulated using miniemulsion polymerization of divinylbenzene (DVB) to form a PDVB layer [106]. The obtained polydimethylsiloxane (PDMS) nanocomposites showed the enhanced dielectric breakdown strength, which was ascribed to the excellent insulating property of PDVB

layer.

In summary, the key point of core@shell structured concept employed in the CDPNs is coating the conductive nanofillers with an insulating shell, including the inorganic and organic shells. However, the uniformity and controllability of the encapsulated shells should be emphasized in order to achieve the excellent dielectric performance with an adjustable ability.

2.4.2 Core@Shell Structure for the DDPNs

Great efforts have also been made to employ the core@shell structure in the DDPNs. The types of core@shell structure can be classified into three types according to the purpose. One is coating the ceramic nanofillers with the conductive shells to reduce the number of nanofillers used in the DDPNs. Another one is developing the core@shell structured nanofillers with the polymer shells to improve the dispersibility of nanofillers and optimize the interfacial coupling between the nanofillers and polymer matrices. The last one is fabricating the inorganic shells on the surface of ceramic nanofillers to decrease the dielectric loss or optimizing the electrical field distribution at the interfacial areas.

1) Core@Shell Structured Nanofillers with the Conductive Shells

For the DDPNs, a large amount of nanofillers loading is usually needed to obtain a considerable dielectric constant, which would dramatically deteriorate the flexibility and electrical breakdown strength of the polymer matrices. Therefore, coating the ceramic nanofillers with conductive shells is a promising way. Xie et al. deposited the Ag nanoparticles on the surface of $BaTiO_3$ cores to fabricate the BT@Ag hybrids [107]. The results showed that the decoration of 1 wt. % Ag on BT surface significantly increased the breakdown strength of the BT filled PVDF nanocomposites. The dielectric constant of the PVDF nanocomposites firstly decreased and then increased when the loading of Ag nanoparticles exceeded 1 wt. %. The introduction of Ag decreased the dielectric loss at the low frequency range due to

the coulomb blockade effect and the quantum confinement effect of the ultra-small Ag nanoparticles. The similar result was further reported by Yang et al in the BT@PDA@Ag hybrids filled nanocomposites [108]. Luo et al. also synthesized Ag-deposited BT hybrids and incorporated these hybrids into PVDF matrices. The obtained nanocomposites exhibited a high dielectric constant of about 94.3 at 43.4 vol. % fillers [109]. A novel type of CCTO@Ag hybrid was further developed by Yang et al. [110]. As shown in Fig. 2-21, the dielectric constant of corresponding CCTO@Ag hybrids filled nanocomposites was significantly increased to 103 (10^2 Hz) at 3 vol. % fillers loading. The increase in dielectric constant was ascribed to the Ag interlayer, which enhanced the space charge polarization and Maxwell-Wagner-Sillars effect.

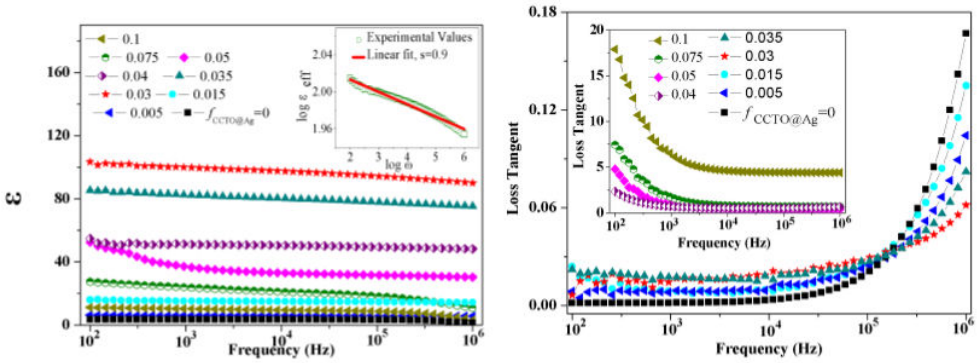

Fig. 2-21 *Dependence of (a) dielectric constant and (b) loss on the frequency of CCTO@Ag filled nanocomposites with different hybrids loadings at room temperature [110].*

Apart from the metallic shells, the conductive carbon shell is another prominent choice. Feng et al. deposited a conductive carbon shell on the surface of $BaTiO_3$ nanoparticles by a chemical vapor deposition (CVD) method [111]. It was found that the BT@C hybrids filled P(VDF-HFP) nanocomposites exhibited a percolative behavior seen from Fig. 2-22. A giant dielectric constant of about 1044 at 30 vol. % fillers loading was obtained. Xu et al. coated the TiO_2 nanoflower with a conductive layer via a hydrothermal reaction [112]. The resultant P(VDF-HFP) nanocomposites also exhibited a similarly percolative behavior.

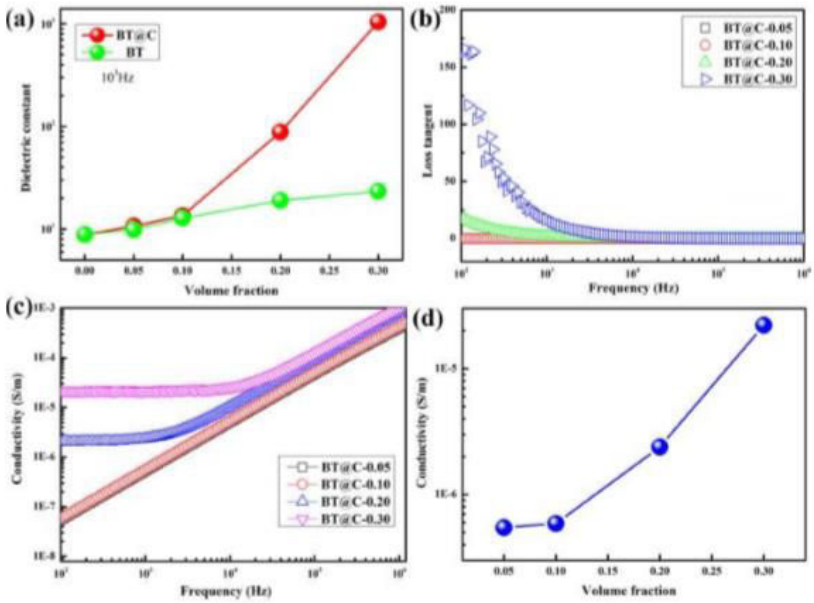

Fig. 2-22 *(a) Dielectric constant of nanocomposites as a function of volume fraction at 10^3 Hz; Dependence of loss (b) and conductivity (c) on the frequency; (d) Conductivity of nanocomposites as a function of volume fraction at 10^3 Hz [111].*

Although a high dielectric constant was obtained at a small of nanofillers loading by converting the DDPNs to percolative CDPNs, the high dielectric loss was usually unavoidable. Therefore, great attention should be paid to this issue to suppress the dielectric loss.

2) Core@Shell Structured Nanofillers with the Polymer Shells

The polymer shell helps to improve the compatibility of nanofillers with host polymers. Thereby, uniform dispersion of nanofillers would minimize the local field distortion at the interface induced by the large dielectric contrast. A series of core@shell structures were prepared via "grafting from" and "grafting to" methods. The "grafting from" method is developed by introducing a sufficient quantity of initiating sites on the surfaces of nanofillers, followed by the controlled/living radical polymerization, such as atom transfer radical polymerization (ATRP) and reversible addition-fragmentation chain transfer (RAFT) polymerization. Marks et al. synthesized the $BaTiO_3$@PP and TiO_2@PP nanocomposites via in-situ metallocene polymerization as shown in Fig. 2-23 [113]. The obtained PP nanocomposites had a

higher dielectric constant and breakdown strength compared with pure PP. The high breakdown strength was attributed to the Al_2O_3 layer during the polymerization procedure. Huang and co-workers fabricated the core@shell structured $BaTiO_3$@PMMA and $BaTiO_3$@PS hybrids via in-situ ATRP and RAFT methods, respectively [114, 115]. As displayed in Fig. 2-24, the thickness of PS shell could be well controlled from 7 nm to 12 nm. The dielectric constant (10^3 Hz) of the nanocomposites increased from 2.8 for the pure PS to 24 for the hybrids filled PS nanocomposites, while the dielectric loss had nearly the same value as the pure PS. Besides, the weak frequency dependence of dielectric constant was observed, which might be attributed to the absence of interfacial polarization. The PS matrice was robustly bonded to the surface of $BaTiO_3$ nanoparticles, thus the migration and accumulation of charge carriers in the nanocomposites became difficult.

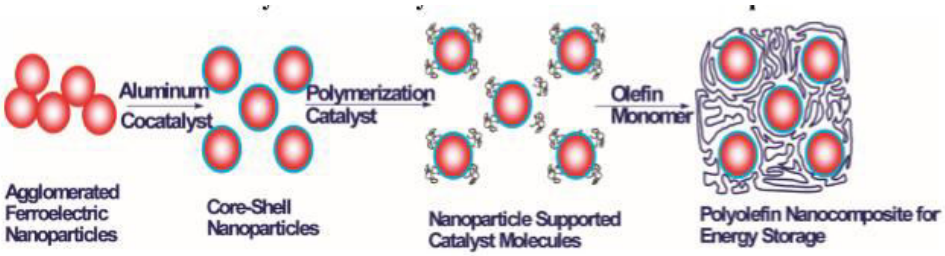

Fig. 2-23 *Synthesis of polyolefin-metal oxide nanocomposites via the in-situ metallocene polymerization [116].*

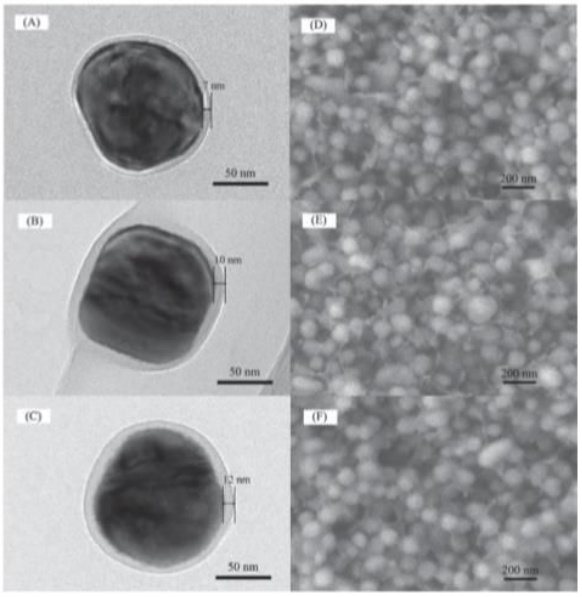

Fig. 2-24 *TEM images of core@shell structured $BaTiO_3$@PS nanoparticles and*

corresponding SEM images of PS nanocomposites [115].

The "grafting to" method is usually implemented by grafting the polymer chains onto the surface of nanofillers via a reaction between the polymer end-groups and the functional groups on the surfaces of nanofillers. Click chemistry is a main method for the linking reaction between organic molecular chains and the surfaces of nanofillers because of its high efficiency, solvent insensitivity, and moderate reaction conditions. Great efforts have been made to fabricate the core@shell structured nanohybrids via click chemistry. Among various click chemistry methods, the thiol-ene click reaction is not only highly efficient and free of byproducts but also does not require transition metals catalysis. Huang et al. prepared $BaTiO_3$@PS and $BaTiO_3$@PMMA hybrids through the combination of RAFT polymerization and thiol-ene click reaction [117]. The thiol-terminated polymer chains were prepared via RAFT polymerization and they were subsequently reacted with vinyl-functionalized $BaTiO_3$ nanoparticles by the thiol-ene click reaction to fabricate the hybrids (Fig. 2-25). It was found that the dielectric constant of all the hybrids filled nanocomposites was significantly enhanced when compared with the corresponding pure polymer, and the dielectric loss was still maintained in a relatively low level.

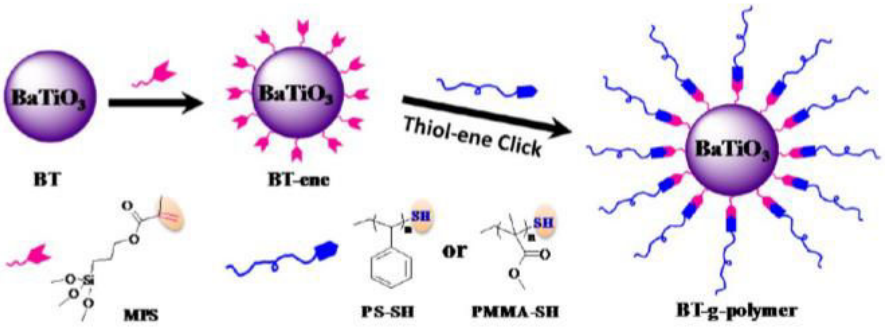

Fig. 2-25 *Preparation of core@shell structure $BaTiO_3$@polymer hybrids [117].*

Apart from the complex polymer chains prepared from the "grafting to" and "grafting from" methods, the PDA polymer shell was widely used to fabricate the core@shell structured hybrids by a simple polymerization. For example, Song et al. reported that the surface modification of $BaTiO_3$ nanoparticles with PDA shells improved the compatibility between $BaTiO_3$ and polymer matrices [83]. The

core@shell structured 1D nanowires with polymer shells were also reported by the "grafting to" and "grafting from" methods. For instance, Huang et al. coated the $Ba_{0.7}Sr_{0.3}TiO_3$ (BST) nanowires with a poly(pentaflurophenyl acrylates) (PPFPA) polymer shell via in-situ RAFT polymerization [118]. The resultant suggested that the grafting of PPFPA shell facilitated the dispersion of BST nanowires in the P(VDF-HFP) matrices and the leakage currents of hybrids filled nanocomposites was suppressed due to the decrease in the mobility of charge carriers. A series of nanowires were coated with PDA polymer shell in the work of Huang et al [119] and it was found that the obtained PDA shell improved the dispersion of nanowires hybrids in the P(VDF-HFP) matrices.

The polymer shell on the surface of core@shell structured nanofillers not only prevents the aggregation of nanofillers in polymer matrices but also suppresses the leakage current. Besides, the controllability of polymerization helps to optimize the microstructure and electrical properties of nanocomposites by engineering the interface between the nanofillers and the polymer matrices.

3) Core@Shell Structured Nanofillers with the Insulating Inorganic Shells

The incorporation of high dielectric constant nanofillers into the polymer matrices can drastically decrease the electrical breakdown strength due to the electric field distortion at the interface caused by the large dielectric constant and conductivity contrast between the nanofillers and matrices. For this reason, an inorganic interfacial buffer layer should be designed by rationally selecting a medium dielectric constant between the nanofillers and matrices to form the core@shell structure, which favors balancing the dielectric constant and mitigation of the electric field concentration and current density. An ideal core@shell structure with a gradual dielectric constant from center to the shell is presented in Fig. 2-26. As a result, the dielectric constant and conductivity gradient across the interface between the inorganic phase and polymer phase can be decreased.

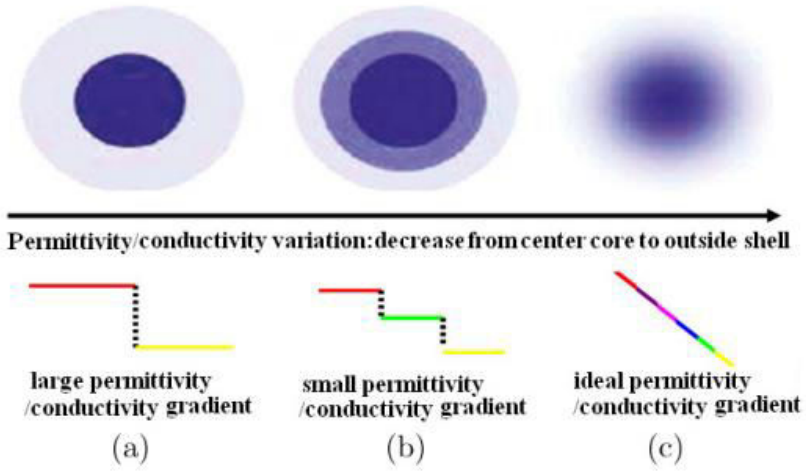

Fig. 2-26 *(a) A simple core@shell structure, (b) one core@multi shells structure, and (c) an ideal structure of inorganic nanoparticles [120].*

Coating the $BaTiO_3$ nanofillers with a TiO_2 shell to decrease the dielectric constant between $BaTiO_3$ and PVDF is a promising strategy. Shen et al. fabricated $BaTiO_3$@TiO_2 nanofibers by embedding the $BaTiO_3$ nanoparticles in TiO_2 fibers with the aid of a modified electro-spinning process [121, 122]. It was found that the simultaneous enhancement of electrical breakdown strength and electrical displacement was achieved. The increased electrical breakdown strength was attributed to the presence of a buffer layer of TiO_2, whose dielectric constant was located in the gap between $BaTiO_3$ and PVDF matrices. The enhanced electrical displacement was ascribed to the interfacial effect inside the integrated nanofibers. As shown in Fig. 2-27, Hu et al. created a crystallized TiO_2 shell onto the $BaTiO_3$ nanofibers by coaxial electro-spinning and heat treatment process [123]. The dielectric constant and electrical displacement of corresponding PVDF nanocomposites were enhanced due to the additional polarization induced by the charges shifting in the interfacial zone between the inside $BaTiO_3$ and the outside TiO_2. In addition, the breakdown strength of the nanocomposite was maintained because the charges shifting were limited in the interfacial zone and cannot form a percolation path in the matrices. Subsequently, Hu and co-workers used the solution method to fabricate the similar $BaTiO_3$@TiO_2 nanoparticles [95]. The results showed that the thin TiO_2 layer favored the generation of high polarization to increase

dielectric constant while the thick TiO_2 layer helped to homogenize the electrical field to maintain breakdown strength.

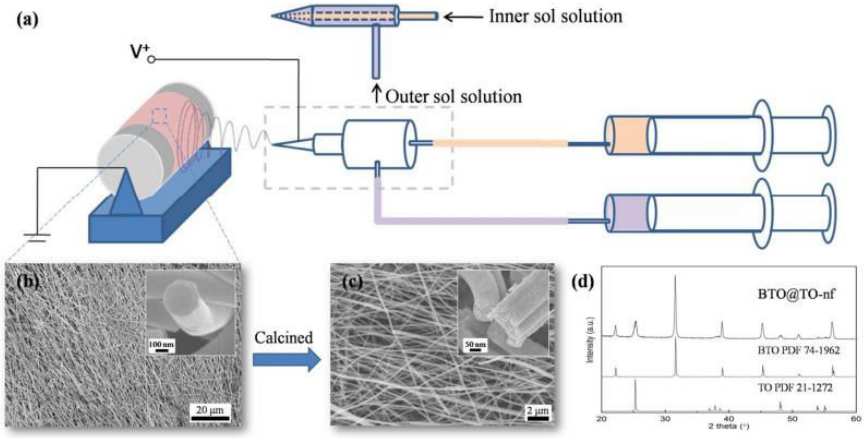

Fig. 2-27 *(a) Schematic drawing of the coaxial electrospinning with a coaxial needle. (b) SEM image of the as-electrospun sheet composed of nanofibers, the inset shows an enlarged view of an end face of a nanofiber. (c) SEM image of calcined $BaTiO_3$@TiO_2 nanofibers, the inset shows the view of crystalline grains at the fracture surface of nanofibers. (d) XRD pattern of the calcined $BaTiO_3$@TiO_2 nanofiber [123].*

Using of SiO_2 and Al_2O_3 shells to decrease the dielectric loss and improve the dielectric breakdown strength is another popular strategy to enhance the dielectric performance of DDPNs. For example, Tang et al. synthesized a SiO_2 shell on the surface of CCTO nanowires [124]. As shown in Fig. 2-28, the dielectric loss of nanocomposites with core@shell structured CCTO@SiO_2 nanowires was greatly suppressed compared with the uncoated CCTO nanowires filled PVDF nanocomposites. He et al. synthesized a uniform amorphous Al_2O_3 layer on the surface of $BaTiO_3$ nanoparticles through an effective, facile and low-cost heterogeneous nucleation method [125]. As shown in Fig. 2-29, the dielectric loss was also significantly suppressed. The excellent insulating properties of SiO_2 and Al_2O_3 shells makes it easy to modify the electrical field distribution at the interface and suppress the dielectric loss yet maintaining high dielectric constant.

Apart from the simple core@shell structure, the core@multi-shells structure was also developed to fabricate the novel hybrids. As shown in Fig. 2-30, Pan et al. synthesized core@double-shells structured $BaTiO_3$@TiO_2@Al_2O_3 nanofibers via a

facile improved three layers coaxial electro-spinning technique [126]. As compared with the nanocomposites loaded with $BaTiO_3$ and $BaTiO_3@TiO_2$ nanofibers, the nanocomposites filled with $BaTiO_3@TiO_2@Al_2O_3$ nanofibers exhibited much decreased dielectric loss, enhanced breakdown strength, and suppressed leakage current densities.

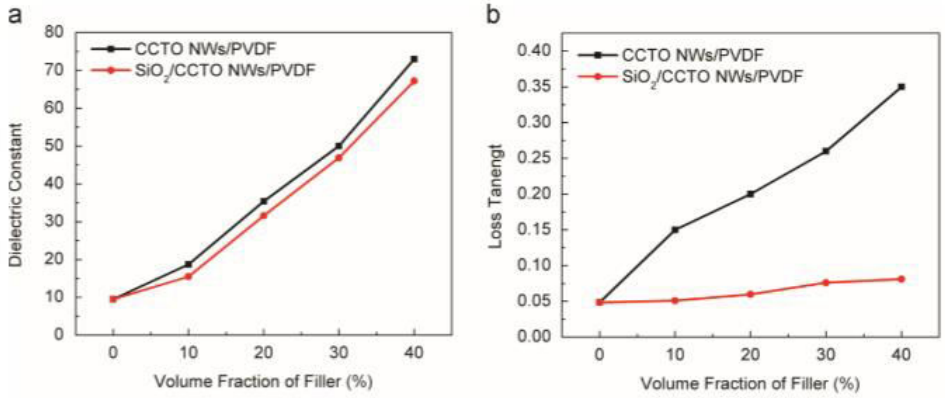

Fig. 2-28 *(a) Comparison of dielectric constant (at 10^3 Hz) (b) dielectric loss of nanocomposites with different nanofillers: CCTO and CCTO@SiO_2 nanowires [124].*

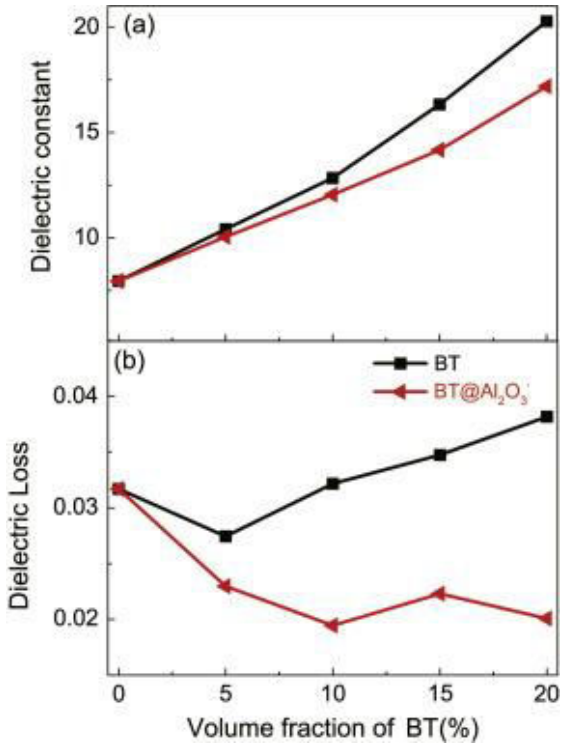

Fig. 2-29 *(a) Dielectric constant and (b) dielectric loss of the nanocomposites as a function the volume fraction of nanofillers at 10^3 Hz [125].*

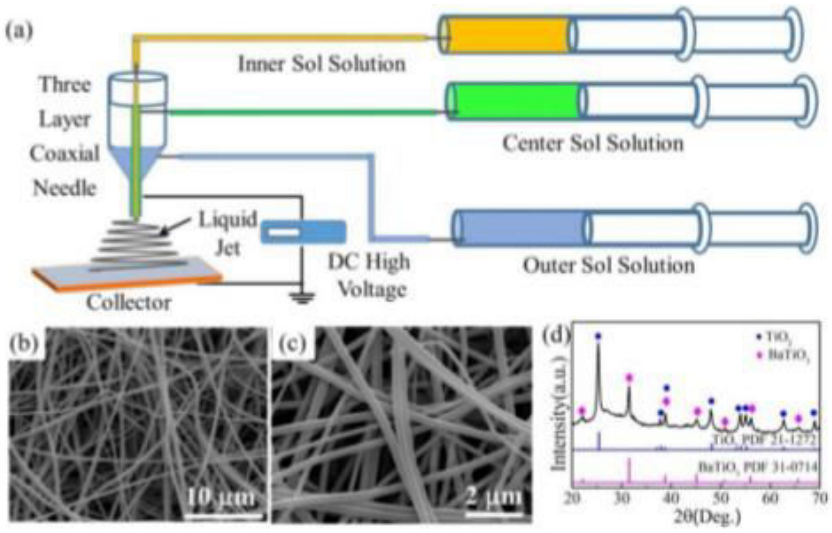

Fig. 2-30 *(a) Schematic of three layers coaxially electro-spinning the core@double-shells structured $BaTiO_3$@TiO_2@Al_2O_3 nanofibers; SEM images (b) of as-spun composed of nanofibers and (c) heat-treated $BaTiO_3$@TiO_2@Al_2O_3 nanofibers; (d) XRD pattern of heat-treated $BaTiO_3$@TiO_2@Al_2O_3 nanofibers [126].*

The core@shell structured strategy provides a powerful and versatile tool for designing and preparing the nanofillers for the application of dielectric polymer nanocomposites. It provides opportunities to control and optimize the microstructure and electrical properties of nanofillers. More importantly, the dielectric performance of nanocomposites can be further optimized by engineering the interface between the nanofillers and the polymer matrices with the help of core@shell structure.

2.5 Orientation and Alignment of Nanofillers on Dielectric Properties of DPNs

Apart from the shape, size, composition, and structure, the orientation and alignment of nanofillers in the polymer matrices is another important factor in determining the dielectric performance of DPNs. For the CDPNs, the alignment of 1D and 2D conductive nanofillers in the direction of the applied electrical field could further decrease the percolation threshold of percolative CDPNs. The alignment of conductive nanofillers could be realized using mechanical stretching, extrusion, magnetic field, and electrical field. For example, a remarkably low percolation value

of 0.12 vol. % was achieved in the rGO filled epoxy nanocomposites by the self-alignment of rGO nanosheets [127].

The alignment of ceramic nanofillers can affect the dielectric and electrical breakdown properties of DDPNs greatly [128-133]. Tomer et al. used the dielectrophoretic assembly method to obtain aligned $BaTiO_3$ nanoparticles in a silicone elastomer thermoset polymer. The results demonstrated that the dielectric constant in the applied electric field direction was much larger than a random one. However, the breakdown strength decreased when compared to the nanocomposites with random orientation [134]. Tang et al. aligned the PZT nanowires in the PVDF matrices through a thermally uniaxial stretching strategy [135]. As shown in Fig. 2-31, the results suggested that the dielectric constants of 3-direction aligned PZT nanowires samples were much higher than that of random and 1-direction aligned PZT nanowires samples at the same volume fraction. The dielectric constant of 3-direction aligned PZT nanowires samples was 35.7% higher than that of the samples with random PZT nanowires at 30 vol. % fillers loading. Fillery et al fabricated the organically modified montmorillonite (MMT) filled polyvinyl butyral (PVB) nanocomposites and the alignment of MMT was realized by increasing the loading of MMT nanofillers as shown in Fig. 2-32 [136]. The results showed that the electrical breakdown strength of nanocomposites increased 2.5 times relative to the unfilled polymer at 25 vol. % loading of MMT.

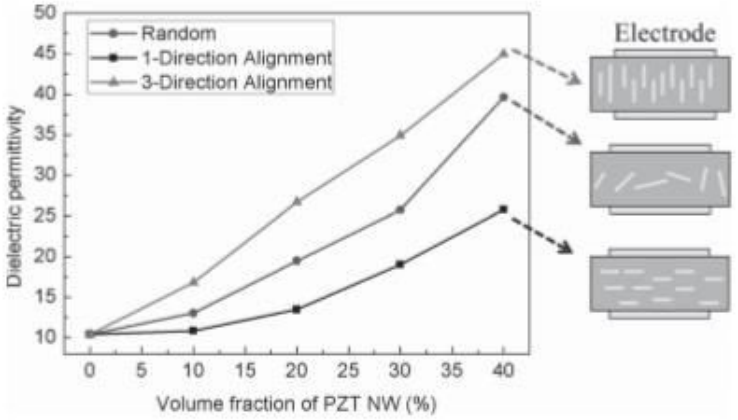

Fig. 2-31 *Comparison of dielectric constant (10^3 Hz) of nanocomposites under*

different orientation (Random, 1-Direction Alignment, and 3-Direction Alignment) as a function of PZT nanowires volume fraction [135].

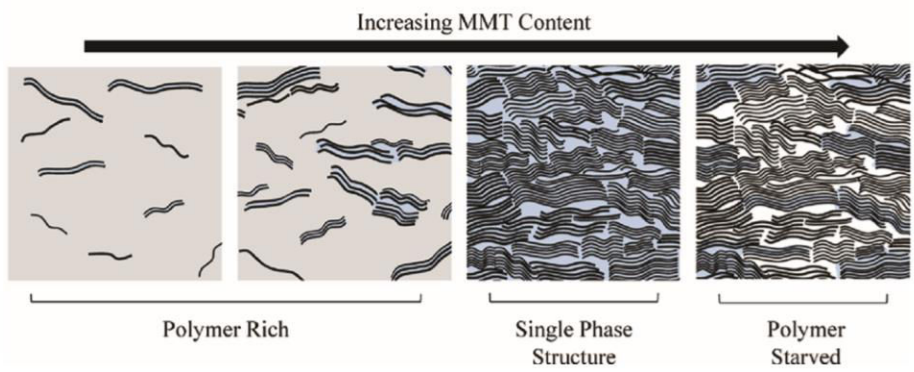

Fig. 2-32 *Schematic showing the alignment process of MMT in PVB with increasing MMT loading [136].*

2.6 Concluding Remarks

This chapter provides a thorough review of the influences of nanofillers on the dielectric performance of dielectric polymer nanocomposites. Although significant progress has been achieved in the development of novel nanofillers in dielectric polymer nanocomposites, there still exist some challenging issues that hinder the improvement of nanofillers for the dielectric polymer nanocomposites field.

Firstly, the dielectric loss of percolative nanocomposites should be further decreased to satisfy the requirement of the high electrical field. Besides, the sensitivity of the dielectric constant in the vicinity of the percolation threshold should be alleviated to obtain the dielectric polymer nanocomposites with a stable dielectric performance. For the DDPNs, the ceramic fillers loading should be further reduced to maintain the flexibility of the nanocomposites.

Secondly, more attention should be paid to the 1D and 2D structural nanofillers. Especially for the carbon family nanomaterials, the dispersion of CNTs or graphene nanosheets in the polymer matrices should be further improved. Thereby, the appropriate surface modification is needed. For the DDPNs, the similar dispersion issue for the 1D and 2D ceramic nanofillers should also be emphasized. Besides, the aspect ratio of these non-spherical nanofillers should be elaborately considered and

designed to satisfy different working environment.

Thirdly, a more complex structure of nanofillers with integrating two or more components should be carefully designed. The core@multi-shells structure provides a promising concept for integrating these multi-functional components. However, the dispersion of nanohybrids, interfacial coupling, multi-interfacial polarizations, and electrical breakdown strength factors should be considered during selecting each component for the multi-shells.

Fourthly, the orientation and alignment of nanofillers should be realized in a much more easy way. The in-situ alignment of nanofillers during the fabrication process is a prominent candidate for the fabrication of anisotropic dielectric nanocomposites.

In this thesis, we will solve these challenging issues by designing different nanofillers for the application of dielectric nanocomposites.

Chapter III

Ternary PVDF Nanocomposites with BNNSs and CNTs

3.1 Introduction

The giant dielectric constant of percolative nanocomposites could be achieved by adding conductive fillers into the polymer matrix [137]. These percolative nanocomposites always undergo a significant increase of dielectric constant in the vicinity of a critical concentration based on the percolation theory. Numerous conductive fillers, especially for CNTs with large aspect ratio, have been filled into the polymer matrix to increase the dielectric constant of polymer nanocomposites [55, 60]. Due to its high aspect ratio, CNTs can provide nanocomposites with a much lower percolation threshold than other conductive fillers. However, CNTs are difficult to be well dispersed in polymer matrix due to its tight van der Waals attraction. Besides, the dielectric properties of this kind of nanocomposite are extremely sensitive to the composition variation in the neighborhood of the percolation threshold, which is not desirable for practical applications. To overcome this bottleneck, a great deal of effort has been adopted to improve the overall dispersion of CNTs in the polymer matrix, for example, the chemical modification of CNTs. However, this method may disrupt the structure of CNTs and result in a distinct decay to their electronic properties. Therefore, it is highly desirable to disperse pristine CNTs in polymer matrix homogeneously while increasing their interactions in order to attain a high dielectric constant.

Recently, the ternary nanocomposites containing conductive filler and second filler, such as ceramic or polymer filler, have been proposed [138, 139]. As the percolative composites with high dielectric constant are obtained, the second filler could be utilized to tune the dielectric properties of nanocomposites. Also, it has been

demonstrated that the filler with microscale dimensions can significantly benefit the dispersion of nanofiller in the nano/micro-reinforced system [140]. For example, $BaTiO_3$/CNTs/PVDF ternary nanocomposites with a dielectric constant of 151 at 10^2 Hz were reported [138]. With the incorporation of a certain amount of BT, the number of conductive paths increased due to the optimization of the conductive network. However, the dielectric loss and ac conductivity also increased after a critical amount of BT due to the ferroelectric nature of BT. Recently, boron nitride nanosheets (BNNSs) with a wide bandgap (ca. 6eV), a layered structure similar to graphene, has elicited widespread attention due to its insulator nature [141-148]. Wang and co-workers reported the dielectric properties of CNTs/BNNSs/PVDF nanocomposites [149]. However, there is a little systematic investigation of the role of BNNSs in the dielectric properties of percolative nanocomposites. Therefore, it is imperative to explore the influence of BNNSs on the conductive network and dielectric properties of percolative nanocomposites before and after the percolation.

In this chapter, CNTs with a length of 1-2 μm were adopted as conductive filler and BNNSs with a lateral size of 0.3-2 μm were chosen as an insulating filler. PVDF was used as a host polymer due to its superior ferroelectric nature. The ternary nanocomposites of BNNSs/CNTs/PVDF are fabricated via a combination of solution casting and extrusion injection processes. The effects of BNNSs on the electrical conductivity, dielectric behavior, and microstructure changes of CNTs/PVDF binary nanocomposites are systematically investigated.

3.2 Experimental

For the fabrication of CNTs/PVDF binary nanocomposites, first, the appropriate amount of CNTs was dispersed into N, N-dimethylformamide (DMF) solvent with ultrasonic treatment for 2 h. Then, PVDF powders were subsequently added into the suspension of CNTs and the mixture was magnetically stirred at 70 ºC for 2 h. The temperature of the CNTs/PVDF solution was increased up to 100 ºC and maintained for 1 h to evaporate most of the solvent. After that, the mixture was further dried in a

vacuum oven at 80 °C for 12 h to remove the residual solvent. Second, the as-prepared CNTs/PVDF mixture was melt-blended under Ar atmosphere by a two-screw micro-extruder with a speed of 90 rpm at 220 °C for 30 min. Finally, the slabs with a thickness of 1.5 mm were obtained by injection molding of the mixed nanocomposites. The final obtained concentration of CNTs in the CNTs/PVDF nanocomposites varied from 0 to 10 vol. %. The BNNSs/CNTs/ PVDF ternary systems were fabricated by the same procedure. For dielectric measurements, electrodes were painted with silver paste on both sides of the samples and then the dielectric properties were characterized by an impedance analyzer (Solatron 1260) at room temperature.

3.3 Results and Discussions

Fig. 3-1 shows the dependence of conductivity and dielectric constant of CNTs/PVDF nanocomposites on f_{CNTs}. As seen in Fig. 3-1a, the conductivity at high frequency (10^6 Hz) increases slightly with f_{CNTs} and exhibits relatively higher values than those at low frequency (1 Hz and 10^2 Hz) due to a significant dissipative effect. However, the conductivity at low frequency increases sharply when f_{CNTs} is approaching f_c. According to the percolation theory (Eq. 2-4), the best fit of the conductivity data at 10^3 Hz to the log-log plot of the power law gives f_c=7.16 ± 0.01 vol. %, s=1.88 ± 0.03 (inset in Fig. 3-1a). The exponent s is larger than the universal one (s=0.8-1) [61]. This discordance could also be found in other percolative composites and may derive from the wide inter-particle distance distribution, as proposed by Balberg [150]. As shown in Fig. 3-1b, besides the conductivity, the dielectric constant of CNTs/PVDF systems also increases significantly as f_{CNTs} approaches f_c. The variation constant of CNTs/PVDF systems can also show a good agreement with the typical equation Eq. 2-5. The result of best linear fitting for dielectric constant at 10^3 Hz is shown in the inset of Fig. 3-1b. The calculated f_c is also 7.16 ± 0.01 vol. %, which is in accordance with the value obtained from the fitting of conductivity. Besides, the critical exponent q (0.86 ± 0.01) agrees with the

universal one (0.8-1). The obtained f_c (7.16 vol. %) is lower than that of the PVDF nanocomposites filled by CNTs with a length of 5-15 μm (10.4 vol. %). Normally, the nanocomposite filled by CNTs with a low aspect ratio leads to a higher f_c compared with the CNTs with a high aspect ratio. The aspect ratio of CNTs used in this work is lower than that of Yuan's work. Besides, the constant of CNTs/PVDF systems with 8 vol. % CNTs at 10^3 Hz is 1325, which is higher than the reported result at the same f_{CNTs}. Both the lower f_c and higher constant all confirm that CNTs disperse well in PVDF matrix with the aid of solution casting and extrusion injection processing, which is helpful for the formation of the distinct conductive network. The dielectric loss of CNTs/PVDF systems also increases sharply from 0.05 for CNTs/PVDF with 6 vol. % CNTs to 0.53 for CNTs/PVDF with 8 vol. % CNTs.

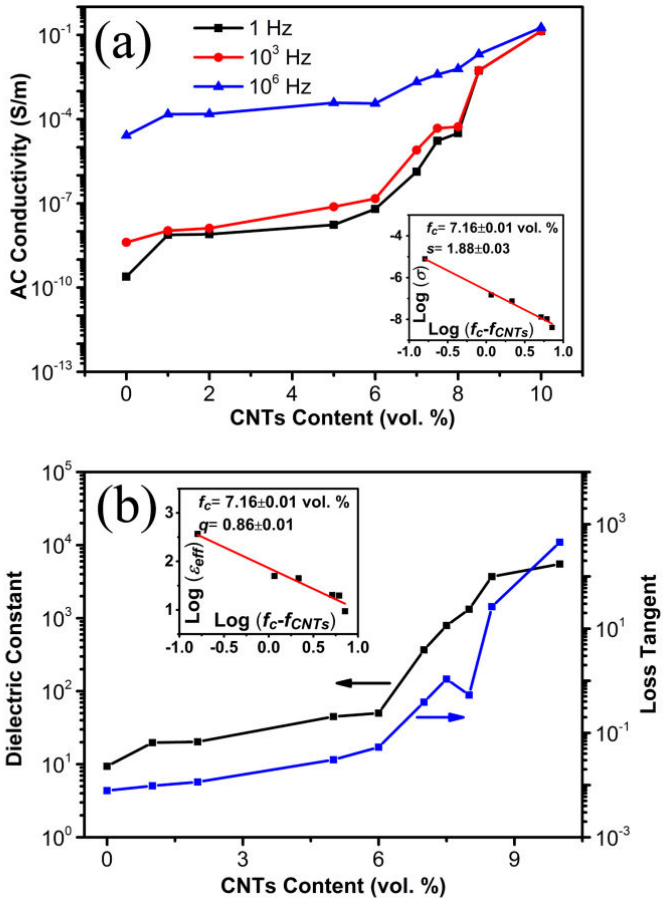

Fig. 3-1 *Dependence of ac conductivity (a) and dielectric constant (b) at 10^3 Hz of CNTs/PVDF nanocomposites on f_{CNTs}. The insets in (a) and (b) show the best fits of the ac conductivity to Eq. 2-4 and dielectric constant to Eq. 2-5, respectively.*

Due to the huge differences of conductive network structure for percolative nanocomposites before and after the percolation effect, two kinds of CNTs/PVDF binary systems with various f_{CNTs} were adopted as the matrix. Since the dielectric properties change significantly in the vicinity of the f_c, the f_{CNTs} are maintained as constant at 6 vol. % ($f_{CNTs}<f_c$) and 8 vol. % ($f_{CNTs}>f_c$), and their relevant CNTs/PVDF binary nanocomposites are denoted as matrix A and matrix B, respectively. Therefore, two series of BNNSs/CNTs/PVDF ternary nanocomposites with various f_{BNNSs} could be marked as BNNSs-x/A and BNNSs-x/B, where x represents f_{BNNSs}. The incorporation of CNTs increases the dielectric constant by the percolation effect. Meanwhile, the addition of hexagonal BNNSs into the CNTs/PVDF matrix can greatly optimize the conductive network and finally affect the dielectric properties.

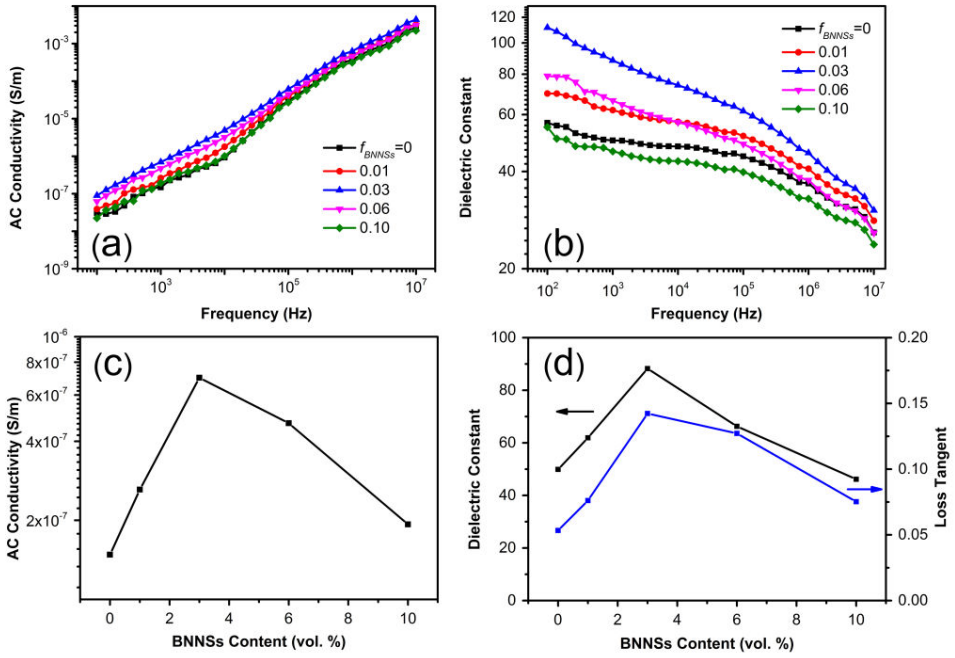

Fig. 3-2 *Frequency dependence of ac conductivity (a) and dielectric constant (b) of BNNSs/CNTs-6 vol. %/PVDF ternary nanocomposites and dependence of ac conductivity (c) and dielectric constant (d) at 10^3 Hz of BNNSs/CNTs-6 vol. %/PVDF on f_{BNNSs}.*

From Fig. 3-2a, we can see that the conductivity of BNNSs/A ternary systems shows a strong dependence of frequency at the whole frequency range, which demonstrates the insulated nature of BNNSs/A. Meanwhile, as seen in Fig. 3-2c, the

conductivity at 10^3 Hz increases slightly with f_{BNNSs} when f_{BNNSs} is lower than 3 vol. % and then decreases with the further increasing f_{BNNSs}. The order of magnitude of the conductivity of BNNSs-3 vol. %/A is ca. 10^{-7}, which also confirms that the conductive network of BNNSs/A ternary nanocomposites has not been formed yet. From Fig. 3-2b, we can observe that the frequency dependence of constant for BNNSs/A at low frequency range (10^2-10^5 Hz) becomes more evident with increasing of f_{BNNSs} to 3 vol. % followed by almost independent of the frequency of constant with further increasing f_{BNNSs} to 10 vol. %. The remarkable frequency dependence of constant can be attributed to the transition of insulator nature to conductor nature for BNNSs/A nanocomposites, which can also be observed in other ternary systems. The relaxation of constant clearly demonstrates that the high constant at low frequency is derived from the Maxwell-Wagner (MW) relaxation, which is originated from the accumulation of injected charges at the interface between two dielectric materials with different relaxation times. In our case, the relaxation times of BNNSs and PVDF are several orders of magnitude longer than that of CNTs. Therefore, charges are tremendously blocked at the interface of CNTs/BNNSs and CNTs/PVDF, accordingly enhancing the constant significantly. As for the negligible difference of relaxation time between BNNSs and PVDF, the charges blocked at the interface of BNNSs/PVDF could be ignored due to the similar insulating nature. Furthermore, as reported by Wang, the relaxation of constant for BNNSs/P(VDF-CTFE) composites is hardly detected and the constant declines monotonically with the increase of f_{BNNSs}. As summarized in Fig. 3-2d, the constant and loss at 10^3 Hz of BNNSs/A show a similar tendency with the increase of f_{BNNSs}. The constant increases significantly from 49 for matrix A to 88 for BNNSs-3 vol. %/A ternary nanocomposites followed by a decrease to 46 for BNNSs-10 vol. %/A. The enhancement of constant can be attributed to the following aspects. Firstly, as confirmed by other reports, the fillers with micrometer scale can benefit the dispersion of nanofillers in the polymer matrix. In our case, the CNTs can be detached from the bundles by BNNSs with micrometer scale and therefore disperse well in the polymer matrix, as shown in Fig. 3-4b. So, the total

interface areas of CNTs/PVDF available for the accumulation of charges augment obviously, which leads to the increment of total blocked charges. Secondly, as discussed above, the addition of BNNSs also brings abundant sites for the accumulation of charges at the interface of CNTs/BNNSs. Lastly, the BNNSs can also optimize the conductive network of CNTs/PVDF. With the addition of BNNSs, the f_{PVDF} in the whole system declines, which would lead to the diminution of the thickness of PVDF between two adjacent CNTs. According to the equation of the parallel plate capacitor,

$$C = \frac{\varepsilon_0 \varepsilon_r A}{d} \tag{3-1}$$

where A is the surface areas of the parallel plate and d is the distance between two parallel plates, the capacitance (C) will undoubtedly increase. However, with the further addition of BNNSs, the constant decreases gradually, which could be ascribed to the destruction of the conductive network. The BNNSs prevent the contact of loaded CNTs and thus the d increases sharply, as indicated by the yellow cycle in Fig. 3-4c, which leads to the decrease in capacitance. More importantly, the dielectric loss for BNNSs-3 vol. %/A is only 0.14. These explanations can be illustrated by variations of microstructures in the three-phase composites as presented in Fig. 3-4.

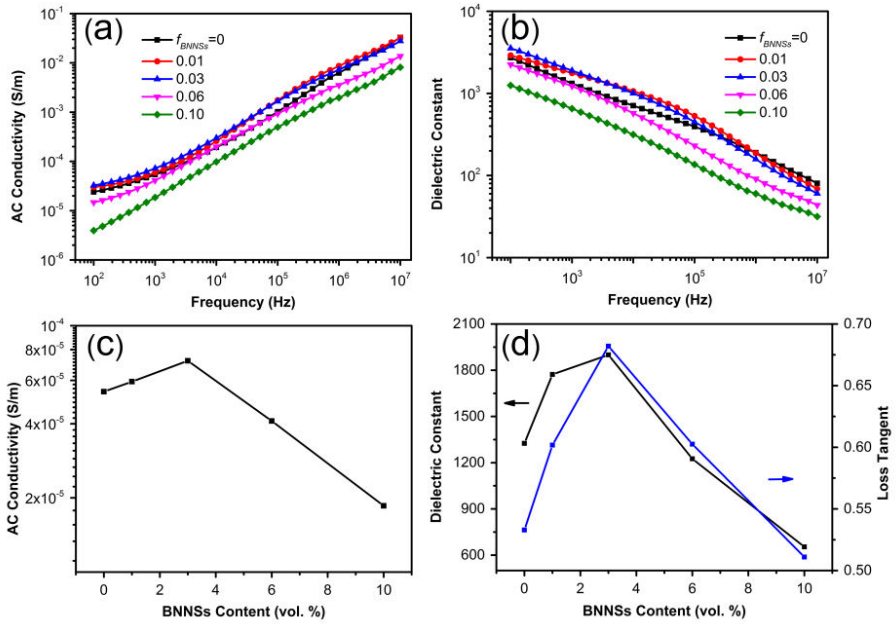

Fig. 3-3 *Frequency dependence of ac conductivity (a) and dielectric constant (b) of*

BNNSs/CNTs-8 vol. %/PVDF ternary nanocomposites and dependence of ac conductivity (c) and dielectric constant (d) at 10^3 Hz of BNNSs/CNTs-8 vol. %/PVDF on f_{BNNSs}.

Fig. 3-3a presents the frequency dependence of ac conductivity of BNNSs/B ternary nanocomposites with various f_{BNNSs}. Compared with the conductivity of BNNSs/A shown in Fig. 3-2a, the conductivity of BNNSs/B with f_{BNNSs} below 10 vol. % is nearly independent of frequency at low frequency range (10^2-10^3 Hz), which reflects the conductor nature of BNNSs/B. As for the BNNSs-10 vol. %/B, the conductivity shows a strong frequency dependence due to insulating nature. Furthermore, the conductivity of BNNSs/B at 10^3 Hz raises with the increase of f_{BNNSs} to 3 vol. % followed by declining sharply with the further addition of BNNSs. For the part of constant, as displayed in Fig. 3-3b, the constant of BNNSs/B with various f_{BNNSs} presents intense frequency dependence, which resulted from the conductor nature of BNNSs/B. Fig. 3-3d reveals that the constant at 10^3 Hz increases significantly from 1325 for matrix B to 1899 for BNNSs-3 vol. %/B followed by decreasing to 653 for BNNSs-10 vol. %/B. The variation of constant can also be illustrated by the aspects discussed above. As for the loss part, it also shows the same tendency. But one thing to stress is that the loss of BNNSs-10 vol. %/B is only 0.68, which is lower than other percolative systems.

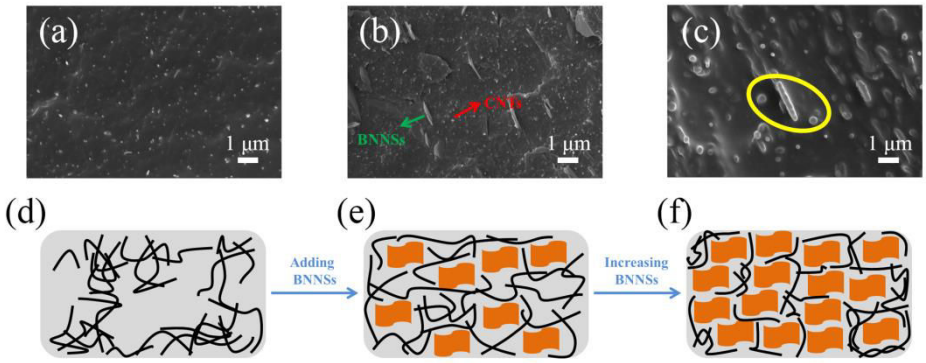

Fig. 3-4 *SEM images of the freeze-fractured and schematic illustration of the microstructure BNNSs/CNTs/PVDF ternary nanocomposites with a fixed CNTs content (f_{CNTs}=6 vol. %) at (a), (d) f_{BNNSs}=0 vol. %, (b), (e) f_{BNNSs}=3 vol. %, and (c), (f)*

f_{BNNSs}=10 vol. %, respectively, in which the black lines stand for CNTs and the orange sheets are BNNSs.

Fig. 3-4 displays SEM images of the freeze-fractured BNNSs/CNTs/PVDF ternary nanocomposites with various f_{BNNSs} and schemes of microstructure evolution with increasing f_{BNNSs} corresponding to the SEM images. As shown in Fig. 3-4a, most of the CNTs are well dispersed in the PVDF matrix. However, it is inevitable that part of the CNTs aggregates together due to the van der Waals force, even after the combination of solution casting and melting blending fabrication process. Then, some CNTs are detached when f_{BNNSs} increases up to 3 vol. %, which helps in the formation of the more effective conductive network. This phenomenon can also be observed in other nano/micro-reinforced systems. However, with the further addition of BNNSs, the prevention effect of BNNSs for the contact of CNTs (indicated by the yellow circle in Fig. 3-4c) and insulator nature of BNNSs will become the dominant role to hinder the conduction of adjacent CNTs, which contributes to the decline of constant.

3.4 Conclusions

In this chapter, the integration of solution and melting blending procedures leads to a lower percolation threshold of CNTs/PVDF nanocomposites. The incorporation of BNNSs into the CNTs/PVDF matrix improves the dispersion of CNTs and optimizes the conductive network, which contributes to the enhanced dielectric constant. The direct connection between CNTs could be interrupted with further increasing the content of BNNS. Due to the microstructure evolution of the nanocomposites, dielectric properties of polymer nanocomposites could be easily modified by employing the ternary system. Therefore, the BNNSs/CNTs/PVDF ternary nanocomposites have great application potential in the embedded capacitors fields due to their adjustable dielectric properties.

Chapter IV

Core@Shell Structured CNTs@AC/PVDF Nanocomposites

4.1 Introduction

With the development of flexible electronic devices and electrical power systems, polymer materials with high dielectric constant have recently aroused considerable interests in the past decades due to their inherent advantages in mechanical flexibility, processing ease, and low cost [151-153]. Nevertheless, most of the currently commercialized polymers cannot meet the requirements of embedded capacitors due to their intrinsic low dielectric constant values. Therefore, the key issue is to substantially raise the dielectric constant of polymer materials, meanwhile retaining their other excellent properties, such as flexibility, low dielectric loss, and high breakdown strength. Many efforts have been made to improve the dielectric constant of polymer materials. A straightforward way to increase the dielectric constant of polymer materials is to homogeneously disperse ceramic nano-particles with high dielectric constant into the polymer matrix [154-156]. However, it has to introduce plenty of ceramic nano-particles into the polymer matrix to afford a considerable dielectric constant. The high loading of inorganic filler would dramatically deteriorate the flexibility and electrical breakdown strength of the polymer matrix, which hinders their development in the dielectric materials field.

Another promising strategy is to prepare percolative polymer nanocomposites by filling conductive nanoparticles, such as metal particles [157], carbon black [48, 158, 159], CNTs and graphene [103, 160, 161] into the polymer matrix. Among these conductive fillers, CNTs have attracted extensive attention in the dielectric materials field because of their excellent electrical conductivity and high aspect ratio [162, 163]. The giant dielectric constant could be achieved as the f_{filler} increases to the

vicinity of f_c, which could be explained by the microcapacitor model [164, 165]. Namely, the adjacent CNTs form a local capacitor with the CNTs as electrodes and the host polymer between the CNTs as the dielectric. As f_{filler} approaches the f_c from below, the exponentially decreased inter-particle distance leads to an abrupt augmentation of capacitance for the local capacitors as well as the enhancement of the local electric field. The enhanced electric field will facilitate the migration of charges within CNTs toward the CNTs-polymer interface. As a result, these charges are blocked at the interface due to the huge different relaxation time between CNTs and polymer matrix [166]. However, the blocked charges inside the nanocomposites are easy to be relaxed either by the tunneling effect or the direct ohmic contact between the pristine CNTs (P-CNTs), which leads to the sharp increase in dielectric loss. Such high dielectric loss near f_c not only counteracts the benefits of the enhancement in dielectric constants, moreover greatly restricts the applications of CNTs based percolative nanocomposites in the embedded capacitors field due to the tremendous energy consumption. The key issue is to largely increase the dielectric constant while suppressing the dielectric loss as low as possible. Therefore, it is imperative to design the microstructure of CNTs reasonably, which not only favors the formation of microcapacitor but also prevents the connection of CNTs in the polymer matrix. Eventually, the desirable dielectric performance with a high dielectric constant and a low dielectric loss could be obtained by employing the CNTs with novel microstructure.

In the past few years, several strategies have been proposed to prevent the conductive nanoparticles from being directly contacted with each other near the f_c, with the aim of suppressing the high dielectric loss [167-169]. The core-shell strategy by introducing an interlayer between the pristine conductive particles and polymer matrix provides an intriguing approach to overcome the well-known paradoxes. The interparticle barrier layer hinders the direct contact of conductive nanoparticles. Thus, the leakage current, caused by the tunneling effect or the direct ohmic contact of conductive nanoparticles, would be greatly suppressed and hence the low dielectric

loss would be achieved by this means. The introduction of an interfacial layer into percolative nanocomposites was first confirmed by Wong and co-workers in aluminum (Al)/epoxy nanocomposites [98]. The Al nanoparticles were self-passivated by a very thin layer of Al_2O_3 with a thickness of ca. 2.8 nm before being introduced into the epoxy matrix. The self-passivated amorphous oxide layer serves as an insulating boundary layer to prevent the Al core from being connected with each other. A higher dielectric constant up to 60 was obtained at f_{filler} of 50 wt. %, at which the dielectric loss was merely approximately 0.02. Shen and his co-workers made their efforts to coat Ag core with carbonaceous organic shells by the hydrothermal method and subsequently fabricate the Ag@C/epoxy nanocomposites [99, 157]. Ag cores were isolated from each other even at f_{filler} of 30 vol. %. Tunable dielectric properties could be achieved by changing the thickness of organic insulating shells. Recently, Guo and his co-workers coated the CNTs with an ultrathin amorphous carbon shell with a thickness of about 2 nm by the hydrothermal reaction [65]. The ultrathin amorphous carbon shell on the surface of CNTs acts as an insulative layer to prevent the direct contact of CNTs. The conductive network was extremely difficult to be constructed even at a high f_{filler} of 10.4 vol. %. Although the dielectric loss is largely suppressed, the method involved in this work is relatively complicated and it is not suitable for industrialized production to fabricate the hybrid nanofillers.

Chemical vapor deposition (CVD) method has been extensively used to fabricate hybrid nanofillers because of its simplicity and controllability [170-172]. In the present study, we report a simple and effective approach to deposit an amorphous carbon (AC) interlayer with different structural features on the surface P-CNTs by CVD. The hybrids (CNTs@AC) were subsequently loaded into the PVDF matrix by the integration of solution and melting blending procedures to fabricate the CNTs@AC/PVDF dielectric nanocomposites with a high dielectric constant and a low dielectric loss. The AC shell around the surface of CNTs provides an effective insulative interlayer for the neighboring CNTs, which not only hinders the direct connection of CNTs but also improves the dispersibility of CNTs in the PVDF matrix.

After coating of the AC interlayer, the dielectric loss is greatly suppressed and the percolation behavior is delayed. The results indicate that the dielectric performance of CNTs/PVDF nanocomposites is greatly enhanced after depositing an AC interlayer on the surface of CNTs. The present approach may be extended to the preparation of other similar carbon hybrids based percolative nanocomposites with a high dielectric constant and a low dielectric loss, which makes them as a prominent potential candidate in the high energy storage capacitors field.

4.2 Experimental

4.2.1 Synthesis of Core-Shell Structured CNTs@AC Hybrids Fillers

The core-shell CNTs@AC hybrids fillers were obtained by the CVD method using C_2H_2 as the carbon source. The pristine CNTs with the diameter about 20-40 nm and the length about 1-2 μm were provided by Shenzhen Nanotech Port Company (China). Briefly, a certain amount of pristine CNTs was homogeneously dispersed on the surface of a quartz plate to serve as the substrate for the deposition of the AC interlayer. The furnace was heated to 700 ^{o}C under an Ar (700 s.c.c.m.) and H_2 (300 s.c.c.m.) atmosphere and annealed for 5 min to reduce the surface oxygen functional group of CNTs. Then a small number of C_2H_2 (40 s.c.c.m.) was introduced into the reaction tube at ambient pressure. After the synthesis, the reactor was cooled down to the room temperature under the Ar atmosphere (1000 s.c.c.m.). The quartz plate containing CNTs@AC hybrids was carefully taken out of the reactor. Finally, the resultant powder after AC deposition was separately collected using a very thin cutting blade. The time for the carbon layer deposition was in the range of 5-60 min.

4.2.2 Preparation of CNTs@AC/PVDF and P-CNTs/PVDF Nanocomposites

The CNTs@AC/PVDF nanocomposites with different CNTs@AC contents ($f_{CNTs@AC}$) were prepared by the combination of solution casting and extrusion injection processing in order to achieve better dispersion of nanofillers in the PVDF

matrix. The details of the experiment are presented as follows. Firstly, a desired amount of CNTs@AC was dispersed into DMF solvent with ultrasonic treatment for 2 h. Then PVDF powders (Kynar 761, Arkema Group, France) were subsequently introduced into the suspension of CNTs@AC and the mixture was magnetically stirred at 70 ºC for 2 h. The temperature of the mixture solution was increased up to 100 ºC and held for 1 h to evaporate most of the solvent. After that, the mixture was further dried in a vacuum oven at 80 ºC for 12 h to eliminate the residual solvent. Secondly, the as-prepared CNTs@AC/PVDF mixture was melt blended under Ar atmosphere by a two-screw micro-extruder with a speed of 90 rpm at 220 ºC for 30 min. Finally, the slabs with a thickness of 1.5 mm were obtained by injection molding of the mixed nanocomposites. The obtained $f_{CNTs@AC}$ in the CNTs@AC/PVDF nanocomposites varied from 0 to 15 vol. %. The P-CNTs/PVDF nanocomposites were fabricated by the same procedure.

4.2.3 Characterizations

The cryo-fractured surfaces morphology of the CNTs@AC/PVDF and P-CNTs/PVDF were characterized by SEM (LEO Gemini 1530) operated at 5.0 kV. Transmission electron microscopy (TEM) was carried out using an FEI Titan instrument equipped with an aberration-corrected condenser operating at 200 kV. For dielectric measurements, electrodes were painted with silver paste on both sides of the samples and then the dielectric properties were characterized by an impedance analyzer (Solatron 1260) at room temperature. X-ray diffraction (XRD) patterns were measured on an XRD detector (Bruker D2 PHASER with X-Flash 430). Fourier transform infrared spectroscopy (FT-IR, Bruker Tensor 27) was employed to characterize the chemical structure of nanofillers. Raman spectroscopy was performed with a Jobin Yvon Lab Ram spectrometer.

4.3 Results and Discussions

As shown in Fig. 4-1, the core-shell structured CNTs@AC hybrids were

synthesized by CVD method using C_2H_2 as the carbon source and Ar as the carrier gas at 700 °C for various times. An appropriate amount of H_2 was utilized to reduce the surface oxygen functional groups of CNTs at the elevated temperature, which can eliminate their influence on the ultimate dielectric performance of polymer nanocomposites. The structure of carbon interlayer in CNTs@AC hybrids depends largely on the carbon deposition condition used. Higher temperatures facilitate the formation of defect-free graphene layers, while low temperatures decrease their graphitization degree and induce the formation of AC layers. As demonstrated in our previous work [172], when the temperature for carbon deposition is below 850 °C, the deposited carbon interlayer around the surface of CNTs exhibits disorder graphene layers with curved segments of individual graphitics sheets and discontinuous graphitic cylinders structure. However, this kind of defects are usually present in P-CNTs as well and can be healed by annealing CNTs under an inert atmosphere at the elevated temperature. Such thermal treatment will increase the ordering degree of CNTs by reducing the inherent defects. Considering the merits of insulative carbon interlayer of CNTs on the final dielectric performance of nanocomposites, the temperature for carbon deposition in this work was fixed at 700 °C, which would benefit the formation of AC interlayers on the surface of P-CNTs. For convenience and simplicity, the core-shell CNTs@AC hybrids with the different structural features are given by CNTs@AC-x, where x represents the carbon deposition time (min).

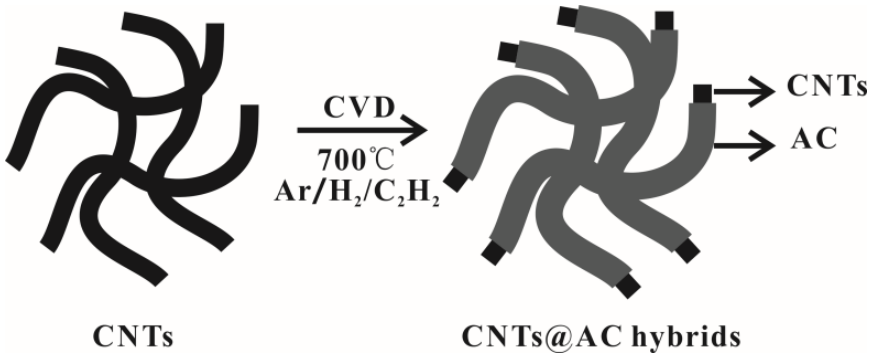

Fig. 4-1 *Schematic illustration showing the synthesis of core-shell CNTs@AC hybrids fillers.*

SEM and TEM measurements were carried out to identify the morphology of the

core-shell structured CNTs@AC hybrids. Due to the ultrathin feature of AC interlayer, it is difficult to identify the AC interlayer from SEM images (Fig. 4-2). Fig. 4-3 and Fig. 4-4 present the TEM images of P-CNTs and CNTs@AC hybrids with different carbon deposition times. As shown in Fig. 4-3, the CNTs are covered by an ultrathin discontinuous AC interlayer due to the short carbon deposition time (5 min). When the carbon deposition time increases up to 20 min, the CNTs are uniformly coated by a continuous ultrathin AC shell with the interlayer thickness of about 2 nm (Fig. 4-4). More importantly, compared with the CNTs@AC-5 hybrids, no bare CNTs parts in CNTs@AC-20 hybrids can be observed in Fig. 4-4. Such an ultrathin interlayer would not only provide a barrier layer between adjacent CNTs for preventing the direct contact of CNTs in PVDF matrix but also improve the dispersibility of CNTs in PVDF matrix. Therefore, the dielectric performance of corresponding polymer nanocomposites would be greatly affected by the AC interlayer, which will be discussed in the following section.

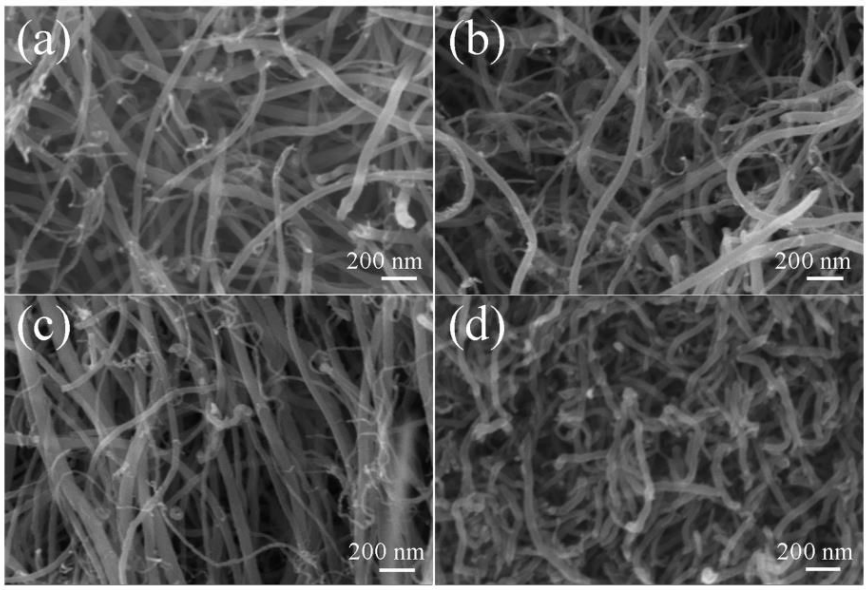

Fig. 4-2 *SEM images of (a) P-CNTs, (b) CNTs@AC-5, (c) CNTs@AC-20 and (d) CNTs@AC-60 hybrids fillers.*

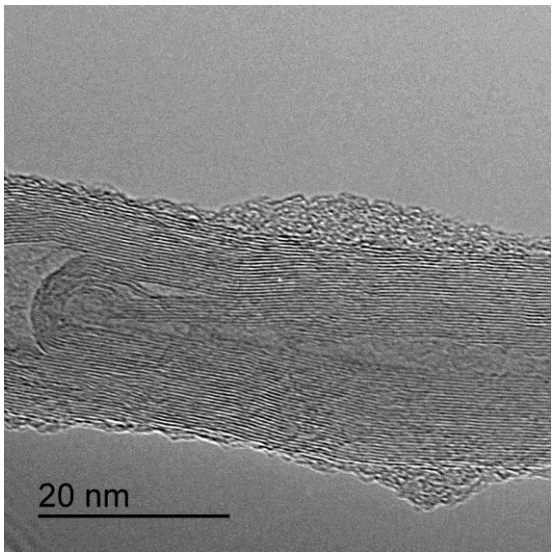

Fig. 4-3 *TEM image of CNTs@AC-5 hybrids fillers.*

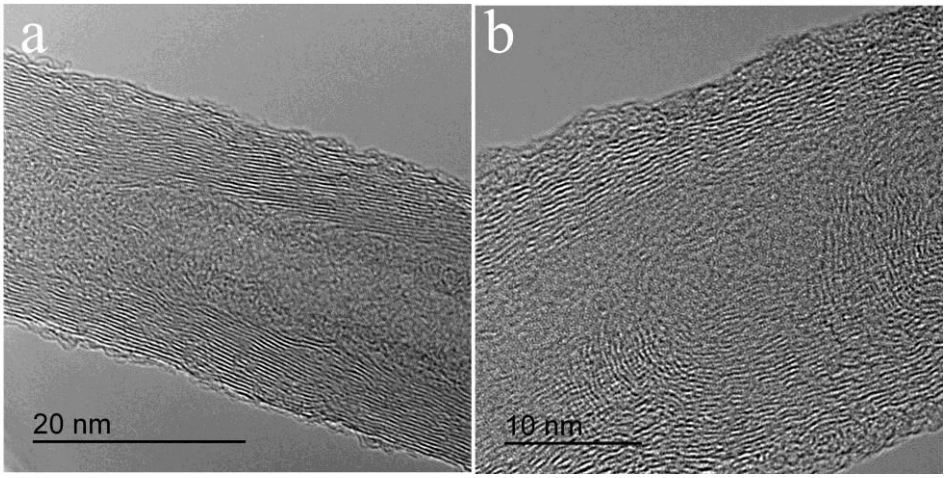

Fig. 4-4 *TEM images of (a) P-CNTs and (b) CNTs@AC-20 hybrids.*

The XRD patterns, as shown in Fig. 4-5a and Fig. 4-6a, reveal that no significant differences in the diffraction patterns of the CNTs after carbon deposition is detected. The chemical structures of the P-CNTs and as-obtained CNT@AC hybrids were characterized by FT-IR spectroscopy. As shown in Fig. 4-5b and Fig. 4-6b, compared with the P-CNTs hybrids, no new peak is observed for the spectrum of CNTs@AC hybrids. Raman spectra analysis was performed to differentiate the structural differences between P-CNTs and CNTs@AC hybrids. As seen in Fig. 4-5c and Fig. 4-6c, both specimens (P-CNTs and CNTs@AC hybrids) display three characteristic peaks around 1325, 1580 and 1608 cm^{-1}, corresponding to the typical D, G and D'

band of CNTs, respectively. The D and D' bands are usually attributed to the presence of amorphous or disordered carbon in the CNTs, due to the structural defects or oxygen-containing groups on the CNTs walls. While the G band is commonly attributed to the sp^2-bonded carbon. The intensity ratio of D band over G band (I_D/I_G) is usually used to quantify the CNTs structural quality, which determines the conductivity of the CNTs. The CNTs with a lower I_D/I_G value normally indicates fewer structural defects, which implies that its conductivity is superior to the one with a higher I_D/I_G value. Fig. 4-5d quantitatively summarizes the relationship between the I_D/I_G and the carbon deposition time. It can be found that the I_D/I_G value increases from 1.49 for P-CNTs to 2.13 for CNTs@AC-60 hybrids with the prolongation of carbon deposition time, which indicates that the CNTs@AC hybrids are less ordered than the P-CNTs due to the introduction of an AC interlayer. Besides, as shown in the inset of Fig. 4-5d and Fig. 4-6d, the P-CNTs precipitate rapidly in DMF while the CNT@AC hybrids with the different structural features are dispersed well in DMF even after 24 h. The improvement of dispersibility of CNT@AC hybrids can be attributed to the shielding effect of AC interlayer. Due to the strong π-π interaction between adjacent CNTs, the P-CNTs are prone to aggregate together and subsequently precipitate in DMF. After deposition with an AC interlayer, the π-π interaction between adjacent CNT@AC is significantly suppressed. In this case, despite the surface chemical structure of CNT@AC hybrids stay unchanged after deposition with an AC interlayer, as confirmed in Fig. 4-5b and Fig. 4-6b, the CNT@AC hybrids can be also dispersed homogeneously in DMF solvent, which would promote the dispersion of CNTs@AC hybrids in PVDF matrix.

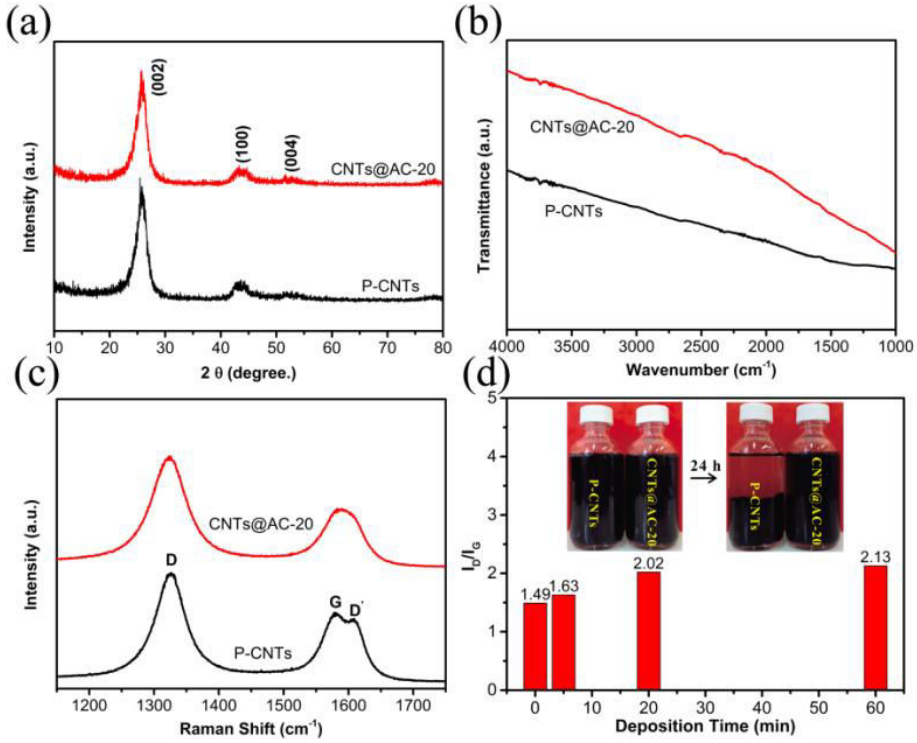

Fig. 4-5 *(a) XRD patterns, (b) FT-IR spectra and (c) Raman spectra of the P-CNTs and CNTs@AC-20 hybrids; (d) the intensity ratio between D band and G band (I_D/I_G) calculated from the Raman spectra of the P-CNTs and CNTs@AC-20 hybrids with different deposition time. The inset in part d shows the photographs of solution (DMF) stability of the suspension with P-CNTs and CNTs@AC-20 hybrids at the same concentration (0.002 g ml^{-1}).*

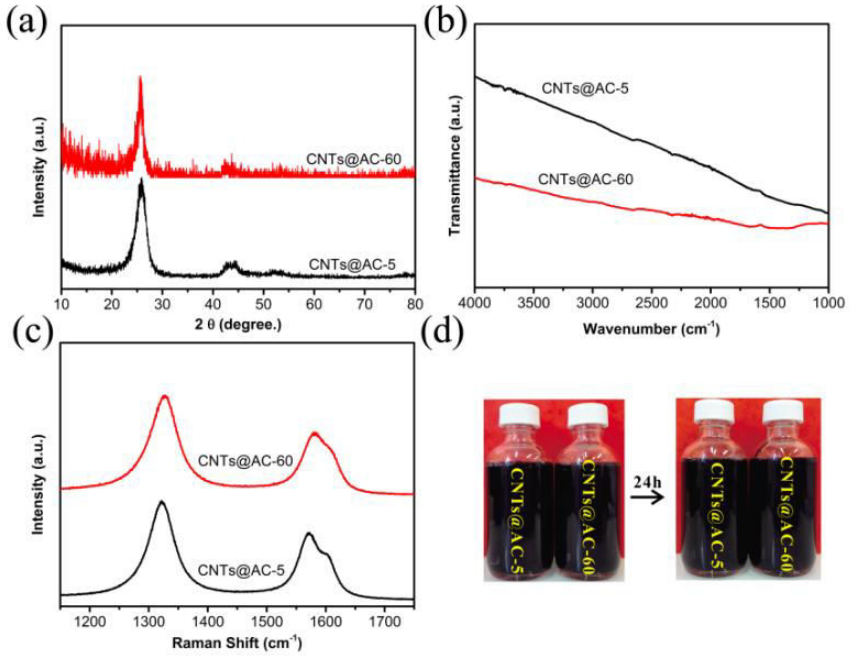

Fig. 4-6 *(a) XRD patterns, (b) FT-IR spectra and (c) Raman spectra of the*

CNTs@AC-5 and CNTs@AC-60 hybrids; (d) the photographs of solution (DMF) stability of the suspension with CNTs@AC-5 and CNTs@AC-60 hybrids at the same concentration (0.002 g ml^{-1}).

The SEM images of the fracture surfaces of the P-CNTs/PVDF and CNTs@AC/PVDF nanocomposites films are shown in Fig. 4-7. The agglomerates of P-CNTs are clearly observed in P-CNTs/PVDF nanocomposites (Fig. 4-7a), whereas the CNTs@AC hybrids are dispersed well in the PVDF matrix (Fig. 4-7b, c, and d), which is in accordance with the results of solution stability. Therefore, the AC interlayer around the surface of CNTs is helpful to disperse CNTs in the polymer matrix.

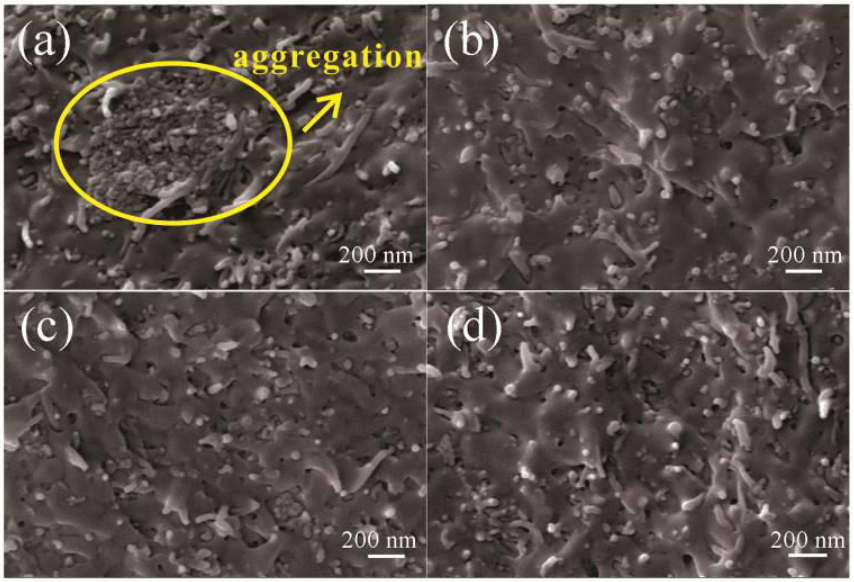

Fig. 4-7 *SEM images of the fracture surfaces of (a) P-CNTs/PVDF, (b) CNTs@AC-5/PVDF, (c) CNTs@AC-20/PVDF and (d) CNTs@AC-60/PVDF nanocomposites at the same filler loading (10 vol. %).*

Fig. 4-8 and Fig. 4-9 display the frequency dependence of the conductivity of P-CNTs/PVDF and CNTs@AC/PVDF nanocomposites with different filler loadings and a comparison of typical conductivity. It can be seen from Fig. 4-8 that the conductivity of P-CNTs/PVDF nanocomposites with $f_{P\text{-}CNTs}$ over 8 vol. % is nearly independent of frequency at low-frequency range (10^2-10^4 Hz), which reflects its conductor nature. However, for the CNTs@AC-5/ PVDF part, as displayed in Fig. 4-

9a, the percolation transition critical point is located between 8.5 vol. % and 9 vol. %. As for the CNTs@AC-20/PVDF nanocomposites, its percolative inversion point is located between 9 vol. % and 9.5 vol. % (as shown in Fig. 4-9b), which is higher than that of the CNTs@AC-5/PVDF system. The transition point from the insulator to the conductor for CNTs@AC-60/PVDF system is located between 11.5 vol. % and 12 vol. % as seen in Fig. 4-9c. Therefore, the calculated percolation threshold may also increase with the prolongation of carbon deposition time, which will be discussed in the following section. As presented in Fig. 4-9d, the conductivity of P-CNTs/PVDF and CNTs@AC/PVDF nanocomposites with different structural features of AC interlayer show a huge difference. For instance, when loading with 8 vol. % filler, the conductivity of P-CNTs/PVDF is approximately two orders magnitude larger than those of nanocomposites with CNTs@AC-5 and CNTs@-20 hybrids. The conductivity of P-CNTs/PVDF is almost independent of the frequency at the low-frequency range, which indicates that the conductive network has been formed due to the direct contact of P-CNTs in the PVDF matrix. However, the conductivities of nanocomposites with CNTs@AC-5 and CNTs@AC-20 hybrids exhibit a strong frequency dependency due to their insulator nature. The conductivity values decrease slightly with the increase of carbon deposition time. The introduction of the AC interlayer prevents direct contact of adjacent CNTs, which hinders the formation of the conductive network in CNT@AC/PVDF nanocomposites. Their electrically connective behavior can mainly be achieved by tunneling effect, which leads to a lower conductivity compared with P-CNTs/PVDF system at the same filler contents. Furthermore, the conductivity decreases when the structural feature of AC interlayer changes from discontinuous state to a continuous one due to enhanced shielding effect. With increasing f_{filler} to 10 vol. %, the conductivity values of all these three kinds of nanocomposites are nearly independent of the frequency at low-frequency range, which demonstrates that the conductive paths have already been formed in the PVDF matrix. Besides, the conductivity of P-CNTs nanocomposites is still two orders magnitude higher than those of CNTs@AC/PVDF nanocomposites with CNTs@AC-

5 and CNTs@AC-20 hybrids. As for the part of CNTs@AC-60/PVDF nanocomposites, the conductivity with 11.5 vol. % hybrids shows the lowest value even loading with a relatively higher volume fraction of fillers compared with other nanocomposites (as shown in Fig. 4-9d). And its conductive network has not been formed, which is confirmed by the relationship of conductivity and the frequency at low-frequency range. With increasing the number of hybrids to 12 vol. %, the conductivity becomes independent with the frequency at low-frequency range, which demonstrates that the conductive network has already been constructed. Therefore, the percolation threshold for CNTs@AC-60/PVDF nanocomposites is located between 11.5 vol. % and 12 vol. %. A precise value will be calculated in the following part.

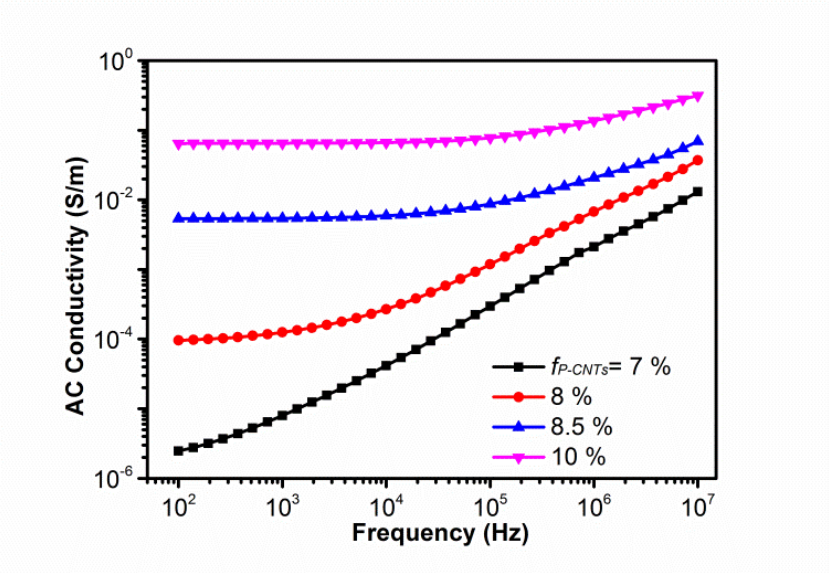

Fig. 4-8 *Frequency dependence of the conductivity of P-CNTs/PVDF nanocomposites at different filler loading.*

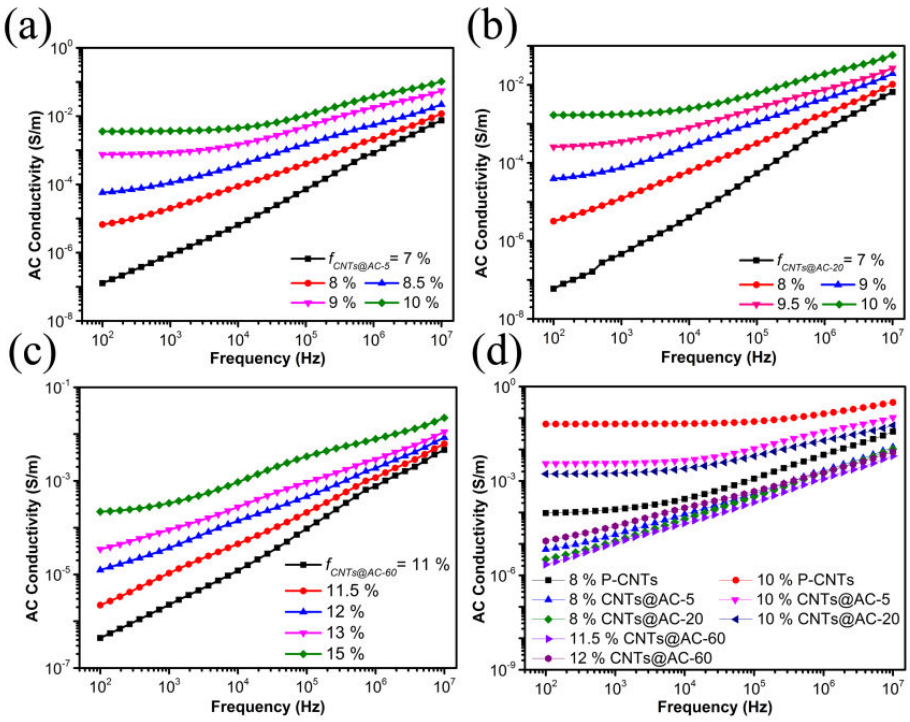

Fig. 4-9 *Frequency dependence of the conductivity of (a) CNTs@AC-5/PVDF, (b) CNTs@AC-20/PVDF and (c) CNTs@AC-60/PVDF nanocomposites at different filler loading; (d) Typical conductivity comparison between P-CNTs@/PVDF and CNTs@AC/PVDF nanocomposites with different CNTs@AC hybrids at different filler loadings.*

Fig. 4-10 shows the frequency dependence of the dielectric constant of the nanocomposites filled with P-CNTs and CNTs@AC hybrids with the different structural features. The data indicates that their dielectric constants are almost independent of the frequency when $f_{filler}<f_c$. Additionally, as f_{filler} is in the neighborhood of f_c, the dielectric constant decreased sharply at low-frequency range due to the Maxwell-Wagner (MW) relaxation. The relaxation of dielectric constant is originated from the accumulation of injected charges at the interface between CNTs and PVDF matrix with different relaxation times.

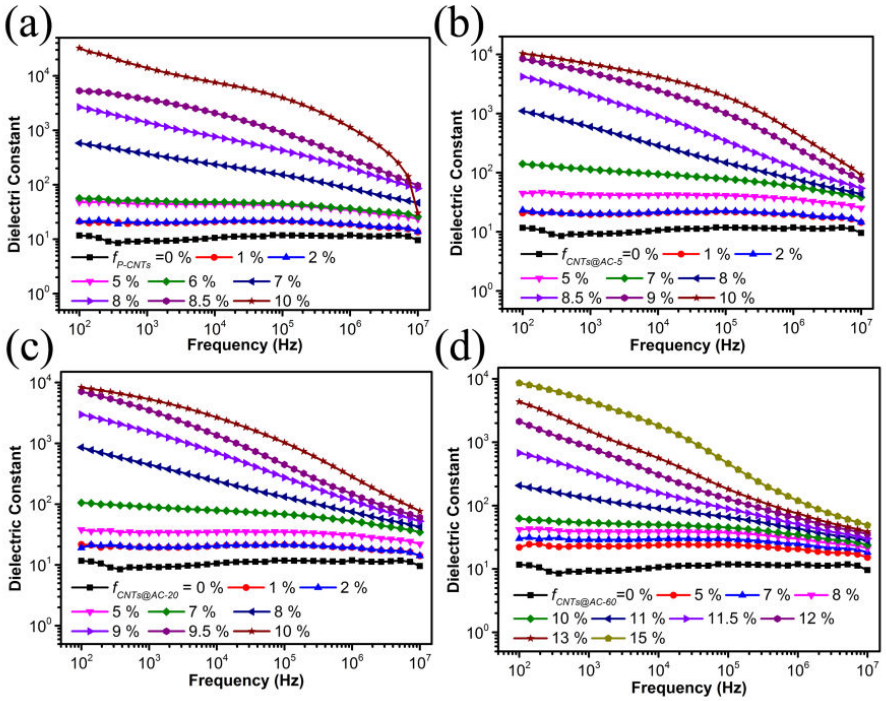

Fig. 4-10 *Frequency dependence of the dielectric constant of (a) P-CNTs/PVDF, (b) CNTs@AC-5/PVDF, (c) CNTs@AC-20/PVDF and (d) CNTs@AC-60/PVDF nanocomposites at different filler loading.*

Fig. 4-11 shows the evolution of the dielectric properties of P-CNTs/PVDF and CNTs@AC/PVDF nanocomposites with increasing f_{filler}. According to Fig. 4-11a, it can be clearly seen that when f_{filler} approaches the f_c, the dielectric constant enhances significantly for all the four types of nanocomposites, which is the typical characteristics of percolative nanocomposites. The dielectric constant of P-CNTs/PVDF is higher than that of CNTs@AC/PVDF nanocomposites when the CNTs are far from each other. The influence of the coated AC interlayer on the dielectric constant of nanocomposites is not obviously observed before the formation of CNTs network, which is attributed to the isolation effect of the PVDF insulating layer on the surface of CNTs. However, as shown in the inset of Fig. 4-11a, the dielectric constant of P-CNTs/PVDF increases much more rapidly than that of CNTs@AC/PVDF in the vicinity of f_c. With the increase of f_{filler} from 7 vol. % to 10 vol. %, the dielectric constant increases from 368 to 13980 for P-CNTs/PVDF nanocomposites. The dielectric constant enhances from 113 to 6874 for CNTs@AC-

5/PVDF nanocomposites and 90 to 5306 for CNTs@AC-20/PVDF nanocomposites, respectively. As for the CNTs@AC-60 part, the dielectric constant increases from 29 to 4454 when the f_{filler} increases from 7 vol. % to 15 vol. %. The huge difference between the dielectric constant after percolation is attributed to the AC interlayer on the surface of CNTs, which acts as interparticle barriers to prevent CNTs from directly connecting. The capacitance of the parallel plate capacitor is obtained by the Eq. 3-1. The AC interlayer makes it difficult for CNTs to connect with each other, which increases the distance between the adjacent CNTs. Therefore, the capacitance will undoubtedly decrease for the nanocomposites with CNTs@AC hybrids. Moreover, the capacitance decreases with the augmentation of the AC interlayer thickness. Based on the percolation theory (Eq. 2-5), the results of best linear fitting for dielectric constant at 10^3 Hz for all the four types of nanocomposites are shown in Fig. 4-12. The best linear fits of the dielectric constant data give $f_c^{P\text{-}CNTs}$=7.16 vol. % and $q^{P\text{-}CNTs}$=0.86 for P-CNTs/PVDF nanocomposites, $f_c^{CNTs@AC\text{-}5}$=8.82 vol. % and $q^{CNTs@AC\text{-}5}$=1.56 for CNTs@AC-5/PVDF nanocomposites, $f_c^{CNTs@AC\text{-}20}$=9.49 vol. % and $q^{CNTs@AC\text{-}20}$=1.69 for CNTs@AC-20/PVDF nanocomposites, and $f_c^{CNTs@AC\text{-}60}$=11.81 vol. % and $q^{CNTs@AC\text{-}60}$=0.91 for CNTs@AC-60/PVDF nanocomposites, respectively. The obtained $f_c^{P\text{-}CNTs}$ for P-CNTs/PVDF is lower than that of the CNTs@AC/PVDF nanocomposites. Besides, the f_c increases with the augmentation of carbon deposition time, as presented in Fig. 4-11d. The percolation effect is delayed after deposition with an AC interlayer. As for the part of dielectric loss shown in Fig. 4-11b, the tendency of dielectric loss as a function of f_{filler} shows identical results that the loss increases abruptly when f_{filler} approaches f_c. Furthermore, as presented in the inset of Fig. 4-11b, the dielectric loss of P-CNTs/PVDF also augments more rapidly than that of CNTs@AC/PVDF. As f_{filler} increases from 7 vol. % to 10 vol. %, the dielectric loss augments sharply from 0.39 to 83.66 for P-CNTs/PVDF nanocomposites. As for the part of CNTs@AC-5/PVDF and CNTs@AC-20/PVDF systems, the dielectric loss increases moderately from 0.12 to 9.64 for CNTs@AC-5/PVDF nanocomposites and 0.09 to 5.99 for CNTs@AC-20/PVDF nanocomposites,

respectively. The dielectric loss of CNTs@AC-60/PVDF nanocomposites increases slightly from 0.01 to 1.35 with the increase of f_{filler} from 7 vol. % to 15 vol. %. After coating with an AC interlayer, the dielectric loss is greatly suppressed due to the diminution of leakage current. For instance, when f_{filler} is 7 vol. % (the conductive network has not been formed for all the four kinds of polymer nanocomposites according to the obtained percolation value in Fig. 4-11d), the dielectric loss drops off moderately from 0.39 to 0.01 for the CNTs@AC-60 hybrids. Nevertheless, when f_{filler} increases up to10 vol. %, the dielectric loss decreases distinctly from 83.66 to 9.64 for the hybrids with a discontinuous AC shell and 5.99 for the hybrids with a continuous AC shell, respectively. For the part of CNTs@AC-60/PVDF, the dielectric loss is merely 1.35 even when the f_{filler} increases to 15 vol. %. As displayed in Fig. 4-11c, the conductivity also shows similar tendency like dielectric constant and loss.

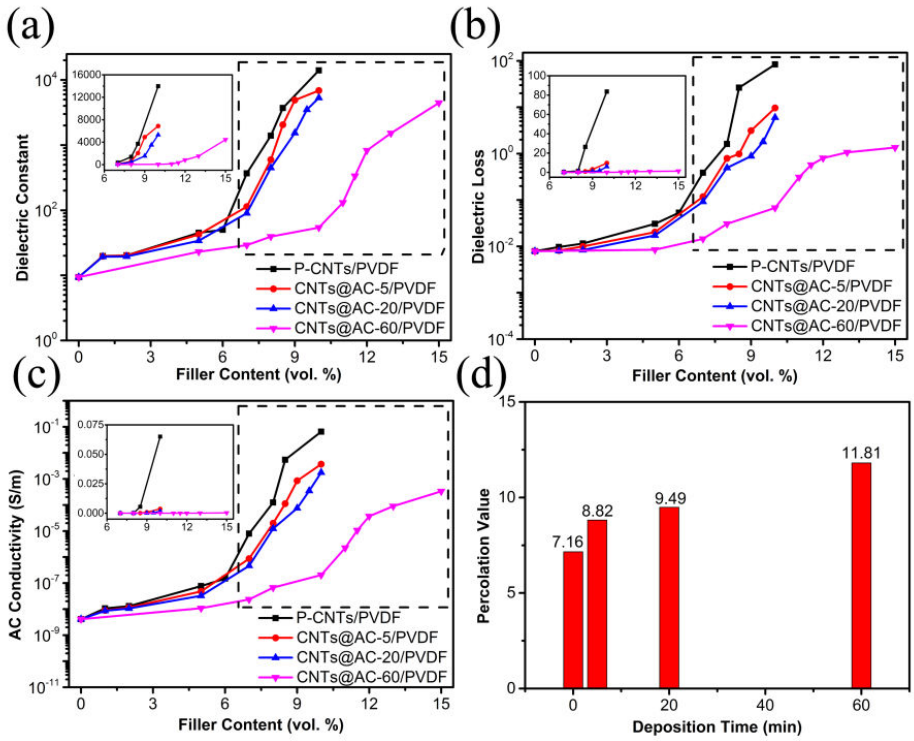

Fig. 4-11 *Dependence of the (a) dielectric constant, (b) dielectric loss and (c) conductivity of P-CNTs/PVDF, CNTs@AC-5/PVDF, CNTs@AC-20/PVDF and CNTs@AC-60/PVDF nanocomposites on the filler contents (measured at 10^3 Hz); (d) Dependence of percolation value of P-CNTs/PVDF, CNTs@AC-5/PVDF, CNTs@AC-20/PVDF and CNTs@AC-60/PVDF nanocomposites on the deposition time. The*

insets in (a), (b) and (c) show the enlarged regions as cycled by the dashed lines.

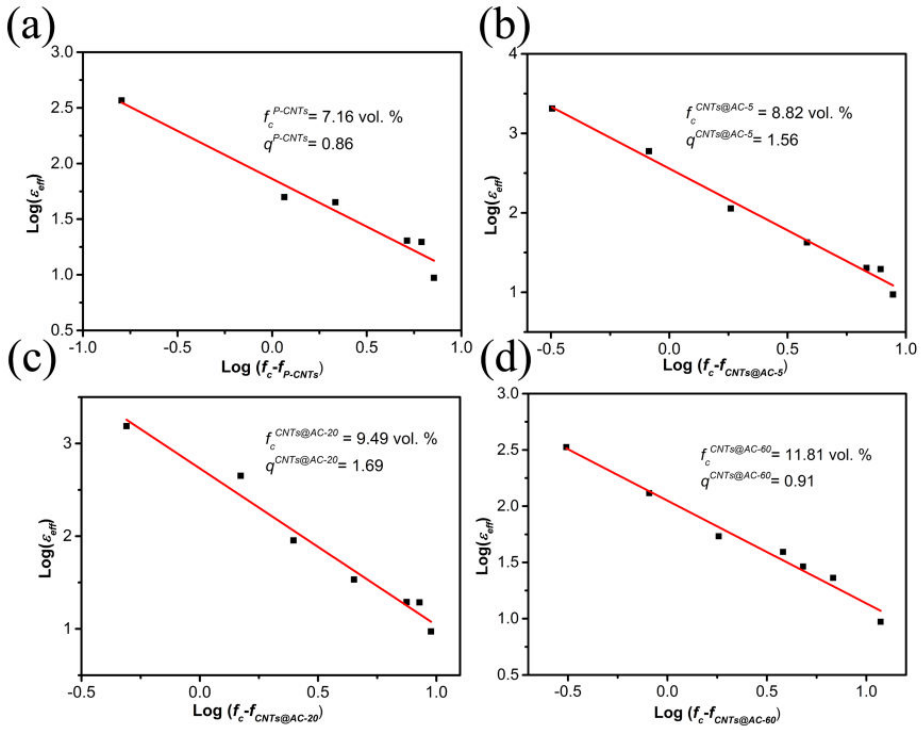

Fig. 4-12 *The best fits of the dielectric constant of (a) P-CNTs/PVDF, (b) CNTs@AC-5/PVDF, (c) CNTs@AC-20/PVDF and (d) CNTs@AC-60/PVDF nanocomposites to Eq. 2-5.*

Fig. 4-13 shows the bar chart for comparing the dielectric constant and corresponding dielectric loss of different types of carbon fillers loaded percolative nanocomposites reported in the literature. The resultant CNTs@AC-60/PVDF nanocomposites with 15 vol. % CNTs@AC-60 hybrids possess a giant dielectric constant (4454) while retaining a low dielectric loss (1.35). In comparison with those reported nanocomposites, the CNTs@AC/PVDF nanocomposite in this work possesses a totally competent dielectric performance.

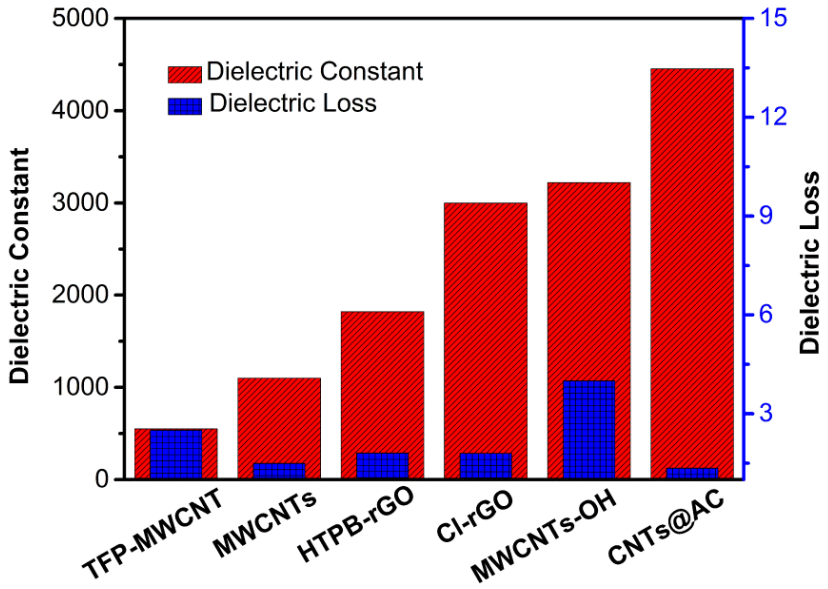

Fig. 4-13 *Bar chart comparing the dielectric constant and corresponding dielectric loss at 10^3 Hz reported in the literature using percolative nanocomposites filled with different types of carbon fillers:* ***TFP-MWCNT****, 8 vol. %;* ***MWCNTs****, 12 vol. %;* ***HTPB-rGO****, 1.02 wt. %;* ***Cl-rGO****, 0.32 vol. %;* ***MWCNTs-OH****, 9 wt. %;* ***CNTs@AC****, 15 vol. % [60, 61, 173-175].*

4.4 Conclusions

In this chapter, core-shell structured CNTs@AC hybrids with the different structural features were obtained by chemical vapor deposition and they were subsequently integrated into PVDF to prepare CNTs@AC/ PVDF dielectric nanocomposites by the integration of solution and melting blending processes. The AC interlayer not only prevents the direct contact of CNTs but also improves the dispersibility of CNTs in the PVDF matrix. The f_c increases with the prolongation of carbon deposition time, which suggests that the percolation behavior is delayed. Moreover, the dielectric loss undergoes a sharp decrease after the deposition with AC interlayer, which is attributed to the decreasing of the leakage current between the adjacent CNTs. The results suggest that the influence of AC interlayer on the final dielectric performance after percolation is much more obvious than that before percolation. The ease of processing and excellent dielectric performance make

CNTs@AC/PVDF nanocomposites as a potential candidate in the dielectric-based capacitor.

Chapter V

Core@Shell Structured BNNSs@Carbon PVDF Nanocomposites

5.1 Introduction

Encapsulating ceramic fillers with conductive layers has drawn tremendous interests to promote the enhancement of dielectric constant for inorganic/polymer nanocomposites in the past decades [109, 110, 112]. According to the conductive layer used, these encapsulating approaches could be mainly classified into two categories. The first type of coating process is obtained by depositing metal particles on the surface of ceramic fillers. For instance, Luo and his co-workers reported that the agglomeration of Ag nanoparticles in PVDF matrix could be suppressed by utilizing the Ag-deposited $BaTiO_3$ (BT-Ag) hybrids, which endows the nanocomposite with a high dielectric constant of about 94.3 at 43.4 vol. % filler loading [109]. The similar $CaCu_3Ti_4O_{12}$ and Ag hybrids (CCTO@Ag) were also synthesized and their corresponding PI nanocomposites could afford a high dielectric constant about 103 at 3 vol. % filler loading [110]. The other type of conductive layer is carbon layer. The core-shell structured ceramic/carbon hybrids have already exhibited their potential advantages in enhancing the dielectric constant of nanocomposites. For example, Feng et al. prepared core-shell structured $BaTiO_3$@carbon (BT@C) hybrids by the chemical vapor deposition (CVD) method and these hybrids were incorporated into the P(VDF-HFP) to fabricate BT@C/P(VDF-HFP) nanocomposites, which endows the nanocomposites with a giant dielectric constant about 1044 at 30 vol. % filler loading [111]. The flower-like TiO_2/carbon (TiO_2/C) hybrids were also fabricated by a solvothermal method and they were subsequently adopted as fillers to prepare P(VDF-HFP) nanocomposites, which affords a dielectric constant about 330.6 at 20 vol. % filler loading [112]. All these

previous studies have confirmed that the core-shell structured hybrids with a conductive layer could endow the nanocomposites with an excellent dielectric property.

The incorporation of hexagonal boron nitride nanosheets (BNNSs) into polymer matrix has been widely reported in last few years because of its high breakdown strength (ca. 800 KV/mm), high thermal conductivity, extraordinary anti-oxidation stability, and excellent mechanical properties [141, 143, 176]. It has been well demonstrated that incorporation of BNNSs into polymer matrix could inhibit the mobility of the charge carrier, thus resulting in a dramatic decrease of dielectric loss. However, the applications of polymer nanocomposites incorporated with BNNSs in embedded capacitors are greatly hindered by the intrinsic low dielectric constant of BNNSs (ca. 3-4). In order to further improve the dielectric constant of BNNSs incorporated polymer nanocomposites, as discussed in the above parts, the combination of the conductive layer with BNNSs provides a promising strategy to enhance the dielectric constant. Our previous research has demonstrated that the existence of BNNSs could be used to adjust the conductive network of carbon nanotubes (CNTs)/PVDF nanocomposites [177]. However, the huge dielectric loss was also obtained due to the occurrence of percolation behavior. Therefore, it is imperative to rationally design an appropriate interaction between BNNSs and carbon conductive layer. Fu et al. immobilized the graphene oxide (GO) on the surface of BNNSs by electrostatic self-assembly and subsequently introduced these hybrids into epoxy accompanied with chemical reduction [176]. The reduced graphene oxide (rGO) sheets are well separated from each other even at a high hybrids loading. The enhancement of the dielectric constant is accompanied by a low dielectric loss, which exhibits a competent dielectric performance. The low dielectric loss could be ascribed to the insulating network of BNNSs to inhibit the mobility of charge carrier and well-separated rGO sheets by immobilization. However, the enhancement degree of dielectric constant is limited due to the limitation of the number of graphene sheets immobilized on the BNNSs surface.

Many previous studies demonstrated that the similar hexagonal structure of BNNSs and graphene layer favored the carbon deposition on the surface of BNNSs [178]. In this study, the BNNSs@carbon (BNNSs@C) hybrids with different carbon contents were synthesized by a CVD method because of its simplicity and controllability [170-172, 179, 180]. The carbon content in BNNSs@C hybrids could be precisely controlled by adjusting the carbon deposition time during the CVD procedure. The BNNSs@C hybrids were subsequently filled into the PVDF matrix by a combination of solution and melting blending processes. The dielectric performances of the as-obtained BNNSs@C/PVDF nanocomposites could be precisely controlled by tuning the carbon content in BNNSs@C hybrids. These results indicate that the dielectric performance of BNNSs@C/PVDF nanocomposites could be largely enhanced after depositing the carbon layer on the surface of BNNSs. The design concept here provides a new thought for the preparation of dielectric materials with the excellent dielectric performance, which makes them a prominent potential candidate in embedded capacitor industry.

5.2 Experimental

5.2.1 Synthesis of BNNSs@C Hybrids Fillers

The BNNSs@C hybrids were fabricated by the CVD method using C_2H_2 as the carbon source. The BNNSs with a lateral size about 0.5-2 μm were supplied by Merck Millipore (Darmstadt, Germany). In brief, a certain number of pristine BNNSs was homogeneously dispersed on a quartz plate to serve as the substrate for carbon deposition. The furnace was heated to 850 ^{o}C under an Ar (1000 s.c.c.m.) atmosphere and annealed for 5 min with a certain amount of H_2 to reduce the surface oxygen functional group of BNNSs. A small number of C_2H_2 (40 s.c.c.m.) was subsequently introduced into the reaction tube at ambient pressure. After the synthesis, the reactor was cooled down to the room temperature under the Ar atmosphere (1000 s.c.c.m.). The quartz plate with the BNNSs@C hybrids was carefully taken out of the reactor.

The resultant powder after carbon deposition was separately collected using a thin cutting blade. The time for the carbon deposition was fixed in the range of 5-45 min.

5.2.2 Preparation of BNNSs/PVDF and BNNSs@C/PVDF Nanocomposites

The BNNSs@C/PVDF nanocomposites with various BNNSs@C filler loadings ($f_{BNNSs@C}$) were prepared by a combination of solution casting and extrusion-injection methods in order to achieve a good and stable dispersion state of BNNSs@C hybrids in PVDF matrix. Briefly, the desired amount of BNNSs@C hybrids was ultrasonically dispersed into DMF solvent for 2 h. The PVDF powders (Kynar 761, Arkema Group, Colombes, France) were subsequently introduced into the suspension of BNNSs@C hybrids and the mixture was magnetically stirred at 70 ºC for 2 h. Afterward, the temperature of the mixture solution was increased up to 100 ºC and held for 1 h to remove the majority of DMF solvent. The residual solvent was further removed by drying the pre-mixture in a vacuum oven at 80 ºC for 12 h. The as-obtained BNNSs@C/PVDF mixture was subsequently melt-blended under Ar protective atmosphere by a two-screw micro-extruder with a speed of 90 rpm at 220 ºC for 30 min. Finally, the slabs with a thickness of 1.5 mm were prepared by injection molding of the nanocomposites. The obtained $f_{BNNSs@C}$ in the BNNSs@C/PVDF nanocomposites varied from 0 to 30 vol. %. The BNNSs/PVDF nanocomposites were prepared by the similar procedures, where f_{BNNSs} represents the filler loading of pristine BNNSs.

5.2.3 Characterizations

Morphological characterizations of the BNNSs@C hybrids were performed by TEM using an FEI Titan instrument equipped with a high-angle annular dark-field (HAADF) detector and an aberration-corrected condenser operating at 200 kV. The elemental mapping was carried out using scanning TEM-energy dispersive X-ray spectroscopy (STEM-EDX). The observation of the freeze-fractured cross-section surfaces of nanocomposites was conducted by the SEM (LEO Gemini 1530, Zeiss,

Oberkochen, Germany) operated at 5.0 kV. X-ray diffraction (XRD) patterns were measured on an XRD detector D2 PHASER (Bruker, Karlsruhe, Germany) with X-Flash 430 (Bruker, Karlsruhe, Germany)). Raman spectroscopy was performed with a Jobin Yvon LabRAM spectrometer (Horiba Scientific, Villeneuve d'Ascq, France). Thermogravimetric analysis (TGA, STA 449 F3, Netzsch, Selb, Germany) was used to evaluate the mass fraction of carbon. The furnace of TGA instrument with the powders was heated from 50 to 800 ºC at a rate of 5 ºC min^{-1} under N_2 (20 s.c.c.m.) and O_2 (20 s.c.c.m.) atmosphere. For dielectric measurements, electrodes were painted with silver paste on both sides of the samples and then the dielectric properties were characterized by a Novocontrol Alpha-A high performance frequency analyzer (Novocontrol Technologies, Montabaur, Germany) at room temperature.

5.3 Results and Discussions

As shown schematically in Fig. 5-1, the BNNSs@C hybrids were synthesized by the CVD method using C_2H_2 as the carbon source and Ar as the carrier gas at 850 ºC for various reaction time. An appropriate amount of H_2 was introduced to reduce the surface oxygen functional groups of BNNSs at the elevated temperature, which could eliminate their influences on the ultimate dielectric performance of polymer nanocomposites. The BNNSs have been extensively utilized as the substrate for the graphene growth due to their similar lattice parameters. As demonstrated in our previous work, when the temperature for carbon deposition is below 850 ºC, the deposited carbon interlayer exhibits disorder graphene layers. Considering the merits of the conductive carbon layer on the final dielectric performance of nanocomposites, the temperature for carbon deposition in this work was fixed at 850 ºC. For convenience and simplicity, the BNNSs@C hybrids with the different carbon deposition time are given by BNNSs@C-x, where x represents the carbon deposition time (min).

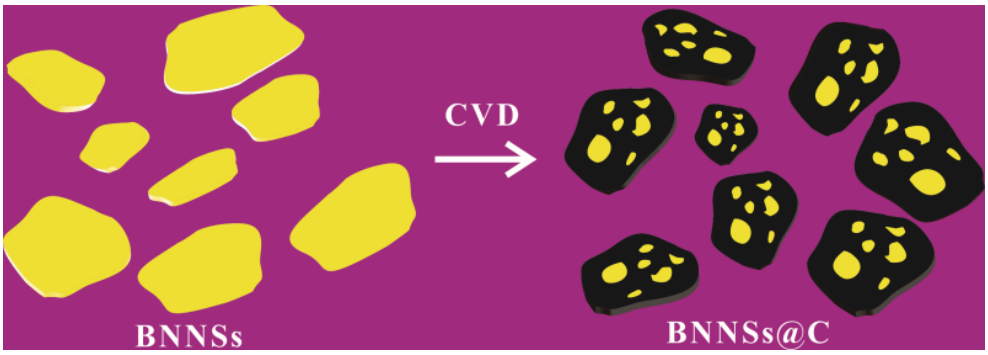

Fig. 5-1 *Schematic illustration of the synthesis procedure of BNNSs@C hybrids*

STEM measurements were conducted to identify the morphology of the BNNSs@C-15 hybrids. Fig. 5-2a shows the HAADF-STEM image of the BNNSs@C hybrids with a mean lateral size of about 0.5-2 μm. The corresponding EDX elemental maps of BNNSs@C-15 hybrids are displayed in Fig. 5-2b, c, and d. The elements B, N, and C are denoted in aqua green, red, and green, respectively. The BNNSs are uniformly covered by a continuous carbon layer for the most part. However, some naked BNNSs portions could be observed due to the existence of defects. The STEM-EDX technique employed in this work could map out the elemental distribution at a nanometer-scale spatial resolution and provide a clear vision of the BNNSs@C hybrids.

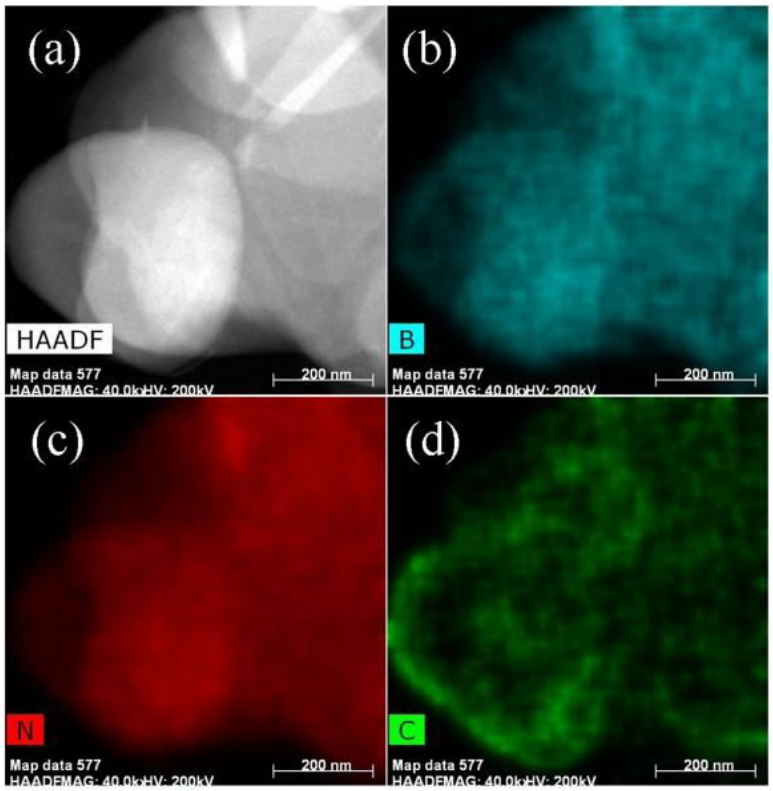

Fig. 5-2 *(a) HAADF-STEM image of the BNNSs@C-15 hybrids; (b-d) EDX elemental maps of B, N, and C, respectively.*

The XRD patterns, Raman spectra, and TGA characterizations were conducted as exhibited in Fig. 5-3 to obtain more precise structure and composition information of BNNSs@C hybrids. The XRD patterns of the pristine BNNSs and representative BNNSs@C-15 hybrids (Fig. 5-3a) reveal that the peak intensity of BNNSs weakens after the deposition of the carbon layer, which is attributed to the shielding effect of the carbon layer. The existence of the carbon layer was confirmed by Raman spectroscopy. As presented in Fig. 5-3b, the BNNSs@C hybrids display two characteristic peaks around 1350 and 1580 cm^{-1}, corresponding to the typical D and G bands of carbon species, respectively. The D band is usually attributed to the presence of amorphous or disordered carbon, while the G band is commonly associated with the sp^2-bonded carbon atoms. As illustrated in Fig. 5-3c, the TGA measurement was performed to calculate the mass fraction of carbon in the hybrids. For comparison, the TGA curve of pristine BNNSs is also displayed in Fig. 5-3c. All three types of BNNSs@C hybrids exhibit a remarkable weight loss stage around 650 ^oC.

Additionally, the mass fraction of carbon shell in the hybrids increases monotonously from 2.50 wt. % for BNNSs@C-5 hybrids to 22.62 wt. % for BNNSs@C-45 hybrids with increasing the CVD time from 5 to 45 min, which demonstrates that the composition of the hybrids could be precisely regulated by controlling the parameters involved in the CVD procedures.

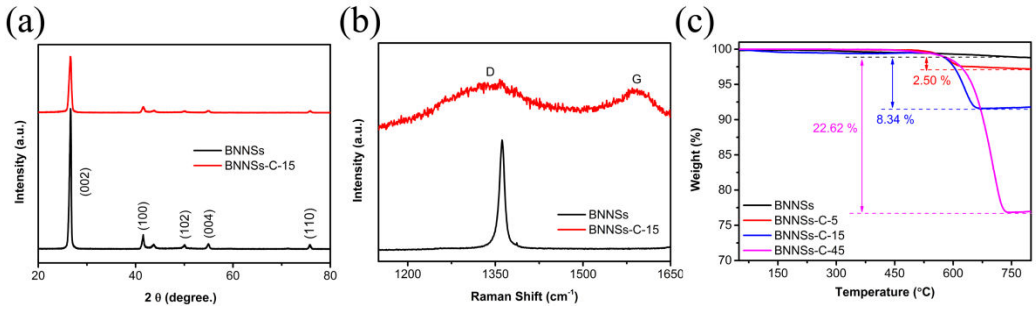

Fig. 5-3 *(a) XRD patterns; (b) Raman spectra; and (c) TGA curves of pristine BNNSs and corresponding BNNSs@C hybrids with different CVD deposition times.*

Fig. 5-4 presents SEM images of the fracture surfaces of pristine BNNSs/PVDF and BNNSs@C/PVDF nanocomposites at 20 vol. % filler loadings. We could observe that most parts of pristine BNNSs or BNNSs@C hybrids align well in the PVDF matrix with the direction of melting injection (as indicated by the yellow arrow in Fig. 5-4) due to the applied shearing force from the injection process. The BNNSs@C hybrids are homogeneously distributed in the PVDF matrix. Moreover, the majority of BNNSs@C hybrids are buried well inside the polymer matrix because of their excellent interfacial bonding with the PVDF matrix. Additionally, the BNNSs@C hybrids are homogeneously distributed in the PVDF matrix. Such microstructure characteristics of freeze-fractured cross-section surfaces indicate that the BNNSs@C hybrids exhibit excellent compatibility with the PVDF matrix.

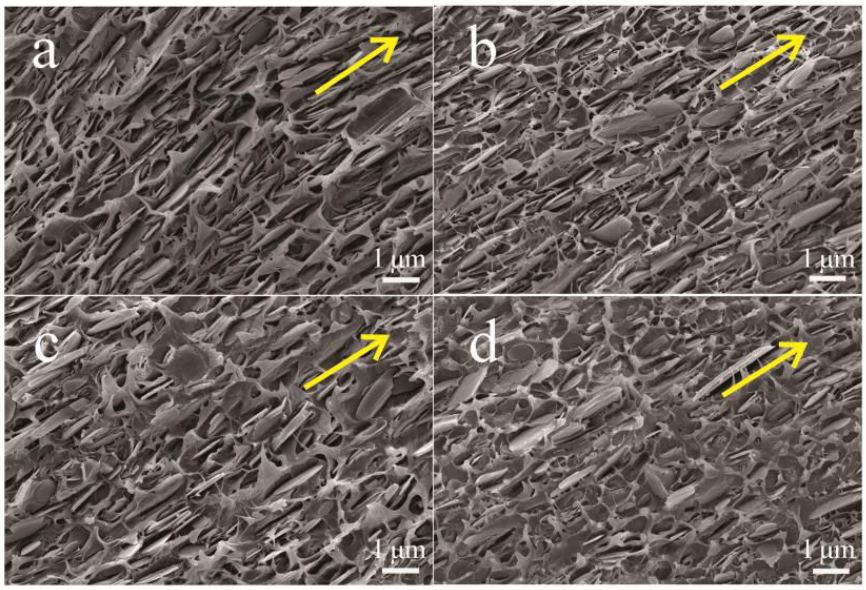

Fig. 5-4 *SEM images of the freeze-fractured cross-section surfaces of (a) BNNSs/PVDF; (b) BNNSs@C-5/PVDF; (c) BNNSs@C-15/PVDF; and (d) BNNSs@C-45/PVDF nanocomposites at 20 vol. % filler loadings.*

After demonstrating the successful deposition of the carbon layer on the surface of BNNSs, the pristine BNNSs and BNNSs@C hybrids were incorporated into PVDF matrix separately by a combination of solution casting and melting blending methods. Fig. 5-5 displays the frequency-dependent dielectric behaviors of the BNNSs/PVDF and BNNSs@C/PVDF nanocomposites incorporated with different types of BNNSs@C hybrids. As shown in Fig. 5-5a, the BNNSs/PVDF nanocomposites exhibit weak frequency dependence characteristics and their dielectric constant decreases slightly with increasing f_{BNNSs} up to 30 vol. %. However, the frequency dependence of dielectric constant for BNNSs@C/PVDF nanocomposites at a low frequency range becomes more evident with increasing the $f_{BNNSs@c}$ up to 30 vol. %. The strong frequency-dependent dielectric behavior could be attributed to the Maxwell-Wagner (MW) polarization, which occurs at the interfaces of heterogeneous components with different relaxation times. The MW polarization only occurs at a low frequency range due to its long relaxation time. Therefore, the variation of dielectric constant and loss becomes relative steady at higher frequencies. The relaxation time of BNNSs and PVDF matrix are several orders of magnitude larger

than that of the carbon layer. Thus, injected charges are tremendously blocked at the interfaces of BNNSs/carbon and carbon/PVDF, accordingly enhancing the dielectric constant at a low frequency range. Besides, the hybrid loading-dependent dielectric behavior of BNNSs@C/PVDF nanocomposites displays a totally different phenomenon compared with that of BNNSs/PVDF nanocomposites. The dielectric constant of BNNSs@C/PVDF nanocomposites increases significantly with increasing BNNS@C hybrid loading up to 30 vol. %. For the part of conductivity, all BNNS/PVDF and BNNSs@C-45/PVDF nanocomposites exhibit similar frequency-dependent behavior. Their conductivity values show a strong dependence of frequency in the whole frequency range, which demonstrates their insulative characteristics. The conductivity values of BNNSs/PVDF nanocomposites decrease slightly with increasing the f_{BNNSs} up to 30 vol. %. Nevertheless, the conductivity values of BNNSs@C 45/PVDF nanocomposites increases with increasing the $f_{BNNSs@C-45}$ up to 30 vol. %, which displays a similar law as discussed in the dielectric constant part. Fig. 5-5c presents the comparison of frequency-dependent behavior for the BNNSs@C/PVDF nanocomposites incorporated with different types of BNNSs@C hybrids at an equivalent hybrids loading (30 vol. %). The frequency dependence behavior of BNNSs@C/PVDF nanocomposites at a low frequency range becomes more significant by prolonging the CVD time in the carbon deposition procedure. Meanwhile, their dielectric constant increases significantly by prolonging the carbon deposition time from 5 to 45 min. Their conductivity values exhibit strong frequency dependent behavior in the whole frequency range, which reflects their insulative characteristics. Even if the nanocomposites are incorporated by the hybrids with a longer carbon deposition time (45 min) at a higher hybrids filler loading (30 vol. %), it is still difficult to construct the percolation network in the PVDF matrix, which could be explained by the discontinuous carbon layer on the surface of BNNSs, as demonstrated in Fig. 5-2. The naked surface of BNNSs inhibits the mobility of the charge carrier, which directly prevents the construction of percolation network. Their conductivity values increase slightly by prolonging the carbon deposition time from 5

to 45 min.

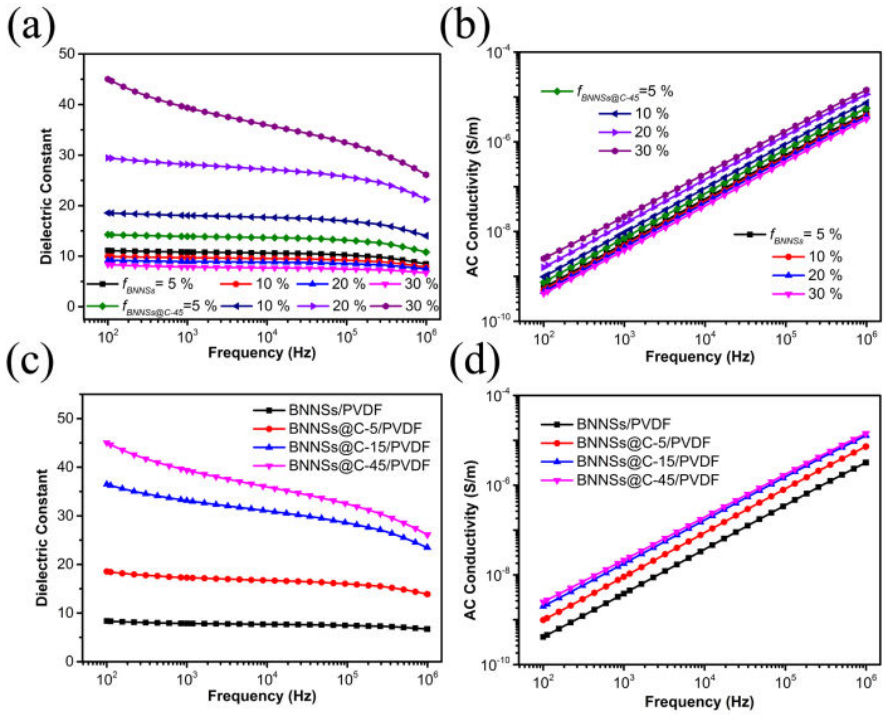

Fig. 5-5 *Frequency dependence of the (a) dielectric constant and (b) conductivity values of BNNSs/PVDF and BNNSs@C-45/PVDF nanocomposites at different filler loadings; Typical frequency-dependent comparison of (c) dielectric constant and (d) conductivity values of BNNSs/PVDF, BNNSs@C-5/PVDF, BNNSs@C-15/PVDF, and BNNSs@C-45/PVDF nanocomposites at equivalent filler loadings (30 vol. %)*

Fig. 5-6 presents the evolution of the dielectric properties of BNNSs/PVDF and BNNSs@C/PVDF nanocomposites with increasing the filler loadings. As shown in Fig. 5-6a, the dielectric constant of BNNSs/PVDF nanocomposites decreases slightly from 11 to 8 with increasing the f_{BNNSs} up to 30 vol. %. However, the BNNSs@C/PVDF nanocomposites exhibit a monotonous increasing tendency with the increasing of hybrids loading. Typically, the dielectric constant increases from 11 to 39 for the BNNSs@C-45/PVDF nanocomposites with increasing the hybrids loading up to 30 vol. %. The remarkable enhancement of dielectric constant after coating with the carbon layer could be mainly attributed to the gradual formation of the micro-capacitor network. Two types of micro-capacitors exist in BNNSs@C/PVDF nanocomposites. Each of BNNSs@C hybrid forms the first type of

capacitor with the carbon layer as the electrode and BNNSs as the dielectric. The other kind of micro-capacitor consists of the adjacent conductive carbon layer in two different hybrids and the host PVDF in between, where the carbon layer and PVDF serve as electrodes and dielectric, respectively. These local micro-capacitor networks would be constructed with gradually increasing hybrids loading, which leads to the remarkable promotion of the dielectric permittivity. Besides, the dielectric constant of nanocomposites at the same amount of filler loading increases monotonously with the thickening carbon layer thickness of BNNSs@C hybrids. As illustrated in the Fig. 5-6d, the dielectric constant augments from 8 for BNNSs/PVDF nanocomposites to 39 for BNNSs@C/PVDF nanocomposites at 30 vol. % filler loading. With prolonging the carbon deposition time, the elevated carbon content in the hybrids will undoubtedly thicken the carbon layer, resulting in the dramatical reduction of PVDF dielectric thickness between the adjacent carbon layers. According to the Eq. 3-1, the total capacitance stored in the second type of capacitor, as mentioned above, would sharply increase at the same amount of filler loading. Nevertheless, compared with the enhancement of dielectric constant in those percolative nanocomposites, the improvement of dielectric constant obtained in the current work is limited. The reported percolation behavior does not occur even if the nanocomposites is incorporated by the hybrids with a longer carbon deposition time (45 min) at a higher hybrids filler loading (30 vol. %). The discontinuous carbon layer on the surface of BNNSs makes it difficult for the construction of percolation network. Therefore, the obtained enhancement of dielectric constant in current work is limited. As displayed in Fig. 5-6b, the tendency of dielectric loss as a function of filler loading for BNNSs@C/PVDF nanocomposites exhibits the identical results that the loss increases monotonously with the increase of hybrid loading. For instance, the dielectric loss augments from 0.013 to 0.084 for the BNNSs@C-45/PVDF nanocomposites with increasing $f_{BNNSs@C\text{-}45}$ up to 30 vol. %. Besides, the nanocomposites at the same amount of filler loading exhibit similar carbon layer thickness-dependent behavior of dielectric loss. The dielectric loss augments from 0.016 for BNNSs/PVDF

nanocomposites to 0.084 for BNNSs@C-45/PVDF nanocomposites at an equivalent filler loading (30 vol. %). The increased dielectric loss of the nanocomposites with increasing the carbon coating amount in the hybrids could be ascribed to thickening of the carbon layer around the surface of BNNSs, which shortens the distance for the adjacent BNNSs@C hybrids. Therefore, the resultant tunneling current is easier to pass through the adjacent hybrids, which leads to the increased dielectric loss after increasing the carbon coating amount. As for the conductivity part presented in Fig. 5-6c, the filler loading and carbon layer thickness-dependent behavior of conductivity show the similar tendency that has been discussed in the dielectric constant and loss parts.

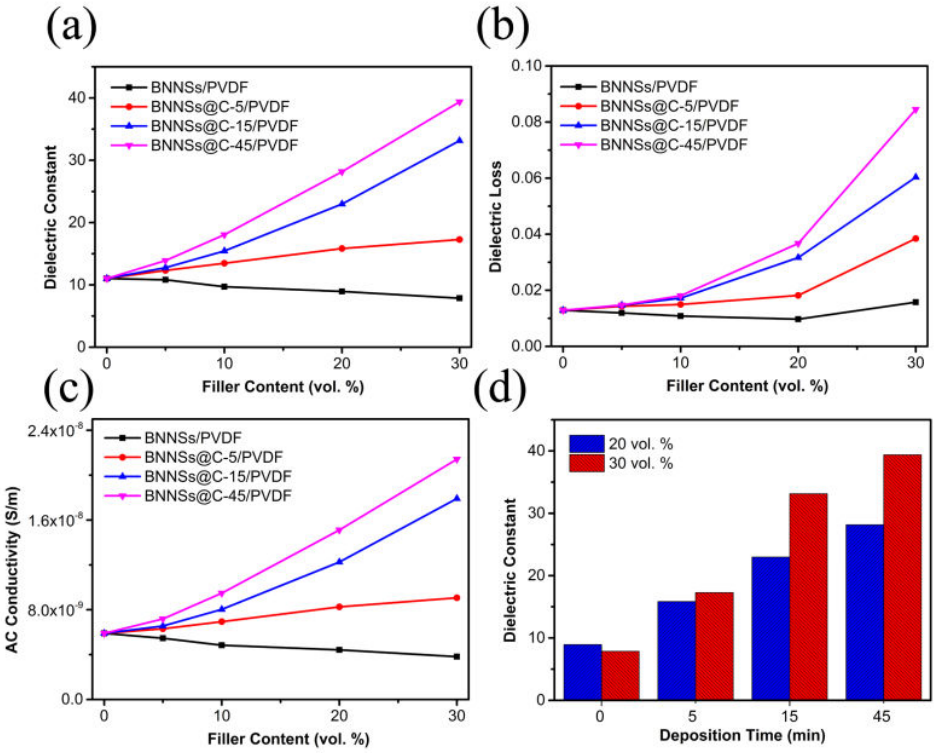

Fig. 5-6 *Dependence of the (a) dielectric constant; (b) dielectric loss; and (c) conductivity values of BNNSs/PVDF, BNNSs@C-5/PVDF, BNNSs@C-15/PVDF, and BNNSs@C-45/PVDF nanocomposites on the filler loadings (10^3 Hz); (d) Typical variation of dielectric constant values (10^3 Hz) of BNNSs/PVDF and BNNSs@C/PVDF nanocomposites as a function of carbon deposition time at different filler loadings (20 and 30 vol. %)*

5.4 Conclusions

In this chapter, the BNNSs@C hybrids with different carbon contents were synthesized by the CVD method. The carbon content in the as-obtained BNNSs@C hybrids could be accurately adjusted from 2.50 to 22.62 wt. % through controlling the carbon deposition time. With the help of solution and melting blending methods, the BNNSs@C/PVDF nanocomposites were obtained by incorporating the BNNSs@C hybrids into PVDF matrix. The as-obtained BNNSs@C/PVDF nanocomposites exhibit an excellent dielectric performance and the dielectric properties could be accurately tuned by adjusting the carbon content. The improved interfacial polarizations of BNNSs/C and C/PVDF interfaces endow the nanocomposites with enhanced dielectric performance. These nanocomposites with distinguished dielectric performance could find their potential applications in the electronics industry.

Chapter VI

Core@Shell Structured TiO_2@Carbon Nanowires PVDF Nanocomposites

6.1 Introduction

Recently, many experimental and theoretical results have demonstrated that inorganic fillers with a high aspect ratio could enhance the dielectric constant of nanocomposites more efficiently than those with a spherical shape [84, 92, 119, 124]. With the help of micromechanics and finite element models, Andrews and his co-workers devoted their efforts to study the influences of aspect ratio and orientation parameters on the electro-elastic properties of the corresponding polymer nanocomposites and demonstrated that these two parameters play a critical role in achieving a high dielectric constant and excellent electromechanical coupling performance [91]. As indicated in their models, the electromechanical coupling could be enhanced as much as 60 times by increasing the aspect ratio of inclusion. Tang et al. reported that the dielectric properties and energy storage density of nanocomposites could be significantly enhanced by utilizing the high aspect ratio lead zirconate titanate (PZT) [135, 181], TiO_2 [182], $BaTiO_3$ [92], and CCTO nanowires (NWs) [124]. For instance, P(VDF-TrFE-CFE) nanocomposites incorporated with 17.5 vol. % BT NWs could afford a dielectric constant of about 69.5, while the dielectric constant of nanocomposites with 30 vol. % BT nanoparticles is merely 52 [84]. Furthermore, the relationship between the aspect ratio and dielectric constant was subsequently revealed by Tang and his co-workers, indicating that the dielectric constant could be extremely efficiently improved by loading polymers with high aspect ratio nanowires [92]. Besides, the dielectric constant could be further improved via aligning these nanowires along the axis of the electric field.

Although enhanced dielectric properties have been achieved by utilizing single

component nanowires, the obtained dielectric constant at a low filler loading still fails to meet the desired expectations. Recently, a promising concept for designing core-shell structured ceramic/conductor hybrids has drawn tremendous interest. Luo and his co-workers utilized Ag-deposited $BaTiO_3$ (BT-Ag) hybrids to avoid the agglomeration of Ag nanoparticles in a PVDF matrix, where a high dielectric constant of about 94.3 at 43.4 vol. % filler loading was obtained [109]. A novel type of CCTO@Ag hybrid was further developed to fabricate PI nanocomposites, which exhibited a high dielectric constant of about 10^3 at 3 vol. % filler loading [110]. Besides the metallic shell, the core-shell structured hybrids with a carbon shell could also be utilized to enhance the dielectric constant of nanocomposites. For example, the core-shell structured $BaTiO_3$@carbon (BT@C) hybrids were obtained by Feng and his co-workers with the aid of the CVD method [111]. The hybrids were subsequently incorporated into P(VDF-HFP) to fabricate BT@C/P(VDF-HFP) nanocomposites, which show a giant dielectric constant of about 1044 at 30 vol. % filler loading. The hierarchical flower-like TiO_2/carbon (TiO_2/C) hybrids obtained by a solvothermal method were also adopted as fillers to prepare P(VDF-HFP) nanocomposites, resulting in a dielectric constant of about 330.6 at 20 vol. % filler loading [112]. All these previous efforts demonstrate that the core-shell structured hybrids with a conductive shell could endow nanocomposites with excellent dielectric properties.

Nevertheless, the rational combination of the geometric merits of a high aspect ratio nanowire core with a conductive carbon shell has not yet been systematically investigated. In this chapter, core-shell structured TiO_2@C nanowires with various carbon shell thicknesses were synthesized by a combination of a modified hydrothermal reaction and the CVD method. The synthesis of the pristine TiO_2 NWs with a high aspect ratio was accomplished by a hydrothermal reaction and the coating of the as-obtained TiO_2 NW core with a uniform carbon shell was achieved by the CVD method because of its simplicity and controllability [183, 184]. The thickness of the carbon shell in the TiO_2@C nanowires could be accurately tuned by controlling

the carbon deposition time employed in the CVD procedure. The TiO_2@C NW hybrids were subsequently incorporated into the PVDF matrix by the integration of solution and melt blending procedures. The dielectric properties of the TiO_2@C NW/PVDF nanocomposites could be precisely adjusted by tuning the carbon shell thickness in the TiO_2@C NW hybrids. The results indicate that coating the TiO_2 NWs with a carbon shell could largely enhance the dielectric performance of the TiO_2@C NWs/PVDF nanocomposites. This successful design of a core-shell structure could also be applicable to other ceramic/conductor hybrids to enhance the interfacial polarization of nanocomposites.

6.2 Experimental

6.2.1 Synthesis of TiO_2 NWs and TiO_2@C NW Hybrids

The TiO_2 NWs were prepared from $Na_2Ti_3O_7$ NWs according to a method in the previous literature [119, 182]. The first step in the reaction is to synthesize $Na_2Ti_3O_7$ NWs with a high aspect ratio, which acts as the template for the subsequent synthesis of TiO_2 NWs. In a typical synthetic procedure, 0.94 g of TiO_2 nano-powder (Sigma-Aldrich, ACS certified, 99%, anatase) was homogeneously dispersed in 45 mL of 10 M NaOH (Sigma-Aldrich, ACS certified, 99%) aqueous solution with the assistance of ultra-sonication for 30 min. The mixture was then transferred into a 60 mL Teflon-lined stainless steel autoclave and stirred at 200 °C for 24 h to obtain $Na_2Ti_3O_7$ NWs. The obtained $Na_2Ti_3O_7$ NWs were washed with deionized water by repeated centrifugation at 5000 rpm for 5 min and vortex mixing. The obtained $Na_2Ti_3O_7$ NWs were then soaked in dilute 0.2 M hydrochloric acid aqueous solution for 4 h to produce $H_2Ti_3O_7$ NWs. The $H_2Ti_3O_7$ NW precipitates were then separated from the suspension by centrifugation at 5000 rpm for 5 min and washed with deionized water through centrifugation and vortex mixing several times until the pH reached around 7. The synthesized $H_2Ti_3O_7$ NWs were subsequently dried at 80 °C overnight. Next, the $H_2Ti_3O_7$ NW powders were put into an alumina crucible and then heated to 600 °C for

3 h to obtain TiO_2 NWs. The core-shell structured TiO_2@carbon NWs (TiO_2@C NWs) were subsequently obtained by the CVD method. Briefly, an appropriate amount of TiO_2 NWs was homogeneously dispersed on a quartz plate to serve as the substrate for the deposition of the carbon shell. Afterward, the furnace was heated to 850 ºC under an Ar (1000 s. c. c. m) atmosphere and a certain amount of H_2 (300 s. c. c. m) was introduced to reduce the oxygen functional groups. Then a small number of C_2H_2 (40 s. c. c. m) was introduced into the reactor and the reaction time was fixed at 15 min. After the synthesis, the reactor was cooled down to room temperature under an Ar atmosphere (1000 s. c. c. m). Finally, the resultant products were separately collected using a cutting blade. According to the time employed in the CVD procedures, the hybrids are denoted as TiO_2@C-x NWs, where x represents the carbon deposition time (min).

6.2.2 Preparation of TiO_2 NWs/PVDF and TiO_2@C NWs/PVDF Nanocomposites

The TiO_2@C NWs/PVDF nanocomposites with different TiO_2@C NW filler loadings ($f_{TiO2@C}$) were prepared by employing a combination of solution casting and extrusion-injection processing in order to achieve a better dispersion of the nano-fillers in the PVDF matrix. Firstly, the desired amount of TiO_2@C NWs was ultrasonically dispersed into DMF solvent for 2 h. Next, the PVDF powders (Kynar 761, Arkema Group, France) were subsequently introduced into the suspension of the TiO_2@C NWs and the mixture was further magnetically stirred at 70 ºC for 2 h. After that, the temperature was increased up to 100 ºC and held for 1 h to evaporate the majority of DMF solvent. The obtained pre-mixture was then dried in a vacuum oven at 80 ºC for 12 h to further eliminate the residual solvent. Secondly, the as-obtained TiO_2@C NWs/PVDF mixture was cut into small pieces and they were subsequently melt-blended using a two-screw micro-extruder with a speed of 90 rpm at 220 ºC for 30 min under an Ar protective atmosphere. Finally, the slabs were obtained by the injection molding strategy. The obtained $f_{TiO2@C}$ in the TiO_2@C NWs/PVDF nanocomposites varied from 0 to 20 vol. %. The TiO_2 NWs/PVDF nanocomposites

were fabricated using similar procedures, where $f_{TiO2@C}$ represents the filler loading of the pristine TiO_2 NWs.

6.2.3 Characterizations

The morphology of the TiO_2 NWs, TiO_2@C NWs, and their nanocomposites were performed using a SEM (HITACHI SU8010) operated at 5.0 kV and a TEM (FEI Titan) equipped with a high angle annular dark-field (HAADF) detector and an aberration-corrected condenser operating at 200 kV. A scanning TEM-energy dispersive X-ray (STEM-EDX) spectroscopy was used to obtain elemental mapping images. X-ray diffraction (XRD) study and Raman spectroscopic study were carried out using an XRD detector (Bruker D2 PHASER with X-Flash 430) and a Jobin Yvon-LabRAM spectrometer, respectively. Fourier transform infrared spectroscopy (FT-IR, Bruker Tensor 27) was employed to characterize the nanocomposites. The mass fraction of carbon was determined by thermogravimetric analysis (TGA, NETZSCH STA 449 F3). The TGA furnace was heated from 50 to 800 ^oC at a rate of 5 ^oC min^{-1} under a N_2 (20 s. c. c. m) and an O_2 (20 s. c. c. m) atmosphere. Both sides of the samples were painted with silver paste and their dielectric properties were characterized using an impedance analyzer (Solatron 1260) at room temperature. D-E loops were collected using a commercial piezoelectric evaluation system Aixacct 2000 with a sine unipolar wave at 10 Hz.

6.3 Results and Discussions

As shown in Fig. 6-1, the core-shell structured TiO_2@C NWs were synthesized by a combination of a modified hydrothermal reaction and the CVD method using C_2H_2 as the carbon source and Ar as the carrier gas. The synthesis of the TiO_2 NWs was accomplished using the $Na_2Ti_3O_7$ NWs by a two-step method described in the previous literature [119, 182]. The obtained TiO_2 NWs were subsequently employed as the substrate for the deposition of carbon in the following CVD process. The TiO_2 NWs were homogeneously dispersed on the surface of a quartz plate which was then

kept in the middle of the heated region. An appropriate amount of H_2 was introduced to reduce the oxygen functional groups on the surface of the TiO_2 NWs at the elevated temperature (850 °C), which can eliminate their influences on the ultimate dielectric performance of the nanocomposites. The structural feature of the carbon shell in the TiO_2@C NW hybrids depends largely on the carbon deposition conditions used. Higher temperatures facilitate the formation of defect-free graphene layers, while low temperatures decrease their graphitization degree and induce the formation of amorphous carbon layers [66, 172].

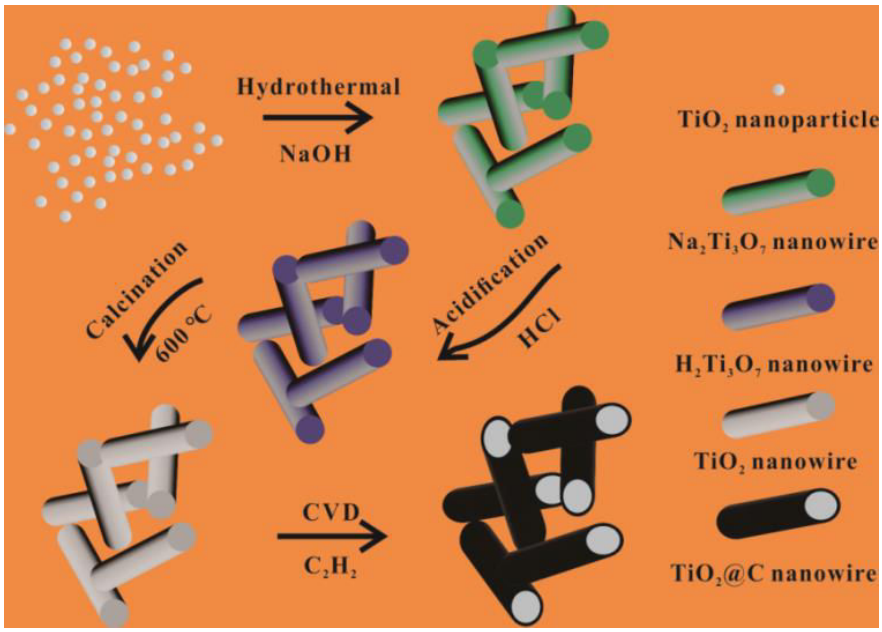

Fig. 6-1 *Schematic illustration of the synthesis procedures of core-shell structured TiO_2@C NWs.*

SEM and TEM measurements were carried out to identify the morphologies of the pristine TiO_2 NWs and the core-shell structured TiO_2@C-15 NWs. Fig. 6-2a shows the free-standing TiO_2 NWs with a mean length of ca. 20 μm and a mean diameter of ca. 40-80 nm. TEM image of a single TiO_2@C-15 NW is displayed in Fig. 6-2b. As indicated by the arrow, the single TiO_2 NW is uniformly covered by a continuous carbon shell with a thickness of 7 nm, where no naked TiO_2 NW part could be observed. Fig. 6-2c presents the HAADF image on a high resolution scale and the corresponding EDS elemental maps of the TiO_2@C-15 nanowire are displayed in Fig. 6-2d and e. Fig. 6-2c suggests that the degree of carbon shell

crystallinity in the TiO_2@C NWs is extremely low. The elements Ti, O, and C are denoted in green, blue, and red, respectively. As shown in Fig. 6-2d and e, the Ti and O signals exhibit strong intensity in the nanowire center and a sharp disappearance in the shell layer. In contrast, the signal intensity of the C atom in the shell is stronger than that in the core (Fig. 6-2f). From the enlargement of nanowire's diameter, the thickness of the carbon shell is calculated to be about 7 nm, which is in agreement with the results in Fig. 6-2b and c. The STEM-EDS technique employed here is able to map out the elemental distribution at a nanometer-scale spatial resolution and provides a clear vision of the core-shell structured TiO_2@C NW hybrids.

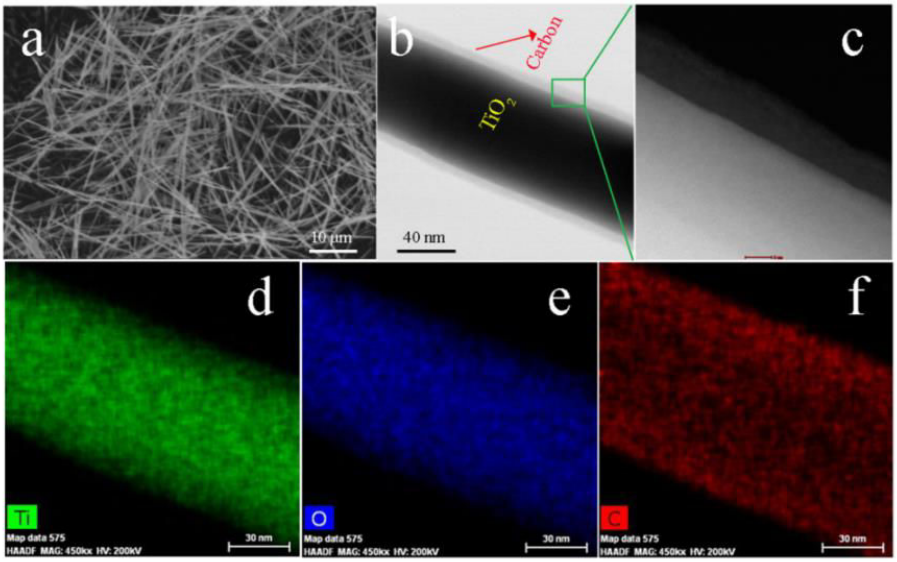

Fig. 6-2 *(a) SEM image of TiO_2 NWs; (b) BF-STEM image of the single core-shell structured TiO_2@C-15 NW hybrid; (c) HAADF-STEM image of the corresponding enlarged region indicated by the green rectangle in part b; (d-f) EDX elemental maps of Ti, O, and C, respectively.*

To get more precise structure and composition information about the TiO_2@C NW hybrids, XRD studies, Raman spectroscopy, and TGA characterization were conducted and the results are presented in Fig. 6-3, Fig. 6-4 and Fig. 6-5. The XRD patterns of the pristine TiO_2 NWs and the as-synthesized TiO_2@C NW hybrids are given in Fig. 6-3a and Fig. 6-4. All the diffraction peaks could be indexed to the anatase-type TiO_2 without any impurity according to JCPDS card no. 21-1272 [119]. Meanwhile, no graphitic structure of the carbon species could be detected, indicating

that the carbon shell might exist in the amorphous phase [185, 186]. A similar crystalline structure of carbon hybrids has been reported in the literature with BT@C and TiO_2/C hybrids [185, 186]. Furthermore, the characteristic peak intensity of the TiO_2 core in the TiO_2@C NWs weakened after coating with the carbon shell, which could be illustrated by the shielding effect of the carbon shell. The existence of the carbon shell was confirmed by Raman spectroscopy, which is a powerful tool to identify carbon and its derivatives. As presented in Fig. 6-3b and Fig. 6-5, all the hybrids display two characteristic peaks around 1350 and 1580 cm^{-1}, corresponding to the typical D and G bands of the carbon species, respectively. The D band is usually attributed to the presence of amorphous or disordered carbon, while the G band is commonly associated with the sp^2-bonded carbon atoms. The intensity ratio of D band over G band (I_D/I_G) is usually used to quantify the graphitic ordering degree. The I_D/I_G value of the as-synthesized TiO_2@C-15 NW hybrids (3.02) is extremely higher than those of the reported carbon hybrid systems [66, 111], which further confirms the conclusion that the carbon shell might exist in the amorphous phase. As illustrated in Fig. 6-3c, the TGA measurement was performed to calculate the mass fraction of the carbon shell in the hybrids. For comparison, the TGA curve of pristine TiO_2 NWs is also displayed in Fig. 6-3c. All three types of TiO_2@C NW hybrids exhibit a remarkable weight loss stage around 450 °C, which is in accordance with the reported decomposition temperature range (< 500 °C) of amorphous carbon [185, 186]. The TGA results not only prove the existence of the carbon shell in the hybrids but also reflect the structured feature of the carbon shell. Additionally, the mass fraction of the carbon shell in the hybrids increases monotonically from 4.46 wt. % for the TiO_2@C-5 NWs to 26.23 wt. % for the TiO_2@C-45 NWs upon increasing the CVD time from 5 min to 45 min, which demonstrates that the composition of the hybrids could be precisely regulated by controlling the parameters involved in the CVD procedures. The thickness of the carbon shell in the TiO_2@C NWs increases from 4 nm to 40 nm upon increasing the deposition time from 5 min to 45 min (Fig. 6-3d).

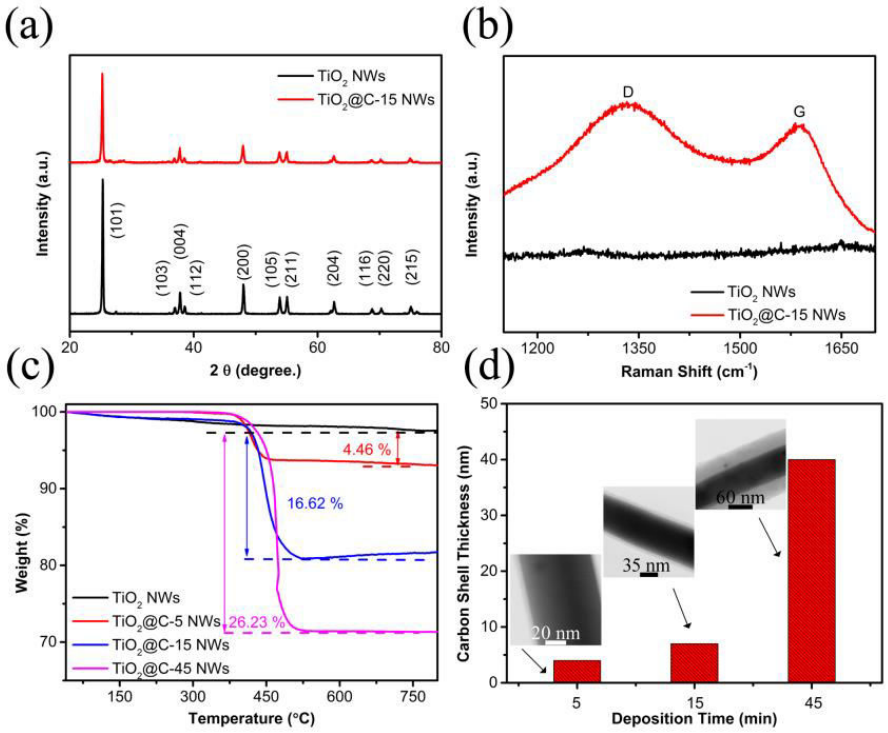

Fig. 6-3 *(a) XRD patterns, (b) Raman spectra, and (c) TGA curves of the pristine TiO_2 NWs and the corresponding TiO_2@C NW hybrids with different carbon shell thicknesses; (d) the dependence of the carbon shell thickness in the core-shell structured TiO_2@C NW hybrids on the deposition time used in the CVD procedure. The insets in part d show the corresponding BF-STEM images of the TiO_2@C NWs with different carbon shell thicknesses.*

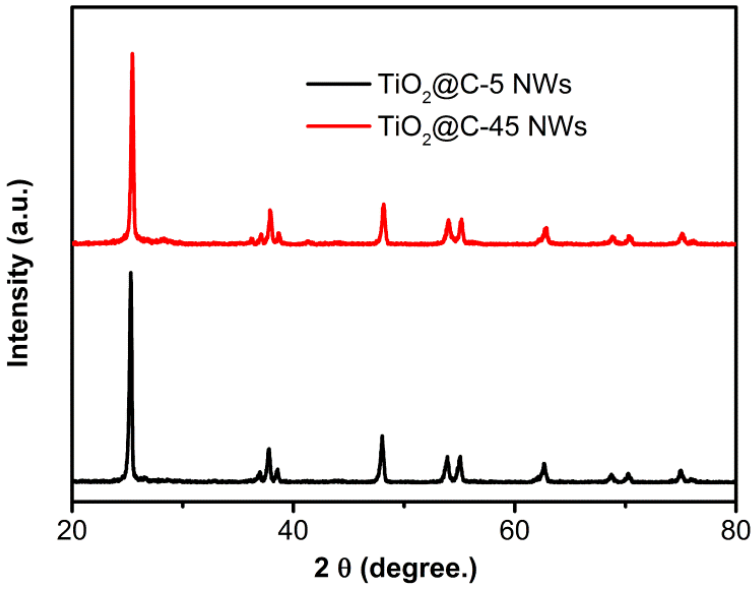

Fig. 6-4 *XRD patterns of TiO_2@C NWs hybrids with different carbon shell thickness.*

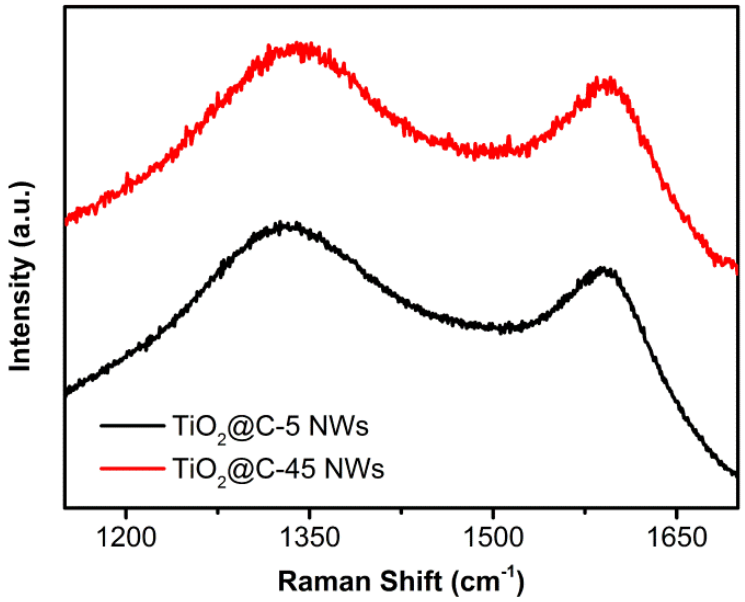

Fig. 6-5 *Raman spectra of TiO_2@C NWs hybrids with different carbon shell thickness.*

The SEM images of the fracture surfaces of the pristine TiO_2 NWs/PVDF and TiO_2@C NWs/PVDF nanocomposites are shown in Fig. 6-6. As shown in Fig. 6-6b, c, and d, the TiO_2@C NWs disperse well in the polymer matrix. Additionally, some pristine TiO_2 NWs were found to be stretched out of the polymer matrix, indicating the weak interface adhesion between the pristine TiO_2 NWs and the PVDF matrix. In contrast, the TiO_2@C NWs were embedded well inside the polymer matrix. All these aforementioned results indicate that the carbon shell of the TiO_2@C NWs is helpful in improving the interface adhesion between the TiO_2 NWs and the PVDF matrix.

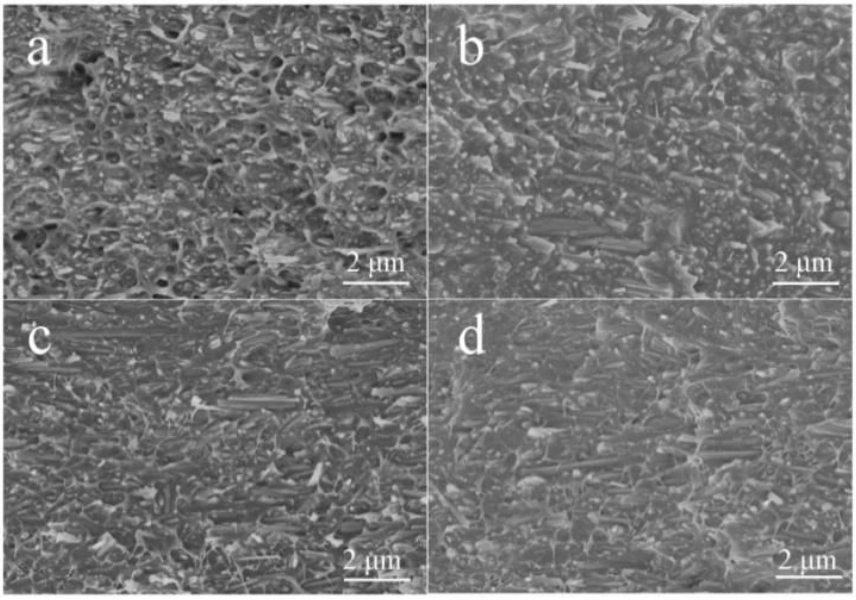

Fig. 6-6 *SEM images of the fracture surfaces of (a) TiO_2 NWs/PVDF, (b) TiO_2@C-5 NWs/PVDF, (c) TiO_2@C-15 NWs/PVDF, and (d) TiO_2@C-45 NWs/PVDF nanocomposites at 15 vol. % filler loading.*

Fig. 6-7 and Fig. 6-8 compare the frequency-dependent dielectric behaviors of the TiO_2@C NWs/PVDF nanocomposites with three types of the TiO_2@C NW hybrids at the equivalent filler loading (15 vol. % and 20 vol. %). As illustrated in Fig. 6-7a and Fig. 6-8, all the nanocomposites exhibit remarkably enhanced dielectric constant and loss compared with those of the pure PVDF resin matrix and the PVDF nanocomposites incorporated with the pristine TiO_2 NWs. The dielectric constant and loss of the PVDF nanocomposites loaded with the same kind of TiO_2@C NW hybrid at a high filler loading (20 vol. %) exhibit a stronger frequency-dependent behavior when compared with those of the nanocomposites at a low filler loading (15 vol. %). Similar trends have also been observed in other percolative nanocomposites [22, 66]. Meanwhile, the dielectric constant and loss values of the TiO_2@C-15 NWs/PVDF and TiO_2@C-45 NWs/PVDF nanocomposites increase sharply upon increasing the filler loading from 15 vol. % to 20 vol. %. The remarkable dielectric behavior enhancement from 15 vol. % to 20 vol. % could be attributed to the established percolation network, which would be discussed in the following part. Nevertheless, the dielectric constant values of the PVDF nanocomposites filled with the TiO_2@C-5 NWs increase

moderately with the increase of the filler loading from 15 vol. % to 20 vol. %. Additionally, the frequency dependence of the dielectric constant and loss of the PVDF nanocomposites incorporated with different kinds of TiO_2@C NW hybrids at the same filler loading becomes more evident with increasing carbon shell thickness of the TiO_2@C NW hybrids. The remarkable frequency dependence of dielectric constant and loss is derived from the Maxwell-Wagner-Sillars (MWS) relaxation, which occurs when there is an accumulation of charge carriers at the interfaces of heterogeneous components with different relaxation times. The MWS polarization occurs only in a low frequency range due to its long relaxation time. Therefore, the variation in dielectric constant and loss becomes relatively steady at higher frequencies. The relaxation times of the TiO_2 core and the PVDF matrix are several orders of magnitude longer than that of the carbon shell. Therefore, the injected charges are tremendously blocked at the interface of TiO_2/carbon and carbon/PVDF, accordingly enhancing the dielectric constant and loss significantly in a low frequency range. The conductivity values of the nanocomposites as a function of frequency in part b of Fig. 6-7 indicate the identical result that the conductivities of the nanocomposites with the same kind of hybrid increase abruptly with increasing filler loading from 15 vol. % to 20 vol. %. The absolute conductivity values at 10^2 Hz of the nanocomposites with the same type of hybrid at 20 vol. % filler loading are approximately two orders of magnitude higher than those of the nanocomposites at 15 vol. % filler loading. The conductivities of the nanocomposites incorporated with 20 vol. % of TiO_2@C-15 NW and TiO_2@C-45 NW hybrids are almost independent of the frequency in the low-frequency range, which indicates that their conductive networks have been established due to the direct contact of the hybrids in the PVDF matrix. However, their conductivities at 15 vol. % filler loading exhibit a strong frequency-dependent characteristic in the whole frequency range, which shows that their percolation values are located in the range of 15 vol. % and 20 vol. %. For the part of the nanocomposites filled with the TiO_2@C-5 NW hybrids, their conductivities exhibit a similar strong frequency dependent characteristic in the whole frequency

range, which reflects that their percolation transition critical point is beyond 20 vol. %. Besides, being similar to the tendency presented in the dielectric constant and loss parts, the conductivity values at the same filler loading increase with increasing carbon shell thickness in the core-shell structured TiO_2@C NW hybrids. In order to make an accurate comparison, the dielectric constant, loss and AC conductivity values of the nanocomposites at 10^3 Hz are taken and given in the following part.

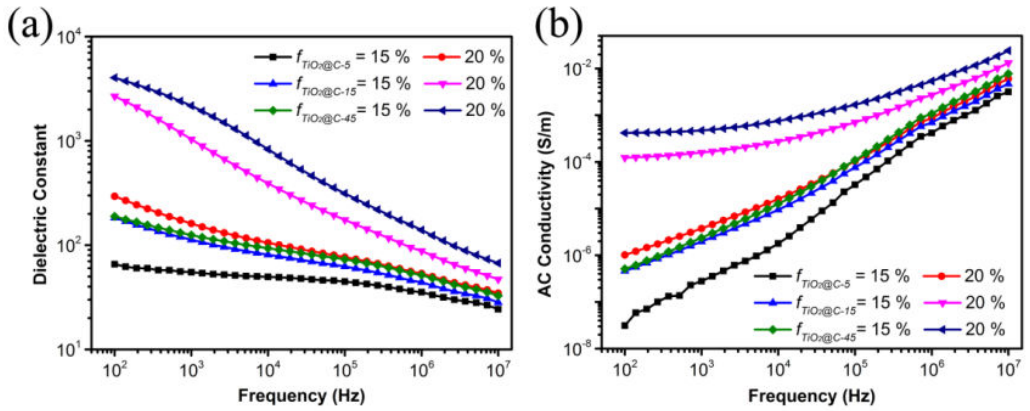

Fig. 6-7 *Frequency dependence of the (a) dielectric constant and (b) AC conductivity values of the TiO_2@C-5 NWs/PVDF, TiO_2@C-15 NWs/PVDF, and TiO_2@C-45 NWs/PVDF nanocomposites at different filler loadings (15 vol. % and 20 vol. %).*

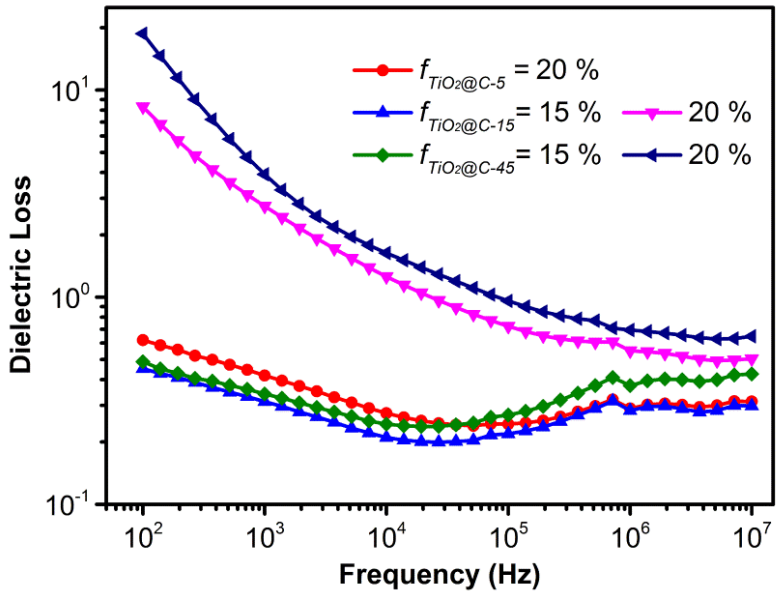

Fig. 6-8 *Frequency dependence of the dielectric loss values of TiO_2@C-5 NWs/PVDF, TiO_2@C-15 NWs/PVDF and TiO_2@C-45 NWs/PVDF nanocomposites at different filler loadings.*

Fig. 6-9 shows the evolution of the dielectric properties of the TiO_2 NWs/PVDF and TiO_2@C NWs/PVDF nanocomposites with increasing filler loading. According to Fig. 6-9a, all the nanocomposites with the same type of hybrid exhibit a monotonic increasing tendency with increasing filler loading. Typically, the dielectric constant increases from 9 to 2171 for the TiO_2@C-45 NWs/PVDF system when the hybrid loading is increased to 20 vol. %. The colossal enhancement of the dielectric constant after wrapping the inorganic TiO_2 NW core with the carbon shell could be mainly attributed to the gradual formation of the interface network. Two types of interfaces used for the accumulation of injection charges exist in the TiO_2@C NWs/PVDF nanocomposites. The first type of interface is the interface between the uniform carbon shell and the TiO_2 NW core. The other type of interface exists in the carbon shell and the host PVDF. With a gradually increasing hybrid loading, these interface networks are gradually constructed, resulting in a significant enhancement of the dielectric permittivity. Meanwhile, the difference in the dielectric constants of the pristine TiO_2 NWs/PVDF and TiO_2@C NWs/PVDF nanocomposites at the same filler loading becomes more obvious when the filler loading exceeds 10 vol. %. The dielectric constants of the TiO_2@C-15 NWs/PVDF and TiO_2@C-45 NWs/PVDF systems undergo a significant augmentation when the hybrid loading increases from 15 vol. % to 20 vol. %, which is a typical characteristic of percolative nanocomposites. Upon increasing the hybrid loading from 15 vol. % to 20 vol. %, the dielectric constant increases from 113 to 1035 for the TiO_2@C-15 NWs/PVDF system and 125 to 2171 for the TiO_2@C-45 NWs/PVDF system, respectively, which undergoes several orders of magnitude enhancement. Nevertheless, the dielectric constant increases moderately from 23 to 27 for the TiO_2 NWs/PVDF system and 55 to 161 for the TiO_2@C-5 NWs/PVDF system, respectively. The exponential enhancement of the dielectric constant of the TiO_2@C-15 NWs/PVDF and TiO_2@C-45 NWs/PVDF systems from 15 vol. % to 20 vol. % originates from two types of contributions as follows. The first part of the contribution could be illustrated by a micro-capacitor model. As the volume fraction of the hybrids approaches the f_c from

below, the exponentially decreased inter-particle distance leads to an abrupt augmentation of the capacitance of the local capacitors. The second part of the contribution results from the gradually increased amount of interfaces between the carbon shell and the TiO_2 NW core. As for the part of the dielectric loss shown in Fig. 6-9b, the tendency of the dielectric loss as a function of the filler loading indicates the identical results that the loss increases monotonically with increasing filler loading. For instance, as displayed in Fig. 6-10, the dielectric loss increases sharply from 0.008 to 3.92 for the TiO_2@C-45 NWs/PVDF nanocomposites upon increasing the hybrids loading to 20 vol. %. Besides, the diversity of the dielectric loss beyond 10 vol. % of filler loading also becomes more evident for the TiO_2 NWs/PVDF and TiO_2@C NWs/PVDF nanocomposites at the same filler loading, which is in accordance with the results in Fig. 6-9a. Upon increasing filler loading from 15 vol. % to 20 vol. %, the dielectric loss increases moderately from 0.06 to 0.07 for the TiO_2 NWs/PVDF system and 0.09 to 0.42 for the TiO_2@C-5 NWs/PVDF system, respectively. However, for the parts of TiO_2@C-15 NWs/PVDF and TiO_2@C-45 NWs/PVDF, their losses increase from 0.31 to 2.75 for the TiO_2@C-15 NWs/PVDF part and 0.34 to 3.92 for the TiO_2@C-45 NWs/PVDF part, respectively. The enhancement of the dielectric loss by several orders of magnitude reflects the typical percolative characteristics as mentioned above. As illustrated in Fig. 6-9c, the filler loading dependent behavior of conductivity also exhibits a similar tendency that has been discussed in the dielectric constant and loss parts.

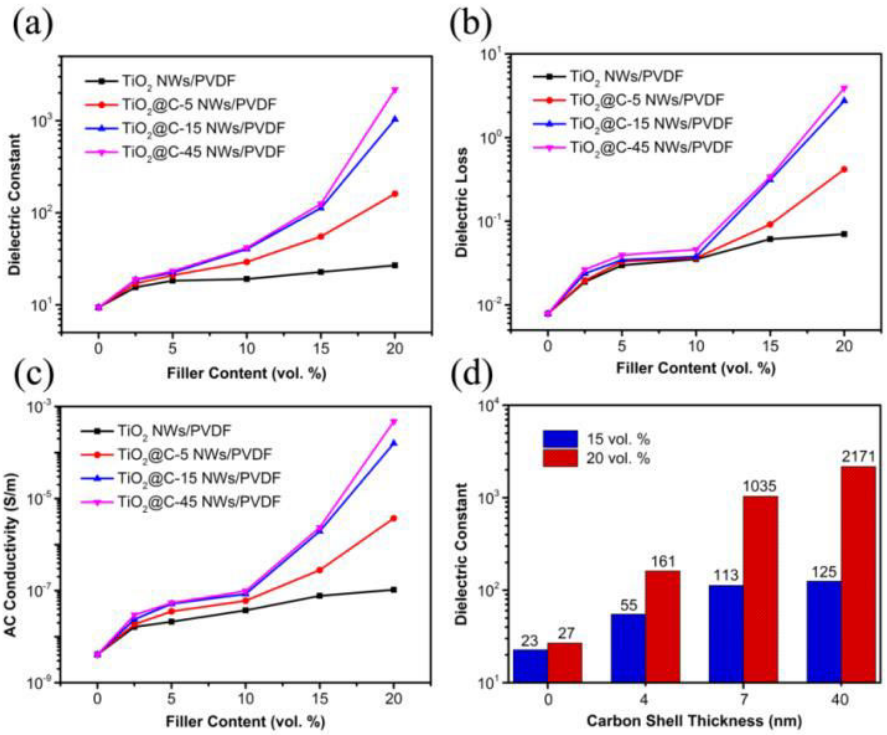

Fig. 6-9 *Dependence of the (a) dielectric constant, (b) dielectric loss, and (c) conductivity values of the TiO_2 NWs/PVDF, TiO_2@C-5 NWs/PVDF, TiO_2@C-15 NWs/PVDF, and TiO_2@C-45 NWs/PVDF nanocomposites on the filler loadings (10^3 Hz); (d) typical variation of the dielectric constant values (10^3 Hz) of the TiO_2 NWs/PVDF and TiO_2@C NWs/PVDF nanocomposites as a function of the carbon shell thickness at different filler loadings (15 vol. % and 20 vol. %).*

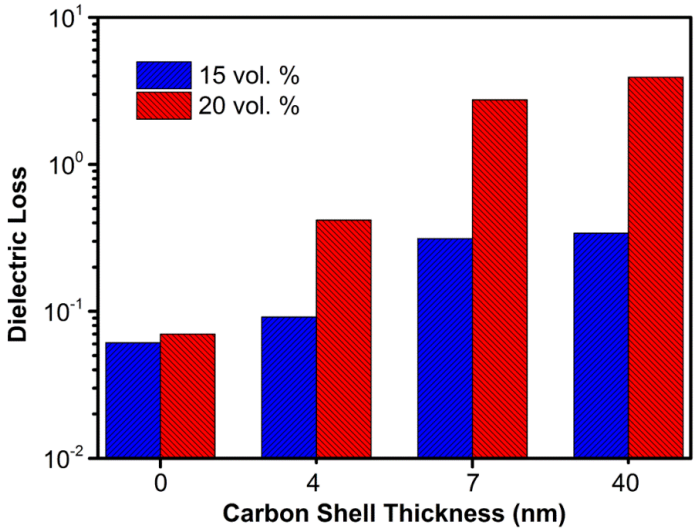

Fig. 6-10 *Typical variation of dielectric loss values (10^3 Hz) of TiO_2 NWs/PVDF, TiO_2@C-5 NWs/PVDF, TiO_2@C-15 NWs/PVDF, and TiO_2@C-45 NWs/PVDF nanocomposites as a function of carbon shell thickness at different filler loadings (15*

vol. % and 20 vol. %).

Besides the contribution associated with the improved interfacial polarization and the typical micro-capacitor model, the crystalline phase composition of PVDF also plays an important role in determining the dielectric performance of the PVDF nanocomposites [186-190]. The semi-crystalline PVDF has two main crystalline forms: α and β phases. The β phase with a high dipolar moment is more attractive because of its superior piezo, pyro, and ferroelectric properties. In particular, the content of the β phase PVDF nanocomposites plays an important role in influencing the dielectric properties. Therefore, FT-IR spectra and XRD patterns of the typical PVDF nanocomposites were recorded, and are displayed in Fig. 6-11 and Fig. 6-12. The crystalline forms and phase composition of pure PVDF and PVDF nanocomposites were revealed by the FT-IR spectra. As presented in Fig. 6-11a and b, the marked transmittance bands at 766 cm^{-1} and 840 cm^{-1} could be attributed to the α and β phases, respectively. The relative fraction of the β phase (f_β) could be evaluated by the following equation.

$$f_\beta = \frac{A_\beta}{(K_\beta/K_\alpha)A_\alpha + A_\beta} \times 100 \quad (6\text{-}1)$$

where A_α and A_β are the areas of the peaks at 766 cm^{-1} and 840 cm^{-1}, respectively. K_α and K_β are the absorption coefficients at the respective wavenumber, whose values are 6.1×10^4 and 7.7×10^4 cm^2 mol^{-1}, respectively. The calculated relative content of the β phase in pure PVDF and TiO_2@C-15 NWs/PVDF nanocomposites with different filler loadings is displayed in Fig. 6-11c. The relative content of the β phase increases with increasing filler loading. As displayed in Fig. 6-11d, the relative β phase content of the PVDF nanocomposites at the same filler loading increases after constructing a carbon shell. The XRD patterns of pure PVDF and typical PVDF nanocomposites are displayed in Fig. 6-12. The typical XRD peaks at 17.6°, 18.3°, and 19.9° could be attributed to the α phase of pure PVDF and its nanocomposites. The XRD peak at 20.26° could be attributed to the β phase. The degree of crystallinity (X_c %) of pure PVDF and its nanocomposites could be obtained by separating and analyzing multiple peaks from the XRD spectra. The detailed peak fitting results are presented in Fig. 6-

13 and Fig. 6-14, respectively. The X_c was calculated according to Murthy's method as follows.

$$X_C = \frac{I_c}{I_c + I_a} \times 100\ \% \tag{6-2}$$

where I_c and I_a are the XRD intensities of the crystalline phase and amorphous halo, respectively. By combining the mentioned two equations, the fraction of the β phase (F_β) could be calculated by

$$F_\beta = X_c \times f_\beta \tag{6-3}$$

The obtained X_c and F_β values are presented in Fig. 6-12c and d. The β phase in the total crystalline phase increases upon increasing the filler loading and the thickness of the carbon shell. Therefore, the increased β phase content in the PVDF nanocomposites would also lead to an improvement in the dielectric performance.

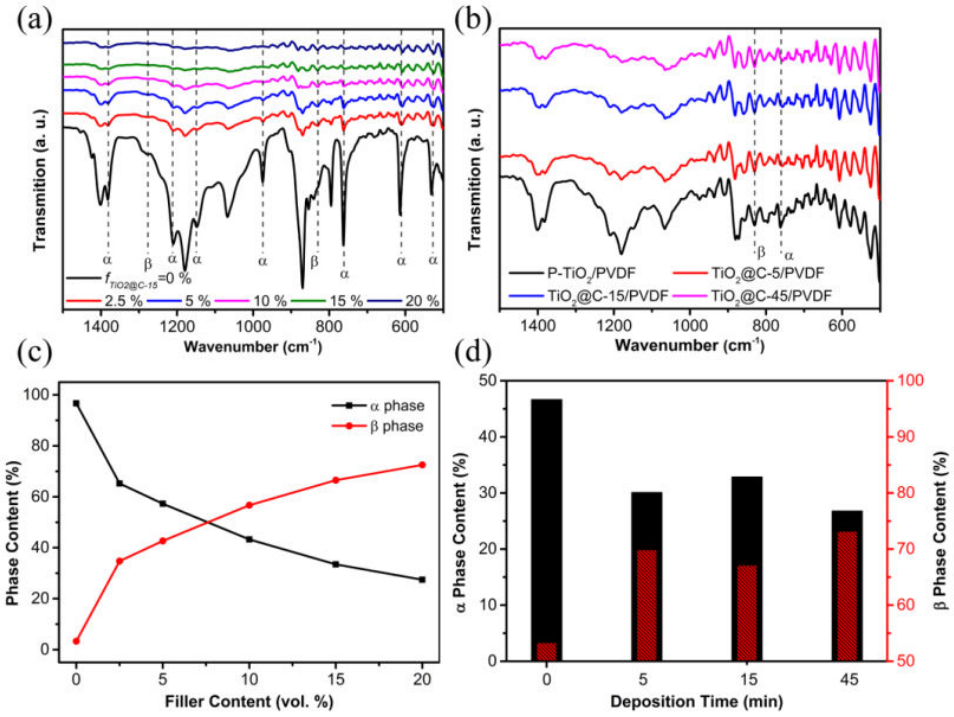

Fig. 6-11 *FT-IR spectra of (a) PVDF and TiO_2@C-15 NWs/PVDF nanocomposites with different filler loadings and (b) TiO_2 NWs/PVDF and TiO_2@C NWs/PVDF nanocomposites with different hybrids at the same filler loading (15 vol. %); (c) The calculated relative content of α and β phase in PVDF and TiO_2@C-15 NWs/PVDF nanocomposites as a function of filler loading; (d) The calculated relative content of α and β phase in TiO_2 NWs/PVDF and TiO_2@C NWs/PVDF nanocomposites at 15*

vol. % filler loading as a function of CVD time.

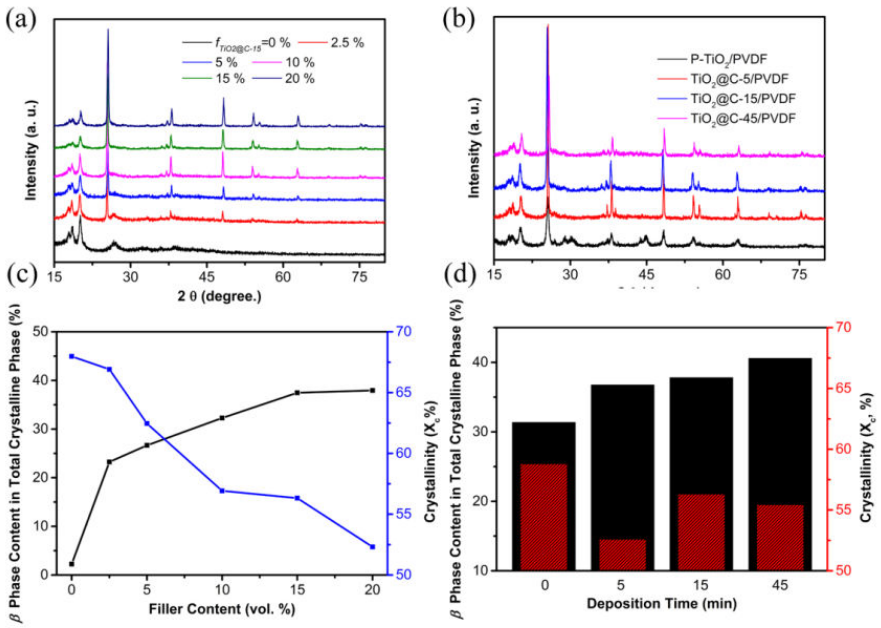

Fig. 6-12 *XRD patterns of (a) PVDF and TiO_2@C-15 NWs/PVDF nanocomposites with different filler loadings and (b) TiO_2 NWs/PVDF and TiO_2@C NWs/PVDF nanocomposites with different hybrids at the same filler loading (15 vol. %); (c) The calculated content of β phase in total crystalline phase of PVDF and TiO_2@C-15 NWs/PVDF nanocomposites as a function of filler loading; (d) The calculated content of β phase in total crystalline phase of TiO_2 NWs/PVDF and TiO_2@C NWs/PVDF nanocomposites at 15 vol. % filler loading as a function of CVD time.*

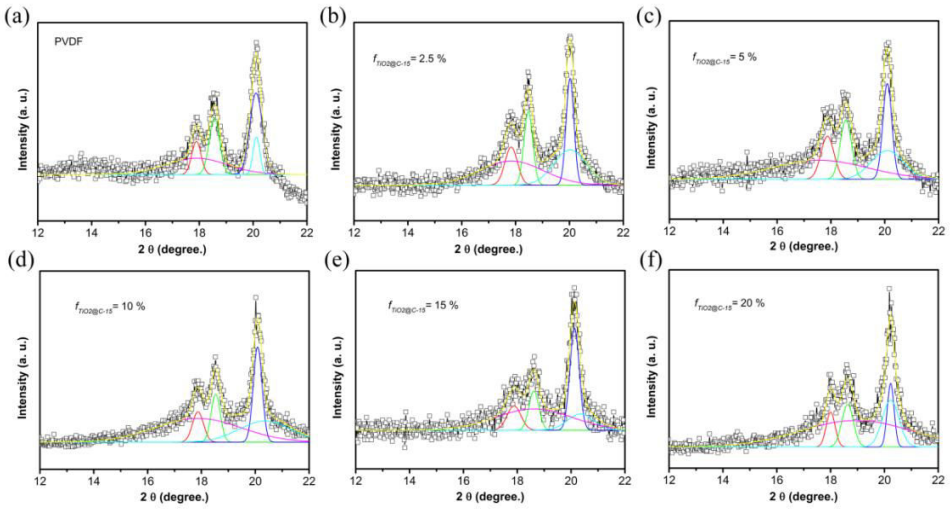

Fig. 6-13 *Origin's multiple peak separation fitting results of PVDF and TiO_2@C-15*

NWs/PVDF nanocomposites with different filler loadings.

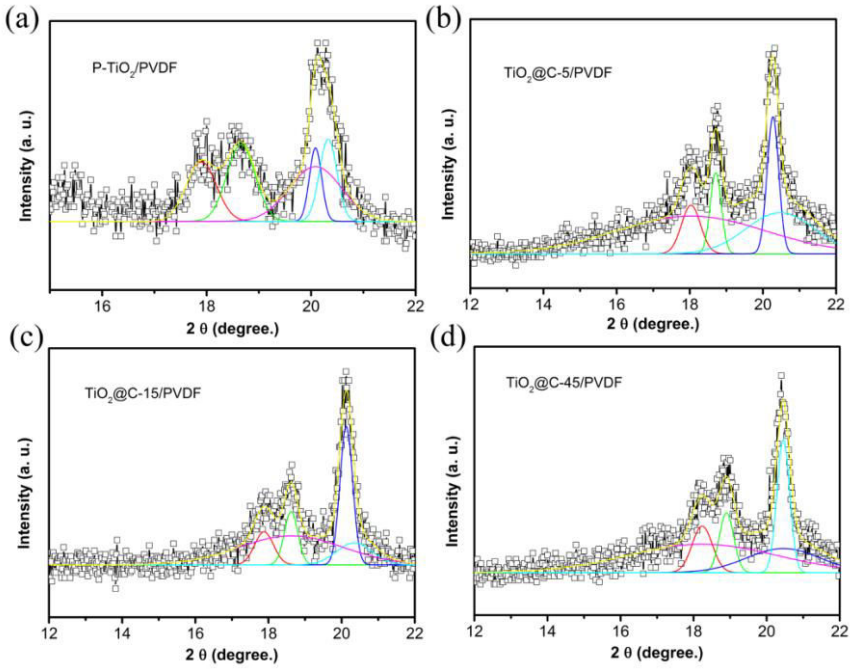

Fig. 6-14 *Origin's multiple peak separation fitting results of TiO_2 NWs/PVDF and TiO_2@C NWs/PVDF nanocomposites with different hybrids at the same filler loading (15 vol. %).*

In order to accurately reveal the relationship between the dielectric properties of the nanocomposites and the thickness of the carbon shell, the volume fractions of the TiO_2 NW core and the carbon shell for the whole nanocomposites were calculated and are presented in Table 6-1. The dependence of the dielectric properties of the corresponding nanocomposites on the volume fraction of the TiO_2 NW core and the carbon shell is displayed in Fig. 6-15 and Fig. 6-16. As indicated by the orange arrow in Fig. 6-15a, the thickness of the carbon shell would increase with prolonging carbon deposition time at an equivalent volume fraction of the TiO_2 NW core for the whole nanocomposite system, resulting in the increasing of the dielectric constant of the nanocomposites. This phenomenon could be explained by the parallel plate capacitor model (Eq. 3-1). An increase in the carbon shell thickness would decrease the distance between the adjacent TiO_2 NW cores. According to Eq. 3-1, the total capacitance stored would increase at the same amount of TiO_2 NW core loading for the whole system. Therefore, it is more efficient to increase the dielectric constant of the

nanocomposites by filling with the hybrids with a thicker carbon shell at an equivalent volume fraction of the TiO_2 NW core. As for the part of the fixed volume fraction of the carbon shell for the whole nanocomposites in Fig. 6-15b, the thickness of the carbon shell would become thinner with decreasing carbon deposition time. Thus, the total amount of TiO_2 NW cores filled in the nanocomposites would increase, which would decrease the distance between the two adjacent TiO_2 NW cores (indicated by the orange arrow in Fig. 6-15b). According to Eq. 3-1, the total capacitance stored would increase. As for the parts of dielectric loss and AC conductivity, they exhibit a similar tendency as shown in the dielectric constant part. The nanocomposites reported in the current work exhibit excellent dielectric performance when compared with those nanocomposites reported in the literature (Fig. 6-17).

Table 6-1 *Summarized results of the volume fraction of the TiO_2 NW core (f_{TiO2}) and the carbon shell (f_{carbon}) for the whole nanocomposite system from Eq. 6-4 and Eq. 6-5.*

$f_{hybrids}$	TiO_2@C-5 NWs		TiO_2@C-15 NWs		TiO_2@C-45 NWs	
(vol. %)	f_{TiO2}	f_{carbon}	f_{TiO2}	f_{carbon}	f_{TiO2}	f_{carbon}
0	0	0	0	0	0	0
2.50	2.29	0.21	1.80	0.70	1.48	1.02
5.00	4.58	0.42	3.60	1.40	2.95	2.05
10.00	9.17	0.83	7.20	2.80	5.91	4.09
15.00	13.75	1.25	10.80	4.20	8.86	6.14
20.00	18.33	1.67	14.40	5.60	11.81	8.19

Note: Eq. 6-4: $f_{TiO2} = (1-\alpha)\times f_{hybrids}$; Eq. 6-5: $f_{carbon} = \alpha\times f_{hybrids}$. The volume fraction of carbon shell in the hybrids (α) could be calculated from the weight fraction of carbon shell (β) as described below. The weight fraction of carbon shell in the hybrids could be obtained from the TGA curves (Fig. 6-3c). The equation for the calculation of α (Eq. 6-6) could be expressed as below.

$$\boldsymbol{\alpha = \frac{V_c}{V_h} = \frac{V_c}{V_c+V_{TiO2}} = \frac{\beta M/\rho_c}{\beta M/\rho_c + (1-\beta)M/\rho_{TiO2}} = \frac{\beta/\rho_c}{\beta/\rho_c + (1-\beta)/\rho_{TiO2}}}$$

where V_c, V_{TiO2}, and V_h are the volume of carbon shell, TiO_2 core, and hybrids, respectively. The ρ_c and ρ_{TiO2} represent the density of carbon shell and TiO_2 core, respectively, and M is the mass of hybrids. The ρ_c and ρ_{TiO2} values are selected as 2.00 g cm^{-3} and 3.90 g cm^{-3}, respectively. The β is directly extracted from the TGA results.

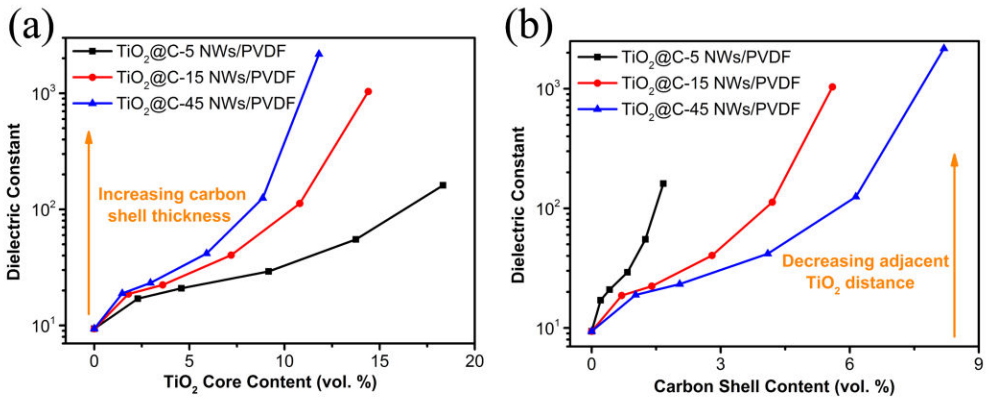

Fig. 6-15 *Dependence of the dielectric constant of the TiO_2@C-5 NWs/PVDF, TiO_2@C-15 NWs/PVDF, and TiO_2@C-45 NWs/PVDF nanocomposites on the volume fraction of the (a) TiO_2 NW core and (b) carbon shell for the whole nanocomposites (10^3 Hz).*

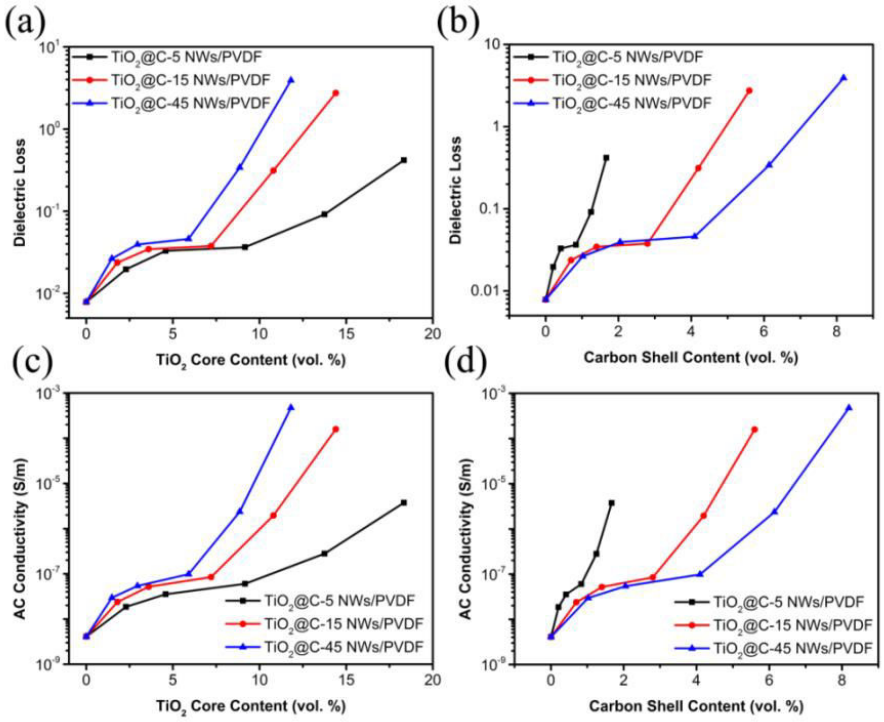

Fig. 6-16 *Dependence of the dielectric loss and AC conductivity of TiO_2@C-5 NWs/PVDF, TiO_2@C-15 NWs/PVDF, and TiO_2@C-45 NWs/PVDF nanocomposites on the volume fraction of the TiO_2 NWs core and carbon shell for the whole nanocomposites (10^3 Hz).*

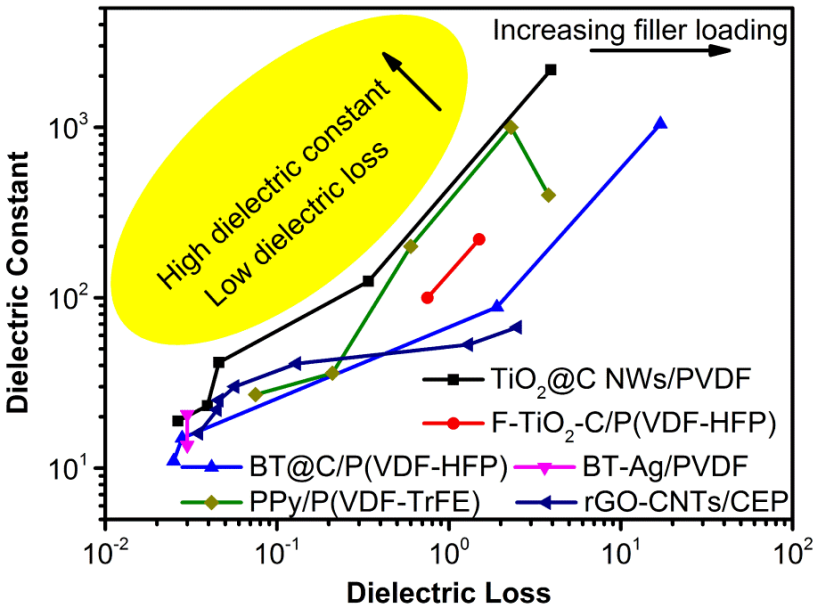

Fig. 6-17 *Comparison of dielectric properties (10^3 Hz) of percolative nanocomposites with different types of nano-fillers:* ***TiO_2@C NWs****, 2.5-20 vol. %;* ***Flower-like TiO_2-C****, 15 and 20 vol. %;* ***BT@C,*** *5-30 vol. %;* ***BT-Ag****, 7.6 and 18 vol. %;* ***PPy nanoclips****, 3-9 wt. %;* ***rGO-CNTs****, 0.02-0.144 wt. % [72, 109, 111, 112, 152].*

Because of the alignment of the hybrid nanowires with the injection direction, the whole nanocomposites could be divided into numerous cylindrical units, where the polymer chains are uniformly wrapped on the surface of the hybrid nanowires. Thus, the length of the central axis of an adjacent TiO_2 NW core is equal to the diameter of the divided unit. Therefore, the average distance between the adjacent TiO_2 NW core of the TiO_2@C NW/PVDF nanocomposites could be calculated using Eq. 6-7 as follows.

$$f_{TiO2} = l_a d_a^2 / l_b d_b^2 \tag{6-7}$$

where l_a, l_b, d_a, and d_b represents the length of TiO_2@C NWs hybrids, the length of the units with polymer chains, the diameter of the TiO_2@C NWs hybrids, and the diameter of the units with polymer chains, respectively. The f_{TiO2} used here represents the volume fraction of the TiO_2 NW core for the whole nanocomposites. In order to simplify the model, we assume that the polymer chains are merely wrapped on the cylindrical surface. The two ends of the cylinder are naked. Therefore, the parameter values of l_a and l_b are equivalent. Thus, Eq. 6-7 could be simplified as follows.

$$f_{TiO2} = d_a^2/d_b^2 \quad (6\text{-}8)$$

Herein, we take the TiO_2@C-45 NWs/PVDF nanocomposites as a typical example. The diameter of the TiO_2 NWs is in the range of 40-80 nm. Thus, two extreme conditions are discussed. According to the f_{TiO2} presented in the TiO_2@C-45 NW part of Table 6-1, the dependence of the distance of adjacent TiO_2 NW cores on f_{TiO2} could be determined (Fig. 6-18). The obtained distance of the adjacent TiO_2 NW cores decreases with increasing f_{TiO2}. For the TiO_2 NW core with a diameter of 40 nm, the distance of the adjacent TiO_2 NW cores decreases from 329 nm to 116 nm upon increasing f_{TiO2} from 1.48 vol. % to 11.81 vol. %. The thickness of the carbon shell in the TiO_2@C-45NW hybrids is 40 nm. Therefore, the critical distance for the contact of the adjacent TiO_2@C-45 NW hybrids is 120 nm. However, the calculated distance of the adjacent TiO_2 NW cores for the nanocomposites with a f_{TiO2} of 11.81 vol. % is 116 nm, which is below the critical value (120 nm). Therefore, we could assume that the conductive network has already been formed, as shown on the right hand side of Fig. 6-18b. For the TiO_2 NW core with a diameter of 80 nm, the critical value for the contact is 160 nm. However, the simulated data are always above the critical value (160 nm), which indicates that the conductive network has not yet been constructed. Considering these two extreme conditions for the TiO_2 NW core with different diameters, it is reasonable to deduce that the percolation behavior of the TiO_2@C-45 NWs/PVDF nanocomposites may occur in the range of 15 vol. % and 20 vol. % (hybrid loading), which is in accordance with the experimental results (Fig. 6-9).

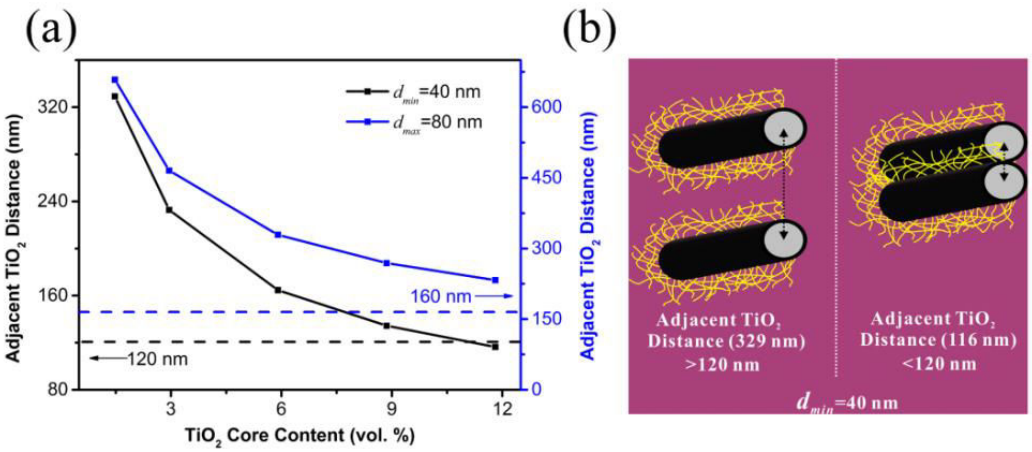

Fig. 6-18 *(a) The simulated distance of adjacent TiO_2 NW cores with two different diameters (40 nm and 80 nm) for the TiO_2@C-45 NW/PVDF nanocomposites; (b) diagrams of neighboring TiO_2@C-45 NW hybrids in the nanocomposites with 1.48 vol. % (left) and 11.81 vol. % (right) TiO_2 NW core (40 nm).*

6.4 Conclusions

In this chapter, core-shell structured TiO_2@C NW hybrids with a uniform carbon shell were synthesized by a combination of a hydrothermal reaction and the CVD method. The carbon shell thickness in the obtained $_{TiO2}$@C NW hybrids could be precisely tuned from 4 nm to 40 nm by controlling the carbon deposition time. The TiO_2@C NW hybrids were subsequently filled into a PVDF matrix to prepare TiO_2@C NWs/PVDF nanocomposites and the resultant nanocomposites exhibit a percolative dielectric behavior. Moreover, the dielectric properties of the TiO_2@C NWs/PVDF nanocomposites could be accurately adjusted by tuning the carbon shell thickness and the highest dielectric constant of about 2171 was obtained, which is 80 times larger than those of the pristine TiO_2 NWs/PVDF nanocomposites at the same filler loading, and 241 times higher than that of the pure PVDF matrix. The enhanced interfacial polarizations of the TiO_2/C and C/PVDF interfaces endow the nanocomposites with excellent dielectric performance. The easy processability and excellent dielectric performance of the TiO_2@C NWs/PVDF nanocomposites make them a potential candidate in the field of high-performance electrostatic capacitors.

Chapter VII

Core@Double-Shells TiO_2@Carbon@SiO_2 PVDF Nanocomposites

7.1 Introduction

The concept of core@shell nano-architecture provides an effective and powerful tool for the design and synthesis of advanced dielectric nanocomposites. Many efforts have been made to improve the dielectric performance using the core@shell structured nano-fillers [191-194]. Generally, two types of core@shell structure have been reported. The first type was conductive fillers or high dielectric constant ceramic cores coated by an insulated shell. The direct contact of adjacent fillers was prevented by the insulated barrier interlayer. Thus, the leakage current, aroused from the tunneling effect or direct electrical contact of the adjacent fillers, would be greatly restricted. This method was firstly reported by Wong and his co-workers [98]. The amorphous aluminum oxide (Al_2O_3) layer, which was obtained from self-passivated of aluminum (Al), acted as an insulated barrier to restrain the contact of Al core. This unique structure endowed the nanocomposites with an extremely low loss of 0.02 at a filler loading as high as 50 wt. %. Apart from the conductive metal fillers, CNTs have also been utilized as the templates for being coated with an insulated shell. Both the hydrothermal reaction and CVD deposition have been used to wrap the CNTs with an amorphous carbon shell to decrease losses and the as-suppressed losses could be further tuned by varying the amorphous carbon thickness. For the coating layers of high dielectric constant ceramic fillers, the SiO_2 and Al_2O_3 layers were widely selected as the insulated shells due to their ease of synthesis characteristic [126, 195, 196]. For example, Tang and his co-workers reported that the dielectric loss of calcium copper titanate NWs (CCTO NWs) filled nanocomposites could be largely restricted by wrapping the CCTO NWs core with a SiO_2 insulated shell [124]. The

coating of $BaTiO_3$ NWs with the Al_2O_3 shell was reported by Pan et al. and the resultant nanocomposites exhibited an extremely low dielectric loss [195, 196]. The other type of core@shell structure was adopted by wrapping the ceramic filler core with a conductive shell to introduce polarizable domains and improve the dielectric constant of ceramic filler based nanocomposites. For instance, the dielectric constant of nanocomposites was largely enhanced by employing the core@shell structured $BaTiO_3$@Carbon hybrids [111]. The similar hybrids synthesized by coating the TiO_2 nano-flowers or TiO_2 NWs with the conductive carbon shell were also adopted to enhance the dielectric constant of nanocomposites [112].

Nevertheless, the moderate dielectric constant and undesirable high dielectric loss were unavoidably caused by employing the aforementioned two types of core@one-shell strategies, respectively [197, 198]. Therefore, it is still difficult to synchronously improve the dielectric constant and suppress dielectric loss of nanocomposites via the traditional core@one-shell concept [199]. Recently, the core@multi-shells strategy reported by Huang and his co-authors verified that the dielectric performance of nanocomposites could be really enhanced by successively grafting the $BaTiO_3$ nanoparticles with a more conductive polymer inner shell and a more insulated polymer outer shell [198]. The confinement of the conductive polymer layer between the $BaTiO_3$ core and insulating polymer layer provided two additional types of interfacial polarization to the nanocomposites. Meanwhile, the excellent insulating property of polymer outer shell afforded a low dielectric loss of the polymer nanocomposites. However, the complicated polymerization procedure for grafting these two kinds of polymer shells onto the surface of ceramic fillers restrains their practical applications.

In this chapter, the inorganic TiO_2@C@SiO_2 nanowires (TiO_2@C@SiO_2 NWs) were synthesized by a combination of modified hydrothermal reaction, CVD, and sol-gel reaction. The TiO_2 NWs is uniformly coated with the carbon and SiO_2 shells. The introducing of carbon as an inner shell between the TiO_2 core and SiO_2 outer shell induces two additional types of interfacial polarizations between the carbon interlayer

and adjacent oxide layers. The obtained PVDF nanocomposites with TiO_2@C@SiO_2 NWs exhibits simultaneously enhanced dielectric constant and suppressed dielectric loss characteristics. Besides, the core@double-shells structured TiO_2@C@SiO_2 NWs with variable carbon shell and SiO_2 shell thickness was achieved by individually adjusting the CVD time and the amount of tetraethyl orthosilicate (TEOS) added in the sol-gel synthesis. The influence of each layer thickness on the dielectric performance of nanocomposites was systematically investigated. The structure reported here could also be extended to other inorganic hybrids to improve the dielectric properties.

7.2 Experimental

7.2.1 Synthesis of Core@Double-Shells Structured TiO_2@C@SiO_2 Nanowires

Firstly, a certain amount of TiO_2 nano-particle (Sigma-Aldrich) was homogeneously dissolved in 10 M NaOH (Sigma-Aldrich) aqueous solution and then the solution was casted into a Teflon-autoclave followed by magnetically stirring at 200 °C for 24 h. The obtained products were cleared with deionized water for several times and then soaked in a HCl aqueous solution with magnetically stirring for 4 h to obtain $H_2Ti_3O_7$ NWs. After being washed with deionized water and then dried in an oven at 80 °C overnight, the resultant powders were further sintered at 600 °C in air for 3 h in order to get TiO_2 NWs.

The carbon deposition on TiO_2 NWs was conducted by a CVD procedure at 850 °C under argon (Ar) and hydrogen (H_2) atmosphere. The gas flow rate was 700 s. c. c. m. for Ar and 300 s. c. c. m. for H_2. After 5 min stabilization, the carbon source C_2H_2 (40 s. c. c. m.) was introduced into the furnace. The deposition time was varied from 15 min to 45 min in order to have different carbon layer thickness. For convenience and simplicity, the core-shell structured TiO_2@C NWs with different carbon shell thickness are denominated by TiO_2@C-X NWs, where X represents the CVD time (min).

The SiO_2 layer was deposited on the previously obtained TiO_2@C NWs by a sol-gel method. A stable TiO_2@C NWs suspension was obtained by dispersing the powders and 0.04 g cationic surfactant cetyltrimethylammonium bromide (CTAB) in 100 mL ethanol and 20 mL deionized water via 1 h ultra-sonication [200, 201]. Then, a certain amount of TEOS was slowly injected into the above suspension and then the solution was ultrasonically treated for another 1 h. Then, 2 mL of ammonium hydroxide was dropwise added under a continuous magnetic stirring for another 4 hours. Finally, the obtained powders were washed with ethanol several times until the solution pH is close to 7. The powders were subsequently dried in a vacuum oven at 75 °C overnight. According to the TEOS volume (μL) used, the TiO_2@C@SiO_2 NWs were denoted as TiO_2@C-30@SiO_2-Y NWs, where Y represents the TEOS volume.

7.2.2 Preparation of TiO_2 NWs/PVDF, TiO_2@C NWs/PVDF and TiO_2@C@SiO_2 NWs/PVDF Nanocomposites

The three types of fillers (TiO_2 NWs, TiO_2@C NWs, and TiO_2@C@SiO_2 NWs) were mixed into the PVDF matrix by a solution casting way in order to fabricate the nanocomposites. Firstly, a suspension containing the desired amount of fillers and DMF was prepared through 2 h bath ultra-sonication. Next, PVDF powders (Kynar 761, Arkema) were dissolved into the homogeneously mixed suspension by using a magnetic stirrer. After 2 h stirring at 70 °C, the DMF solvent was evaporated by increasing the temperature up to 100 °C. Then, the resultant products were heat-treated at 80 °C for 12 h in a vacuum oven. Finally, the PVDF nanocomposites incorporated with different fillers were obtained, in which the mass fraction of fillers varied from 0 to 30 wt. %.

7.2.3 Characterizations

Transmission electron microscopy (TEM) was used to study the coating microstructure and chemical composition of TiO_2@C NWs and TiO_2@C@SiO_2 NWs. A high-resolution TEM (FEI Titan Cube G2 60-300) equipped with a high-angle

annular dark-field (HAADF) detector and an aberration-corrected condenser was operated at 200 kV. The elemental mapping was done with a scanning TEM-energy dispersive X-ray spectroscopy (STEM-EDX). The crystallographic structure of three types of nanowires was analyzed by X-ray diffraction (XRD, Bruker D2 PHASER with X-Flash 430). Raman spectroscopy (Jobin Yvon Lab Ram) was also employed to study the carbon layer characteristics before and after being coated with SiO_2. The thermal stability and detailed carbon composition of the different fillers were analyzed by thermo-gravimetric (TGA, NETZSCH STA 449 F3) heating from room temperature to 800 °C at 5 °C min^{-1} with an N_2/O_2 (20/20 s. c. c. m.) gas flow. The distribution of the nanowires in the PVDF matrix was characterized by scanning electron microscopy (SEM, HITACHI SU8010) operated at 5.0 kV. The dielectric properties (constant and loss) of the different nanocomposites films were investigated with an impedance analyzer (Solatron 1260). Before the measurement, the two sides of each sample were metalized by coating a thin layer of silver paste to decrease the contact resistance between the sample and the electrodes. All the measurements were done at room temperature.

7.3 Results and Discussions

7.3.1 The Morphology and Composition of Core@Double-Shells Structured TiO_2@C@SiO_2 NWs with Variable Thickness of Carbon and SiO_2 Layers

Fig. 7-1a displays the synthesis procedures of core@double-shells TiO_2@C@SiO_2 NWs. The synthesized TiO_2 NWs are uniformly wrapped by a continuous carbon shell with a thickness of 14 nm after a 30 min CVD procedure (Fig. 7-1b). After that, the obtained TiO_2@C NWs were further utilized as the template to fabricate TiO_2@C@SiO_2 NWs. As displayed in Fig. 7-1c, the shell thickness increases from 14 nm to 39 nm after the sol-gel procedure (300 μL TEOS), which is attributed to the introducing of the SiO_2 shell on the surface of TiO_2@C NWs. The STEM-EDS technique further provides a visual evidence to map out the

elemental distribution at a nanometer-scale spatial resolution (Fig. 7-1e, f, g, and h). As shown in Fig. 7-1e, the Ti signal exhibits a strong intensity in the nanowire center and a sharp disappearance in the shell layer. For the part of carbon element, its signal intensity in the shell is stronger than that in the core (Fig. 7-1g). From the enlargement of diameter, the carbon shell thickness is calculated about 14 nm, which is in agreement with the results in Fig. 7-1b. Besides, the signal of Si element (Fig. 7-1h) exhibits a stronger intensity in the shell compared with that in the core, which is similar to the carbon element behavior. Therefore, the SiO_2 shell thickness could also be calculated from the enlargement of the diameter. The calculated value for the thickness of the SiO_2 shell is 25 nm, which is in accordance with the value from Fig. 7-1c. More interestingly, the signal of O element exhibits a hollow structure, which is due to the lack of O element in the carbon interlayer. Besides, the thickness of carbon layer and SiO_2 layer could be accurately modulated by controlling the CVD time and the amount of TEOS added in the sol-gel synthesis process, respectively (Fig. 7-2 and Fig. 7-3). The thickness of the carbon layer could be accurately adjusted from 7 nm to 20 nm by modulating the CVD time from 15 min to 45 min (Fig. 7-2) and the thickness of the SiO_2 layer could also be accurately controlled from 10 nm to 25 nm by adjusting the amount of TEOS involved in the sol-gel synthesis from 100 μL to 300 μL (Fig. 7-3).

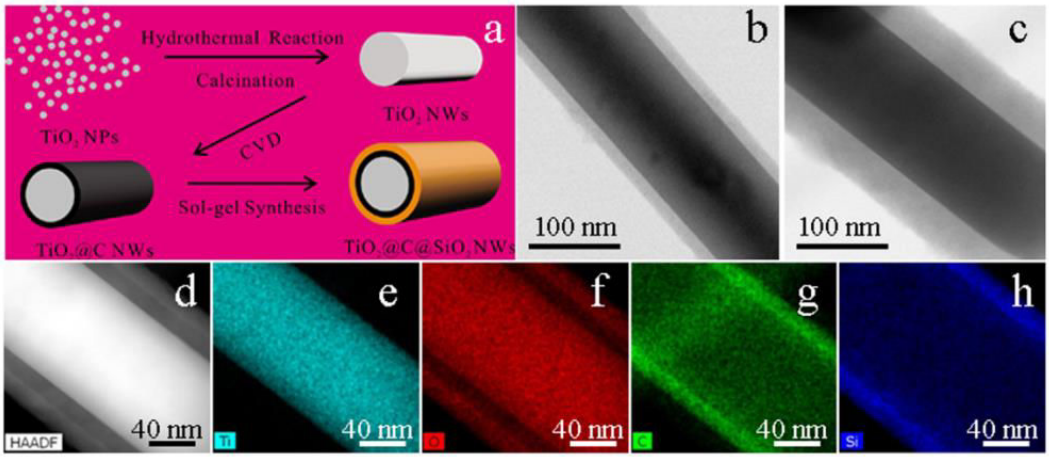

Fig. 7-1 *(a) Schematic illustration of the synthesis procedures of TiO_2@C@SiO_2 NWs; BF-STEM images of the (b) core@shell TiO_2@C-30 NWs and (c) TiO_2@C-*

30@SiO_2-300 NWs; (d) HAADF-STEM image of TiO_2@C-30@SiO_2-300 NWs and corresponding (e-h) STEM-EDS element maps of Ti, O, C, and Si, respectively.

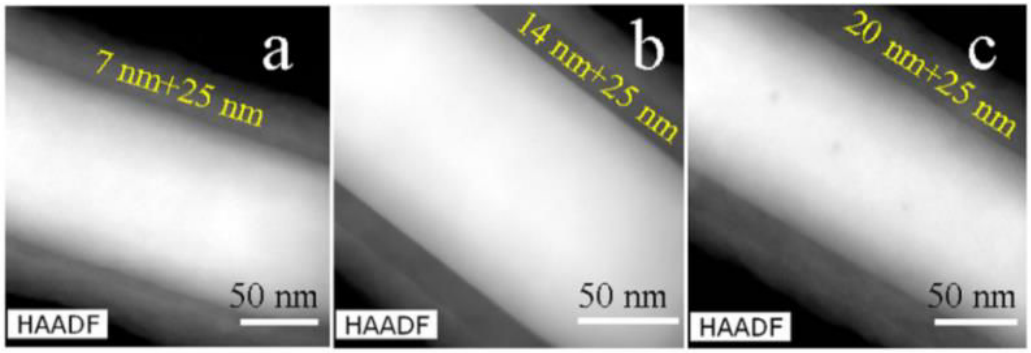

***Fig. 7-2** HAADF-STEM images of the TiO_2@C-X@SiO_2-300 NWs with different carbon layer thickness.*

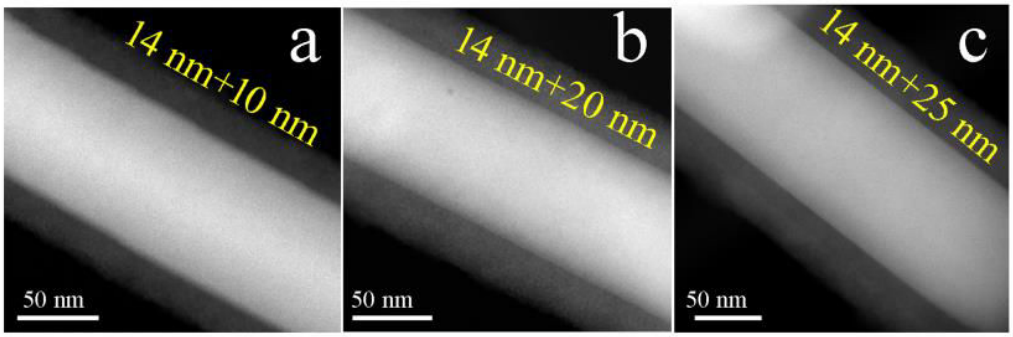

***Fig. 7-3** HAADF-STEM images of the TiO_2@C-30@SiO_2-Y NWs with different SiO_2 layer thickness.*

To obtain the accurate composition information about TiO_2@C and TiO_2@C@SiO_2 NWs hybrids, TGA characterizations were carried out as displayed in Fig. 7-4a, b, and c. The diffraction peaks from XRD patterns (Fig. 7-5a) is ascribed to the TiO_2 according to JCPDS card No. 21-1272 [119]. After wrapped with the first carbon shell, the intensity of corresponding diffraction peaks of TiO_2 was weakened. The Raman spectroscopy (Fig. 7-5b) confirms the existence of carbon shell, which exhibits two typical peaks with D band and G band. The intensity of corresponding diffraction peaks was further weakened after constructing the SiO_2 shell. However, due to the amorphous state of SiO_2, no obvious diffraction peak was observed in Fig. 7-5a. Additionally, no significant band shift of D and G bands was detected after constructing the SiO_2 layer, which indicates that the SiO_2 and carbon shell is

interacted by the non-covalent bond [200, 201]. The TGA results of TiO_2@C NWs (Fig. 7-4a and Fig. 7-4d(i)) further verify the carbon content could be regulated from 11.64 % to 24.72 % by adjusting the deposition time from 15 min to 45 min. As indicated in Fig. 7-4b, the temperature of carbon decomposition increase from ca. 450 °C to ca. 500 °C after coating the TiO_2@C-30 NWs with SiO_2 outer layer, which is ascribed to the shielding effect of the SiO_2 outer layer. Besides, the monotonous decreasing of carbon content in TiO_2@C-30@SiO_2 NWs from 21.96 % to 14.75 % confirms that the carbon content could be controlled by changing the amount of TEOS in the sol-gel process (Fig. 7-4b and Fig. 7-4d(ii)), which reflects that the SiO_2 content could also be regulated. The evolution of carbon content for the TiO_2@C@SiO_2-300 NWs with the CVD time exhibits the similar law to that of TiO_2@C NWs (Fig. 7-4c and Fig. 7-4d(i)). The evolution law of carbon content with the CVD time and the amount of TEOS, obtained from the TGA curves, suggests that the carbon inner shell thickness and SiO_2 outer shell thickness could be accurately modulated by adjusting the experimental parameters involved in the CVD procedure and sol-gel synthesis.

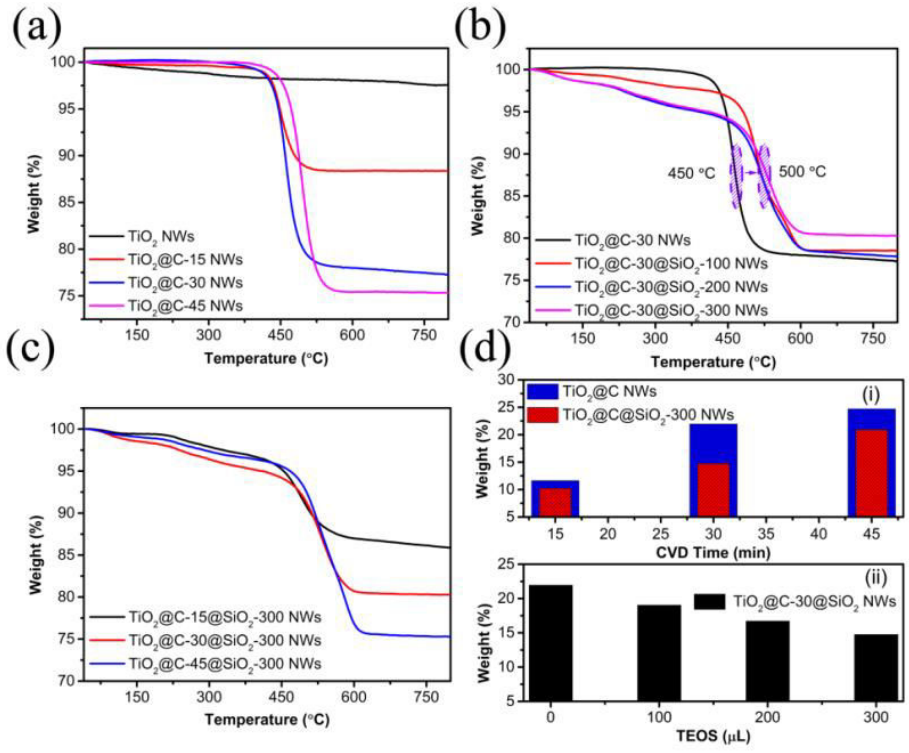

Fig. 7-4 *TGA curves of (a) TiO_2@C NWs with different carbon layer thickness, (b)*

TiO_2@C-30@SiO_2 NWs with different SiO_2 outer shell thickness, and (c) TiO_2@C@SiO_2-300 NWs with different carbon layer thickness; (d) the evolution of carbon weight loss calculated from TGA curves on the experimental parameters during CVD deposition and sol-gel synthesis procedures.

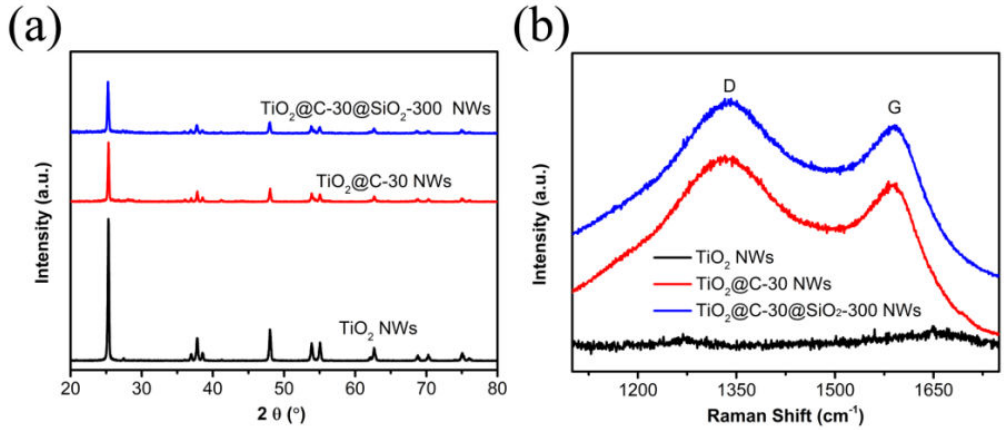

Fig. 7-5. *(a) XRD patterns and (b) Raman spectra of TiO_2 NWs, TiO_2@C-30 NWs, and TiO_2@C-30@SiO_2-300 NWs.*

As for the interface adhesion between nanowires and polymer matrix, the SEM images of the fractured surfaces indicate that the interfacial adhesion could be strengthened by wrapping the TiO_2 core with the carbon and SiO_2 layers (Fig. 7-6b and c). Even for the nanocomposite with 30 wt. % filler loading, the distribution of fillers in the matrix is homogeneous and the interface adhesion is strong (Fig. 7-6d).

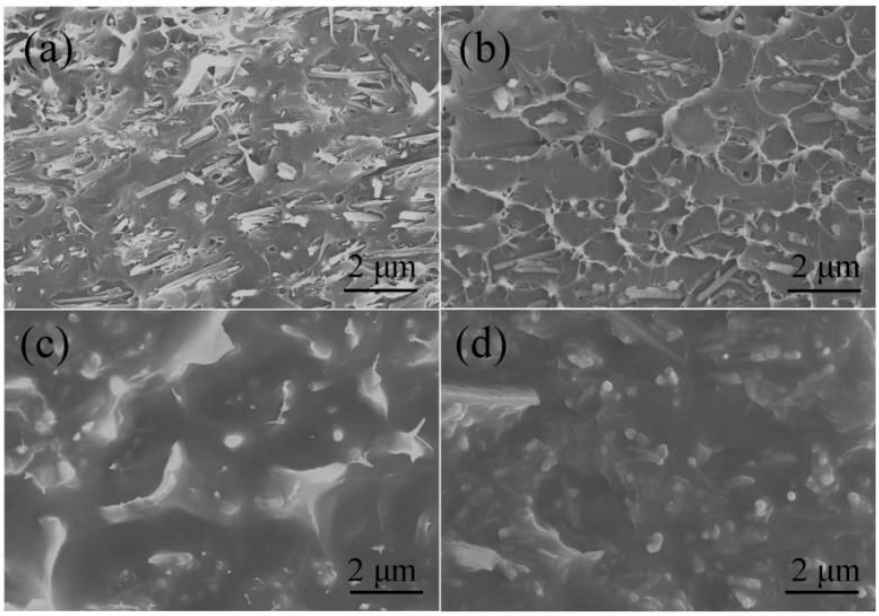

Fig. 7-6 *SEM images of cross-section of (a) TiO_2 NWs/PVDF and (b) TiO_2@C-30*

NWs/PVDF nanocomposites with 10 wt. % filler loading; TiO_2@C-30@SiO_2-300 NWs/PVDF nanocomposites with (c) 10 wt. % and (d) 30 wt. % filler loadings.

7.3.2 The Influence of SiO_2 Layer Thickness on the Dielectric Performance of PVDF Nanocomposites

As shown in Fig. 7-7, Fig. 7-8a, b, and c, and Fig. 7-12a and b, the dielectric constants and losses of PVDF nanocomposites filled with different type of fillers all show a similarly gradual increase as the filler loadings increases. The dielectric constant of PVDF nanocomposites with TiO_2 NWs at 10^3 Hz increases slightly from 9 to 20 with increasing the filler loading to 30 wt. % and the corresponding dielectric loss increases from 0.01 to 0.15. Compared with the dielectric constant of TiO_2 NWs filled nanocomposites, the constant of nanocomposites with TiO_2@C NWs shows a sharp increase as the filler loading increases to a certain value after wrapping the TiO_2 NWs core with a carbon layer (Fig. 7-9a), which is a typical percolative behavior for the nanocomposites with the conductive fillers. However, the dramatic increase of dielectric constant is always along with the sudden jump of dielectric loss (Fig. 7-9b), which hinders their further applications in the electrostatic capacitors field. Besides, the dielectric properties of nanocomposites with TiO_2@C NWs could be precisely modulated by controlling the carbon layer thickness. As displayed in Fig. 7-8d, both the constant and loss of the nanocomposites with different types of TiO_2@C NWs increase with increasing the carbon shell thickness at the same filler fraction.

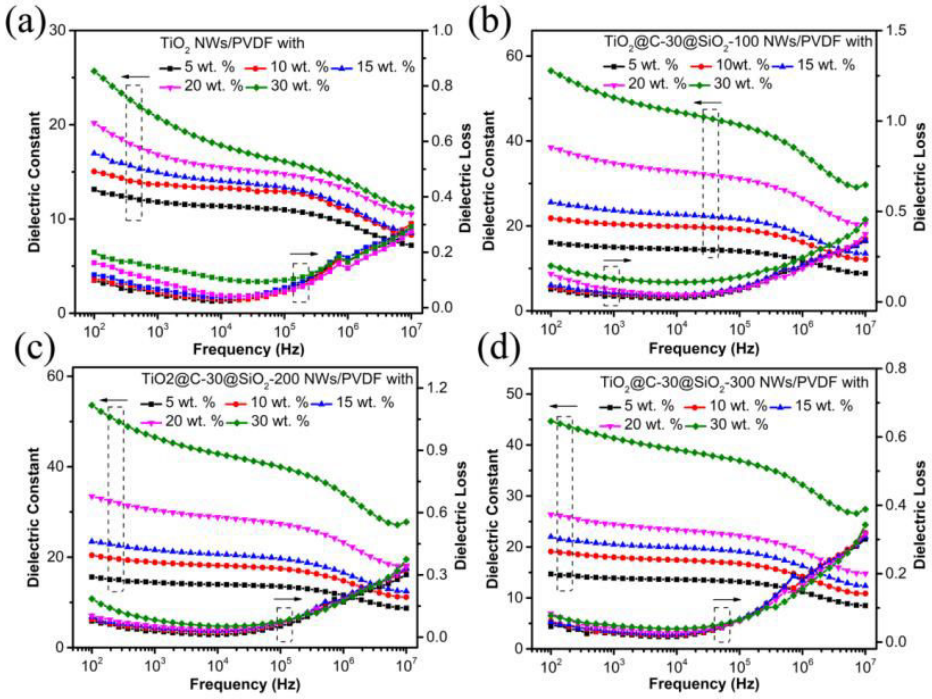

Fig. 7-7 *Dielectric constants and losses spectra for PVDF nanocomposites with different filler loadings of (a) TiO_2 NWs, (b) TiO_2@C-30@SiO_2-100 NWs, (c) TiO_2@C-30@SiO_2-200 NWs, and (d) TiO_2@C-30@SiO_2-300 NWs.*

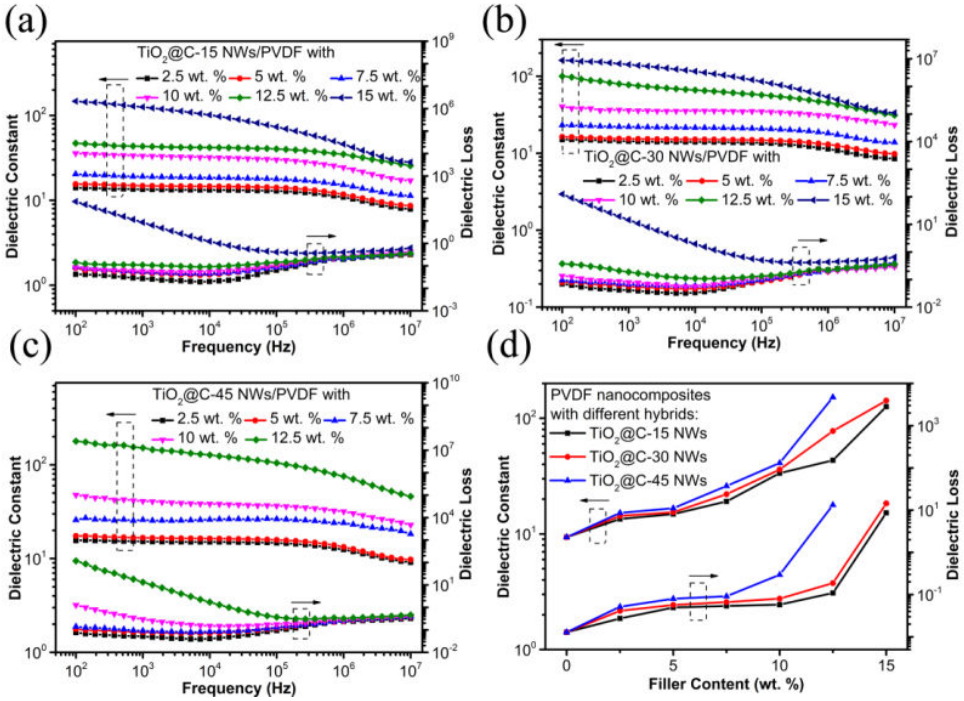

Fig. 7-8 *Dielectric constants and losses spectra for PVDF nanocomposites with different filler loadings of (a) TiO_2@C-15 NWs, (b) TiO_2@C-30 NWs, and (c) TiO_2@C-45 NWs; (d) Dielectric constants and losses of PVDF nanocomposites*

loaded with TiO_2@C NWs with different carbon shell thickness as a function of filler content (measured at 10^3 Hz).

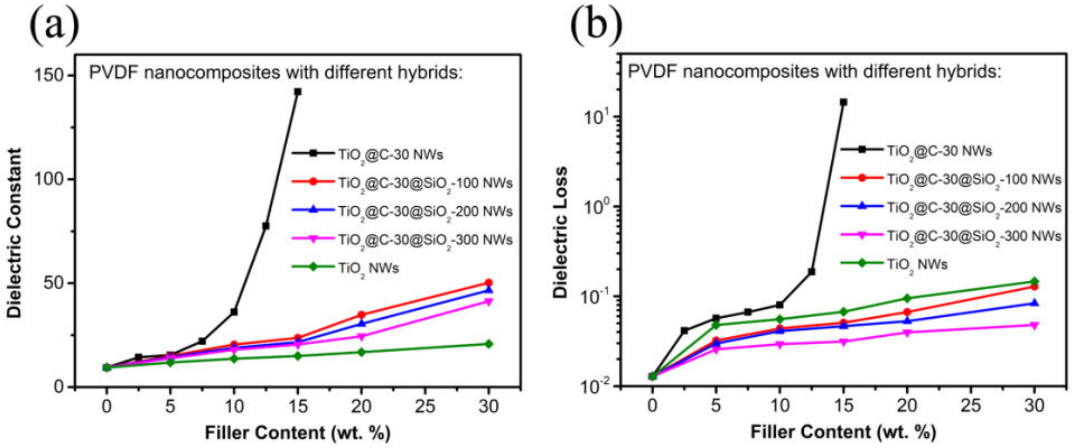

Fig. 7-9 *(a) Dielectric constants and (b) losses of PVDF nanocomposites loaded with TiO_2 NWs, TiO_2@C-30 NWs, and TiO_2@C-30@SiO_2 NWs with different SiO_2 outer shell thickness as a function of filler content (measured at 10^3 Hz).*

After coating the TiO_2@C NWs with the SiO_2 layer, both the dielectric constant and loss of TiO_2@C@SiO_2 NWs filled nanocomposites are significantly suppressed compared with those of nanocomposites with TiO_2@C NWs (Fig. 7-9). Besides, the percolative behavior doesn't display even when the filler loading of TiO_2@C@SiO_2 NWs is 30 wt. %, which reflects that the direct contact of the conductive TiO_2@C NWs is efficiently prevented by the insulated SiO_2 outer shell. Moreover, it is worthy to note that the dielectric constant of the nanocomposites with core@double-shells structured TiO_2@C@SiO_2 NWs is largely improved after successively wrapping the TiO_2 NWs core with the carbon inner shell and SiO_2 outer shell when compared with that of TiO_2 NWs filled nanocomposites (Fig. 7-10a). More importantly, the dielectric losses of the nanocomposites with core@double-shells structured nanowires are simultaneously suppressed. The significantly improved dielectric constant is attributed to the enhanced interfacial polarizations. For the TiO_2 NWs filled nanocomposites, only one type of interfacial polarization (TiO_2/PVDF interfacial polarization) exists in the nanocomposites. However, additional interfacial polarization ((i) TiO_2/carbon and (ii) carbon/SiO_2 interfacial polarization) are introduced into the nanocomposites after successively wrapping the TiO_2 NWs core

with the carbon inner shell and SiO_2 outer shell, which leads to a largely improved dielectric constant. As to the dielectric loss part, the largely suppressed loss could be attributed to the uniform layered structure and excellent insulating property of SiO_2 shell. In recent years, many researchers focused their attention on either coating the ceramic fillers with the conductive shell to promote the dielectric constant or coating the conductive or high-*k* fillers with the insulated shell to suppress the loss. This simple core@one-shell strategy reported could not simultaneously promote the constant and restrict the loss. The enhanced dielectric constant is always along with the high dielectric loss. The simultaneous improvement of dielectric constant and restriction of dielectric loss is obtained here by this all-inorganic core@double-shells structured method. The carbon layer with a high conductivity serves as the polarizable domain, while the SiO_2 layer with a large resistivity is utilized to restrain the leakage current and dielectric loss when the neighboring particles contact with each other.

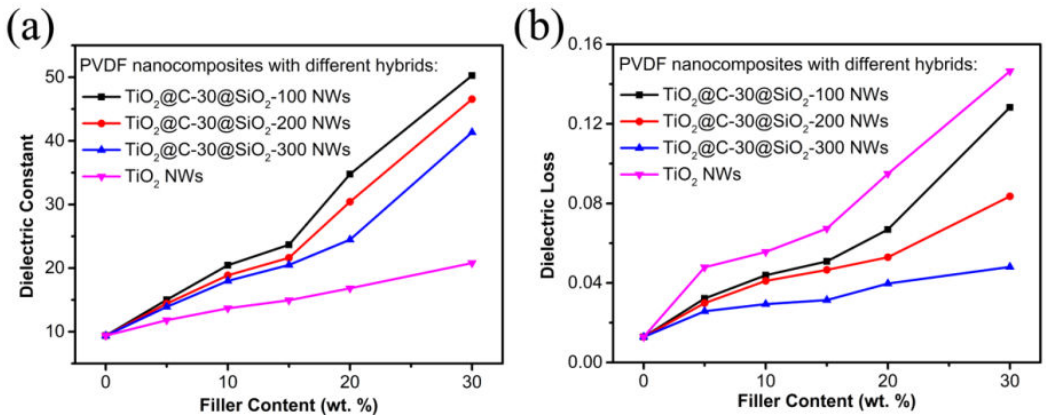

Fig. 7-10 *(a) Dielectric constants and (b) losses of PVDF nanocomposites incorporated with TiO_2 NWs and TiO_2@C-30@SiO_2 NWs with different SiO_2 outer shell thickness as a function of filler loading at 10^3 Hz.*

Besides, the dielectric properties of core@double-shells structured TiO_2@C@SiO_2 NWs filled PVDF nanocomposites could be accurately regulated by adjusting the carbon and SiO_2 layers thickness. As presented in Fig. 7-10a, the dielectric constant of the TiO_2@C-30@SiO_2 NWs filled nanocomposites decreases with increasing the SiO_2 outer shell thickness at the same filler fraction. For instance, the dielectric constant of the nanocomposites decreases from 50 to 41 at the same filler fraction of 30 wt. % as the SiO_2 layer thickness increases from 10 nm to 25 nm.

For the dielectric loss part, as given in Fig. 7-10b, it exhibits a similar tendency that the loss decreases with increasing the SiO_2 outer shell thickness. For example, the loss decreases from 0.13 to 0.05 at the same filler fraction of 30 wt. % when the SiO_2 outer shell thickness increases from 10 nm to 25 nm. The frequency dependent behavior of AC conductivity for the corresponding nanocomposites is given in Fig. 7-11a, b, c, d, and e. For the TiO_2 NWs and TiO_2@C-30@SiO_2 NWs filled parts, their conductivities exhibit a strong frequency-dependent behavior in the whole frequency range, which reflects their insulated characteristic. However, the conductivity of TiO_2@C-30 NWs filled nanocomposites are almost independent of the frequency in the low-frequency range at the filler loading of 15 wt. %, which reflects the conductive path has been formed because of the direct contact of the hybrids in the matrix. The SiO_2 outer shell thickness dependent behavior of AC conductivities for TiO_2@C-30@SiO_2 NWs filled nanocomposites exhibits similar tendency to those of dielectric constant and loss parts, which would not be described in detail (Fig. 7-11f).

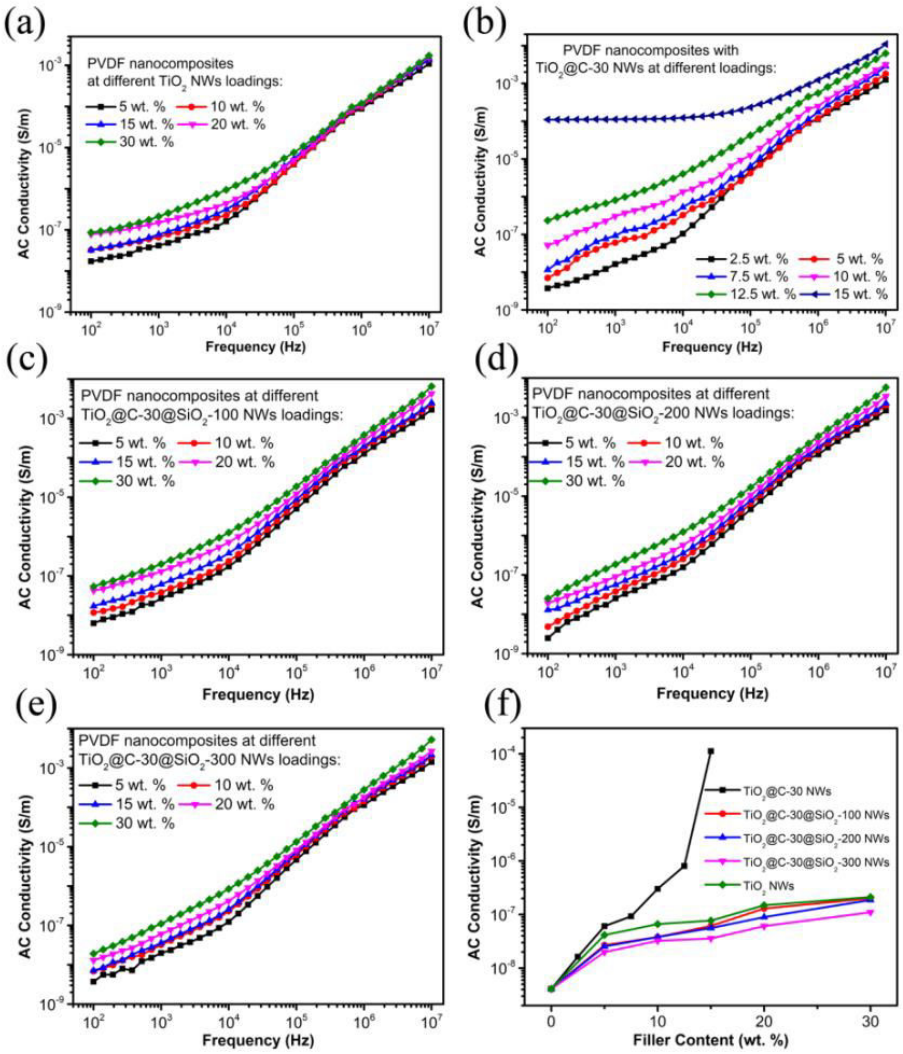

Fig. 7-11 *AC conductivities spectra for PVDF nanocomposites loaded with (a) TiO_2 NWs, (b) TiO_2@C-30 NWs, and (c-e) TiO_2@C-30@SiO_2 NWs with different SiO_2 outer shell thickness; (f) AC conductivities of PVDF nanocomposites loaded with TiO_2 NWs, TiO_2@C-30 NWs, and TiO_2@C-30@SiO_2 NWs with different SiO_2 outer shell thickness as a function of filler content (measured at 10^3 Hz).*

7.3.3 The Influence of Carbon Inner Shell Thickness on the Dielectric Performance of PVDF Nanocomposites

The influence of carbon inner layer thickness on the dielectric constant and loss of the core@double-shells structured TiO_2@C@SiO_2 NWS filled nanocomposites is given in Fig. 7-12. As shown in Fig. 7-7d and Fig. 7-12a and b, the constant and loss

of TiO_2@C@SiO_2-300 NWS filled PVDF nanocomposites increases slightly with increasing of filler loading. Compared with the dielectric performance of TiO_2 NWs filled nanocomposites, the dielectric constants and losses of the nanocomposites with TiO_2@C@SiO_2-300 NWs are synchronously improved and restricted, respectively (Fig. 7-12c and d). Besides, the dielectric properties could also be accurately modulated by changing the carbon inner shell thickness. As compared with the effect of SiO_2 outer shell on the dielectric property, the influence of carbon inner shell exhibits a contrary tendency that both the dielectric constant and loss increase with the increase of the carbon inner shell thickness. For instance, the dielectric constant of the nanocomposites increases from 37 to 52 as the carbon inner shell thickness increases from 7 nm to 20 nm at the same filler fraction of 30 wt. %. As for the dielectric loss, it increases from 0.04 to 0.08 with increasing the carbon inner shell thickness from 7 nm to 20 nm at the same filler fraction of 30 wt. %. The evolution of the dielectric constant and loss of the nanocomposites with carbon inner shell thickness is similar to that of core@one-shell TiO_2@C NWs filled nanocomposites. The increasing of conductive carbon inner shell thickness enhances the interfacial polarization between the TiO_2 core and SiO_2 layer, which promotes the enhancement of the dielectric constant and loss. As presented in Fig. 7-13, the effect of carbon layer thickness on the AC conductivity exhibits the similar tendency to that of dielectric constant and loss parts, which would not be discussed in details.

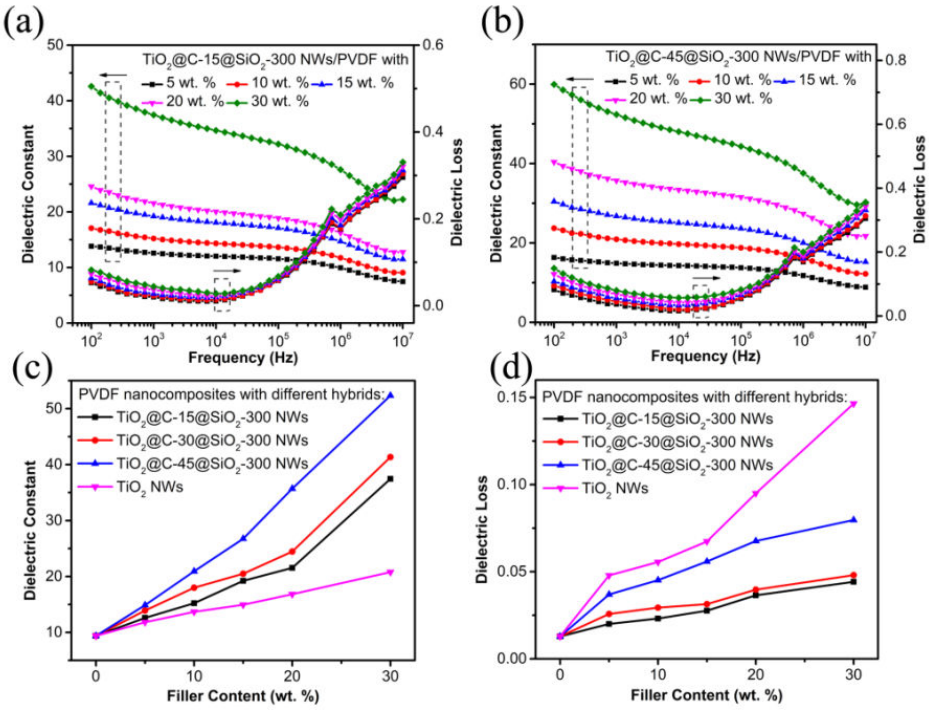

Fig. 7-12 *Dielectric constants and loss spectra for PVDF nanocomposites with different filler loadings of (a) TiO_2@C-15@SiO_2-300 NWs and (b) TiO_2@C-45@SiO_2-300 NWs; (c) Dielectric constants and (d) losses of PVDF nanocomposites filled with TiO_2 NWs and TiO_2@C@SiO_2-300 NWs with different carbon inner shell thickness as a function of filler fraction at 10^3 Hz.*

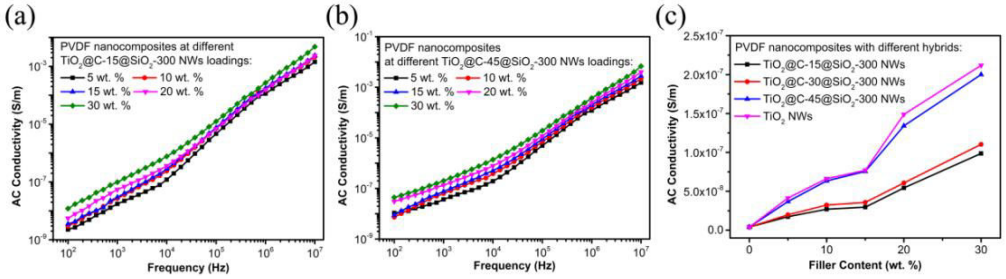

Fig. 7-13 *AC conductivities spectra for PVDF nanocomposites loaded with (a) TiO_2@C-15@SiO_2-300 NWs and (b) TiO_2@C-45@SiO_2-300 NWs; (c) AC conductivities of PVDF nanocomposites loaded with TiO_2 NWs and TiO_2@C@SiO_2-300 NWs with different carbon inner shell thickness as a function of filler content (measured at 10^3 Hz).*

7.3.4 Insights from the Computer Simulation

As known, the current density was an important factor determining the dielectric

loss of PVDF nanocomposites. In order to theoretically explain the evolution of dielectric loss with the SiO_2 outer shell thickness, the simulation of the finite element was used to analyze the current density distribution in the polymer nanocomposites. As confirmed by the SEM images (Fig. 7-6), most of the nanowires in the PVDF matrix were aligned along the in-plane-oriented direction. The distribution of current density was simulated as displayed in Fig. 7-14 and Fig. 7-15. The contrast of local electric current density was mainly aroused from the local electric resistivity difference between fillers and polymer matrix. The simulated current densities of nanocomposites with pristine TiO_2 NWs and TiO_2@C NWs change more abruptly than that of nanocomposites with core@double-shells structured TiO_2@C@SiO_2 NWs with different SiO_2 outer shell thickness from top to bottom part (Fig. 7-14 and Fig. 7-15). Moreover, the simulated current density changes more gradually with increasing the SiO_2 outer shell thickness (Fig. 7-14b, c, and d). Besides, the nanocomposites with core@double-shells hybrids exhibit the lowest current density compared with pristine TiO_2 NWs and TiO_2@C NWs filled ones. The excellent insulating property of SiO_2 layer afford the nanocomposites with the lowest current density by confining the mobility of free electrons and the percolated current from carbon inner shell. The absolute current density values also decrease with increasing the SiO_2 outer shell thickness (Fig. 7-14b, c, and d). The current density evolution law and the absolute current density values for the nanocomposites with different hybrids fillers all verify the accuracy and reliability of experimental results that the TiO_2@C@SiO_2 NWs filled nanocomposites own the lowest dielectric loss and the dielectric loss decrease with increasing the SiO_2 outer shell thickness.

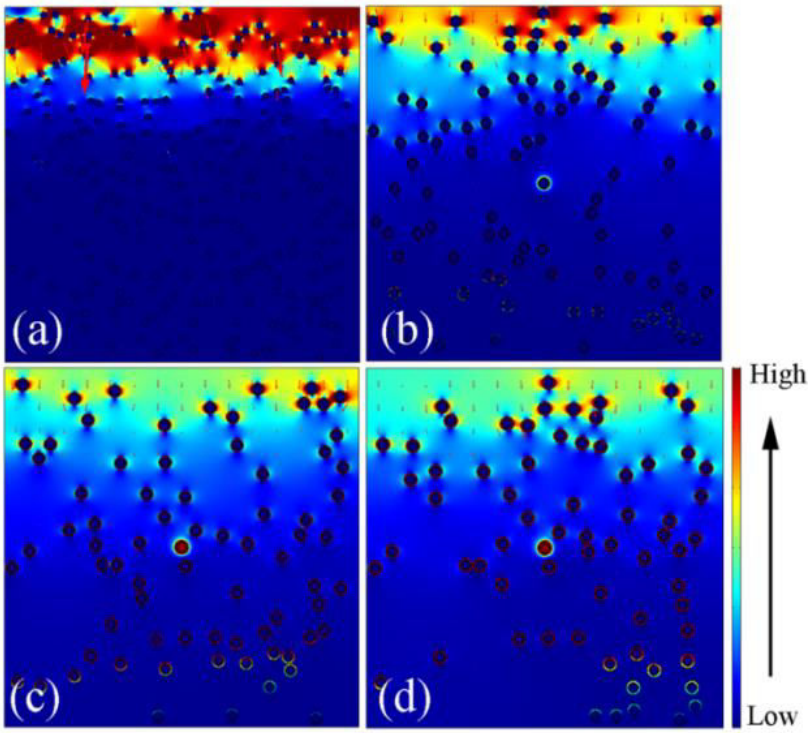

Fig. 7-14 *Distribution of current density simulated for the PVDF nanocomposites with 5 wt. % (a) pristine TiO_2 NWs, (b) TiO_2@C-30@SiO_2-100 NWs, (c) TiO_2@C-30@SiO_2-200 NWs and (d) TiO_2@C-30@SiO_2-300 NWs.*

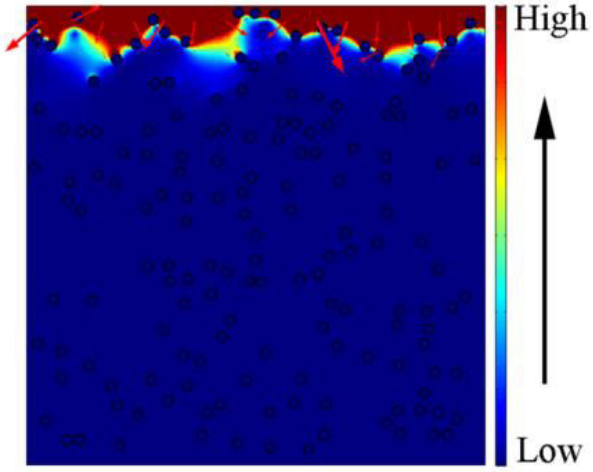

Fig. 7-15 *Distribution of current density simulated for the PVDF nanocomposites with 5 wt. % TiO_2@C-30 NWs.*

7.4 Conclusions

In this chapter, the controllable synthesis of core@double-shells structured nanowires with variable shells thickness was realized by regulating the CVD time and

amount of silicon precursor in the sol-gel synthesis process. All core@double-shells structured nanowires filled nanocomposites exhibit an outstanding dielectric property with simultaneously improved dielectric constant and suppressed loss when compared with that of the TiO_2 NWs incorporated ones at the same filler fraction. More importantly, the dielectric performance could be precisely regulated by individually changing the thickness of the conductive carbon and insulated SiO_2 layers. The influences of carbon and SiO_2 layers thickness on the dielectric performance of nanocomposites were systematically investigated. The dielectric constant and loss of nanocomposites increase with the increase of carbon inner shell thickness and decrease with the increasing of SiO_2 outer shell thickness. The relationship between the dielectric loss and SiO_2 outer shell thickness was further demonstrated by the finite simulation results. The controllable core@double-shells structure reported here makes them become a promising candidate to tailor the dielectric performance of advanced dielectric nanocomposites.

General Conclusions

This thesis is mainly focused on designing various nanofillers to ameliorate the dielectric performance of PVDF nanocomposites. The main results could be concluded as follows:

1. Ternary PVDF Nanocomposites with BNNSs and CNTs

The percolation threshold of CNTs/PVDF nanocomposites decreases via the combination of solution and melting blending procedures. The incorporation of BNNSs into the binary CNTs/PVDF nanocomposites improves the dispersion of CNTs and optimizes the conductive network, which contributes to the enhanced dielectric constant. The direct connection between CNTs can be hindered by increasing the content of BNNS. Due to the microstructure evolution of the nanocomposites, the dielectric property of polymer nanocomposites can be easily modified by employing the ternary system.

2. Core@Shell Structured CNTs@AC/PVDF Nanocomposites

The core-shell structured CNTs@AC hybrids with different structural features were prepared by CVD method and they were subsequently integrated into PVDF matrix to prepare CNTs@AC/PVDF dielectric nanocomposites by the integration of solution and melting blending processes. The AC layer not only hinders the direct contact of CNTs but also improves the dispersibility of CNTs in the PVDF matrix. The percolation threshold increases with the prolongation of carbon deposition time. More importantly, the dielectric loss undergoes a sharp decrease after the coating process, which is attributed to the decrease in leakage current. The results suggest that the influence of AC interlayer on the final dielectric performance after percolation is much more obvious than that before percolation.

3. Core@Shell Structured BNNSs@Carbon PVDF Nanocomposites

The BNNSs@C hybrids with different carbon contents were synthesized by the CVD method. The carbon fraction in the as-obtained BNNSs@C hybrids can be accurately adjusted from 2.50 to 22.62 wt. % through controlling the carbon deposition time. With the help of solution and melting blending methods, the BNNSs@C/PVDF nanocomposites were obtained by incorporating the BNNSs@C hybrids into PVDF matrix. The as-obtained BNNSs@C/PVDF nanocomposites exhibit an excellent dielectric performance and the dielectric properties can be accurately tuned by adjusting the carbon content. The improved interfacial polarizations of BNNSs/C and C/PVDF interfaces endow the nanocomposites with enhanced dielectric performance.

4. Core@Shell Structured TiO_2@Carbon Nanowires PVDF Nanocomposites

The core-shell structured TiO_2@C NW hybrids with a uniform carbon shell were synthesized by a combination of a hydrothermal reaction and the CVD method. The carbon shell thickness in the obtained TiO_2@C NW hybrids could be precisely tuned from 4 nm to 40 nm by controlling the carbon deposition time. The TiO_2@C NW hybrids were subsequently filled into a PVDF matrix to prepare TiO_2@C NWs/PVDF nanocomposites and the resultant nanocomposites exhibit a percolative dielectric behavior. Moreover, the dielectric properties of the TiO_2@C NWs/PVDF nanocomposites can be accurately adjusted by tuning the carbon shell thickness. The enhanced interfacial polarizations of the TiO_2/C and C/PVDF interfaces endow the nanocomposites with excellent dielectric performance.

5. Core@Double-Shells TiO_2@Carbon@SiO_2 PVDF Nanocomposites

The controllable synthesis of core@double-shells structured nanowires with variable shells thickness was realized by regulating the CVD time and amount of silicon precursor in the sol-gel synthesis process. All core@double-shells structured nanowires filled nanocomposites exhibit an outstanding dielectric property with

simultaneously improved dielectric constant and suppressed loss when compared with that of the TiO_2 NWs incorporated ones at the same filler fraction. More importantly, the dielectric performance can be precisely regulated by individually changing the thickness of the conductive carbon and insulated SiO_2 layers. The dielectric constant and loss of nanocomposites increase with the increase of carbon inner shell thickness and decrease with the increasing of SiO_2 outer shell thickness. The relationship between the dielectric loss and SiO_2 outer shell thickness was further demonstrated by the finite simulation results.

Perspectives

1. The boron nitride nanosheets should be exfoliated into the single layer or few layers, after which the amount of boron nitride nanosheets used in the ternary nanocomposites can be minimized. Besides, the surface of CNTs should be chemically modified to improve the compatibility with the PVDF matrix.

2. Efforts are needed to investigate the influence of CVD temperature on the intrinsic structure of the amorphous carbon layer. The dielectric loss of CNTs hybrids filled PVDF nanocomposites should be further decreased and the sensitivity of dielectric constant to the CNTs loading in the vicinity of percolation threshold should be alleviated.

3. The components in the core@multi-shells structure should be further optimized. $BaTiO_3$ core with different morphology is attractive for the core@shell structure. The inner shell can be replaced with other high dielectric constant or conductive components, such as TiO_2, metal nanoparticles, and conductive polymers. The outer shell can be replaced with other inorganic or organic shells, such as Al_2O_3 and insulating polymers. More importantly, the crystal structure of the inorganic outer shell is a vital factor in determining the final dielectric performance and the outer shell should be chemically modified to improve the compatibility with the host polymer matrix.

4. More attention should be paid to the 2D nanoplates due to its excellent blocking effect in the direction of perpendicular to the plate. As a result, the dielectric loss and leakage current can be further suppressed, thus leading to a high electrical breakdown strength.

5. Apart from the experimental work, theoretical investigations are needed to figure out the influence of each shell on the different types of polarization in the dielectric nanocomposites.

References

1. BP Statistical Review of World Energy 2017, https://www.bp.com/content/dam/bp-country/de_ch/PDF/bp-statistical-review-of-world-energy-2017-full-report.pdf
2. M. Aneke, M. Wang, Energy Storage Technologies and Real Life Applications-A State of the Art Review, ***Applied Energy***, 179 (2016), 350-377.
3. X. Luo, J. Wang, M. Dooner, J. Clarke, Overview of Current Development in Electrical Energy Storage Technologies and the Application Potential in Power System Operation, ***Applied Energy***, 137 (2015), 511-536.
4. B. Dunn, H. Kamath, J.-M. Tarascon, Electrical Energy Storage for the Grid: A Battery of Choices, ***Science***, 334 (2011), 928-935.
5. H. Chen, T. Cong, W. Yang, C. Tan, Y. Li, Y. Ding, Progress in Electrical Energy Storage System: A Critical Review, ***Progress in Natural Science***, 19 (2009), 291-312.
6. S. Donadei, G. Schneider, Long-Term Energy Storage with Compressed Air Storages, ***EES Magazine***, 2014.
7. Z. Zhou, Modeling and Power Control of A Marine Current Turbine System with Energy Storage Devices, ***Université de Bretagne Occidentale***, 2014.
8. J. Jerz, P. Tobolka, V. Michenka, T. Dvorak, Heat Storage in Future Zero-Energy Buildings, ***International Journal of Innovative Research in Science, Engineering and Technology***, 4 (2015), 6722-6728.
9. S. Badwal, S. Giddey, C. Munnings, A. Bhatt, A. Hollenkamp, Emerging Electrochemical Energy Conversion and Storage Technologies, ***Frontiers in Chemistry***, 2 (2014), 1-28.
10. W. Antweiler, Can Fow Batteries Solve the Electricity Storage Problem? 2014, https://wernerantweiler.ca/blog.php?item=2014-09-28.
11. G.-L. Xu, Q. Wang, J.-C. Fang, Y.-F. Xu, J.-T. Li, L. Huang, S.-G. Sun, Tuning the Structure and Property of Nanostructured Cathode Materials of Lithium Ion and Lithium Sulfur Batteries, ***Journal of Materials Chemistry A***, 2 (2014), 19941-19962.
12. Z. Yang, J. Zhang, M. Kintner-Meyer, X. Lu, D. Choi, J. Lemmon, J. Liu, Electrochemical Energy Storage for Green Grid, ***Chemical Reviews***, 111 (2011), 3577-3613.
13. L. L. Zhang, X. S. Zhao, Carbon-based Materials as Supercapacitor Electrodes, ***Chemical Society Reviews***, 38 (2009), 2520-2531.
14. Y. Sun, Q. Wu, G. Shi, Graphene based New Energy Materials, ***Energy & Environmental Science***, 4 (2011), 1113-1132.
15. D. P. Dubal, O. Ayyad, V. Ruiz, P. Gomez-Romero, Hybrid Energy Storage: the Merging of Battery and Supercapacitor Chemistries, ***Chemical Society Reviews***, 44 (2015), 1777-1790.
16. Z. Yu, L. Tetard, L. Zhai, J. Thomas, Supercapacitor Electrode Materials:

Nanostructures from 0 to 3 Dimensions, ***Energy & Environmental Science***, 8 (2015), 702-730.

17. X.-L. Wu, A.-W. Xu, Carbonaceous Hydrogels and Aerogels for Supercapacitors, ***Journal of Materials Chemistry A***, 2 (2014), 4852-4864.
18. Z.-M. Dang, J.-K. Yuan, S.-H. Yao, R.-J. Liao, Flexible Nanodielectric Materials with High Permittivity for Power Energy Storage, ***Advanced Materials***, 25 (2013), 6334-6365.
19. Z.-M. Dang, J.-K. Yuan, J.-W. Zha, T. Zhou, S.-T. Li, G.-H. Hu, Fundamentals, Processes and Applications of High-Permittivity Polymer-Matrix Composites, ***Progress in Materials Science***, 57 (2012), 660-723.
20. Prateek, V. K. Thakur, R. K. Gupta, Recent Progress on Ferroelectric Polymer-based Nanocomposites for High Energy Density Capacitors: Synthesis, Dielectric Properties, and Future Aspects, ***Chemical Reviews***, 116 (2016), 4260-4317.
21. Z. Pan, L. Yao, J. Zhai, X. Yao, H. Chen, Interfacial Coupling Effect in Organic/Inorganic Nanocomposites with High Energy Density, ***Advanced Materials***, 30 (2018), 1705662.
22. Z. M. Dang, M. S. Zheng, J. W. Zha, 1D/2D Carbon Nanomaterial-Polymer Dielectric Composites with High Permittivity for Power Energy Storage Applications, ***Small***, 12 (2016), 1688-1701.
23. S. Kwon, W. Hackenberger, E. Alberta, E. Furman, M. Lanagan, Nonlinear Dielectric Ceramics and their Applications to Capacitors and Tunable Dielectrics, ***IEEE Electrical Insulation Magazine***, 27 (2011), 43-45.
24. Y. K. Tan, S. K. Panda, Review of Energy Harvesting Technologies for Sustainable WSN, in Sustainable Wireless Sensor Networks, 2010, 15-43.
25. S. Adireddy, V. S. Puli, S. C. Sklare, T. J. Lou, B. C. Riggs, R. Elupula, S. M. Grayson, D. B. Chrisey, PVDF-$BaSrTiO_3$ Nanocomposites for Flexible Electrical Energy Storage Devices, ***Emerging Materials Research***, 3 (2014), 265-270.
26. A. Ameli, M. Nofar, C. B. Park, P. Potschke, G. Rizvi, Polypropylene/Carbon Nanotube Nano/Microcellular Structures with High Dielectric Permittivity, Low Dielectric Loss, and Low Percolation Threshold, ***Carbon***, 71 (2014), 206-217.
27. J. Li, P. C. Ma, W. S. Chow, C. K. To, B. Z. Tang, J.-K. Kim, Correlations between Percolation Threshold, Dispersion State, and Aspect Ratio of Carbon Nanotubes, ***Advanced Functional Materials***, 17 (2007), 3207-3215.
28. Z.-M. Dang, Y.-H. Lin, C.-W. Nan, Novel Ferroelectric Polymer Composites with High Dielectric Constants. ***Advanced Materials***, 15 (2003), 1625-1629.
29. E. Thommerel, J. C. Valmalette, J. Musso, S. Villain, J. R. Gavarri, D. Spada, Relations between Microstructure, Electrical Percolation and Corrosion in Metal-Insulator Composites, ***Materials Science and Engineering: A***, 328 (2002), 67-79.
30. Z.-M. Dang, B. Peng, D. Xie, S.-H. Yao, M.-J. Jiang, J. Bai, High Dielectric Permittivity Silver/Polyimide Composite Films with Excellent Thermal

Stability, ***Applied Physics Letters***, 92 (2008), 112910.

31. L. Qi, B. I. Lee, S. Chen, W. D. Samuels, G. J. Exarhos, High-Dielectric-Constant Silver-Epoxy Composites as Embedded Dielectrics, ***Advanced Materials***, 17 (2005), 1777-1781.
32. H. Liang, D. Yu, Y. Xie, C. Min, J. Zhang, G. Hu, Preparation of Nano-Ag Particles and their Modification on the Mechanical and Dielectric Properties of Epoxy Resin, ***Polymer Engineering & Science***, 49 (2009), 2189-2194.
33. A. B. da Silva, M. Arjmand, U. Sundararaj, R. E. S. Bretas, Novel Composites of Copper Nanowire/PVDF with Superior Dielectric Properties, ***Polymer***, 55 (2014), 226-234.
34. H.-Y. Mi, Z. Li, L.-S. Turng, Y. Sun, S. Gong, Silver Nanowire/Thermoplastic Polyurethane Elastomer Nanocomposites: Thermal, Mechanical, and Dielectric Properties, ***Materials & Design,*** 56 (2014), 398-404.
35. M. R. Zakaria, M. H. A. Kudus, H. M. Akil, M. Z. M. Thirmizir, Comparative Study of Graphene Nanoparticle and Multiwall Carbon Nanotube Filled Epoxy Nanocomposites based on Mechanical, Thermal and Dielectric Properties, ***Composites Part B: Engineering***, 119 (2017), 57-66.
36. Z. Chen, L. Xie, X. Huang, S. Li, P. Jiang, Achieving Large Dielectric Property Improvement in Polymer/Carbon Nanotube Composites by Engineering the Nanotube Surface via Atom Transfer Radical Polymerization, ***Carbon***, 95 (2015), 895-903.
37. Y. Chen, S. Zhang, X. Liu, Q. Pei, J. Qian, Q. Zhuang, Z. Han, Preparation of Solution-Processable Reduced Graphene Oxide/Polybenzoxazole Nanocomposites with Improved Dielectric Properties, ***Macromolecules***, 48 (2015), 365-372.
38. K. K. Sadasivuni, D. Ponnamma, B. Kumar, M. Strankowski, R. Cardinaels, P. Moldenaers, S. Thomas, Y. Grohens, Dielectric Properties of Modified Graphene Oxide Filled Polyurethane Nanocomposites and its Correlation with Rheology, ***Composites Science and Technology***, 104 (2014), 18-25.
39. A. Xie, Y. Wang, P. Jiang, S. Li, X. Huang, Nondestructive Functionalization of Carbon Nanotubes by Combining Mussel-Inspired Chemistry and RAFT Polymerization: Towards High Dielectric Nanocomposites with Improved Thermal Management Capability, ***Composites Science and Technology***, 154 (2018), 154-164.
40. R. Wang, D. Zhuo, Z. Weng, L. Wu, X. Cheng, Y. Zhou, J. Wang, B. Xuan, A Novel Nanosilica/Graphene Oxide Hybrid and its Flame Retarding Epoxy Resin with Simultaneously Improved Mechanical, Thermal Conductivity, and Dielectric Properties, ***Journal of Materials Chemistry A***, 3 (2015), 9826-9836.
41. H. Feng, W. Ma, Z.-K. Cui, X. Liu, J. Gu, S. Lin, Q. Zhuang, Core/Shell-Structured Hyperbranched Aromatic Polyamide Functionalized Graphene Nanosheets-Poly (p-phenylene benzobisoxazole) Nanocomposite Films with Improved Dielectric Properties and Thermostability, ***Journal of Materials Chemistry A***, 5 (2017), 8705-8713.

42. X. Han, S. Chen, X. Lv, H. Luo, D .Zhang, C. R. Bowen, Using A Novel Rigid-Fluoride Polymer to Control the Interfacial Thickness of Graphene and Tailor the Dielectric Behavior of Poly (vinylidene fluoride-trifluoroethylene-chlorotrifluoroethylene) Nanocomposites, ***Physical Chemistry Chemical Physics***, 20 (2018), 2826-2837.
43. M. N. Almadhoun, M. N. Hedhili, I. N. Odeh, P. Xavier, U. S. Bhansali, H. N. Alshareef, Influence of Stacking Morphology and Edge Nitrogen Doping on the Dielectric Performance of Graphene-Polymer Nanocomposites, ***Chemistry of Materials***, 26 (2014), 2856-2861.
44. N. Maity, A. Mandal, A. K. Nandi, Hierarchical Nanostructured Polyaniline Functionalized Graphene/Poly (vinylidene fluoride) Composites for Improved Dielectric Performances, ***Polymer***, 103 (2016), 83-97.
45. C. Brosseau, F. Boulic, P. Queffelec, C. Bourbigot, Y. Le Mest, J. Loaec, Dielectric and Microstructure Properties of Polymer Carbon Black Composites, ***Journal of Applied Physics***, 81 (1997), 882-891.
46. J. Yacubowicz, M. Narkis, Dielectric Behavior of Carbon Black Filled Polymer Composites, ***Polymer Engineering & Science***, 26 (1986), 1568-1573.
47. J. Yacubowicz, M. Narkis, L. Benguigui, Electrical and Dielectric Properties of Segregated Carbon Black-Polyethylene Systems, ***Polymer Engineering & Science***, 30 (1990), 459-468.
48. H.-P. Xu, Z.-M. Dang, M.-J. Jiang, S.-H. Yao, J. Bai, Enhanced Dielectric Properties and Positive Temperature Coefficient Effect in the Binary Polymer Composites with Surface Modified Carbon Black, ***Journal of Materials Chemistry***, 18 (2008), 229-234.
49. C. Brosseau, A. Mdarhri, A. Vidal, Mechanical Fatigue and Dielectric Relaxation of Carbon Black/Polymer Composites, ***Journal of Applied Physics***, 104 (2008), 074105.
50. J. Belattar, M. P. F. Graca, L. C. Costa, M. E. Achour, C. Brosseau, Electric Modulus-based Analysis of the Dielectric Relaxation in Carbon Black Loaded Polymer Composites, ***Journal of Applied Physics***, 107 (2010), 124111.
51. J. Chen, H. Iwata, N. Tsubokawa, Y. Maekawa, M. Yoshida, Novel Vapor Sensor from Polymer-Grafted Carbon Black: Effects of Heat-Treatment and γ-Ray Radiation-Treatment on the Response of Sensor Material in Cyclohexane Vapor, ***Polymer***, 43 (2002), 2201-2206.
52. P. J. Mather, K. M. Thomas, Carbon Black/High Density Polyethylene Conducting Composite Materials: Part I Structural Modification of A Carbon Black by Gasification in Carbon Dioxide and the Effect on the Electrical and Mechanical Properties of the Composite, ***Journal of Materials Science***, 32 (1997), 401-407.
53. S. Jia, P. Jiang, Z. Zhang, Z. Wang, Effect of Carbon-Black Treatment by Radiation Emulsion Polymerization on Temperature Dependence of Resistivity of Carbon-Black-Filled Polymer Blends, ***Radiation Physics and Chemistry***, 75 (2006), 524-531.

54. S. Iijima, Helical Microtubules of Graphitic Carbon, ***Nature***, 354 (1991), 56.
55. L. Wang, Z.-M. Dang, Carbon Nanotube Composites with High Dielectric Constant at Low Percolation Threshold, ***Applied Physics Letters***, 87 (2005), 042903.
56. C. Y. Wang, T. H. Chen, S. C. Chang, S. Y. Cheng, T. S. Chin, Strong Carbon-Nanotube-Polymer Bonding by Microwave Irradiation, ***Advanced Functional Materials***, 17 (2007), 1979-1983.
57. V. K. Rangari, M. S. Bhuyan, S. Jeelani, Microwave Processing and Characterization of EPON 862/CNT Nanocomposites, ***Materials Science and Engineering: B***, 168 (2010), 117-121.
58. J. Chang, G. Liang, A. Gu, S. Cai, L. Yuan, The Production of Carbon Nanotube/Epoxy Composites with A very High Dielectric Constant and Low Dielectric Loss by Microwave Curing, ***Carbon***, 50 (2012), 689-698.
59. B. Krause, P. Pötschke, L. Häußler, Influence of Small Scale Melt Mixing Conditions on Electrical Resistivity of Carbon Nanotube-Polyamide Composites, ***Composites Science and Technology***, 69 (2009), 1505-1515.
60. J.-K. Yuan, S.-H. Yao, Z.-M. Dang, A. Sylvestre, M. Genestoux, J. Bai, Giant Dielectric Permittivity Nanocomposites: Realizing True Potential of Pristine Carbon Nanotubes in Polyvinylidene Fluoride Matrix through an Enhanced Interfacial Interaction, ***The Journal of Physical Chemistry C***, 115 (2011), 5515-5521.
61. Z.-M. Dang, L. Wang, Y. Lin, Q. Zhang, Q.-Q. Lei, Giant Dielectric Permittivities in Functionalized Carbon-Nanotube/Electroactive-Polymer Nanocomposites, ***Advanced Materials***, 19 (2007), 852-857.
62. C. A. Mitchell, J. L. Bahr, S. Arepalli, J. M. Tour, R. Krishnamoorti, Dispersion of Functionalized Carbon Nanotubes in Polystyrene, ***Macromolecules***, 35 (2002), 8825-8830.
63. T. Liu, Y. Tong, W.-D. Zhang, Preparation and Characterization of Carbon Nanotube/Polyetherimide Nanocomposite Films, ***Composites Science and Technology***, 67 (2007), 406-412.
64. L. Li, B. Li, M. A. Hood, C. Y. Li, Carbon Nanotube Induced Polymer Crystallization: The Formation of Nanohybrid Shish-Kebabs, ***Polymer***, 50 (2009), 953-965.
65. Q. Guo, Q. Xue, J. Sun, M. Dong, F. Xia, Z. Zhang, Gigantic Enhancement in the Dielectric Properties of Polymer-based Composites using Core/Shell MWCNT/Amorphous Carbon Nanohybrids, ***Nanoscale***, 7 (2015), 3660-3667.
66. M. Yang, H. Zhao, D. He, J. Bai, Constructing A Continuous Amorphous Carbon Interlayer to Enhance Dielectric Performance of Carbon Nanotubes/Polyvinylidene Fluoride Nanocomposites, ***Carbon***, 116 (2017), 94-102.
67. J. Safari, S. Gandomi-Ravandi, S. Ashiri, Organosilane Sulfonated Graphene Oxide in the Biginelli and Biginelli-like Reactions, ***New Journal of Chemistry***, 40 (2016), 512-520.
68. J.-Y. Wang, S.-Y. Yang, Y.-L. Huang, H.-W. Tien, W.-K. Chin, C.-C. M. Ma,

Preparation and Properties of Graphene Oxide/Polyimide Composite Films with Low Dielectric Constant and Ultrahigh Strength via in situ Polymerization, ***Journal of Materials Chemistry***, 21 (2011), 13569-13575.

69. S.-T. Hsiao, C.-C. M. Ma, H.-W. Tien, W.-H. Liao, Y.-S. Wang, S.-M. Li, Y.-C. Huang, Using A Non-Covalent Modification to Prepare A High Electromagnetic Interference Shielding Performance Graphene Nanosheet/Water-Borne Polyurethane Composite, ***Carbon***, 60 (2013), 57-66.
70. D. Wang, Y. Bao, J.-W. Zha, J. Zhao, Z.-M. Dang, G.-H. Hu, Improved Dielectric Properties of Nanocomposites based on Poly (vinylidene fluoride) and Poly (vinyl alcohol)-Functionalized Graphene, ***ACS Applied Materials & Interfaces***, 4 (2012), 6273-6279.
71. J.-K. Yuan, Z.-M. Dang, S.-H. Yao, J.-W. Zha, T. Zhou, S.-T. Li, J. Bai, Fabrication and Dielectric Properties of Advanced High Permittivity Polyaniline/Poly (vinylidene fluoride) Nanohybrid Films with High Energy Storage Density, ***Journal of Materials Chemistry***, 20 (2010), 2441-2447.
72. L. Zhang, Z. Liu, X. Lu, G. Yang, X. Zhang, Z.-Y. Cheng, Nano-Clip based Composites with A Low Percolation Threshold and High Dielectric Constant, ***Nano Energy***, 26 (2016), 550-557.
73. Z.-M. Dang, Y.-Q. Lin, H.-P. Xu, C.-Y. Shi, S.-T. Li, J. Bai, Fabrication and Dielectric Characterization of Advanced $BaTiO_3$/Polyimide Nanocomposite Films with High Thermal Stability, ***Advanced Functional Materials***, 18 (2008), 1509-1517.
74. P. Kim, S. C. Jones, P. J. Hotchkiss, J. N. Haddock, B. Kippelen, S. R. Marder, J. W. Perry, Phosphonic Acid-Modified Barium Titanate Polymer Nanocomposites with High Permittivity and Dielectric Strength, ***Advanced Materials***, 19 (2007), 1001-1005.
75. T. Zhou, J.-W. Zha, R.-Y. Cui, B.-H. Fan, J.-K. Yuan, Z.-M. Dang, Improving Dielectric Properties of $BaTiO_3$/Ferroelectric Polymer Composites by Employing Surface Hydroxylated $BaTiO_3$ Nanoparticles, ***ACS Applied Materials & Interfaces***, 3 (2011), 2184-2188.
76. L. Gao, J. He, J. Hu, Y. Li, Large Enhancement in Polarization Response and Energy Storage Properties of Poly (vinylidene fluoride) by Improving the Interface Effect in Nanocomposites, ***The Journal of Physical Chemistry C***, 118 (2014), 831-838.
77. Y. Niu, Y. Bai, K. Yu, Y. Wang, F. Xiang, H. Wang, Effect of the Modifier Structure on the Performance of Barium Titanate/Poly (vinylidene fluoride) Nanocomposites for Energy Storage Applications, ***ACS Applied Materials & Interfaces***, 7 (2015), 24168-24176.
78. D.-H. Kuo, C.-C. Chang, T.-Y. Su, W.-K. Wang, B.-Y. Lin, Dielectric Behaviours of Multi-Doped $BaTiO_3$/Epoxy Composites, ***Journal of the European Ceramic Society***, 21 (2001), 1171-1177.
79. X. Huang, P. Jiang, L. Xie, Ferroelectric Polymer/Silver Nanocomposites with High Dielectric Constant and High Thermal Conductivity, ***Applied Physics Letters***, 95 (2009), 242901.

80. J. Audoit, L. Laffont, A. Lonjon, E. Dantras, C. Lacabanne, Percolative Silver Nanoplates/PVDF Nanocomposites: Bulk and Surface Electrical Conduction, ***Polymer***, 78 (2015), 104-110.
81. P.-C. Ma, M.-Y. Liu, H. Zhang, S.-Q. Wang, R. Wang, K. Wang, Y.-K. Wong, B.-Z. Tang, S.-H. Hong, K.-W. Park, J.-K. Kim, Enhanced Electrical Conductivity of Nanocomposites Containing Hybrid Fillers of Carbon Nanotubes and Carbon Black, ***ACS Applied Materials & Interfaces***, 1 (2009), 1090-1096.
82. L. Wang, J. Hong, G. Chen, Comparison Study of Graphite Nanosheets and Carbon Black as Fillers for High Density Polyethylene, ***Polymer Engineering & Science***, 50 (2010), 2176-2181.
83. Y. Song, Y. Shen, H. Liu, Y. Lin, M. Li, C.-W. Nan, Improving the Dielectric Constants and Breakdown Strength of Polymer Composites: Effects of the Shape of the $BaTiO_3$ Nanoinclusions, Surface Modification and Polymer Matrix, ***Journal of Materials Chemistry***, 22 (2012), 16491-16498.
84. H. Tang, Y. Lin, H. A. Sodano, Synthesis of High Aspect Ratio $BaTiO_3$ Nanowires for High Energy Density Nanocomposite Capacitors, ***Advanced Energy Materials***, 3 (2013), 451-456.
85. Y. Zhu, H. Yao, P. Jiang, J. Wu, X. Zhu, X. Huang, Two-Dimensional High-k Nanosheets for Dielectric Polymer Nanocomposites with Ultrahigh Discharged Energy Density, ***The Journal of Physical Chemistry C***, 122 (2018), 18282-18293.
86. J. Li, J. Claude, L. E. Norena-Franco, S. II. Seok, Q. Wang, Electrical Energy Storage in Ferroelectric Polymer Nanocomposites Containing Surface-Functionalized $BaTiO_3$ Nanoparticles, ***Chemistry of Materials***, 20 (2008), 6304-6306.
87. Q. Xue, The Influence of Particle Shape and Size on Electric Conductivity of Metal-Polymer Composites, ***European Polymer Journal***, 40 (2004), 323-327.
88. J. Li, J.-K. Kim, Percolation Threshold of Conducting Polymer Composites Containing 3D Randomly Distributed Graphite Nanoplatelets, ***Composites Science and Technology***, 67 (2007), 2114-2120.
89. Y. Kobayashi, T. Tanase, T. Tabata, T. Miwa, M. Konno, Fabrication and Dielectric Properties of the $BaTiO_3$-Polymer Nano-Composite Thin Films, ***Journal of the European Ceramic Society***, 28 (2008), 117-122.
90. S. F. Mendes, C. M. Costa, C. Caparros, V. Sencadas, S. Lanceros-Mendez, Effect of Filler Size and Concentration on the Structure and Properties of Poly (vinylidene fluoride)/$BaTiO_3$ Nanocomposites, ***Journal of Materials Science***, 47 (2012), 1378-1388.
91. C. Andrews, Y. Lin, H. A. Sodano, The Effect of Particle Aspect Ratio on the Electroelastic Properties of Piezoelectric Nanocomposites, ***Smart Materials and Structures***, 19 (2010), 025018.
92. H. Tang, Z. Zhou, H. A. Sodano, Relationship between $BaTiO_3$ Nanowire Aspect Ratio and the Dielectric Permittivity of Nanocomposites, ***ACS Applied Materials & Interfaces***, 6 (2014), 5450-5455.

93. H. Tang, Y. Lin, C. Andrews, H. A. Sodano, Nanocomposites with Increased Energy Density through High Aspect Ratio PZT Nanowires, ***Nanotechnology***, 22 (2010), 015702.
94. Y. Li, W. Yang, S. Ding, X.-Z. Fu, R. Sun, W.-H. Liao, C.-P. Wong, Tuning Dielectric Properties and Energy Density of Poly (vinylidene fluoride) Nanocomposites by Quasi Core-Shell Structured $BaTiO_3$@Graphene Oxide Hybrids, ***Journal of Materials Science: Materials in Electronics***, 29 (2018), 1082-1092.
95. P. Hu, Z. Jia, Z. Shen, P. Wang, X. Liu, High Dielectric Constant and Energy Density Induced by the Tunable TiO_2 Interfacial Buffer Layer in PVDF Nanocomposite Contained with Core@Shell Structured TiO_2@$BaTiO_3$ Nanoparticles, ***Applied Surface Science***, 441 (2018), 824-831.
96. M.-S. Zheng, Y.-T. Zheng, J.-W. Zha, Y. Yang, P. Han, Y.-Q. Wen, Z.-M. Dang, Improved Dielectric, Tensile and Energy Storage Properties of Surface Rubberized $BaTiO_3$/Polypropylene Nanocomposites, ***Nano Energy***, 48 (2018), 144-151.
97. J. Chen, X. Wang, X. Yu, L. Yao, Z. Duan, Y. Fan, Y. Jiang, Y. Zhou, Z. Pan, High Dielectric Constant and Low Dielectric Loss Poly (vinylidene fluoride) Nanocomposites via A Small Loading of Two-Dimensional Bi_2Te_3@Al_2O_3 Hexagonal Nanoplates, ***Journal of Materials Chemistry C***, 6 (2018), 271-279.
98. J. Xu, C. Wong, Low-Loss Percolative Dielectric Composite, ***Applied Physics Letters***, 87 (2005), 082907.
99. Y. Shen, Y. Lin, C. W. Nan, Interfacial Effect on Dielectric Properties of Polymer Nanocomposites Filled with Core/Shell-Structured Particles, ***Advanced Functional Materials***, 17 (2007), 2405-2410.
100. Y. Zhang, Y. Wang, Y. Deng, M. Li, J. Bai, Enhanced Dielectric Properties of Ferroelectric Polymer Composites Induced by Metal-Semiconductor Zn-ZnO Core-Shell Structure, ***ACS Applied Materials & Interfaces***, 4 (2012), 65-68.
101. H. Liu, Y. Shen, Y. Song, C.-W. Nan, Y. Lin, X. Yang, Carbon Nanotube Array/Polymer Core/Shell Structured Composites with High Dielectric Permittivity, Low Dielectric Loss, and Large Energy Density, ***Advanced Materials***, 23 (2011), 5104-5108.
102. C. Xu, L. Yuan, G. Liang, A. Gu, Building A Poly (epoxy propylimidazolium ionic liquid)/Graphene Hybrid through π_{cation}-π Interaction for Fabricating High-k Polymer Composites with Low Dielectric Loss and Percolation Threshold, ***Journal of Materials Chemistry C***, 4 (2016), 3175-3184.
103. K. Yang, X. Huang, L. Fang, J. He, P. Jiang, Fluoro-Polymer Functionalized Graphene for Flexible Ferroelectric Polymer-based High-k Nanocomposites with Suppressed Dielectric Loss and Low Percolation Threshold, ***Nanoscale***, 6 (2014), 14740-14753.
104. Y. Li, M. Fan, K. Wu, F. Yu, S. Chai, F. Chen, Q. Fu, Polydopamine Coating Layer on Graphene for Suppressing Loss Tangent and Enhancing Dielectric Constant of Poly (vinylidene fluoride)/Graphene Composites, ***Composites Part A: Applied Science and Manufacturing***, 73 (2015), 85-92.

105. H. Li, Z. Chen, L. Liu, J. Chen, M. Jiang, C. Xiong, Poly (vinyl pyrrolidone)-Coated Graphene/Poly (vinylidene fluoride) Composite Films with High Dielectric Permittivity and Low Loss, ***Composites Science and Technology***, 121 (2015), 49-55.
106. M. Molberg, D. Crespy, P. Rupper, F. Nuesch, J.-A. E. Manson, C. Lowe, D. M. Opris, High Breakdown Field Dielectric Elastomer Actuators using Encapsulated Polyaniline as High Dielectric Constant Filler, ***Advanced Functional Materials***, 20 (2010), 3280-3291.
107. L. Xie, X. Huang, B.-W. Li, C. Zhi, T. Tanaka, P. Jiang, Core-Satellite Ag@$BaTiO_3$ Nanoassemblies for Fabrication of Polymer Nanocomposites with High Discharged Energy Density, High Breakdown Strength and Low Dielectric Loss, ***Physical Chemistry Chemical Physics***, 15 (2013), 17560-17569.
108. K. Yang, X. Huang, J. He, P. Jiang, Strawberry-like Core-Shell Ag@Polydopamine@$BaTiO_3$ Hybrid Nanoparticles for High-k Polymer Nanocomposites with High Energy Density and Low Dielectric Loss, ***Advanced Materials Interfaces***, 2 (2015), 1500361.
109. S. Luo, S. Yu, R. Sun, C.-P. Wong, Nano Ag-Deposited $BaTiO_3$ Hybrid Particles as Fillers for Polymeric Dielectric Composites: Toward High Dielectric Constant and Suppressed Loss, ***ACS Applied Materials & Interfaces***, 6 (2013), 176-182.
110. Y. Yang, H. Sun, D. Yin, Z. Lu, J. Wei, R. Xiong, J. Shi, Z. Wang, Z. Liu, Q. Lei, High Performance of Polyimide/$CaCu_3Ti_4O_{12}$@Ag Hybrid Films with Enhanced Dielectric Permittivity and Low Dielectric Loss, ***Journal of Materials Chemistry A***, 3 (2015), 4916-4921.
111. Y. Feng, W. L. Li, J. P. Wang, J. H. Yin, W. D. Fei, Core-Shell Structured $BaTiO_3$@Carbon Hybrid Particles for Polymer Composites with Enhanced Dielectric Performance, ***Journal of Materials Chemistry A***, 3 (2015), 20313-20321.
112. N. Xu, Q. Zhang, H. Yang, Y. Xia, Y. Jiang, In-Situ Preparation of Hierarchical Flower-like TiO_2/Carbon Nanostructures as Fillers for Polymer Composites with Enhanced Dielectric Properties, ***Scientific Reports***, 7 (2017), 43970.
113. N. Guo, S. A. DiBenedetto, D.-K. Kwon, L. Wang, M. T. Russell, M. T. Lanagan, A. Facchetti, T. J. Marks, Supported Metallocene Catalysis for in situ Synthesis of High Energy Density Metal Oxide Nanocomposites, ***Journal of the American Chemical Society***, 129 (2007), 766-767.
114. L. Xie, X. Huang, C. Wu, P. Jiang, Core-Shell Structured Poly (methyl methacrylate)/$BaTiO_3$ Nanocomposites Prepared by in situ Atom Transfer Radical Polymerization: A Route to High Dielectric Constant Materials with the Inherent Low Loss of the base Polymer, ***Journal of Materials Chemistry***, 21 (2011), 5897-5906.
115. K. Yang, X. Huang, L. Xie, C. Wu, P. Jiang, T. Tanaka, Core-Shell Structured Polystyrene/$BaTiO_3$ Hybrid Nanodielectrics Prepared by in situ RAFT

Polymerization: A Route to High Dielectric Constant and Low Loss Materials with Weak Frequency Fependence, ***Macromolecular Rapid Communications***, 33 (2012), 1921-1926.

116. N. Guo, S. A. DiBenedetto, P. Tewari, M. T. Lanagan, M. A. Ratner, T. J. Marks, Nanoparticle, Size, Shape, and Interfacial Effects on Leakage Current Density, Permittivity, and Breakdown Strength of Metal Oxide-Polyolefin Nanocomposites: Experiment and Theory, ***Chemistry of Materials***, 22 (2010), 1567-1578.
117. K. Yang, X. Huang, M. Zhu, L. Xie, T. Tanaka, P. Jiang, Combining RAFT Polymerization and Thiol-Ene Click Reaction for Core-Shell Structured Polymer@$BaTiO_3$ Nanodielectrics with High Dielectric Constant, Low Dielectric Loss, and High Energy Storage Capability, ***ACS Applied Materials & Interfaces***, 6 (2014), 1812-1822.
118. S. Wang, X. Huang, G. Wang, Y. Wang, J. He, P. Jiang, Increasing the Energy Efficiency and Breakdown Strength of High-Energy-Density Polymer Nanocomposites by Engineering the $Ba_{0.7}Sr_{0.3}TiO_3$ Nanowire Surface via Reversible Addition-Fragmentation Chain Transfer Polymerization, ***The Journal of Physical Chemistry C***, 119 (2015), 25307-25318.
119. G. Wang, X. Huang, P. Jiang, Tailoring Dielectric Properties and Energy Density of Ferroelectric Polymer Nanocomposites by High-k Nanowires, ***ACS Applied Materials & Interfaces***, 7 (2015), 18017-18027.
120. Z.-M. Dang, J.-K. Yuan, J.-W. Zha, P.-H. Hu, D.-R. Wang, Z.-Y. Cheng, High-Permittivity Polymer Nanocomposites: Influence of Interface on Dielectric Properties, ***Journal of Advanced Dielectrics***, 3 (2013), 1330004.
121. X. Zhang, Y. Shen, Q. Zhang, L. Gu, Y. Hu, J. Du, Y. Lin, C.-W. Nan, Ultrahigh Energy Density of Polymer Nanocomposites Containing $BaTiO_3$@TiO_2 Nanofibers by Atomic-Scale Interface Engineering, ***Advanced Materials***, 27 (2015), 819-824.
122. X. Zhang, Y. Shen, B. Xu, Q. Zhang, L. Gu, J. Jiang, J. Ma, Y. Lin, C.-W. Nan, Giant Energy Density and Improved Discharge Efficiency of Solution-Processed Polymer Nanocomposites for Dielectric Energy Storage, ***Advanced Materials***, 28 (2016), 2055-2061.
123. X. Lin, P. Hu, Z. Jia, S. Gao, Enhanced Dlectric Displacement Induces Large Energy Density in Polymer Nanocomposites Containing Core-Shell Structured $BaTiO_3$@TiO_2 Nanofibers, ***Journal of Materials Chemistry A***, 4 (2016), 2314-2320.
124. H. Tang, Z. Zhou, C. C. Bowland, H. A. Sodano, Synthesis of Calcium Copper Titanate ($CaCu_3Ti_4O_{12}$) Nanowires with Insulating SiO_2 Barrier for Low Loss High Dielectric Constant Nanocomposites, ***Nano Energy***, 17 (2015), 302-307.
125. D. He, Y. Wang, X. Chen, Y. Deng, Core-Shell Structured $BaTiO_3$@Al_2O_3 Nanoparticles in Polymer Composites for Dielectric Loss Suppression and Breakdown Strength Enhancement, ***Composites Part A: Applied Science and Manufacturing***, 93 (2017), 137-143.

126. Z. Pan, J. Zhai, B. Shen, Multilayer Hierarchical Interfaces with High Energy Density in Polymer Nanocomposites Composed of $BaTiO_3$@TiO_2@Al_2O_3 Nanofibers, ***Journal of Materials Chemistry A***, 5 (2017), 15217-15226.
127. N. Yousefi, X. Sun, X. Lin, X. Shen, J. Jia, B. Zhang, B. Tang, M. Chan, J.-K. Kim, Highly Aligned Graphene/Polymer Nanocomposites with Excellent Dielectric Properties for High-Performance Electromagnetic Interference Shielding, ***Advanced Materials***, 26 (2014), 5480-5487.
128. D. Zhang, W. Liu, R. Guo, K. Zhou, H. Luo, High Discharge Energy Density at Low Electric Field using an Aligned Titanium Dioxide/Lead Zirconate Titanate Nanowire Array, ***Advanced Science***, 5 (2018), 1700512.
129. B. Xie, H. Zhang, Q. Zhang, J. Zang, C. Yang, Q. Wang, M.-Y. Li, S. Jiang, Enhanced Energy Density of Polymer Nanocomposites at a Low Electric Field through Aligned $BaTiO_3$ Nanowires, ***Journal of Materials Chemistry A***, 5 (2017), 6070-6078.
130. D. Zhang, W. Liu, L. Tang, K. Zhou, H. Luo, High Performance Capacitors via Aligned TiO_2 Nanowire Array, ***Applied Physics Letters***, 110 (2017), 133902.
131. Y. Zhan, Z. Long, X. Wan, C. Zhan, J. Zhang, Y. He, Enhanced Dielectric Permittivity and Thermal Conductivity of Hexagonal Boron Nitride/Poly (arylene ether nitrile) Composites through Magnetic Alignment and Mussel Inspired Co-Modification, ***Ceramics International***, 43 (2017), 12109-12119.
132. D. S. Kim, C. Baek, H. J. Ma, D. K. Kim, Enhanced Dielectric Permittivity of $BaTiO_3$/Epoxy Resin Composites by Particle Alignment, ***Ceramics International***, 42 (2016), 7141-7147.
133. J. Zhu, J. Shen, S. Guo, H.-J. Sue, Confined Distribution of Conductive Particles in Polyvinylidene Fluoride-based Multilayered Dielectrics: Toward High Permittivity and Breakdown Strength, ***Carbon***, 84 (2015), 355-364.
134. V. Tomer, C. Randall, High Field Dielectric Properties of Anisotropic Polymer-Ceramic Composites, ***Journal of Applied Physics***, 104 (2008), 074106.
135. H. Tang, Y. Lin, H. A. Sodano, Enhanced Energy Storage in Nanocomposite Capacitors through Aligned PZT Nanowires by Uniaxial Srain Assembly, ***Advanced Energy Materials***, 2 (2012), 469-476.
136. S. P. Fillery, H. Koerner, L. Drummy, E. Dunkerley, M. F. Durstock, D. F. Schmidt, R. .A. Vaia, Nanolaminates: Increasing Dielectric Breakdown Strength of Composites, ***ACS Applied Materials & Interfaces***, 4 (2012), 1388-1396.
137. B. J. Last, D. J. Thouless, Percolation Theory and Electrical Conductivity, ***Physical Review Letters***, 27 (1971), 1719.
138. S.-H. Yao, Z.-M. Dang, M.-J. Jiang, J. Bai, $BaTiO_3$-Carbon Nanotube/Polyvinylidene Fluoride Three-Phase Composites with High Dielectric Constant and Low Dielectric Loss, ***Applied Physics Letters***, 93 (2008), 182905.
139. Z.-M. Dang, S.-H. Yao, J.-K. Yuan, J. Bai, Tailored Dielectric Properties

based on Microstructure Change in $BaTiO_3$-Carbon Nanotube/Polyvinylidene Fluoride Three-Phase Nanocomposites, ***The Journal of Physical Chemistry C***, 114 (2010), 13204-13209.

140. M.-J. Jiang, Z.-M. Dang, M. Bozlar, F. Miomandre, J. Bai, Broad-Frequency Dielectric Behaviors in Multiwalled Carbon Nanotube/Rubber Nanocomposites, ***Journal of Applied Physics***, 106 (2009), 084902.
141. Q. Li, K. Han, M. R. Gadinski, G. Zhang, Q. Wang, High Energy and Power Density Capacitors from Solution-Processed Ternary Ferroelectric Polymer Nanocomposites, ***Advanced Materials***, 26 (2014), 6244-6249.
142. Q. Li, L. Chen, M. R. Gadinski, S. Zhang, G. Zhang, H. U. Li, E. Lagodkine, A. Haque, L.-Q. Chen, T. N. Jackson, Q. Wang, Flexible High-Temperature Dielectric Materials from Polymer Nanocomposites, ***Nature***, 523 (2015), 576.
143. Q. Li, G. Zhang, F. Liu, K. Han, M. R. Gadinski, C. Xiong, Q. Wang, Solution-Processed Ferroelectric Terpolymer Nanocomposites with High Breakdown Strength and Energy Density Utilizing Boron Nitride Nanosheets, ***Energy & Environmental Science***, 8 (2015), 922-931.
144. L. Wu, K. Wu, D. Liu, R. Huang, J. Huo, F. Chen, Q. Fu, Largely Enhanced Energy Storage Density of Poly (vinylidene fluoride) Nanocomposites based on Surface Hydroxylation of Boron Nitride Nanosheets, ***Journal of Materials Chemistry A***, 6 (2018), 7573-7584.
145. J. Lao, H. Xie, Z. Shi, G. Li, B. Li, G.-H. Hu, Q. Yang, C. Xiong, Flexible Regenerated Cellulose/Boron Nitride Nanosheet High-Temperature Dielectric Nanocomposite Films with High Energy Density and Breakdown Strength, ***ACS Sustainable Chemistry & Engineering***, 6 (2018), 7151-7158.
146. D.-L. Zhang, J.-W. Zha, W.-K. Li, C.-Q. Li, S.-J. Wang, Y. Wen, Z.-M. Dang, Enhanced Thermal Conductivity and Mechanical Property through Boron Nitride Hot String in Polyvinylidene Fluoride Fibers by Electrospinning, ***Composites Science and Technology***, 156 (2018), 1-7.
147. Y. Xie, J. Wang, Y. Yu, W. Jiang, Z. Zhang, Enhancing Breakdown Strength and Energy Storage Performance of PVDF-based Nanocomposites by Adding Exfoliated Boron Nitride, ***Applied Surface Science***, 440 (2018), 1150-1158.
148. F. Liu, Q. Li, Z. Li, Y. Liu, L. Dong, C. Xiong, Q. Wang, Poly (methyl methacrylate)/Boron Nitride Nanocomposites with Enhanced Energy Density as High Temperature Dielectrics, ***Composites Science and Technology***, 142 (2017), 139-144.
149. Y.-J. Xiao, W.-Y. Wang, T. Lin, X.-J. Chen, Y.-T. Zhang, J.-H. Yang, Y. Wang, Z.-W. Zhou, Largely Enhanced Thermal Conductivity and High Dielectric Constant of Poly (vinylidene fluoride)/Boron Nitride Composites Achieved by Adding a few Carbon Nanotubes, ***The Journal of Physical Chemistry C***, 120 (2016), 6344-6355.
150. I. Balberg, A Comprehensive Picture of the Electrical Phenomena in Carbon Black-Polymer Composites, ***Carbon***, 40 (2002), 139-143.
151. X. Huang, P. Jiang, Core-Shell Structured High-k Polymer Nanocomposites for Energy Storage and Dielectric Applications, ***Advanced Materials***, 27

(2015), 546-554.

152. J. Y. Kim, T. Kim, J. W. Suk, H. Chou, J.-H. Jang, J. H. Lee, I. N. Kholmanov, D. Akinwande, R. S. Ruoff, Enhanced Dielectric Performance in Polymer Composite Films with Carbon Nanotube-Reduced Graphene Oxide Hybrid Filler, ***Small***, 10 (2014), 3405-3411.
153. H. Zhao, M.-H. Yang, D. He, J. Bai, Enhanced Dielectric Performance of Polyvinylidene Fluoride Composites with an All-Carbon Hybrid Architecture: Vertically Aligned Carbon Nanotube Arrays on Graphite Nanoplatelets, ***Journal of Materials Chemistry C***, 4 (2016), 8911-8919.
154. Z.-M. Dang, H.-P. Xu, and H.-Y. Wang, Significantly Enhanced Low-Frequency Dielectric Permittivity in the $BaTiO_3$/Poly (vinylidene fluoride) Nanocomposite, ***Applied Physics Letters***, 90 (2007), 012901.
155. Z.-M. Dang, T. Zhou, S.-H. Yao, J.-K. Yuan, J.-W. Zha, H.-T. Song, J.-Y. Li, Q. Chen, W.-T. Yang, J. Bai, Advanced Calcium Copper Titanate/Polyimide Functional Hybrid Films with High Dielectric Permittivity, ***Advanced Materials***, 21 (2009), 2077-2082.
156. Y. Li, X. Huang, Z. Hu, P. Jiang, S. Li, T. Tanaka, Large Dielectric Constant and High Thermal Conductivity in Poly (vinylidene fluoride)/Barium Titanate/Silicon Carbide Three-Phase Nanocomposites, ***ACS Applied Materials & Interfaces***, 3 (2011), 4396-4403.
157. Y. Shen, Y. Lin, C.-W. Nan, High Dielectric Performance of Polymer Composite Films Induced by a Percolating Interparticle Barrier Layer, ***Advanced Materials***, 19 (2007), 1418-1422.
158. X. Zhao, J. Zhao, J.-P. Cao, X. Wang, M. Chen, Z.-M. Dang, Tuning the Dielectric Properties of Polystyrene/Poly (vinylidene fluoride) Blends by Selectively Localizing Carbon Black Nanoparticles, ***The Journal of Physical Chemistry B***, 117 (2013), 2505-2515.
159. X. Yin, J.-F. Capsal, D. Guyomar, A Comprehensive Investigation of Poly (vinylidene fluoride-trifluoroethylene-chlorofluoroethylene) Terpolymer Nanocomposites with Carbon Black for Electrostrictive Applications, ***Applied Physics Letters***, 104 (2014), 052913.
160. Z. Wang, J. K. Nelson, H. Hillborg, S. Zhao, L. S. Schadler, Graphene Oxide Filled Nanocomposite with Novel Electrical and Dielectric Properties, ***Advanced Materials***, 24 (2012), 3134-3137.
161. J. Yuan, A. Luna, W. Neri, C. Zakri, T. Schilling, A. Colin, P. Poulin, Graphene Liquid Crystal Retarded Percolation for New High-k Materials, ***Nature Communications***, 6 (2015), 8700.
162. A. Ameli, M. Arjmand, P. Potschke, B. Krause, U. Sundararaj, Effects of Synthesis Catalyst and Temperature on Broadband Dielectric Properties of Nitrogen-Doped Carbon Nanotube/Polyvinylidene Fluoride Nanocomposites, ***Carbon***, 106 (2016), 260-278.
163. M. Arjmand, U. Sundararaj, Effects of Nitrogen Doping on X-Band Dielectric Properties of Carbon Nanotube/Polymer Nanocomposites, ***ACS Applied Materials & Interfaces***, 7 (2015), 17844-17850.

164. C.-W. Nan, Y. Shen, J. Ma, Physical Properties of Composites Near Percolation, ***Annual Review of Materials Research***, 40 (2010), 131-151.
165. J. Yuan, S. Yao, W. Li, A. Sylvestre, J. Bai, Vertically Aligned Carbon Nanotube Arrays on SiC Microplatelets: A High Figure-of-Merit Strategy for Achieving Large Dielectric Constant and Low Loss in Polymer Composites, ***The Journal of Physical Chemistry C***, 118 (2014), 22975-22983.
166. Q. Li, P. Peng, G.-X. Chen, S. W. Yoon, High-k Polymer/Carbon Nanotube Composites based on a Polyhedral Oligomeric Silsesquioxane Matrix Facilitated by Ionic Liquid, ***Journal of Materials Chemistry C***, 2 (2014), 8216-8221.
167. Y. Zhou, Y. Bai, K. Yu, Y. Kang, H. Wang, Excellent Thermal Conductivity and Dielectric Properties of Polyimide Composites Filled with Silica Coated Self-Passivated Aluminum Fibers and Nanoparticles, ***Applied Physics Letters***, 102 (2013), 252903.
168. A. Mahadevegowda, N. P. Young, P. S. Grant, Engineering the Nanostructure of a Polymer-Nanocomposite Film Containing Ti-based Core-Shell Particles to Enhance Dielectric Response, ***Nanoscale***, 7 (2015), 15727-15733.
169. J. E. Q. Quinsaat, M. Alexandru, F. A. Nuesch, H. Hofmann, A. Borgschulte, D. M. Opris, Highly Stretchable Dielectric Elastomer Composites Containing High Volume Fractions of Silver Nanoparticles, ***Journal of Materials Chemistry A***, 3 (2015), 14675-14685.
170. W. Li, J. Yuan, Y. Lin, S. Yao, Z. Ren, H. Wang, M. Wang, J. Bai, The Controlled Formation of Hybrid Structures of Multi-Walled Carbon Nanotubes on SiC Plate-like Particles and their Synergetic Effect as a Filler in Poly (vinylidene fluoride) based Composites, ***Carbon***, 51 (2013), 355-364.
171. D. He, M. Bozlar, M. Genestoux, J. Bai, Diameter-and Length-Dependent Self-Organizations of Multi-Walled Carbon Nanotubes on Spherical Alumina Microparticles, ***Carbon***, 48 (2010), 1159-1170.
172. Y. Lin, A. Dichiara, D. He, P. Haghi-Ashtiani, J. Bai, Uniform Diameter Multi-Walled Carbon Nanotubes with a Controlled Wall Number Obtained by a Simple Chemical Vapor Deposition Method, ***Chemical Physics Letters***, 554 (2012), 137-142.
173. J. Wang, J. Wu, W. Xu, Q. Zhang, Q. Fu, Preparation of Poly (vinylidene fluoride) Films with Excellent Electric Property, Improved Dielectric Property and Dominant Polar Crystalline Forms by Adding a Quaternary Phosphorus Salt Functionalized Graphene, ***Composites Science and Technology***, 91 (2014), 1-7.
174. R. R. Kohlmeyer, A. Javadi, B. Pradhan, S. Pilla, K. Setyowati, J. Chen, S. Gong, Electrical and Dielectric Properties of Hydroxylated Carbon Nanotube-Elastomer Composites, ***The Journal of Physical Chemistry C***, 113 (2009), 17626-17629.
175. Y. Wu, X. Lin, X. Shen, X. Sun, X. Liu, Z. Wang, J.-K. Kim, Exceptional Dielectric Properties of Chlorine-Doped Graphene Oxide/Poly (vinylidene fluoride) Nanocomposites, ***Carbon***, 89 (2015), 102-112.

176. K. Wu, C. Lei, W. Yang, S. Chai, F. Chen, Q. Fu, Surface Modification of Boron Nitride by Reduced Graphene Oxide for Preparation of Dielectric Material with Enhanced Dielectric Constant and Well-Suppressed Dielectric Loss, ***Composites Science and Technology***, 134 (2016), 191-200.
177. M. Yang, H. Zhao, D. He, J. Bai, Largely Enhanced Dielectric Properties of Carbon Nanotubes/Polyvinylidene Fluoride Binary Nanocomposites by Loading a few Boron Nitride Nanosheets, ***Applied Physics Letters***, 109 (2016), 072906.
178. X. Ding, G. Ding, X. Xie, F. Huang, M. Jiang, Direct Growth of few Layer Graphene on Hexagonal Boron Nitride by Chemical Vapor Deposition, ***Carbon***, 49 (2011), 2522-2525.
179. D. He, H. Li, J. Bai, Experimental and Numerical Investigation of the Position-Dependent Growth of Carbon Nanotube-Alumina Microparticle Hybrid Structures in a Horizontal CVD Reactor, ***Carbon***, 49 (2011), 5359-5372.
180. D. He, H. Li, W. Li, P. Haghi-Ashtiani, P. Lejay, J. Bai, Growth of Carbon Nanotubes in Six Orthogonal Directions on Spherical Alumina Microparticles, ***Carbon***, 49 (2011), 2273-2286.
181. H. Tang, M. H. Malakooti, H. A. Sodano, Relationship between Orientation Factor of Lead Zirconate Titanate Nanowires and Dielectric Permittivity of Nanocomposites, ***Applied Physics Letters***, 103 (2013), 222901.
182. H. Tang, H. A. Sodano, High Energy Density Nanocomposite Capacitors using Non-Ferroelectric Nanowires, ***Applied Physics Letters***, 102 (2013), 063901.
183. M. Bozlar, D. He, J. Bai, Y. Chalopin, N. Mingo, S. Volz, Carbon Nanotube Microarchitectures for Enhanced Thermal Conduction at Ultralow Mass Fraction in Polymer Composites, ***Advanced materials***, 22 (2010), 1654-1658.
184. D. He, B. Fan, H. Zhao, X. Lu, M. Yang, Y. Liu, J. Bai, Design of Electrically Conductive Structural Composites by Modulating Aligned CVD-Grown Carbon Nanotube Length on Glass Fibers, ***ACS Applied Materials & Interfaces***, 9 (2017), 2948-2958.
185. T. Xia, W. Zhang, Z. Wang, Y. Zhang, X. Song, J. Murowchick, V. Battaglia, G. Liu, X. Chen, Amorphous Carbon-Coated TiO_2 Nanocrystals for Improved Lithium-Ion Battery and Photocatalytic Performance, ***Nano Energy***, 6 (2014), 109-118.
186. M. M. Rahman, J.-Z. Wang, M. F. Hassan, D. Wexler, H. K. Liu, Amorphous Carbon Coated High Grain Boundary Density Dual Phase $Li_4Ti_5O_{12}$-TiO_2: A Nanocomposite Anode Material for Li-Ion Batteries, ***Advanced Energy Materials***, 1 (2011), 212-220.
187. M. M. Alam, S. K. Ghosh, D. Sarkar, S. Sen, D. Mandal, Improved Dielectric Constant and Breakdown Strength of γ-Phase Dominant Super Toughened Polyvinylidene Fluoride/TiO_2 Nanocomposite Film: An Excellent Material for Energy Storage Applications and Piezoelectric Throughput, ***Nanotechnology***, 28 (2016), 015503.

188. S. K. Ghosh, W. Rahman, T. R. Middya, S. Sen, D. Mandal, Improved Breakdown Strength and Electrical Energy Storage Performance of γ-Poly (vinylidene fluoride)/Unmodified Montmorillonite Clay Nano-Dielectrics, ***Nanotechnology***, 27 (2016), 215401.
189. S. K. Ghosh, M. M. Alam, D. Mandal, The in situ Formation of Platinum Nanoparticles and their Catalytic Role in Electroactive Phase Formation in Poly (vinylidene fluoride): A Simple Preparation of Multifunctional Poly (vinylidene fluoride) Films Doped with Platinum Nanoparticles, ***RSC Advances***, 4 (2014), 41886-41894.
190. M. M. Alam, A. Sultana, D. Sarkar, D. Mandal, Electroactive β-Crystalline Phase Inclusion and Photoluminescence Response of a Heat-Controlled Spin-Coated PVDF/TiO_2 Free-Standing Nanocomposite Film for a Nanogenerator and an Active Nanosensor, ***Nanotechnology***, 28 (2017), 365401.
191. M. Yang, H. Zhao, C. Hu, P. Haghi-Ashtiani, D. He, Z.-M. Dang, J. Bai, Largely Enhanced Dielectric Constant of PVDF Nanocomposites through a Core-Shell Strategy, ***Physical Chemistry Chemical Physics***, 20 (2018), 2777-2786.
192. D. He, Y. Wang, S. Song, S. Liu, Y. Deng, Significantly Enhanced Dielectric Performances and High Thermal Conductivity in Poly (vinylidene fluoride)-Based Composites Enabled by SiC@SiO_2 Core-Shell Whiskers Alignment, ***ACS Applied Materials & Interfaces***, 9 (2017), 44839-44846.
193. M. Yang, H. Zhao, D. He, C. Hu, H. Chen, J. Bai, Carbon Coated Boron Nitride Nanosheets for Polymer Nanocomposites with Enhanced Dielectric Performance, ***Materials***, 10 (2017), 741.
194. D. He, Y. Wang, S. Song, S. Liu, Y. Luo, Y. Deng, Polymer-based Nanocomposites Employing Bi_2S_3@SiO_2 Nanorods for High Dielectric Performance: Understanding the Role of Interfacial Polarization in Semiconductor-Insulator Core-Shell Nanostructure, ***Composites Science and Technology***, 151 (2017), 25-33.
195. Z. Pan, L. Yao, J. Zhai, B. Shen, S. Liu, H. Wang, J. Liu, Excellent Energy Density of Polymer Nanocomposites Containing $BaTiO_3$@Al_2O_3 Nanofibers Induced by Moderate Interfacial Area, ***Journal of Materials Chemistry A***, 4 (2016), 13259-13264.
196. Z. Pan, L. Yao, J. Zhai, D. Fu, B. Shen, H. Wang, High-Energy-Density Polymer Nanocomposites Composed of newly Structured One-Dimensional $BaTiO_3$@Al_2O_3 Nanofibers, ***ACS Applied Materials & Interfaces***, 9 (2017), 4024-4033.
197. L. Xie, X. Huang, Y. Huang, K. Yang, P. Jiang, Core@Double-Shell Structured $BaTiO_3$-Polymer Nanocomposites with High Dielectric Constant and Low Dielectric Loss for Energy Storage Application, ***The Journal of Physical Chemistry C***, 117 (2013), 22525-22537.
198. Y. Huang, X. Huang, L. S. Schadler, J. He, P. Jiang, Core@Double-Shell Structured Nanocomposites: A Route to High Dielectric Constant and Low loss Material, ***ACS Applied Materials & Interfaces***, 8 (2016), 25496-25507.

199. M. Yang, C. Hu, H. Zhao, P. Haghi-Ashtiani, D. He, Y. Yang, J. Yuan, J. Bai, Core@Double-Shells Nanowires Strategy for Simultaneously Improving Dielectric Constants and Suppressing Losses of Poly (vinylidene fluoride) Nanocomposites, ***Carbon,*** 132 (2018), 152-156.
200. K. Ding, B. Hu, Y. Xie, G. An, R. Tao, H. Zhang, Z. Liu, A Simple Route to Coat Mesoporous SiO_2 Layer on Carbon Nanotubes, ***Journal of Materials Chemistry***, 19 (2009), 3725-3731.
201. M. Zhang, Y. Wu, X. Feng, X. He, L. Chen, Y. Zhang, Fabrication of Mesoporous Silica-Coated CNTs and Application in Size-Selective Protein Separation, ***Journal of Materials Chemistry***, 20 (2010), 5835-5842.

Publications

1. **M. Yang**, C. Hu, H. Zhao, P. Haghi-Ashtiani, D. He, Y. Yang, J. Yuan, J. Bai, Core@Double-Shells Nanowires Strategy for Simultaneously Improving Dielectric Constants and Suppressing Losses of Poly(vinylidene fluoride) Nanocomposites, ***Carbon***, 132 (2018), 152-156. (**Impact Factor: 7.082**)

2. **M. Yang**, H. Zhao, C. Hu, P. Haghi-Ashtiani, D. He, Z.-M. Dang, J. Bai, Largely Improved Dielectric Constant of Polyvinylidene Fluoride Nanocomposites through a Core-Shell Strategy, ***Physical Chemistry Chemical Physics***, 20 (2018), 2777-2786. (**2018 PCCP HOT Article**) (**Impact Factor: 3.906**)

3. **M. Yang**, H. Zhao, D. He, J. Bai, Constructing a Continuous Amorphous Carbon Interlayer to Enhance Dielectric Performance of Carbon Nanotubes/Polyvinylidene Fluoride Nanocomposites, ***Carbon***, 116 (2017), 94-102. (**Impact Factor: 7.082**)

4. **M. Yang**, H. Zhao, D. He, C. Hu, H. Chen, J. Bai, Carbon Coated Boron Nitride Nanosheets for Polymer Nanocomposites with Enhanced Dielectric Performance, ***Materials***, 10 (2017), 741. (**Impact Factor: 2.467**)

5. **M. Yang**, H. Zhao, D. He, J. Bai, Largely Enhanced Dielectric Properties of Carbon Nanotubes/Polyvinylidene Fluoride Binary Nanocomposites by Loading a few Boron Nitride Nanosheets, ***Applied Physics Letters***, 109 (2016), 072906. (**Impact Factor: 3.495**)

6. **M. Yang**, H. Zhao, C. Hu, P. Haghi-Ashtiani, D. He, J. Bai, Regulating Dielectric Performances of PVDF Nanocomposites by Individually Controlling Shell Thickness of Core@Double-Shells Structured Nanowires, 2018, ***Submitted***.

7. **M. Yang**, C. Hu, H. Zhao, P. Haghi-Ashtiani, L. Yedra, J. Yuan, D. He, J. Bai, Multilayer Hierarchical TiO_2@Carbon@Al_2O_3 Nanowires for High Energy Density Polymer Nanocomposites with Adjustable Feature, 2018, ***In Preparation***.

8. H. Zhang, S. Feng, D. He, Y. Xu, **M. Yang**, J. Bai, An Electret Film-based Triboelectric Nanogenerator with Largely Improved Performance via a Tape-Peeling Charging Method, ***Nano Enegy***, 48 (2018), 256-265.

9. Y. Liu, Y. Xu, B. Fan, **M. Yang**, A. Hamon, P. Haghi-Ashtiani, D. He, J. Bai,

Constructing 3D CNTs-SiO2@RGO Structures by using GO Sheets as Template, ***Chemical Physics Letters***, 713 (2018), 189-193.

10. Y. Yang, **M. Yang**, S. Zhang, X. Lin, Z. Dang, D. Wang, Photoinduced Healing of Polyolefin Dielectrics Enabled by Surface Plasmon Resonance of Gold Nanoparticles, ***Journal of Applied Polymer Science***, 2018, In press.

11. D. He, B. Fan, H. Zhao, X. Lu, **M. Yang**, Y. Liu, J. Bai, Design of Electrically Conductive Structural Composites by Modulating Aligned CVD-Grown Carbon Nanotube Length on Glass Fibers, ***ACS Applied Materials & Interfaces***, 9 (2017), 2948-2958.

12. D. He, B. Fan, H. Zhao, **M. Yang**, H. Wang, J. Bai, W. Li, X. Zhou, J. Bai, Multifunctional Polymer Composites Reinforced by Carbon Nanotubes-Alumina Hybrids with Urchin-like Structure, ***Materials Today Communications***, 11 (2017), 94-102.

13. H. Zhao, **M.Yang**, D. He, J. Bai, Enhanced Dielectric Performance of Polyvinylidene Fluoride Composites with an All-Carbon Hybrid Architecture: Vertically Aligned Carbon Nanotube Arrays on Graphite Nanoplatelets, ***Journal of Materials Chemistry C***, 4 (2016), 8911-8919.

14. X. Lin, Y. Wu, L. Tang, **M. Yang**, D. Ren, J. Zha, Z. Dang, Experimental Study of the Rheological, Mechanical, and Dielectric Properties of MgO/LDPE Nanocomposites, ***Journal of Applied Polymer Science***, 133 (2016), 43038.

15. H. Zhao, **M. Yang**, D. He, Y. Liu, J. Bai, H. Wang, H. Chen, J. Bai, Typical Synergistic Effect of Graphite Nanoplatelets and Carbon Nanotubes and its Influence on Polymer-based Dielectric Composites, ***High Voltage***, 1 (2016), 140-145.

16. H. Zhao, L. Zhang, **M. Yang**, Z. Dang, J. Bai, Temperature-dependent Electro-Mechanical Actuation Sensitivity in Stiffness-Tunable $BaTiO_3$/Polydimethylsiloxane Dielectric Elastomer Nanocomposites, ***Applied Physics Letters***, 106 (2015), 092904.

17. Z. Wang, J. Zhao, M. Chen, **M. Yang**, L. Tang, Z. Dang, F. Chen, M. Huang, X. Dong, Dually Actuated Triple Shape Memory Polymers of Cross-Linked Polycyclooctene-Carbon Nanotube/Polyethylene Nanocomposites, ***ACS Applied***

Materials & Interfaces, 6 (2014), 20051-20059.

Titre: Conception rationnelle de nano-hybrides de carbone 1D pour l'application de nanocomposites diélectriques

Mots clés: Nanocomposites polymères diélectriques; Constante diélectrique; Perte diélectrique; Nanofils; Coeur-coquille

Résumé: Les nanocomposites polymères diélectriques ayant une constante diélectrique élevée et une faible perte diélectrique ont reçu un large intérêt pour une large application dans le domaine du condensateur électrostatique. De manière générale, les performances diélectriques des nanocomposites sont déterminées par le type et la nature des polymères et des nanocharges sélectionnées, ainsi que par l'effet de couplage interfacial entre la matrice et les nanocharges. Selon les conductivités des nanocharges, les nanocomposites polymères diélectriques peuvent être classés en deux catégories: les nanocomposites polymères diélectriques avec des nanocharges conductrices (CDPN) et les nanocomposites polymères diélectriques avec des nanocharges céramiques à constante diélectrique élevée (DDPN). Cependant, la perte diélectrique élevée accompagnée au voisinage du seuil de percolation pour les CDPN et la charge élevée de nanocharges en céramique entravent le développement de nanocomposites polymères diélectriques à haute performance. Cette thèse portera sur l'augmentation de la constante diélectrique et la suppression de la forte perte diélectrique des nanocomposites polymères diélectriques en optimisant rationnellement la structure des nanocharges sélectionnées.

Tout d'abord, les nanocomposites ternaires BNNS/CNTs/PVDF ont été fabriqués. L'incorporation de BNNS dans les nanocomposites binaires CNTs/PVDF a permis d'améliorer la dispersion des CNTs et d'optimiser le réseau conducteur. La connexion directe entre CNTs pourrait être entravée en augmentant le contenu de BNNS.

Deuxièmement, des hybrides CNT@AC à structure cœur-coquille ont été préparés par la méthode CVD et ont ensuite été utilisés pour préparer des nanocomposites. La couche de carbone amorphe entrave le contact direct des CNTs, mais améliore également la dispersibilité des CNTs. Le seuil de percolation augmente avec la prolongation du temps de dépôt du carbone. En plus, la perte diélectrique a subi une forte diminution après le processus de revêtement, ce qui a été attribué à la diminution du courant de fuite.

Troisièmement, les hybrides BNNSs@C avec des teneurs en carbone différentes ont été synthétisés par la méthode CVD. La fraction de carbone dans les hybrides BNNSs@C ainsi obtenus a été ajustée en faisant varier le temps de dépôt de carbone. Les nanocomposites BNNSs@C/PVDF obtenus ont présenté une excellente performance diélectrique qui ont pu être ajustées avec précision en ajustant la teneur en carbone.

Quatrièmement, on a synthétisé des nanofils de TiO_2@C avec une enveloppe de carbone uniforme en combinant une réaction hydrothermale et la méthode CVD. L'épaisseur de la couche de carbone pourrait être précisément ajustée en contrôlant le temps de dépôt du carbone. Les nanofils de TiO_2@C ont ensuite été introduits dans une matrice de PVDF pour préparer des nanocomposites. De plus, les propriétés diélectriques des nanocomposites avec nanofils de TiO_2@C pourraient être ajustées avec précision en ajustant l'épaisseur de la coque en carbone.

Enfin, des nanofils de TiO_2@C@SiO_2 structurés à double coques ont été synthétisés par une combinaison de réactions hydrothermales modifiées, de CVD et de réactions sol-gel. Les nanocomposites de PVDF avec les nanofils de TiO_2@C@SiO_2 présentaient simultanément une constante diélectrique améliorée et des caractéristiques de perte diélectrique dimuniée. En outre, le noyau à double coque nanofils de TiO_2@C@SiO_2 structuré avec une coque en carbone et une épaisseur de coque SiO_2 variables a été obtenu en ajustant individuellement le temps CVD et la quantité de tétraéthyle orthosilicate. La constante diélectrique des nanocomposites a été augmenté avec l'épaisseur de la couche interne de carbone et la perte diélectrique a été diminuée avec l'épaisseur de la couche externe de SiO_2. La relation entre la perte diélectrique et l'épaisseur de l'enveloppe extérieure en SiO_2 a été démontrée par les résultats de la simulation finie.

université PARIS-SACLAY
ÉCOLE DOCTORALE
Sciences mécaniques et énergétiques, matériaux et géosciences (SMEMAG)

Title: Rational design of 1D carbon nano-hybrids for dielectric nanocomposites application

Keywords: Dielectric Polymer Nanocomposites; Nanofillers; Dielectric Constant; Dielectric Loss; Nanowires; Core@Shell

Abstract: Dielectric polymer nanocomposites with a high dielectric constant and low dielectric loss have received broad interest for use in the field of the electrostatic capacitor and they are usually composed of dielectric polymers as matrix and inorganic or organic nanofillers as the reinforcement. Generally, the improved dielectric performance of nanocomposites is decided by the type and nature of selected polymers and nanofillers as well as interfacial coupling effect between matrices and nanofillers. Among these factors, the physical properties, geometries, component structures of nanofillers play a critical role in deciding the dielectric performance of nanocomposites. According to the conductivities of nanofillers, the dielectric polymer nanocomposites can be classified into two types: conductive-dielectric polymer nanocomposites (CDPNs) and dielectric-dielectric polymer nanocomposites (DDPNs). However, the accompanied high dielectric loss in the vicinity of the percolation threshold for CDPNs and high loading of ceramic nanofillers hinders the development of high performance dielectric nanocomposites.

Firstly, ternary BNNSs/CNTs/PVDF nanocomposites were fabricated. The incorporation of BNNSs into the binary CNTs/PVDF nanocomposites improved the dispersion of CNTs and optimized the conductive network, which contributed to the enhanced dielectric constant. The direct connection between CNTs could be hindered by increasing the content of BNNS.

Secondly, core-shell structured CNTs@AC hybrids were prepared by CVD method. The amorphous carbon layer not only hindered the direct contact of CNTs but also improved the dispersibility of CNTs in the PVDF matrix. The percolation threshold increased with the prolongation of carbon deposition time. More importantly, the dielectric loss underwent a sharp decrease after the coating process, which was attributed to the decrease in leakage current. The results suggested that the influence of AC interlayer on the final dielectric performance after percolation was much more obvious than that before percolation.

Thirdly, BNNSs@C hybrids were synthesized by the CVD method. The carbon fraction in the BNNSs@C hybrids could be adjusted through controlling the carbon deposition time. The dielectric properties of BNNSs@C/PVDF nanocomposites could be tuned by adjusting the carbon content. The improved interfacial polarizations of BNNSs/C and C/PVDF interfaces endowed the nanocomposites with enhanced dielectric performance.

Fourthly, core-shell structured TiO_2@C NW hybrids were synthesized by a combination of a hydrothermal reaction and the CVD method. The carbon shell thickness in the obtained TiO_2@C NW hybrids could be precisely tuned by controlling the carbon deposition time. The TiO_2@C NWs/PVDF nanocomposites exhibited a percolative dielectric behavior. Moreover, the dielectric properties of the TiO_2@C NWs/PVDF nanocomposites could be accurately adjusted by tuning the carbon shell thickness. The enhanced interfacial polarizations of the TiO_2/C and C/PVDF interfaces endowed the nanocomposites with excellent dielectric performance.

Lastly, core@double-shells structured TiO_2@C@SiO_2 nanowires were synthesized by a combination of modified hydrothermal reaction, CVD, and sol-gel reaction. The introducing of carbon as an inner shell between the TiO_2 core and SiO_2 outer shell induced two additional types of interfacial polarization. The obtained PVDF nanocomposites with TiO_2@C@SiO_2 NWs exhibited simultaneously enhanced dielectric constant and suppressed dielectric loss characteristics. The dielectric constant and loss of nanocomposites increased with the increase of carbon inner shell thickness and decreased with the increasing of SiO_2 outer shell thickness. The relationship between the dielectric loss and SiO_2 outer shell thickness was further demonstrated by the finite simulation results.

Université Paris-Saclay
Espace Technologique / Immeuble Discovery
Route de l'Orme aux Merisiers RD 128 / 91190 Saint-Aubin, France